Dynamics and correlations of driven diffusive systems

Alexis Poncet

THÈSE DE DOCTORAT
DE SORBONNE UNIVERSITÉ

Spécialité : Physique

École doctorale n°564 : Physique en Île-de-France

réalisée

au Laboratoire de physique théorique de la matière condensée

sous la direction d'Olivier BÉNICHOU et Vincent DÉMERY

présentée par

Alexis PONCET

pour obtenir le grade de :

DOCTEUR DE SORBONNE UNIVERSITÉ

Sujet de la thèse :

Dynamique et corrélations de systèmes diffusifs forcés

Dynamics and correlations of driven diffusive systems

soutenue le 15 septembre 2020

devant le jury composé de :

M.	Éric BERTIN	Rapporteur
M.	Andrea PARMEGGIANI	Rapporteur
M.	Jean-François JOANNY	Examinateur, Président du jury
Mme	Cécile APPERT-ROLLAND	Examinatrice
M.	Thomas GUÉRIN	Examinateur
M.	Olivier BÉNICHOU	Directeur de thèse
M.	Vincent DÉMERY	Invité

Contents

Chapitre 0

Résultats principaux

Table des matières

0.1 Introduction

Les systèmes avec un grand nombre de particules en interaction sont omniprésents dans la nature. Des petites aux grandes échelles nous pouvons citer les liquides [1] et solutions électrolytiques [2] ; le transport en milieu confiné dans des nanotubes [3, 4], zéolites [5–7] et microcanaux [8–10] ; les systèmes biologiques comme les colonies de bactéries [11–13] et les moteurs moléculaires [14] ; ou encore les foules de piétons [15–17], nuages d'oiseaux [18] et troupeaux de moutons [19]. Alors que les systèmes sans interaction (gaz parfait, phonons dans les solides, etc.) sont bien connus [20–23], la caractérisation de l'influence des interactions est un enjeu fondamental de la physique statistique moderne. Nous nous intéresserons particulièrement aux systèmes hors d'équilibre, c'est-à-dire ceux pour lesquels de l'énergie est injectée, soit à grande

échelle (par exemple via un champ électrique extérieur), soit à l'échelle des particules (matière active). Indépendamment des détails du système, nous nous poserons deux questions génériques qui structureront notre approche. Quelles sont les observables pertinentes pour caractériser les systèmes en interaction ? Et quel type de théorie nous donnera ces observables ?

Cette thèse est divisée en deux parties. La première concernera les systèmes en file et en particulier le processus symétrique d'exclusion. Nous verrons que ces systèmes présentent un comportement anormal de sous-diffusion lié à de fortes contraintes géométriques. Alors que la littérature s'est principalement focalisée sur les conséquences de ces contraintes sur une seule particle, notre but sera de les caractériser à l'aide d'observables à plusieurs points : corrélations et réponse à un forçage local. Nous utiliserons deux types d'approches : une approche exactement soluble à haute densité, et des équations hydrodynamiques valables à toute densité. La deuxième partie s'intéressera à des systèmes bidimensionnels forcés et actifs : le mélange binaire forcé et les particules browniennes actives. Les questions ouvertes sous-jacentes sont le problème de l'alignement pour des populations entraînées dans des directions différentes, et l'étude d'un liquide actif dans sa phase homogène. Nous montrerons que le comportement collectif de ces systèmes peut être étudié à travers la structure spatiale des fonctions de corrélation de paire, qui sont anisotropes, ainsi que par leur décroissance à grande distance. Notre approche sera basée sur l'équation de Dean, une équation exacte pour le champ fluctuant de densité, mais difficile à manipuler. Nous la linéariserons autour d'un profil uniforme [2,24,25] et obtiendrons ainsi des résultats analytiques dans une limite de faible interaction.

0.2 Systèmes en file et processus symétrique d'exclusion

La première partie de cette thèse est consacrée aux systèmes en file (*single-file systems*) et en particulier au processus symétrique d'exclusion (*symmetric exclusion process*, SEP). Les systèmes en file (Chap. 2) correspondent à des particules diffusives dans une géométrie quasi-unidimensionnelle où elles ne peuvent pas se dépasser. L'ordre des particules est donc conservé à tout temps. Expérimentalement, ce type de géométrie a été observé dans des zéolites [5–7], des systèmes de colloïdes [8–10] ou des nanotubes de carbone [3,4]. Une particularité importante des systèmes en file est que le mouvement $X(t)$ d'une particule donnée est sous-diffusif, avec une variance $\langle X(t)^2\rangle \propto t^{1/2}$ (au lieu de t pour un mouvement diffusif). Ceci est une conséquence de fortes corrélations spatiales, essentiellement ignorées jusque-là, que nous chercherons à caractériser.

Un modèle de système en file très étudié historiquement [26,27] est le processus symétrique d'exclusion (Fig. 0.1 avec $p_1 = p_{-1} = 1/2$). La solution complète pour la loi à un point n'a été trouvée que récemment [28,29]. Le problème général de la caractérisation des corrélations du SEP reste ouvert, les résultats connus se concentrant sur les corrélations à deux points (souvent à l'ordre le plus bas) de modèles plus restrictifs [30–34]. De plus, très peu de travaux s'intéressent aux corrélations dans un système avec une ou plusieurs particules biaisées alors que ces observables permettent de discuter l'existence de théorèmes de fluctuation-dissipation généralisés [35]. Ici, nous obtenons des résultats explicites sur les corrélations du SEP et sur les effets collectifs en présence de particules biaisées.

Nous nous intéresserons dans un premier temps à la limite dense du SEP, en utilisant une approche exacte. Nous étudierons les effets collectifs et les corrélations aussi bien dans le SEP habituel qu'en présence d'une ou plusieurs particules biaisées. Dans un deuxième temps, nous développerons des approches hydrodynamiques pour le champ de densité du SEP. Celles-ci permettrons en outre d'étendre certains résultats à des systèmes en file arbitraires. Nous mettrons en lumière une transition de déliaison qui se produit entre deux particules forcées dans une géo-

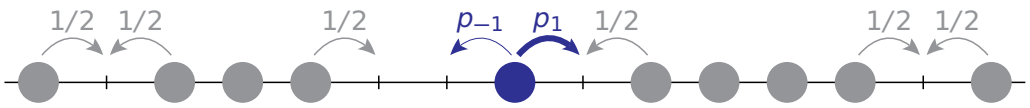

Figure 0.1 : Processus simple d'exclusion (SEP) avec une particule biaisée (en bleu). Le biais sur la particule est $s_1 = p_1 - p_{-1}$.

métrie en file. Puis nous développerons une nouvelle approche hydrodynamique pour des profils généralisés permettant d'obtenir une caractérisation complète à un point dans certaines limites.

0.2.1 Processus symétrique d'exclusion à haute densité

Nous étudions dans un premier temps le cas du SEP avec N particules marquées (*tagged particles*, TP) et éventuellement biaisées (Fig. 0.1, une particule biaisée). Nous appelons ρ la densité, c'est-à-dire la fraction de sites occupés. Notre approche à haute densité ($\rho \to 1$) repose sur l'étude des marches aléatoires des lacunes (sites vides), que l'on considérera comme indépendantes dans cette limite dense [36–39].

a) Méthode

L'observable clé dans un SEP où N particules sont marquées est la fonction génératrice des cumulants associés aux déplacements $Y_i(t)$ de ces particules marquées (TP).

$$\psi^{(t)}(\mathbf{k}) \equiv \ln\left\langle e^{i[k_1 Y_1(t)+\cdots+k_N Y_N(t)]}\right\rangle \equiv \sum_{p_1=0}^{\infty}\cdots\sum_{p_N=0}^{\infty}\frac{(ik_1)^{p_1}\dots(ik_N)^{p_N}}{p_1!\dots p_N!}\kappa^{(N)}_{p_1,\dots,p_N}(t) \tag{0.1}$$

Le développement en puissances de $\mathbf{k}$ donne les cumulants à N points $\kappa^{(N)}_{p_1,\dots,p_N}$ (déplacements, variances, corrélations, etc.). Nous cherchons à déterminer ψ à haute densité $\rho = 1-\rho_0$ avec ρ_0 faible. Nous montrons que les sites vides, qui sont en faible nombre, peuvent être considérés comme des marcheurs aléatoires indépendants [36–39]. Dès lors, l'étude se restreint au problème où un seul site du système est vide. Si cette unique lacune est initialement à la position Z, nous considérons la probabilité $p_Z^{(t)}(Y_1,\dots,Y_N)$ d'observer des déplacements Y_i à l'instant t. À haute densité, la fonction génératrice [Éq. (0.1)] peut alors s'exprimer simplement en fonction de cette quantité :

$$\lim_{\rho_0\to 0}\frac{\psi^{(t)}(\mathbf{k})}{\rho_0} = \sum_{Z\notin\{X_i^0\}}\left(\tilde{p}_Z^{(t)}(\mathbf{k})-1\right), \tag{0.2}$$

où $p_Z^{(t)}(\mathbf{k}) = \sum_{Y_1,\dots Y_N} e^{i(k_1Y_1+\cdots+k_NY_N)}p_Z^{(t)}(Y_1,\dots,Y_N)$ est une transformée de Fourier et X_i^0 est la position initiale de la TP i.

Le problème à haute densité se ramène donc à l'étude d'une unique lacune, considérée comme un marcheur aléatoire, qui génère les déplacements des N particules marquées. Cette étude sera effectuée, que les TP soient biaisées ou non, grâce à des résultats standards sur les marches aléatoires [40] : probabilité de premier passage d'une marche de Polya, probabilité de premier passage avec sites absorbants, etc.

b) Résultats à une seule particule

Le cas d'une unique TP biaisée (Fig. 0.1 et Chap. 3) est celui de la référence [38]. Nous retrouvons le résultat de temps long pour la fonction génératrice,

$$\lim_{\rho_0\to 0}\frac{\psi^{(t)}(k)}{\rho_0}\underset{t\to\infty}{\sim}\sqrt{\frac{2t}{\pi}}(\cos k-1+is\sin k), \tag{0.3}$$

où $s=p_1-p_{-1}$ est le biais de la TP. Tous les cumulants se comportent en $t^{1/2}$, en particulier le déplacement $\langle Y_1\rangle$ est sous-balistique et la variance $\langle Y_1^2\rangle-\langle Y_1\rangle^2$ est sous-diffusive. En étudiant les propriétés de la marche aléatoire d'une unique lacune en temps continu, nous étendons cette formule à temps arbitraire, ce qui constitue un nouveau résultat,

$$\lim_{\rho_0\to 0}\frac{\psi^{(t)}(k)}{\rho_0}=te^{-t}[I_0(t)+I_1(t)](\cos k-1+is\sin k), \tag{0.4}$$

où I_0 et I_1 sont des fonctions de Bessel modifiées. Cette expression décrit, comme attendu, une transition entre un régime en t à temps faible (mouvement balistique, diffusion normale) et le régime en $t^{1/2}$ à temps long.

Nous nous intéressons également au cas de conditions initiales trempées (*quenched initial conditions*) où le système est initialement dans une configuration typique, correspondant à un profil de densité uniforme à grande échelle [41], et non dans une configuration d'équilibre. Nous obtenons alors l'expression de la fonction génératrice ψ_Q à temps long,

$$\lim_{\rho_0\to 0}\frac{\psi_Q^{(t)}(k)}{\rho_0}\underset{t\to\infty}{\sim}\sqrt{2t}\int_0^\infty dz\log\left[1+p_1\left(e^{ik}-1\right)\operatorname{erfc}z\right]\left[1+p_{-1}\left(e^{-ik}-1\right)\operatorname{erfc}z\right]. \tag{0.5}$$

Ce nouveau résultat a une structure similaire à celui du cas sans biais dans la limite opposée de basse densité [41]. Le déplacement de la TP est le même que dans le cas de conditions initiales d'équilibre : $\kappa_{1,Q}^{(1)}=\kappa_1^{(1)}=\rho_0\sqrt{2t/\pi}$. Par contre, nous trouvons une différence d'un facteur $\sqrt{2}$ pour la variance d'une particule non biaisée, $\kappa_{2,Q}^{(1)}=\rho_0\sqrt{t/\pi}$ au lieu de $\kappa_2^{(1)}=\rho_0\sqrt{2t/\pi}$ pour le cas d'équilibre. Cette différence est habituellement interprétée comme la signature d'effets de mémoire à temps long dans les systèmes en file [35,41]. De plus, contrairement au cas d'équilibre, la variance d'une particule biaisée dépend du biais.

c) Loi de probabilité à N points du processus symétrique d'exclusion dense

Notre but étant d'étudier les effets collectifs dans le SEP, intéressons-nous maintenant au cas de N TP non biaisées (Chap. 4, Fig. 0.2). Un résultat structurant pour la suite est qu'à densité arbitraire les TP se comportent à temps long comme une seule particule : les cumulants à N points [Éq. (0.1)] sont égaux aux cumulants à un seul point,

$$\lim_{t\to\infty}\frac{\kappa_{p_1,\dots,p_N}^{(N)}}{\sqrt{t}}=\lim_{t\to\infty}\frac{\kappa_{p_1+\cdots+p_N}^{(1)}}{\sqrt{t}}. \tag{0.6}$$

Notre approche basée sur les lacunes nous permet d'aller plus loin à haute densité et d'obtenir l'évolution à temps intermédiaire, c'est-à-dire la transition entre le régime où les TP sont indépendantes et le régime de temps long. Notons L la distance initiale entre les TP extrémales, $\tau=t/L^2$ le temps relatif à une échelle diffusive et $\lambda_i^{(n)}=(L_i+\cdots+L_{i+n-1})/L$ les rapports de

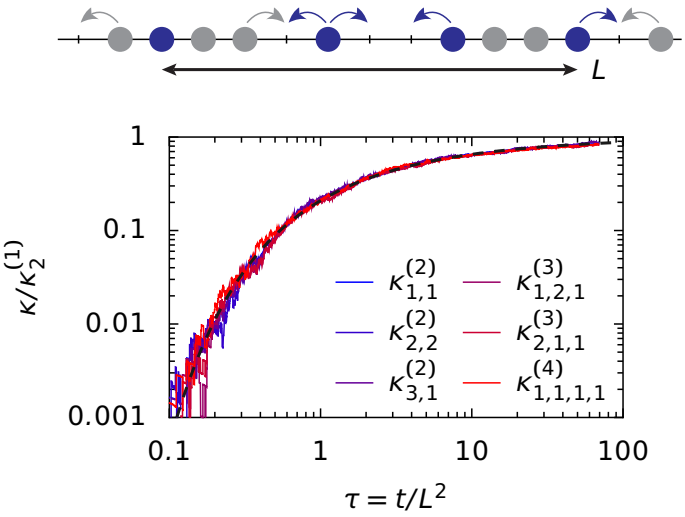

Figure 0.2 : N particules marquées dans le SEP. L'évolution temporelle de divers cumulants [Éq. (0.1)] pour des paramètres $\rho_0 = 0.002$, $L = 12$ et $N = 2,3,4$. Les cumulants sont divisés par la variance $\kappa_2^{(1)} = \rho_0\sqrt{\frac{2t}{\pi}}$. La ligne noire est la prédiction de l'équation (0.8).

longueurs, avec L_i la distance initiale entre TP i et TP $i+1$. L'expression explicite de la fonction génératrice à N points que nous trouvons dans la limite dense est

$$\lim_{\rho_0\to 0}\frac{\psi^{(t)}(\mathbf{k})}{\rho_0} \underset{t\to\infty}{\sim} \sqrt{\frac{2t}{\pi}}\sum_{n=0}^{N-1}\sum_{i=1}^{N-n}\left[g\left(\frac{\lambda_i^{(n)}}{\sqrt{2\tau}}\right)-g\left(\frac{\lambda_{i-1}^{(n+1)}}{\sqrt{2\tau}}\right)-g\left(\frac{\lambda_i^{(n+1)}}{\sqrt{2\tau}}\right)+g\left(\frac{\lambda_{i-1}^{(n+2)}}{\sqrt{2\tau}}\right)\right] \times\left(\cos(k_i+\cdots+k_{i+n})-1\right), \quad (0.7)$$

avec $g(u) = e^{-u^2} - \sqrt{\pi}u\,\mathrm{erfc}\,u$. Une conséquence importante est que les cumulants pairs à N points (c'est-à-dire $\kappa^{(N)}_{p_1,\ldots,p_N}$ avec $p_1+\cdots+p_N$ pair) vérifient une forme d'échelle universelle,

$$\lim_{\rho_0\to 0}\frac{\kappa^{(N)}_{\mathrm{pair}}(t)}{\rho_0} \underset{t\to\infty}{\sim} \sqrt{\frac{2t}{\pi}}\,g\left(\frac{1}{\sqrt{2\tau}}\right). \quad (0.8)$$

Cette forme remarquable ne dépend ni du nombre de TP, ni de la configuration initiale, ni de l'ordre du cumulant. À temps long devant l'échelle diffusive, nous retrouvons comme attendu les cumulants à un seul point [Éq. (0.3)]. Notons que des formules très proches ont été obtenues pour la corrélation $\kappa^{(2)}_{1,1}$ à partir de l'équation d'Edwards-Wilkinson [30] et dans le *random average process* [33]. Le fait que pour $N \geq 3$ TP seule l'échelle diffusive la plus grande (t/L^2) intervient, et non les échelles intermédiaires (t/L_1^2, etc.), est non trivial et il serait intéressant de voir comment ces échelles intermédiaires interviennent à densité arbitraire.

d) Coopérativité et compétition entre traceurs biaisés

Nous poursuivons notre objectif d'étudier les effets collectifs dans le SEP en regardant maintenant le cas de N TP biaisées dans le SEP (Chap. 5). En plus des corrélations, nous nous intéressons aussi aux fonctions de réponse.

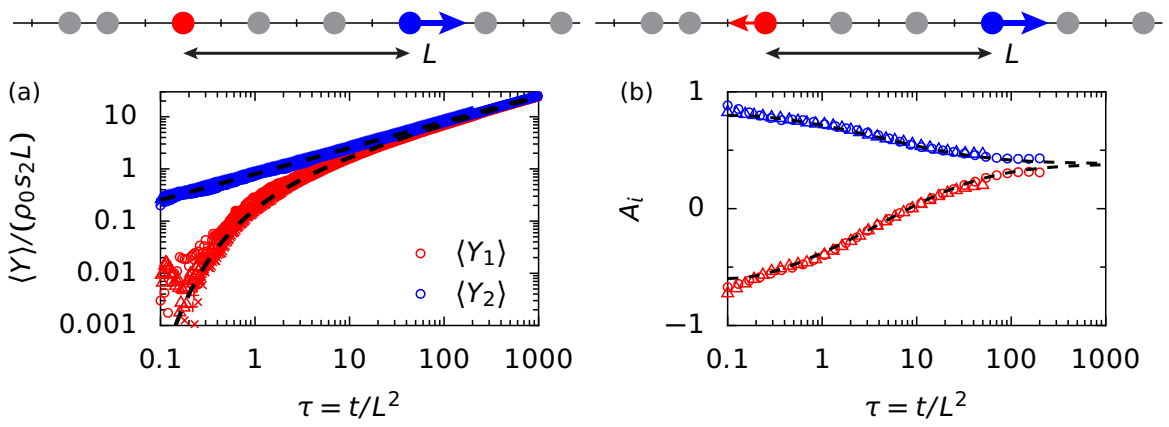

Figure 0.3 : Deux particules biaisées dans le SEP (TP 1 en rouge, TP 2 en bleu). (a) Seule la TP 2 est biaisée (biais s_2). Les déplacements des deux TP sont tracés en fonction de t/L^2 pour $L = 10, 50$ et $s_2 = -0.2, 0.8$ (symboles différents). Les lignes noires en pointillés sont les prédictions de (0.11). (b) Les deux TP sont biaisées dans des directions différentes. $\rho_0 = 0.01, s_1 = -0.6, s_2 = 0.8$ et $L = 50, 200$ (cercles, triangles). Les vitesses mises à l'échelle [Éq. (0.12)] sont tracées en fonction de t/L^2. Les lignes noires sont les prédictions analytiques. On observe les régimes limites de l'équation (0.13).

À haute densité et à temps long, les N particules sont liées entre elles par le bain : elles se comportent comme une unique particle. Si l'on note $Z = (Y_1 + \cdots + Y_N)/N$ le déplacement du centre de masse, on obtient

$$\kappa^{(N)}_{p_1,\dots,p_N} \underset{t\to\infty}{\sim} \left\langle Z^{p_1+\cdots+p_N} \right\rangle_c , \tag{0.9}$$

où $\langle \bullet \rangle_c$ est une autre notation pour les cumulants. Le centre de masse, lui, se comporte comme une particule effective de biais S lié aux biais individuels s_i,

$$\lim_{\rho_0\to 0} \frac{\langle Z(t)^{2n}\rangle_c}{\rho_0} \underset{t\to\infty}{\sim} \lim_{\rho_0\to 0} \frac{\langle Z(t)^{2n+1}\rangle_c}{\rho_0 S} \underset{t\to\infty}{\sim} \sqrt{\frac{2t}{\pi}}. \tag{0.10}$$

Nous verrons que l'on peut associer une force à chaque biais et que la force effective sur le centre de masse est la somme des forces sur chacune des particules.

Regardons le cas de deux TP et intéressons-nous d'abord à la situation où une seule des deux (la deuxième) est biaisée (Fig. 0.3a). Dans ce cas, la TP 1 est entraînée par la TP 2 avec une dépendance en temps que nous déterminons. En particulier, les cumulants impairs s'écrivent

$$\lim_{\rho_0\to 0} \frac{\langle Y_1^{2p+1}(t)\rangle_c}{\rho_0} \underset{t\to\infty}{\sim} s_2 \sqrt{\frac{2t}{\pi}}\, g\left(\frac{L}{\sqrt{2t}}\right), \qquad \lim_{\rho_0\to 0} \frac{\langle Y_2^{2p+1}(t)\rangle_c}{\rho_0} \underset{t\to\infty}{\sim} s_2 \sqrt{\frac{2t}{\pi}}, \tag{0.11}$$

où g est la fonction introduite précédemment et L la distance initiale entre les TP. À temps court seule la TP 2 bouge alors qu'à temps long les deux TP bougent de manière identique. Cette prédiction est en accord avec les simulations numériques du SEP, pour les déplacements moyens des particules (Fig. 0.3a). La similarité de structure entre $\langle Y_1\rangle$ dans (0.11) et $\langle Y_1 Y_2\rangle$ dans (0.8) correspond à une relation de fluctuation-dissipation généralisée [35]. Notons que nous obtenons également des expressions explicites pour tous les cumulants croisés des deux particules.

Finalement, considérons deux TP de biais respectifs s_1 et s_2 (Fig. 0.3b) et voyons comment elles interagissent entre elles. Pour des questions de commodité, nous définissons les vitesses

mises à l'échelle

$$A_j(t) = \frac{\sqrt{2\pi t}}{\rho_0}\frac{d\langle Y_j\rangle}{dt}. \tag{0.12}$$

Dans les limites de temps faible et de temps long, elles vérifient

$$A_j(t) \underset{t\ll L^2}{\sim} s_j \qquad\qquad A_j(t) \underset{t\gg L^2}{\sim} S = \frac{s_1+s_2}{1+s_1s_2}, \tag{0.13}$$

où s_j est le biais de la TP j et S le biais effectif mentionné plus haut. Nous obtenons des expressions explicites pour A_1 et A_2 qui interpolent entre ces deux régimes limites, et nous les comparons à des simulations dans le cas de biais opposés (Fig. 0.3b). Nous observons un effet de compétition entre les deux particules, la plus biaisée des deux entraîne l'autre à temps long. Dans le cas de biais de même signe, nous montrons un effet de coopération entre les deux particules : elles bougent plus vite à temps long que si elles étaient seules.

0.2.2 Approche hydrodynamique

L'approche que nous venons de développer donne des résultats analytiques précis pour le SEP dense. Mais elle reste spécifique à la limite de haute densité et ne s'intéresse qu'au SEP. Pour combler ces deux restrictions, nous développons maintenant une approche hydrodynamique, c'est-à-dire basée sur des équations macroscopiques valides à grande distance et à temps long. Nous dérivons ces équations dans le cas du SEP où elles sont valides à toute densité et nous montrons qu'elles peuvent s'étendre, au moins en partie, à des systèmes en file plus généraux.

a) Transition de déliaison

Nous avons vu précédemment qu'à haute densité plusieurs particules biaisées ne se séparent jamais. Il est légitime de se demander ce qu'il en est à densité arbitraire. Nous décrivons le SEP à l'aide d'un profil de densité continu $\rho(x,t)$ qui obéit à une équation de diffusion. Les TP, qui ont pour positions moyennes $\bar{X}_i(t)$, imposent des conditions aux limites de flux nul pour le bain. De plus, le mouvement des TP est déterminé entièrement par le champ de densité devant et derrière elles par l'équation

$$\frac{d\bar{X}_i(t)}{dt} = p_{+i}\big[1-\rho(\bar{X}_i^+,t)\big] - p_{-i}\big[1-\rho(\bar{X}_i^+,t)\big], \tag{0.14}$$

où p_{+i} et p_{-i} correspondent respectivement aux probabilités de saut de la TP i vers la droite et vers la gauche. À temps long, le champ de densité vérifie une loi d'échelle $x \sim \sqrt{t}$ et les mouvements des TP vérifient $\bar{X}_i(t) = \mathcal{O}(t^{1/2})$ (en particulier les vitesses s'annulent à temps long). L'équation (0.14) devient un bilan de forces :

$$P(\rho(X_i^+)) - P(\rho(X_i^-)) = f_i. \tag{0.15}$$

Les forces $f_i = \log(p_{+i}/p_{-i})$ correspondent à un bilan détaillé, et $P(\rho) = -\log(1-\rho)$ est l'équation d'état du SEP. En appliquant notre approche pour une seule TP, nous retrouvons le résultat des références [42, 43] : le déplacement est sous-balistique $\bar{X}_1(t) \propto t^{1/2}$ avec un préfacteur donné par une équation implicite.

Le cas central de notre approche est celui de deux TP subissant des forces opposées de même intensité : $f_2 = -f_1 = f$ (Fig. 0.4a). Nous mettons en lumière une transition de déliaison : en

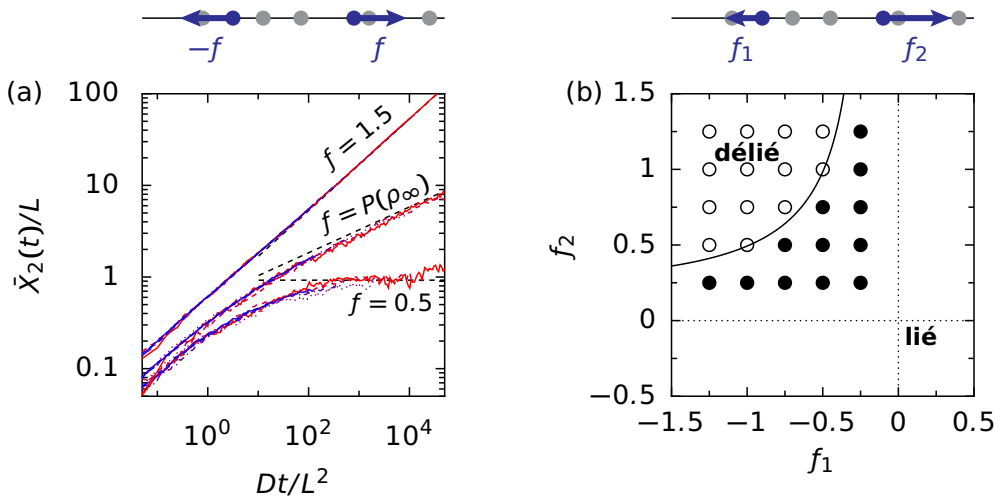

Figure 0.4 : Transition de déliaison dans le SEP (densité $\rho_\infty = 0.5$). (a) Forces opposées. Déplacement $\bar{X}_2(t)$ pour les simulations numériques dans les trois régimes de l'équation (0.16). Les pointillés noirs sont les prédictions à grand temps. Du rouge au bleu, $L = 10, 20, 50, 100, 200, 500$. (b) Forces arbitraires. Les points noirs correspondent aux simulations où l'on observe un état lié, les points creux aux états où les particules se séparent. La ligne noire est la prédiction de la frontière.

dessous d'une certaine force les TP restent à une distance finie, alors qu'au-dessus d'une certaine force elles se séparent et bougent chacune avec une dépendance en temps $t^{1/2}$. De manière remarquable, le bilan des forces (0.15) permet de montrer que la force critique est la pression d'équilibre du système à sa densité moyenne ρ_∞ : $f_c = P(\rho_\infty)$. Le régime critique est lui caractérisé par une dépendance en temps $t^{1/4}$. Pour résumer, nous trouvons les comportements suivants

$$\bar{X}_2(t) = -\bar{X}_1(t) \underset{t\to\infty}{\propto} \begin{cases} t^0 & \text{si } f < P(\rho_\infty) \\ t^{1/4} & \text{si } f = P(\rho_\infty) \\ t^{1/2} & \text{si } f > P(\rho_\infty) \end{cases} \tag{0.16}$$

avec des préfacteurs que nous déterminons. En particulier nous caractérisons l'approche de la transition pour $f \to P(\rho_\infty)^-$ (divergence de la distance) et pour $f \to P(\rho_\infty)^+$ (préfacteur qui s'annule). La comparaison avec les simulations numériques est donnée en figure 0.4a. Dans le cas de deux forces arbitraires, nous sommes en mesure d'établir le diagramme de phase présenté en figure 0.4b. Notre approche s'étend également au cas de N TP avec des forces arbitraires. Nous montrons qu'elles peuvent soit toutes rester liées, soit se séparer en deux groupes.

Nos résultats sont basés principalement sur le bilan des forces (0.15). Nous montrons que celui-ci peut être généralisé pour un système en file quelconque avec une équation d'état $P(\rho)$. La transition de déliaison est donc présente dans tous les systèmes en file. Nous le vérifions numériquement pour deux modèles suggérés dans des articles expérimentaux le gaz de bâtons durs [9] et le gaz de particules ponctuelles avec interactions dipôle-dipôle [10]. Nous approche est donc robuste, et la transition de déliaison devrait être observable dans des systèmes expérimentaux.

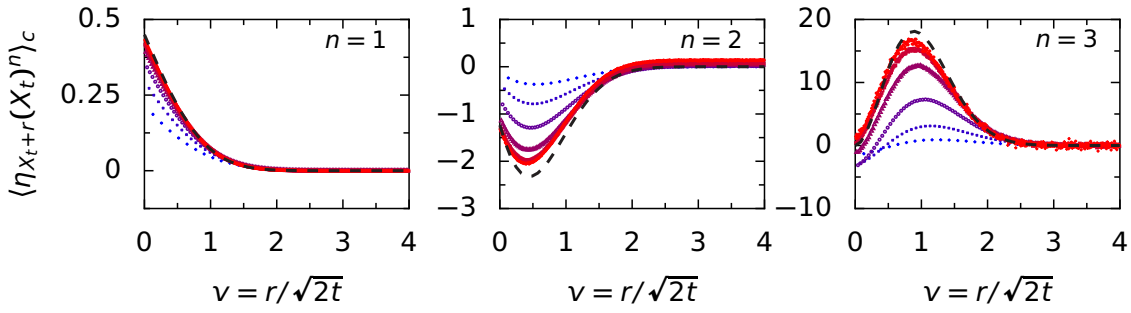

Figure 0.5 : Profils généralisés dans le SEP à basse densité ($\rho = 0.1$). Les symboles correspondent à des simulations numériques aux temps $t = 30, 100, 300, 1000, 3000, 10000$ (du bleu au rouge). Les pointillés noirs sont les prédictions asymptotiques de l'équation (0.23) avec une correction d'un facteur $(1-\rho)$.

b) Profils généralisés

Nous venons de voir qu'établir des équations hydrodynamiques pour le champ de densité du SEP permet de caractériser le déplacement de particules biaisées dans celui-ci. Nous tentons maintenant d'obtenir les cumulants d'ordre supérieur (variance, etc.) par une approche similaire. Nous nous restreignons à une seule TP, éventuellement biaisée, dont la fonction caractéristique du déplacement X_t est $\psi(\lambda, t) = \ln\langle e^{\lambda X_t}\rangle$.

Le nombre d'occupation η_r du site r dans le SEP vaut $\eta_r = 0$ si le site est vide et $\eta_r = 1$ si le site est occupé par une particule. Les profils que nous regardions pour la transition de déliaison étaient du type $\langle \eta_{X_t+r}\rangle$. Nous définissons maintenant les profils généralisés $\tilde{w}_r$ comme le couplage entre le champ de densité et le déplacement de la TP,

$$\tilde{w}_r(\lambda, t) = \frac{\langle \eta_{X_t+r} e^{\lambda X_t}\rangle}{\langle e^{\lambda X_t}\rangle} = \sum_{n=0}^{\infty} \frac{\lambda^n}{n!} \langle \eta_{X_t+r} X_t^n \rangle_c. \tag{0.17}$$

Ces profils généralisés génèrent les cumulants $\langle \eta_{X_t+r} X_t^n\rangle_c$ couplant l'occupation dans le référentiel de la TP au déplacement de celle-ci. Leur intérêt vient en particulier du fait que l'équation (0.14) peut être généralisée et que la fonction génératrice peut être exprimée en fonction de $\tilde{w}_{\pm 1}$,

$$\frac{d\psi}{dt} = p_{+1}(e^{\lambda} - 1)(1 - \tilde{w}_1) + p_{-1}(e^{-\lambda} - 1)(1 - \tilde{w}_{-1}). \tag{0.18}$$

Les profils généralisés vérifient une équation avec des termes diffusifs, et des équations aux limites sur $\tilde{w}_{\pm 1}$. Ces équations ne sont pas fermées : elles impliquent des termes de corrélation du type $\langle \eta_{X_t+1} \eta_{X_t+r} e^{\lambda X_t}\rangle$. Nous sommes particulièrement intéressés par la limite de temps long, dans laquelle les profils généralisés vérifient la loi d'échelle

$$\tilde{w}_r(\lambda, t) - \rho \underset{t\to\infty}{\sim} \Phi\left(\lambda, v = \frac{r}{\sqrt{2t}}\right), \tag{0.19}$$

et dans laquelle $\frac{d\psi}{dt} \sim t^{-1/2} \to 0$. Un résultat important en lui-même est l'obtention des équations hydrodynamiques suivantes,

$$\Phi''(v) + 2(v + b_\mu)\Phi'(v) + \chi(v) = 0, \tag{0.20}$$

$$\Phi'(0^{\pm}) + 2b_{\pm 1}\left[\rho + \Phi(0^{\pm})\right] = 0, \tag{0.21}$$

$$p_1(e^{\lambda} - 1)[1 - \rho - \Phi(0^{+})] + p_{-1}(e^{-\lambda} - 1)[1 - \rho - \Phi(0^{-})] = 0, \tag{0.22}$$

avec μ le signe de v et $b_\mu(\lambda) \equiv \lim_{t\to\infty} \psi(\lambda,t)/[\sqrt{2t}(e^{\mu\lambda-1})]$. Le terme $\chi(v)$ implique des corrélations d'ordre supérieur. Nous ne connaissons pas d'expression fermée dans le cas général mais certains cas particuliers importants peuvent être résolus.

Le premier cas est celui de l'ordre λ^0 dans lequel il n'y a pas de termes d'ordre supérieur. Nous retrouvons les résultats pour la moyenne du déplacement présentés dans la partie sur la transition de déliaison. De la même manière l'ordre λ^1 dans le cas non biaisé ($p_{\pm1} = 1/2$) peut être résolu et redonne la solution bien connue pour la variance [27], $\langle X_t^2\rangle \sim \frac{1-\rho}{\rho}\sqrt{\frac{2t}{\pi}}$. Nous montrons que cette dernière est associée à des profils $\langle \eta_{X_t+r} X_t\rangle \sim (1-\rho)\,\mathrm{erfc}(r/\sqrt{2t})/2$ ($r>0$).

Dans la limite de haute densité, $\chi(v)$ est négligeable par rapport aux autres termes. Les profils sont parfaitement déterminés à tous les ordres en présence d'un biais et nous retrouvons la fonction génératrice de l'équation (0.3) (et même celle à tout temps de l'équation (0.4)). Dans la limite opposée, de basse densité, nous dévoilons une relation de fermeture pour $\chi(v)$. Nous obtenons alors la solution suivante pour les profils, qui est un résultat majeur donné par notre approche,

$$\Phi(v \gtrless 0, \lambda) \underset{\rho\to 0}{\sim} \rho \frac{\pm\beta\,\mathrm{erfc}\,[\pm(v+\xi)]}{\pi^{-1/2}e^{-\xi^2} \mp \beta\,\mathrm{erfc}(\pm\xi)} \tag{0.23}$$

avec $\beta(\lambda) = \lim_{t\to\infty}(2t)^{-1/2}\lambda^{-1}\psi(\lambda,t)$ et $\xi = \lim_{t\to\infty}(2t)^{-1/2}\frac{d\psi}{d\lambda}$. L'équation (0.22) donne une solution implicite pour les cumulants du déplacement de la particule. Cette solution correspond à celle des références [41,44,45]. Les profils généralisés de simulations numériques à basse densité sont donnés dans la figure 0.5.

Finalement, nous montrons que notre approche dans le cas sans biais, à l'ordre λ^1 des profils (qui correspond à la variance de la TP) peut être étendue à un système en file caractérisé par ses deux coefficients d'hydrodynamique fluctuante [45–47] : le coefficient de diffusion $D(\rho)$ et la mobilité $\sigma(\rho)$. En conclusion, notre approche hydrodynamique est prometteuse et devrait constituer le sujet d'études futures.

0.3 Corrélations de systèmes bidimensionnels forcés et actifs

Dans la partie précédente, nous avons mis en évidence l'importance d'étudier les corrélations des systèmes en file pour caractériser leur comportement anormal, en particulier dans des cas hors d'équilibre. En théorie des liquides à l'équilibre [1] (dimension deux ou plus), l'aspect central des observables à deux points, et surtout des corrélations de paire $g(r)$, est également bien connu. Nous montrons maintenant que ces mêmes observables sont cruciales pour la caractérisation de systèmes hors d'équilibre.

La deuxième partie de cette thèse est dédiée à l'étude des corrélations dans des systèmes bidimensionnels en interaction, en particulier le mélange binaire forcé et les particules browniennes actives. Le mélange binaire forcé, dans lequel deux espèces sont entraînées dans des directions opposées, présente un alignement des particules de même espèce [48, 49]. L'existence ou non d'une transition d'alignement reste débattue [50, 51] et nous apportons un angle de réflexion en caractérisant la structure spatiale des corrélations. Les particules browniennes actives, un modèle minimal de particules autopropulsées, sont très étudiées notamment pour la séparation de phase induite par la motilité qui s'y produit à haute activité [52, 53]. Les corrélations de paire ont surtout été regardées du point de vue de leur composante isotrope ou de leur caractérisation à courte portée [54–57]. Nous proposons ici de caractériser analytiquement leur structure à grande distance dans la phase homogène ; celle-ci se révèle être surprenante.

Nous expliquons brièvement notre approche commune à tous les systèmes étudiés avant d'expliciter les résultats obtenus, les plus notables étant les formes d'échelle trouvées pour la structure spatiale des corrélations.

0.3.1 Systèmes étudiés

Nous analysons les corrélations dans trois systèmes différents de particules en interaction en dimension 2 ou plus. Le premier est un simple liquide passif (Chapitre 8), dans lequel N particules diffusives ayant des positions $X_i(t)$ interagissent par un potentiel de paire $V(\mathbf{r})$. Les équations de Langevin associées s'écrivent

$$\frac{d\mathbf{X}_i}{dt} = -\sum_{j=1}^{N} \nabla_i V(\mathbf{X}_i(t) - \mathbf{X}_j(t)) + \boldsymbol{\eta}_i(t), \tag{0.24}$$

avec $\boldsymbol{\eta}$ un bruit blanc Gaussien de covariance $\langle \eta_i^\mu(t)\eta_j^\nu(t')\rangle = 2D_0\delta_{i,j}\delta^{\mu,\nu}\delta(t-t')$ et de moyenne nulle. Dans ce qui suit, les équations pour un liquide passif ne seront pas explicitées. Elles correspondent à celles du mélange binaire pour une unique espèce en l'absence de forces, ou à celles des particules browniennes actives en l'absence d'activité.

Le deuxième système étudié est un mélange binaire de particules forcées (noté BM, *binary mixture*, cf. chapitre 9). Les particules sont divisées en deux espèces. Les particules de l'espèce 1 subissent une force extérieure $\mathbf{F}_1 = \mathbf{F}$ alors que les particules de l'espèce 2 ne subissent aucune force, $\mathbf{F}_2 = \mathbf{0}$. Les équations de Langevin correspondent à l'équation (0.24) avec l'ajout d'un terme $\mathbf{F}_{\alpha_i}$ où $\alpha_i \in \{1,2\}$ est l'espèce de la particule i.

Le dernier système est une assemblée de particules browniennes actives (ABP, *active Brownian particles*), un système clé de l'étude de la matière active (Chapitre 10). Chaque particule a une position $\mathbf{X}_i(t)$ et une orientation $\Theta_i(t)$ et se dirige à une vitesse constante U dans la direction donnée par son orientation. De plus, les particules subissent une diffusion translationnelle avec un coefficient D_0, une diffusion rotationnelle avec un coefficient D_r et interagissent via un potentiel de paire $V(\mathbf{r})$. Les équations de Langevin sont

$$\frac{d\mathbf{X}_i}{dt} = U\hat{\mathbf{e}}_{\Theta_i(t)} - \sum_{j\neq i} \nabla_i V(\mathbf{X}_i(t) - \mathbf{X}_j(t)) + \boldsymbol{\eta}_i(t), \qquad \frac{d\Theta_i}{dt} = \nu_i, \tag{0.25}$$

avec $\hat{\boldsymbol{\eta}}_i$ explicité précédemment et ν_i un bruit blanc gaussien de covariance $\langle \nu_i(t)\nu_j(t')\rangle = 2D_r\delta_{i,j}\delta(t-t')$. $\mathbf{e}_\theta$ est le vecteur unitaire du plan qui est positionné à un angle θ par rapport à l'axe horizontal.

0.3.2 Méthode

Nous détaillons maintenant la méthode qui nous permettra d'étudier les trois systèmes définis précédemment. Dans chaque cas, nous pouvons définir un champ de densité qui est la somme des fonctions de Dirac associées aux particules. Pour le mélange binaire, ce champ $\rho_\alpha^{\mathrm{BM}}$ est défini pour chaque espèce $\alpha = 1,2$, et pour le mélange binaire f^{ABP} est le champ de densité position-orientation :

$$\rho_\alpha^{\mathrm{BM}}(\mathbf{x},t) \equiv \sum_{i\in\mathscr{T}_\alpha} \delta(\mathbf{X}_i(t) - \mathbf{x}), \qquad f^{\mathrm{ABP}}(\mathbf{x},\theta,t) = \sum_{i=1}^{N} \delta(\mathbf{X}_i(t) - \mathbf{x})\delta(\Theta_i(t) - \theta), \tag{0.26}$$

où $\mathscr{T}_\alpha$ désigne l'ensemble des particules de l'espèce α. Notre point de départ est l'équation de Dean [58] pour les champs fluctuants de densité. Dans les deux cas précédents, elle s'écrit

$$\frac{\partial \rho_\alpha^{\mathrm{BM}}}{\partial t} = -\nabla \cdot \mathbf{J}_\alpha^{\mathrm{BM}}, \qquad \frac{\partial f^{\mathrm{ABP}}}{\partial t}(\mathbf{x},\theta,t) = -\nabla \cdot \mathbf{J}^{\mathrm{ABP}} - \frac{\partial K^{\mathrm{ABP}}}{\partial \theta}, \tag{0.27}$$

avec les flux suivants

$$\mathbf{J}_\alpha^{\mathrm{BM}} = -D_0 \nabla \rho_\alpha + \rho_\alpha \mathbf{F}_\alpha - \rho_\alpha \sum_{\beta=1}^{q} \nabla (V * \rho_\beta) \rho_\alpha^{1/2} \boldsymbol{\eta}_\alpha, \tag{0.28}$$

$$\mathbf{J}^{\mathrm{ABP}} = -D_0 \nabla f - f \int_0^{2\pi} d\theta \nabla (V * f)(\theta) + f U \hat{\mathbf{e}}_\theta - f^{1/2} \boldsymbol{\eta}, \quad K^{\mathrm{ABP}} = -D_r \frac{\partial f}{\partial \theta} - f^{1/2} \nu. \tag{0.29}$$

$(g*h)(\mathbf{x}) = \int d\mathbf{y} g(\mathbf{y}) h(\mathbf{x}-\mathbf{y})$ désigne la convolution spatiale. Les bruits spatiaux sont locaux, non corrélés dans le temps, non corrélés entre espèces, de composantes spatiales non corrélées et de moyenne nulle. Ils ont pour covariances $\langle \eta_\alpha^\mu(\mathbf{x},t)^2 \rangle = 2D_0$, $\langle \eta^\mu(\mathbf{x},\theta,t)^2 \rangle = 2D_0$ et $\langle \nu(\mathbf{x},\theta,t)^2 \rangle = 2D_r$ (les corrélations non mentionnées étant nulles). L'équation de Dean est une équation exacte pour le champ de densité, mais elle est non-linéaire et fait intervenir un bruit multiplicatif. Pour ces raisons, il est difficile d'en tirer de l'information.

Notre approximation consistera à linéariser l'équation de Dean autour d'un profil de densité uniforme, comme l'ont fait les références [2, 24, 25],

$$\rho_\alpha^{\mathrm{BM}}(\mathbf{x},t) = \bar{\rho}_\alpha + \delta\rho_\alpha^{\mathrm{BM}}(\mathbf{x},t), \qquad f^{\mathrm{ABP}}(\mathbf{r},\theta,t) = \frac{\bar{\rho}}{2\pi} + \delta f^{\mathrm{ABP}}(\mathbf{r},\theta,t), \tag{0.30}$$

avec $\delta\rho_\alpha^{\mathrm{BM}} \ll \bar{\rho}$ et $\delta f^{\mathrm{ABP}} \ll \bar{\rho}$. $\bar{\rho}_\alpha$ est la densité moyenne de l'espèce α, $\bar{\rho}$ est la densité moyenne du système. En ne gardant que l'ordre le plus bas des perturbations, les équations de Dean (0.27) deviennent linéaires avec un bruit additif et le champ de densité devient gaussien. Nous verrons que cela correspond à une limite d'interactions faibles. Les équations de Dean linéarisées nous permettent entre autres de calculer les fonctions de corrélation du système.

0.3.3 Fonctions de corrélation

Pour le mélange binaire, la corrélation $h_{\alpha,\beta}$ entre les espèces α et β est définie par

$$h_{\alpha,\beta}^{\mathrm{BM}}(\mathbf{r}) = \frac{\left\langle \rho_\alpha^{\mathrm{BM}}(\mathbf{r}) \rho_\beta^{\mathrm{BM}}(\mathbf{0}) \right\rangle}{\bar{\rho}_\alpha \bar{\rho}_\beta} - \frac{\delta_{\alpha,\beta}\delta(\mathbf{x})}{\bar{\rho}_\alpha} - 1. \tag{0.31}$$

En l'absence de forçage externe, on retrouve la fonction de corrélation de paire habituelle $h(r)$ [1]. Nous nous concentrerons sur le cas des corrélations stationnaires. Une fois l'équation de Dean linéarisée, les quatre transformées de Fourier $\tilde{h}_{1,1}^{\mathrm{BM}}$, $\tilde{h}_{1,2}^{\mathrm{BM}}$, $\tilde{h}_{2,1}^{\mathrm{BM}}$ et $\tilde{h}_{2,2}^{\mathrm{BM}}$ sont solutions d'un système linéaire de quatre équations. La résolution de ce système donne la solution explicite des fonctions de corrélation en espace de Fourier. Cette solution est en accord avec des simulations de particules molles et denses, comme montré sur la figure 0.6. Nous en étudierons les conséquences dans la sous-section suivante.

Dans le cas des particules browniennes actives, la corrélation entre deux particules espacées de $\mathbf{r}$ et ayant des orientations θ et θ' est

$$C^{\mathrm{ABP}}(\mathbf{r},\theta,\theta') = \frac{\left\langle f^{\mathrm{ABP}}(\mathbf{0},\theta) f^{\mathrm{ABP}}(\mathbf{r},\theta') \right\rangle}{[\bar{\rho}/(2\pi)]^2} - \frac{\delta(\mathbf{r})\delta(\theta-\theta')}{\bar{\rho}/(2\pi)} - 1. \tag{0.32}$$

Par invariance par rotation, toute l'information est contenue dans $C(\mathbf{r}, 0, \theta')$. Nous nous limiterons à la valeur moyenne sur l'orientation de la deuxième particule et étudierons la corrélation dans le référentiel d'une particule donnée définie par

$$B^{\mathrm{ABP}}(\mathbf{r}) = \frac{1}{2\pi}\int_0^{2\pi} d\theta' C^{\mathrm{ABP}}(\mathbf{r}, 0, \theta'). \tag{0.33}$$

En l'absence d'activité, C et B redonnent la fonction $h(\mathbf{r})$ usuelle. Nous nous intéresserons tout particulièrement à la limite de basse densité dans laquelle les effets à trois corps sont négligeables. Dans ce cas, les corrélations C et B sont bien décrites par les corrélations directes dans lesquelles sont incluses uniquement les interactions à deux corps. $C^{\mathrm{ABP}}(\mathbf{r}, \theta, \theta')$ vérifie alors l'équation suivante dans l'état stationnaire,

$$\left[2D_0\nabla^2 + D_r(\partial_\theta + \partial_{\theta'}) + U(\hat{\mathbf{e}}_\theta - \hat{\mathbf{e}}_{\theta'})\cdot\nabla\right] C^{\mathrm{ABP}}(\mathbf{r}, \theta, \theta') = -2\nabla^2 V(\mathbf{r}). \tag{0.34}$$

Cette équation, bien que linéaire, décrit une variété de comportements différents dans l'espace des paramètres (U, D_0, D_r). Son intégration numérique est en accord avec des simulations numériques de particules molles et diluées (Chap. 10). Nous verrons dans la sous-section suivante que l'on peut résoudre analytiquement les trois régimes limites de faible activité ($U \to 0$), faible diffusion rotationnelle ($D_r \to 0$) et faible diffusion translationnelle ($D_0 \to 0$) et que ceux-ci correspondent à des comportements qualitativement distincts les uns des autres (Fig. 0.7).

0.3.4 Résultats principaux

Avant de donner les résultats de notre approche pour le mélange binaire forcé et les particules browniennes actives, intéressons-nous au cas du liquide à l'équilibre. Le point notable est que la linéarisation de l'équation de Dean mène aux mêmes corrélations de paire qu'une approximation bien connue en théorie des liquides [1] : l'approximation de phase aléatoire (*random phase approximation*, RPA, cf. appendice C). Il s'agit d'une approximation de champ moyen qui donne de bons résultats pour un système dense avec des interactions faibles. Contrairement à la RPA, l'équation de Dean linéarisée s'étend à des systèmes hors d'équilibre.

Pour le mélange binaire forcé, notre résultat principal est une forme d'échelle vérifiée par les corrélations à grande distance. Notons $x_\parallel$ la coordonnée parallèle à la force appliquée sur l'espèce 1, et $\mathbf{x}_\perp$ le vecteur dans le plan perpendiculaire. Les corrélations $h_{\alpha,\beta}$ vérifient

$$h_{\alpha,\beta}(\mathbf{x}) \underset{x_\parallel\to\pm\infty}{\sim} \hat{H}^{\pm}_{\alpha,\beta}\frac{F^{\frac{d-1}{2}}}{|x_\parallel|^{\frac{d+1}{2}}} g\left(\frac{\mathbf{x}_\perp}{\sqrt{D|x_\parallel|}}\right), \tag{0.35}$$

$$g(\mathbf{u}) = \nabla^2_{\mathbf{u}}\left(e^{-\mathbf{u}^2/2}\right) = (\mathbf{u}^2 - d + 1)e^{-\mathbf{u}^2/2}, \tag{0.36}$$

avec d la dimension du système et $\hat{H}^{\pm}_{\alpha,\beta}$ et D des coefficients que nous déterminons analytiquement. Les corrélations décroissent donc en loi de puissance dans la direction du forçage, et exponentiellement dans la direction perpendiculaire. De plus cette forme d'échelle est indépendante de la forme exacte du potentiel V, à condition que celui-ci soit à courte portée. Notre prédiction est vérifiée quantitativement dans des simulations numériques de particules molles (Fig. 0.6). Nous verrons également que la forme d'échelle est observée pour des particules dures, c'est-à-dire hors du régime de validité de notre approche. Nous montrerons que l'on peut l'obtenir avec des arguments qualitatifs. Le signe des corrélations dans l'axe longitudinal (positif pour $h_{1,2}$ et

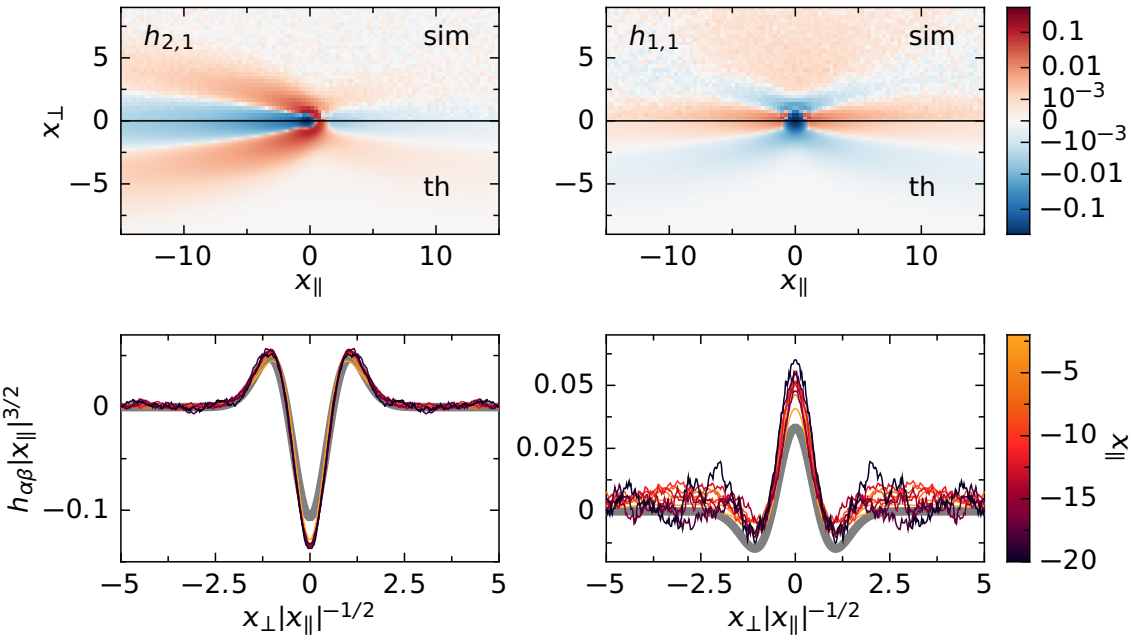

Figure 0.6 : Mélange binaire forcé ($\bar{\rho} = 2, D_0 = 0.2, F = 4$, les deux espèces sont présentes dans les mêmes proportions). En haut : corrélations entre espèces $h_{2,1}$, et dans la même espèce $h_{1,1}$. Dans la partie supérieure les simulations numériques, dans la partie inférieure l'inversion numérique de la solution analytique en espace de Fourier. En bas : coupes verticales de $h_{2,1}$ et $h_{1,1}$ issues des simulations et mises à l'échelle. Les courbes grises sont les prédictions de l'équation (0.35).

négatif pour $h_{2,1}$) montre que les particules d'une même espèce ont tendance à s'aligner, alors que les particules d'espèces différentes s'anti-alignent.

Pour les particules browniennes actives, les corrélations dans la limite diluée et molle vérifient l'équation (0.34). Trois échelles de longueur ℓ_r, ℓ_U et ℓ_p entrent en jeu, ainsi qu'un nombre sans dimension Pe qui est le nombre de Péclet,

$$\ell_r = \frac{D_0}{U}, \qquad \ell_U = \sqrt{\frac{D_0}{D_r}}, \qquad \ell_p = \frac{U}{D_r}, \qquad \mathrm{Pe} = \frac{U}{\sqrt{D_0 D_r}} = \frac{\ell_U}{\ell_r} = \frac{\ell_p}{\ell_U}. \tag{0.37}$$

En comparant la distance r à laquelle les corrélations sont regardées (et en la supposant grande devant la portée du potentiel de paire), nous construisons le diagramme de phases de la figure 0.7. Nous montrons qu'à faible activité ($\mathrm{Pe} \ll 1$) les corrélations décroissent exponentiellement sur une distance ℓ_U alors qu'à haute activité ($\mathrm{Pe} \gg 1$) la décroissance est gouvernée par ℓ_p. Les trois limites $U \to 0$, $D_r \to 0$ et $D_0 \to 0$ correspondent à trois directions limites dans le diagramme de phase. Le cas $U \to 0$ correspond à une corrélation $B(\mathbf{r})$ [Éq. (0.33)] dipolaire qui décroit exponentiellement sur une échelle ℓ_U. Les deux autres cas correspondent à des formes d'échelle remarquables,

$$B(x,y) \underset{\substack{D_r \to 0 \\ r \gg \ell_r}}{\sim} \frac{1}{y^2} F\left(\frac{x}{\ell_r^{1/3}|y|^{2/3}}\right), \qquad B(x,y) \underset{\substack{D_0 \to 0 \\ r \ll \ell_U}}{\sim} \frac{1}{y^4} G\left(\frac{\ell_p^{1/3} x}{|y|^{4/3}}\right), \tag{0.38}$$

avec des fonctions F et G que nous déterminons. Ces formes d'échelle sont testées numériquement en figure 0.7. Les deux formes correspondent à une corrélation positive pour $x > 0$ mais aussi,

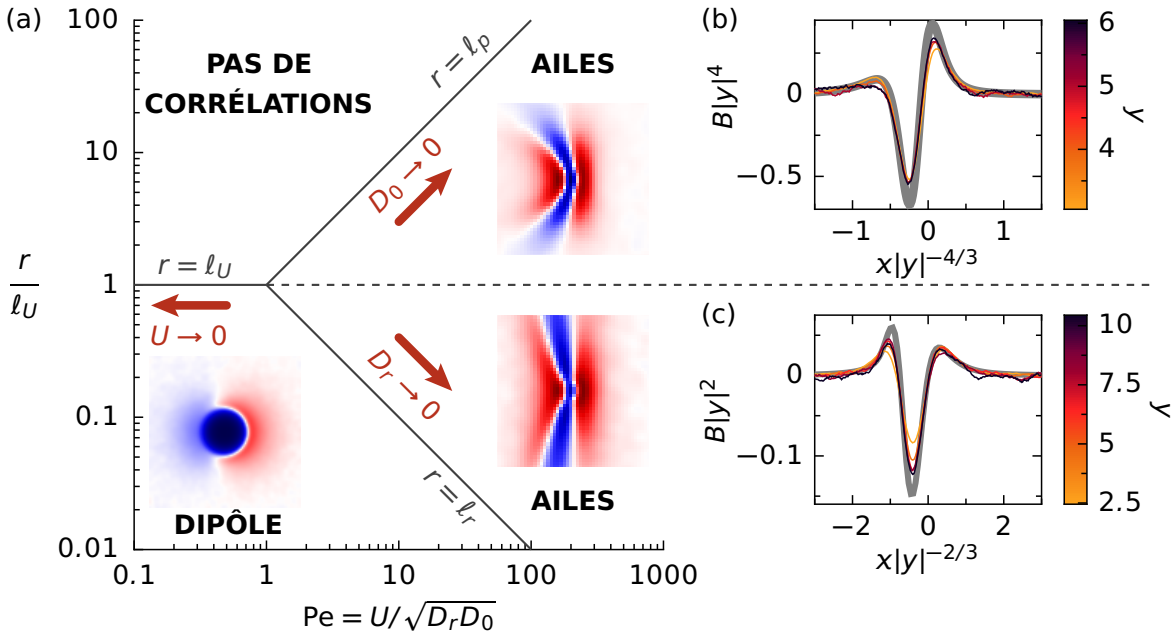

Figure 0.7 : Particules browniennes actives diluées. (a) Diagramme de phase : distance versus nombre de Péclet. Les lignes $r = \ell_r, \ell_U, \ell_p$ séparent les différents régimes. Les flèches rouges indiquent les régimes limites. Pour chacun d'entre eux les corrélations $B(\mathbf{r})$ sont esquissées (rouge : corrélation positive, bleu : corrélation négative). (b) Coupes horizontales de la fonction de corrélation numérique à $D_0 = 0$ (avec $\bar{\rho} = 0.02, D_r = 0.1$ et $U = 10$) avec les exposants d'échelle. La courbe grise est la courbe limite provenant de l'intégration de l'équation (0.34). (c) Coupes horizontales de la fonction de corrélation numérique à $D_r = 0$ (avec $\bar{\rho} = 0.02, D_0 = 0.1$ et $U = 10$) avec les exposants d'échelle. La courbe grise est la prédiction analytique.

de manière surprenante, à deux ailes négatives pour $x < 0$ (là où l'on aurait pu s'attendre à un seul sillage négatif). Notons que la transition entre les deux formes limites a lieu pour $y \sim \ell_U$.

Compressibilité, mobilité effective et vitesse effective. Disons enfin quelques mots de certaines observables physiques qui peuvent être obtenues à partir des fonctions de corrélation. Dans la partie précédente, les équations (0.14) et (0.18) relient respectivement la vitesse aux profils et la fonction génératrice des cumulants aux profils généralisés. De plus, en théorie des liquides, un résultat standard [1, 20] stipule que $h(r)$ donne accès à la compressibilité et, si on connait le potentiel, à l'équation d'état. De manière similaire, la mobilité effective des particules forcées (espèce 1) du mélange binaire (c'est-à-dire leur ralentissement par rapport à l'absence d'interactions) peut être exprimée en fonction de la corrélation croisée $h_{2,1}$. Et pour les particules browniennes actives, la vitesse effective (c.-à-d. la vitesse à laquelle bougent les particules selon leur orientation) est reliée au premier coefficient de Fourier de $B(\mathbf{r})$. Même si notre approche donne principalement les formes limites à grande distance, il est notable de pouvoir obtenir les quantités précédemment citées dans le régime où elle est aussi valide à courte distance.

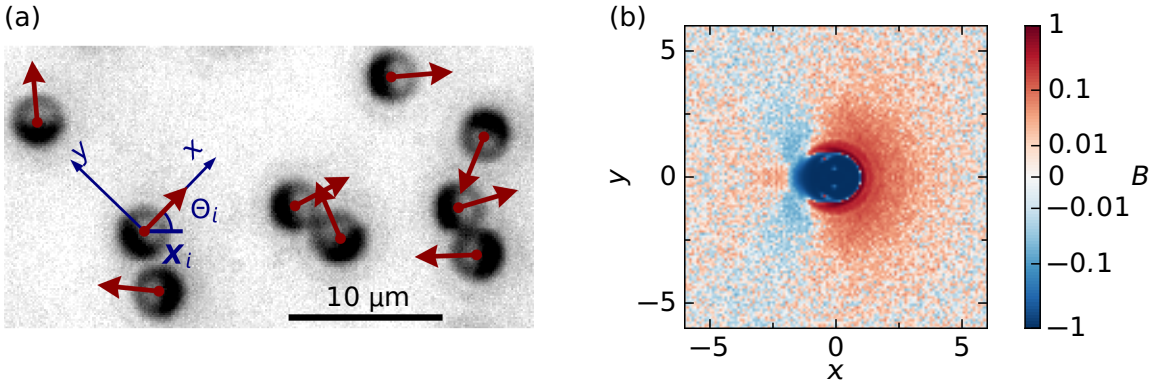

Figure 0.8 : Particules de Janus. (a) Photographie du système. L'hémisphère recouvert de titane apparaît noir. Les positions et orientations détectées par analyse d'image sont montrées en rouge. Les axes x et y pour la corrélation $B(x, y)$ apparaissent en bleu. (b) Corrélation expérimentale $B(x, y)$. Pour $x < 0$, on observe les deux ailes négatives caractéristiques des particules browniennes actives à haute activité.

0.3.5 Étude expérimentale de particules de Janus

Dans un dernier temps (Chap. 11), nous présentons des résultats expérimentaux obtenus lors d'un séjour de deux mois dans le Takeuchi Lab de l'Université de Tokyo, en collaboration avec Daiki Nishiguchi. Nous étudions des particules de Janus propulsées par un champ électrique extérieur. Ce sont des billes de verre de diamètre $a \simeq 3$ µm dont l'un des hémisphères a été recouvert de titane. Elles sont placées dans une solution aqueuse de chlorure de sodium introduite entre deux électrodes créant un champ électrique vertical. Les particules sédimentent et bougent *perpendiculairement* au champ électrique dans la direction de l'hémisphère non recouvert (Figure 0.8). Le mécanisme, nommé électrophorèse par charge induite (*Induced-charge electrophoresis*, ICEP), est décrit dans l'appendice D.

Les particules de Janus sont bien décrites par le modèle des particules browniennes actives en interaction. Nous mesurons expérimentalement la vitesse U, le coefficient de diffusion rotationnelle D_r et estimons le coefficient de diffusion translationnelle D_0. La diffusion translationnelle est faible par rapport aux autres effets, et nous montrons que le système expérimental correspond à une limite d'activité élevée. Le nombre de Péclet est $\mathrm{Pe} \simeq 90$ et les longueurs caractéristiques sont $\ell_U \simeq 0.2a$ et $\ell_r \simeq 20a$, ce qui correspond au coin supérieur droit du diagramme de phases de la figure 0.7. De plus la fraction d'espace occupée par les particules est faible ($\phi \simeq 0.04$), ce qui correspond au régime dans lequel ce diagramme de phases a été établi.

Nous capturons des vidéos du système et détectons les positions et orientations des particules. Cela permet de mesurer expérimentalement les corrélations $B(x, y)$ dans le référentiel d'une particule (Figure 0.8). Nous retrouvons la forme caractéristique des particules browniennes actives, avec deux ailes négatives dans le sillage de la particule. De plus, nous montrons que la corrélation expérimentale est en accord qualitatif avec les simulations numériques correspondant aux paramètres expérimentaux. Le fait que notre approche théorique prédise la forme des corrélations expérimentales démontre la solidité de cette approche, que l'on pourrait envisager d'étendre à des systèmes encore plus complexes : couplage orientation-vitesse, interactions d'alignement, etc.

0.4 Conclusion

Dans cette thèse, nous montrons l'importance des observables collectives pour l'étude aussi bien des systèmes en file que des systèmes bidimensionnels hors d'équilibre. Dans les deux cas, nous ouvrons de nouvelles perspectives. Caractériser les observables à plusieurs points du SEP est un problème rarement abordé car complexe. Notre approche à haute densité nous permet d'obtenir la loi à N points du SEP, et de caractériser les effets collectifs quand plusieurs particules sont biaisées. À densité intermédiaire, nous mettons en lumière et caractérisons une nouvelle transition, qui conduit deux particules forcées à se séparer ou non selon les forces appliquées. Enfin, nous bâtissons une approche hydrodynamique pour des profils généralisés qui permet d'obtenir les cumulants d'ordre arbitraire. Cette approche se révèle fructueuse dans certaines limites et nous espérons pouvoir l'étendre plus généralement.

Pour les systèmes bidimensionnels, notre contribution la plus importante est de caractériser la structure spatiale des corrélations de paire entre particules, qui sont anisotropes pour les systèmes hors d'équilibre étudiés. Notre approche, valable à faible interaction, permet de mettre en lumière des formes d'échelle pour ces corrélations. Dans le cas du mélange binaire forcé, nous trouvons que les particules d'une même espèce ont tendance à s'aligner, avec une corrélation qui décroît en loi de puissance dans l'axe de la force et vérifie une loi d'échelle diffusive. Pour les particules browniennes actives, nous obtenons deux formes d'échelle distinctes à haute activité. Plus généralement, nous établissons un diagramme de phase gouvernant la forme des corrélations. La structure caractéristique à haute activité, avec deux ailes négatives, est retrouvée dans des expériences de particules de Janus. Nous suggérons que notre approche pourrait s'étendre à des systèmes avec des couplages plus complexes.

Chapter 1

Global introduction

Systems with large numbers of interacting particles are ubiquitous at all length scales. One may think about liquids [1] or electrolytic solutions [2]; confined transport in nanotubes [3, 4], zeolites [5–7] or microchannels [8–10]; biological systems such as bacterial colonies [11–13] or molecular motors [14]; and at larger scales pedestrian crowds [15–17] or flocks of birds or cattle [18, 19]. Indeed, since interaction-free systems such as the ideal gas or phonons in crystals appear in every textbook [20–23], one may say that the study of interactions in many-body systems is one of the key goals of modern statistical physics. The usual distinction is made between equilibrium and non-equilibrium systems. Equilibrium systems are those described at large scale by thermodynamics, no external energy is injected and no net flux of energy is observed. They are usually thought of as being rather well understood, at least compared to non-equilibrium systems. But tricky questions include the prediction of two-point correlations or even, as we will see for confined geometries, of single-point observables. On the other hand, out-of-equilibrium systems in which energy is injected and fluxes are observed are a very active area of research. One reason for that is that they cannot be unified under a single framework as the equilibrium systems are with the canonical ensemble. One standard example of out-of-equilibrium system is one where some or all the particles are driven by an external field, for instance an electrolytic solution under an electric field. A very different example is a so-called active matter system in which the energy is injected at the scale of the particles, for instance a colony of self-propelling bacteria. But whatever the system, some very basic yet important questions may be asked. What are the relevant observables to characterize the system, those who enable us to get the most insight on, e.g., its collective dynamics? And then, what theoretical approach will provide us with these observables? That is to say, how can we best describe the system? These two questions of the observables and of the framework are common to both equilibrium and non-equilibrium systems. And answering them may somehow help us bridge the gap between the two situations. To give an example, it has been shown that while thermodynamic potentials are specific to equilibrium systems, large-deviation functions are tools that can be extended to out-of-equilibrium situations [59]. Throughout this thesis, even when we describe an equilibrium system we will be careful to do it in a framework that can be extended to non equilibrium.

We first address the question of the relevant observables. At equilibrium, one of course wants to characterize the thermodynamic quantities: pressure and equation of state, compressibility, specific heat, etc. But these are not the only ones. In liquid theory [1], a very important quantity is the pair correlation function $g(r)$. Another interesting example of correlations are those of

the hexatic order parameter [53] that enable one to quantify the deviations of a bidimensional system from an hexagonal lattice. Generically, the observables associated with several points of the system are of key interest. And even those associated with a unique microscopic particle can be interesting: we will see that in single-file systems a given particle undergoes a subdiffusive motion. In out-of-equilibrium systems, the most obvious observables are the fluxes. In the regime of small deviations from equilibrium, the response is usually linear and important results can be obtained such as fluctuation-dissipation theorems or Onsager reciprocity relations [20, Chap. 9]. But the question of the response is also interesting at arbitrary forcing. What is the conductivity of an electrolytic solution with strongly interacting ions [2]? How does a driven intruder behave in a bath that hinders its motion [24, 38]? Correlation functions, that are usually studied at equilibrium are also of key importance in driven system [2, 24] and we will emphasize this point several times in this thesis. To summarize, correlations will be our key observables in all systems whether at equilibrium or not; and for out-of-equilibrium systems we will also focus on response functions.

Now, let us say a few words about some theoretical frameworks that one may develop, without trying to be exhaustive. The first possibility is to exhibit an exactly solvable problem. This approach has proven to be possible for some one-dimensional systems such as interacting particles on a line [41, 44, 45] or even for one-tag observables of the symmetric exclusion process [28, 29]. The framework that we will develop in Part I for the dense symmetric exclusion process falls into this line of works. A more flexible approach, possible in arbitrary dimension, is to describe the individual particles as a density field. Standard example are the Boltzmann equation [22, 23] or N-body Fokker-Planck equations [56, 60]. Another notable instance, in the field of active matter is the Toner and Tu hydrodynamics [61, 62]. But we also have in mind equations for a fluctuating, non deterministic, density field. A case in point is the Dean equation [58] which is an exact equation for the fluctuating density field of interacting particles. In dimension one, we should also mention fluctuating hydrodynamic equations [46] and the macroscopic fluctuation theory based upon them [45]. Part II will take the Dean equation as a starting point. And the last two chapters of Part I are devoted to the derivation of hydrodynamic equations for single-file systems.

It is now time to state what precise systems we will describe in this thesis. We will be interested in two different types of problems, corresponding to the two parts of this thesis. In both cases, the key observables will be the correlation functions. And although the frameworks are different, the reader may find similarities in the field equations written in each part. The first systems of interest are single-file systems (Part I). These systems are one-dimensional, or quasi one-dimensional, and the particles trapped in this geometry cannot pass each other. The fact that the order of the particles is conserved at all times induces strong geometrical constraints responsible for anomalous behaviors. Indeed, the motion of a given particle is shown to be subdiffusive with a mean-square displacement at time t scaling as $t^{1/2}$ (instead of t for usual diffusion). Similarly, the motion of a driven intruder is sub-ballistic, with a displacement also scaling as $t^{1/2}$. While the focus is often put on single-tag observables, one should keep in mind that these anomalous behaviors are closely linked to strong spatial correlations that are seldom characterized. This characterization, and the study of the collective effects that emerge from the geometric constraints, will be our main goal. Two kinds of approaches will be developed: first we show that the dense limit can be solved exactly and then we derive hydrodynamic equations valid at arbitrary density. The second kind of systems that we will focus on are bi-dimensional (or tri-dimensional) systems of particles interacting by a pair potential (Part. II). This include usual liquids but extends to out-of-equilibrium systems such as driven mixtures or active systems. Our work is motivated by important open questions such as the issue of laning in oppositely driven populations, and the characterization

of a homogeneous active liquid below motility-induced phase separation. We focus on the pair-correlations which are anisotropic for out-of-equilibrium systems. In particular, our goal is to probe the large-distance behavior of these correlation functions. Our starting point is the Dean equation [58] and our approach consists in linearizing it around a uniform density profile. This gives quantitative results in the limit of weakly interacting particles, but also qualitative results holding outside this limit.

As detailed introductions will be given at the beginning of each part, and at the beginning of each chapter, we only give a brief summary. Part I starts with an overview of single-file systems that recalls general results about them (Chap. 2). In the three chapters that follow, the focus is put on the high-density limit of the symmetric exclusion process (SEP). We first recall and extend the known results on the probability law of a single biased intruder in the dense SEP (Chap. 3). We move on and use the same method to compute the N-tag probability law of the dense SEP (Chap. 4). And introducing several biased intruders in this dense SEP, we uncover striking cooperation and competition effects (Chap. 5). Finally, the last two chapters are dedicated to hydrodynamic approaches that hold for the SEP at arbitrary density and can be extended to generic single-file systems. An unbinding transition is found for the displacements of two driven probes in a single-file system (Chap. 6). The hydrodynamic approach used to characterize the profiles of this unbinding transition is extended to generalized profiles leading to a promising unified approach to compute arbitrary cumulants (Chap. 7). Part II starts by the derivation of the Dean equation, an exact stochastic equation for the macroscopic density field of particles in interaction. Linearizing this equation, we obtain an analytical expression for the pair correlation function $g(r)$ that corresponds to the one of the random phase approximation of liquid theory (Chap. 8). We then show that this framework, namely the linearized Dean equation, can be extended to an out-of-equilibrium system: a binary mixture in which different species are driven in opposite directions (Chap. 9). We uncover a striking scaling form of the anisotropic pair correlations. A last system in which our framework is applied is an assembly of active Brownian particles (ABPs), a paradigmatic model of active matter (Chap. 10). The pair correlations are described analytically in several limit regimes. At high activity, they exhibit a characteristic wing-like structure which is associated with scaling forms. Finally, our findings on ABPs are compared to experiments of Janus particles performed in Takeuchi laboratory (Chap. 11). A list of publications is provided at the end of this thesis (Chap. 13).

Part I

Single-file systems and symmetric exclusion process

Chapter 2

Overview of single-file systems

Contents

2.1 Introduction

Single-file systems are one-dimensional or quasi-one-dimensional systems in which particles that are trapped cannot bypass each other. One should think of particles within a channel whose diameter is close to the size of the particles. The particles are thus ordered and this order is conserved at all times (Fig. 2.1a). The single-file geometry has been found in various experimental setups (zeolites, colloids, nanotubes) and has led to a large number of theoretical studies. The reader may look at the review of Taloni and coworkers [63] for a quick overview.

The most salient feature of single-file systems is the subdiffusive behavior of a tagged particle. Let us consider a particle at position $X(t)$ at time t that would be diffusive if it were alone,

$$\left\langle [X(t)-X(0)]^2 \right\rangle_{\text{free}} \propto t. \tag{2.1}$$

If the same particle is placed in single-file geometry with identical particles, it becomes subdiffusive with a scaling

$$\left\langle [X(t)-X(0)]^2 \right\rangle_{\text{single-file}} \propto t^{1/2}. \tag{2.2}$$

This subdiffusion has been observed experimentally, is easily reproduced numerically and has been proven rigorously in several theoretical models. However, the full extent of the collective effects that lead to the subdiffusion and other anomalous behaviors is still not characterized. This characterization will be the main goal of the first part of this manuscript.

We now review first the experimental setups in which the single-file dynamics is relevant. Then we give an overview of the main theoretical models that have been developed. Finally, we state the importance of several-tag observables and explain our approaches to compute them.

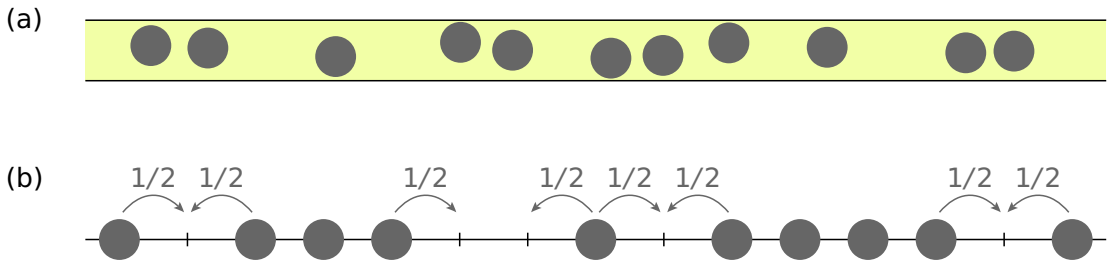

Figure 2.1: (a) Example of particles in single-file geometry. (b) Symmetric exclusion process.

2.2 Experimental systems

The first experimental evidence of subdiffusion in a single-file system [Eq (2.2)], was done in 1995 for molecules diffusing within zeolites [5–7]. Zeolites are porous materials which can be used as molecular sieves, that is to say to separate molecules based on their size. The one used in experiments, $AlP0_4$-5, has channels of diameter 7.3 Å while the ethane molecules that diffuse have a kinetic diameter 4.4 Å [5]. This explains why ethane molecules cannot pass each other and are thus in single-file geometry. The subdiffusive behavior, Eq (2.2) is probed by measuring the signal attenuation in pulsed field gradient NMR. The experiments were later reproduced using methane and carbon tetrafluoride and are backed by numerical simulations [6,7].

Another key system in which single-file dynamics was observed are colloids trapped in channels [8–10]. The subdiffusive, non-Fickian, behavior was first reported for paramagnetic polystyrene colloids (3.6 μm) trapped in circular trenches (width: 7 μm) [10]. The mean-square displacement scales with time as $t^{1/2}$ as expected from the theory and the probability distribution of the displacement was measured. The crossover between diffusive motion at short time and subdiffusive motion at large time was observed later in experiments of polystyrene beads in a circular laser channel [8], and for weakly interacting silica colloids (1.6 μm) in a printed groove [9]. A crucial remark is that the interactions between particles are very different between experimental systems (long-range repulsion [8,10], short-range attraction with hardcore exclusion [9]) but the subdiffusive scaling is universally observed.

In a different field, the single-file geometry has recently been shown to be relevant for water transport in single-wall carbon nanotubes [3] and carbon nanotube porins [4] of sizes $0.5-1$ nm. Note however that this situation is quite different from the ones we presented before as a constant flux of water is induced and strong effects of the walls are expected. Finally, even if few studies exist, applications of the single-file geometry to micro and nano-fluidics, and to biodevices have been suggested [63].

2.3 Theoretical models in continuous space

A variety of models have been developed to account for the peculiar behavior of single-file systems. Before introducing the symmetric exclusion process (SEP), on which a large part of our analysis will be built, we first focus on models in continuous space. The simplest one is point-like diffusive particles on a line, with hard-core interactions between the particles (that is to say that they cannot cross). This is the first model in which Eq. (2.2) was obtained: in 1965 Harris showed [40] that the probability distribution of the rescaled displacement $X(t)(2t/\pi)^{-1/4}$ of a tagged particle converges at large time to a standard normal distribution. The propagators were computed in

1998 [64]. But the full probability distribution of $X(t)$ at large time was obtained only in 2014, by three teams using three different methods: a computation of propagators [44], macroscopic fluctuation theory [45] and a mapping to uninteracting particles [41]. Additionally, the two-tag probability distribution [31] and the two-time correlations [65] of this model has been computed.

Another continuous space model that has been introduced is the random average process [32–34]. Pointlike particles have exponential clocks making them jump towards one of their neighbors. The displacement during a jump is a fraction of the distance between the particle and its neighbor, drawn with a given probability law on $[0,1]$. Displacements, profiles and two-point correlations can be derived exactly for this model for an unbiased intruder as well as a biased intruder, and for different initial conditions. These exact results give precious insight on single-file systems.

Finally, we note that experimental systems have been described by rather simple models. Ref. [9] suggests that their colloids are well described by a Tonks gas [66] that is to say a gas of interacting hard rods. Other colloids in Ref. [10] have been shown to behave as point-like particles interacting with dipole-dipole interactions. We come back to these descriptions in Chap 6.

2.4 Symmetric exclusion process

Let us now introduce a paradigmatic model of single-file systems on which most of this part will focus: the symmetric exclusion process (SEP, Fig. 2.1b). Particles occupy the sites of a discrete line and are embedded with exponential clocks of rate 1. When its clock rings, a particle tries to jump to one of its neighboring sites (with equal probability). The jump is performed only if the arrival site is empty. This hard-core constraint enforces the single-file nature of the system.

The subdiffusive behavior of a tagged particle (TP) in the SEP was first established by Alexander and Pincus [26] in 1978 by linking density fluctuations to the displacement of the TP. The exact result was then proved by Arratia [27] in 1983: the variance of a tagged particle in the SEP at density ρ is given by

$$\langle X(t)^2 \rangle = \frac{1-\rho}{\rho}\sqrt{\frac{2t}{\pi}}. \tag{2.3}$$

However, the full probability law of such a tagged particle remained a challenge for a long time. In 2009, Derrida and Gershenfeld [67] obtained the statistics of the integrated current at the origin of the SEP. The fourth cumulant was computed in 2014 [45, 47] using macroscopic fluctuation theory. And it is only in 2017 that Imamura, Sasamoto and Mallick [28, 29] managed to obtain the full probability law by relying on exact results for the asymmetric exclusion process. We give some details about their approach and their results in Appendix A.

Another line of studies focused on what happens to a single biased TP in the SEP. It is shown that its average displacement scales with time as $t^{1/2}$. The prefactor is the solution of an implicit equation that was first derived in Ref. [42] and proven rigorously in Ref. [43]. The full probability law of a biased TP is known in the high density limit [37, 38] by an approach that we will reproduce in Chap 3.

While studies show interest for one-tag observables, it is notable that very few of them focused on the characterization of spatial correlations. These correlations are nonetheless crucial to understand the peculiar behavior of the SEP and the importance of the geometrical constraints. Two-point and N-point observables will be the key quantities that we characterize in Chaps 4 and 5.

2.5 Outline

The first part of this thesis can be thought of as divided into two subparts. The first three chapters (Chaps 3, 4 and 5) are dedicated to the dense limit of the SEP, using a vacancy-based approach introduced in Refs. [36–38]. On the other hand, the last two chapters of this part (Chaps 6 and 7) are dedicated to approaches based on hydrodynamic equations. They hold for the SEP at arbitrary density and can be partially extended to generic single-file systems.

Chapter 3 recalls the vacancy-based approach and the results of Ref. [38] for the probability law of a biased intruder in the SEP. Two majors extensions are given: the probability law at arbitrary time, and the case of quenched initial conditions. Then, Chapter 4 uses the same approach to compute the N-tag probability law of the dense SEP. While we show that the large-time behavior of N particles at any density is identical to the one of a single particle, we are crucially able to derive the intermediate time behavior in the high density limit. In particular, we exhibit a universal scaling for the N-tag cumulants. Finally, Chapter 5 is dedicated to the case of two or more biased intruders in the dense SEP. We unveil a bath-mediated binding effect: the biased intruders move as a single one at large time. Moreover, we obtain the intermediate-time behavior and exhibit cooperativity and competition effects depending on the relative signs of the biases.

The bath-mediated binding at high density is remarkable, but at arbitrary density an even more remarkable effect is observed: biased particles can unbind and move apart from one another. We study this unbinding transition in Chapter 6 using a hydrodynamic approach for the density field of the SEP. We fully characterize the transition and show that it holds for arbitrary single-file systems. This framework with hydrodynamic equations for the profiles is extended in Chapter 7 to generalized profiles, that is to say to correlations between the density and the displacement of a given particle. In general, such equations are not closed but we nonetheless show that several limits can be obtained. A tentative extension to generic single-file systems is put forward and the variance of a particle is recovered.

Chapter 3

Dense symmetric exclusion process: single-tag observables

Contents

3.1 Introduction

The anomalous behavior of the symmetric exclusion process has been known for a long time. In 1983, Arratia [27] derived the subdiffusive behavior of the mean square displacement $\langle Y^2(t)\rangle$ of a TP in the SEP,

$$\langle Y^2(t)\rangle \underset{t\to\infty}{\sim} \frac{1-\rho}{\rho}\sqrt{\frac{2t}{\pi}}, \tag{3.1}$$

where ρ is the density of the system, and the time constant of a particle is set to $\tau = 1$. The study of the higher order cumulants, in other words of the full probability distribution of $Y(t)$, is more recent. It has been done first in the two limit cases: at high density ($\rho \to 1$) [38], and for pointlike interacting particles [41, 44, 45] which corresponds to the low density limit of the SEP

($\rho \to 0$)[1]. But the breakthrough came in 2017, when Imamura, Sasamoto and Mallick derived the full probability law of a tagged particle in the SEP [28, 29]. We dedicate Appendix A to their solution.

Another interesting setup is when a biased intruder (the TP) is introduced in the SEP (see Fig. 3.1). The TP has arbitrary jump probabilities while the other particles still perform unbiased walks with exclusion. The displacement of the TP obeys $\langle Y(t)\rangle \underset{t\to\infty}{\sim} A(\rho)\sqrt{t}$, which corresponds to a sub-ballistic behavior. The prefactor $A(\rho)$ is the solution of an implicit equation first derived phenomenologically [42], then rigorously [43]. Higher order cumulants have been computed only in the high density limit [38].

In this chapter, we revisit the results of Ref. [38] for the probability distribution of a biased TP in the SEP at high density (Fig. 3.1). The usual SEP is recovered by setting the bias to zero. The vacancy-based approach that we use has been first introduced by Brummelhuis and Hilhorst [36] and has been shown to be useful in a variety of other setups [37] such as confined environments [39] and comb-like stucture [68]. We introduce a technical difference: the random walks of the vacancies are considered in continuous time instead of discrete time. This enables us to derive new expressions valid at arbitrary time instead of large time only. Additionally, we also obtain results for a different set of initial conditions: the so-called *quenched* initial conditions in which the initial configuration is frozen. In addition to these new results, this chapter paves the way for the study of multiple TPs. This is the main focus of Part I and will be analyzed in the next two chapters.

3.2 System

The system that we study is the symmetric exclusion process (SEP). Particles are initially positioned uniformly at random on the infinite discrete line. The density ρ is the fraction of particles compared to the number of sites: it can vary between 0 and 1. Each particle has an exponential clock of time constant $\tau = 1$. When the clock ticks, the particle chooses to jump either to the left (with probability 1/2) or to the right (with probability 1/2). If the arrival site is empty, the jump is done. Otherwise, if the arrival site is occupied, the jump is canceled.

We consider a tagged particle (TP) and we allow it to have different jumping rates: p_1 to the right and p_{-1} to the left (see Fig. 3.1). The TP is initially at the origin $X(t=0)=0$ and we study its displacement with time $Y(t) = X(t) - X(0)$. We define the cumulant-generating function

$$\psi^{(t)}(k) \equiv \ln\langle e^{ikX(t)}\rangle. \tag{3.2}$$

$\psi^{(t)}(k)$ gives us the full probability law of $Y(t)$. The expansion of this function in powers of k gives the cumulants $\kappa_n(t)$,

$$\psi^{(t)}(k) \equiv \sum_{n=1}^{\infty} \frac{(ik)^n}{n!}\kappa_n(t). \tag{3.3}$$

$\kappa_1 = \langle Y(t)\rangle$ is the average displacement, $\kappa_2 = \left\langle [Y(t) - \langle Y(t)\rangle]^2 \right\rangle$ is the variance, $\kappa_3 = \left\langle [Y(t) - \langle Y(t)\rangle]^3 \right\rangle$, $\kappa_4 = \left\langle [Y(t) - \langle Y(t)\rangle]^4 \right\rangle - 3\kappa_2^2$, etc. If $Y(t)$ were Gaussian (we will see that it is not), we would have $\kappa_n = 0\ \forall n \geq 3$.

In this chapter, our main goal is the determination of the cumulant-generating function $\psi^{(t)}(k)$ and the cumulants $\kappa_n(t)$ in the high density limit $\rho \to 1$.

[1] Note that the variance of a tagged particle in the latter system is one of the first results derived historically [40].

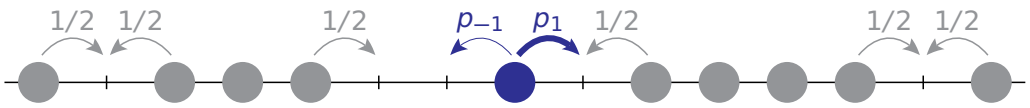

Figure 3.1: SEP with a biased TP. The jump probabilities of the TP are $p_{\pm 1} = (1 \pm s)/2$ where s is the bias.

3.3 From a single vacancy to the dense SEP

Let us consider a system of finite size $\mathcal{N}$ in which all the sites are occupied except M of them. We call these empty sites *vacancies*, and their fraction $\rho_0 = M/\mathcal{N} = 1-\rho$. The high density limit of the SEP corresponds to $\rho_0 \to 0$. Instead of looking at the motion of the particles, one can equivalently study the motion of the vacancies. The latter perform (a priori correlated) random walks on the line.

Our TP is initially at the origin: $X(t=0) = 0$ and its displacement is $Y(t) = X(t) - X(0)$. This displacement can be said to be generated by the random walks of the vacancies: when a vacancy crosses the TP from left to right, the TP moves to the left and vice versa. We number the vacancies and call $Y^j(t)$ the displacement of the TP generated by the j-th vacancy. We have $Y(t) = Y^1(t) + \cdots + Y^j(t)$.

The initial positions of the vacancies are called Z_j. $P^{(t)}(Y|\{Z_j\})$ is the probability of a displacement Y at time t knowing the initial positions of the vacancies. Similarly, $\mathscr{P}^{(t)}(\{Y^j\}|\{Z_j\})$ is the probability that up to time t vacancies induced displacements $\{Y^j\}$ of the TP knowing their initial positions (see Fig. 3.2). By definition,

$$P^{(t)}(Y|\{Z_j\}) = \sum_{Y_1,\dots,Y_M} \delta_{Y,Y_1+\cdots+Y_M} \mathscr{P}^{(t)}(\{Y^j\}|\{Z_j\}). \tag{3.4}$$

Now, in the high density limit ($\rho_0 = M/\mathcal{N} \to 0$), we assume that the vacancies perform independent random walks and interact independently with the TP. We neglect events of order $\mathcal{O}(\rho_0^2)$ in which two vacancies interact with each other, compared to events of order $\mathcal{O}(\rho_0)$ in which one vacancy interact with the TP. This is indeed a strong statement, but we will see that it gives exact results in the limit $\rho_0 \to 0$. We call $p_Z^{(t)}(Y)$ the probability that in a system with a single vacancy initially at Z, the TP has displacement Y at time t. Our assumption leads to

$$\mathscr{P}^{(t)}(\{Y^j\}|\{Z_j\}) \underset{\rho_0\to 0}{\sim} \prod_{j=1}^{M} p_{Z_j}^{(t)}(Y^j) \tag{3.5}$$

with $\rho_0 = 1-\rho$. Note that there are only two values of Y for which $p_Z^{(t)}(Y)$ is non-zero ($Y = 0$ and ± 1 for $Z \lessgtr 0$)). As we show in the following our problem now becomes much simpler.

Eq. (3.4) now gives

$$P^{(t)}(Y|\{Z_j\}) \underset{\rho_0\to 0}{\sim} \sum_{Y_1,\dots,Y_M} \delta_{Y,Y_1+\cdots+Y_M} \prod_{j=1}^{M} p_{Z_j}^{(t)}(Y^j). \tag{3.6}$$

We define the Fourier transform $\tilde{p}_Z^{(t)}(k) = \sum_{Y=-\infty}^{\infty} e^{ikY} p_Z^{(t)}(Y)$ and obtain

$$\tilde{P}^{(t)}(k|\{Z_j\}) \underset{\rho_0\to 0}{\sim} \prod_{j=1}^{M} \tilde{p}_{Z_j}^{(t)}(k). \tag{3.7}$$

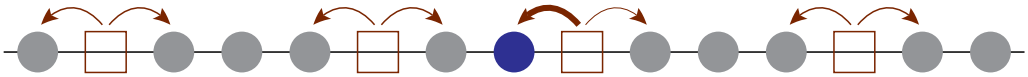

Figure 3.2: The SEP can be seen in terms of random walks of vacancies (brown squares). They are symmetric walks, except on the two sites next to the TP that we consider as defective sites. At high density, these walks are assumed to be independent.

We consider an initial condition in which the vacancies have equal probability to be on any site (except the origin). This corresponds to an equilibrated system and is known in the literature as *annealed* initial conditions. The cumulant-generating function of $X(t)$ is the logarithm of the average of $\tilde{P}^{(t)}(k|\{Z_j\})$,

$$\psi^{(t)}(k) = \ln \tilde{P}^{(t)}(k), \tag{3.8}$$

$$\tilde{P}^{(t)}(k) \equiv \frac{1}{(\mathcal{N}-1)^M} \sum_{Z_1,\dots,Z_M \neq 0} \tilde{P}^{(t)}(k|\{Z_j\}). \tag{3.9}$$

In the limit $\rho_0 \to 0$, we obtain

$$\tilde{P}^{(t)}(k) \underset{\rho_0 \to 0}{\sim} \left[\frac{1}{\mathcal{N}-1} \sum_{Z \neq 0} \tilde{p}_Z^{(t)}(k) \right]^M = \left[1 + \frac{1}{\mathcal{N}-1} \sum_{Z \neq 0} \left(\tilde{p}_Z^{(t)}(k) - 1 \right) \right]^M . \tag{3.10}$$

We consider the large-size limit $M, \mathcal{N} \to \infty$ with $\rho_0 = M/\mathcal{N} = 1-\rho$ constant. We obtain an expression for the cumulant-generating function in the high-density limit.

$$\lim_{\rho_0 \to 0} \frac{\psi^{(t)}(k)}{\rho_0} = \sum_{Z \neq 0} \left(\tilde{p}_Z^{(t)}(k) - 1 \right) \tag{3.11}$$

Let us emphasize the meaning of this equation: the full probability law of a TP at high density is encoded in a much simpler quantity: the propagator in a system where there is only one vacancy.

3.4 Symmetric exclusion process with a single vacancy

In this section, we consider a SEP with a single vacancy, initially at position Z. The dynamics of the TP, initially at zero, is entirely determined by the random walk performed by the vacancy: when the vacancy arrives at the origin, the TP moves by one unit. We call f_Z^t the probability that the vacancy arrives at the origin *for the first time* at time t. We are able to decompose the propagator $p_Z^{(t)}(Y)$ over the first-passage of the vacancy at the origin (see Fig. 3.3):

$$p_Z^{(t)}(Y) = \delta_{Y,0} \left(1 - \int_0^t d\tau f_Z^{(\tau)} \right) + \int_0^t dt_1 p_{-\mu}^{(t-t_1)}(Y-\mu) f_Z^{(t_1)}, \tag{3.12}$$

where $\mu = \text{sign}(Z) = \pm 1$. In the first term, the vacancy never touches the origin. In the second term, the vacancy touches the origin at time t_1, the TP has a movement $-\mu$ and the vacancy is now on $-\mu$ with respect to the TP.

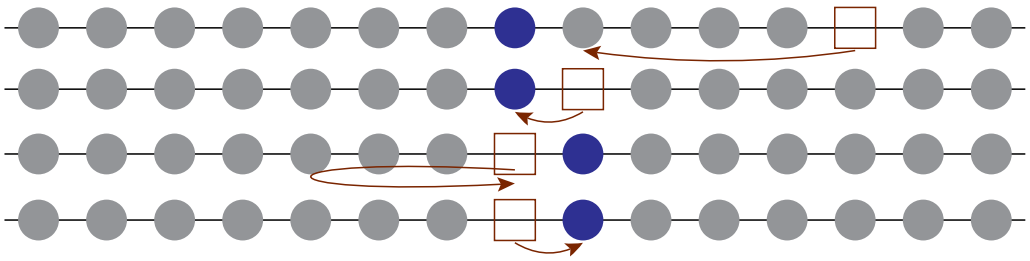

Figure 3.3: Successive passages of a single vacancy to the origin. The random walk is symmetric except for the two sites next to the TP. We see that the vacancy induces a motion of the TP (by one site).

One remarks that the same procedure can be applied to the total number n of arrivals of the vacancy at the origin before time t. For simplicity, we write it for $Z = \nu = \pm 1$,

$$p_\nu^{(t)}(Y) = \sum_{n=0}^{\infty} \delta_{Y,\nu[1-(-1)^{n+1}]} \int_0^\infty dt_1 \dots dt_n \int_0^\infty d\tau \delta\left(t - \sum_{i=1}^n t_i - \tau\right) \times \left(1 - f^{(\tau)}_{\nu(-1)^n}\right) f^{(t_n)}_{\nu(-1)^{n-1}} \dots f^{(t_2)}_{-\nu} f^{(t_1)}_{\nu}. \quad (3.13)$$

We define the Fourier-transform in space and Laplace transform in time by

$$\hat{\tilde{p}}_Z(k,u) \equiv \sum_{Y=-\infty}^{\infty} e^{ikY} \int_0^\infty dt e^{-ut} p_Z^{(t)}(Y). \quad (3.14)$$

Applying it to Eqs. (3.12) and (3.13), we obtain

$$\hat{\tilde{p}}_Z(k,u) = \frac{1}{u} + \left[\hat{\tilde{p}}_{-\mu}(k,u) e^{i\mu k} - \frac{1}{u}\right] \hat{f}_Z(u), \quad (3.15)$$

$$\hat{\tilde{p}}_\nu(k,u) = \frac{1}{u} \frac{\left[1 - \hat{f}_\nu(u)\right] + e^{i\nu k} \hat{f}_\nu(u) \left[1 - \hat{f}_{-\nu}(u)\right]}{1 - \hat{f}_1(u)\hat{f}_{-1}(u)}. \quad (3.16)$$

We combine the two equations and obtain the propagator of the displacement of the TP in terms of the first passage probabilities of the vacancy,

$$\hat{\tilde{p}}_Z(k,u) = \frac{1}{u}\left[1 + \left(e^{i\mu k} - 1\right) \frac{1 - \hat{f}_{-\mu}(u)}{1 - \hat{f}_1(u)\hat{f}_{-1}(u)} \hat{f}_Z(u)\right]. \quad (3.17)$$

One can inject this equation into Eq. (3.11) to obtain the cumulant-generating function at high density in terms of first passage quantities of a single vacancy.

The reader may have guessed that our last step consists in studying the random walk of a single vacancy to compute $\hat{f}_Z(u)$.

3.5 First passage quantities

We consider a SEP with only one vacancy and a TP initially at the origin. The first question to be asked is: what is the random walk performed by this unique vacancy? The vacancy is surrounded

by two particles with exponential clocks with ticking probability $\chi(t)$ [Laplace transform $\hat{\chi}(u)$] given by

$$\chi(t) = e^{-t} \qquad \hat{\chi}(u) = \frac{1}{1+u}. \tag{3.18}$$

Except when it is next to the biased TP, the vacancy thus performs a symmetric Montroll-Weiss walk [69] with a distribution of jumping times given by $\chi(t)$. When the TP is not biased, the walk becomes symmetric for all sites. We first study this situation before accounting for defective sites next to the TP.

3.5.1 Unbiased tagged particle

Let us call $f_Z^{\mathrm{UB}}(t)$ the probability of first passage at the origin at time t of a vacancy initially at Z, assuming that the TP is not biased ($p_{\pm 1} = 1/2, s = 0$). The Montroll-Weiss walk (in continuous time) of the vacancy is linked to the associated Polya walk (in discrete time) by the formula [Ref. [69], Eq. (5.46)]

$$\hat{f}_Z^{\mathrm{UB}}(u) = \hat{F}_Z(\hat{\chi}(u)) \tag{3.19}$$

where $\hat{\chi}$ is given by Eq. (3.18), and $\hat{F}_Z(\xi) = \sum_{t=0}^{\infty} \xi^t F_Z(t)$ is the discrete Laplace transform of the probability of first passage at the origin of the Polya walk starting from Z. It is known to be given [Ref. [69], Eq. (3.135)] by $\hat{F}_Z(\xi) = \alpha^{|\xi|}$ with $\alpha = \xi^{-1}\left(1 - \sqrt{1-\xi^2}\right)$. At the end of the day, we obtain the following expression for the first passage probability that we study:

$$\hat{f}_Z^{\mathrm{UB}}(u) = \alpha^{|Z|}, \tag{3.20}$$

$$\alpha = 1 + u - \sqrt{u(2+u)}. \tag{3.21}$$

One notes that α is a solution of the equation $\alpha^2 - 2(1+u)\alpha + 1 = 0$, this leads to the non-trivial relation

$$1 + u = \frac{1+\alpha^2}{2\alpha} = \frac{1}{2}\left(\alpha + \alpha^{-1}\right). \tag{3.22}$$

Now that we have the expression for an unbiased TP, we turn to the case of a biased TP.

3.5.2 Biased tagged particle

We consider a unique vacancy on the site $\nu = \pm 1$, next to a biased TP. Two events can happen, either the TP jumps on site ν or the particle on site 2ν jumps on site ν. The first event is governed by an exponential law of rate (inverse time) p_ν, while the second is associated with an exponential clock of rate $1/2$. The motion of the vacancy is thus governed by the exponential law of rate $(p_\nu + 1/2)$, $\chi_V(t) = (p_\nu + 1/2)e^{-(p_\nu+1/2)t}$. When such a jump of the vacancy occurs, there is a probability $p_\nu/(p_\nu + 1/2)$ that it is done in the direction of the TP, and $(1/2)/(p_\nu + 1/2)$ that it is done in the opposite direction.

We call $f_\nu(t)$ the probability of first passage of the vacancy at the origin, knowing that it starts from site ν. Either it is due to the first jump of the vacancy at time t, or the vacancy jumps on site 2ν at time $t_0 < t$, comes back to site ν by an unbiased random walk at time $t_0 + t_1$ and then arrives at the origin. This leads us to the relation,

$$f_\nu(t) = p_\nu e^{-(p_\nu+1/2)t} + \int_0^t dt_0 \frac{1}{2} e^{-(p_\nu+1/2)t_0} \int_0^{t-t_0} dt_1 f_1^{\mathrm{UB}}(t_1) f_\nu(t - t_0 - t_1). \tag{3.23}$$

We compute the Laplace transform of this equation and remember that $\hat{f}_\nu^{\mathrm{UB}}(u) = \alpha$ with α given by Eq. (3.21). Moreover, $1+u$ and α are linked by Eq. (3.22). We end up with

$$\hat{f}_\nu(u) = \frac{p_\nu}{u + p_\nu + 1/2 - \alpha/2} = \frac{\alpha(1+\nu s)}{1+\nu s\alpha} \tag{3.24}$$

where s is the bias. In particular, as expected, if $p_\nu = 1/2$, $\hat{f}_\nu(u) = \hat{f}_\nu^{\mathrm{UB}}(u) = \alpha$.

$$f_Z(t) = \int_0^t dt_0 f_{|Z|-1}^{\mathrm{UB}}(t_0) f_\mu(t-t_0) \tag{3.25}$$

$$\hat{f}_Z(u) = \hat{f}_{|Z|-1}^{\mathrm{UB}}(t_0)\hat{f}_\mu(u) = \frac{1+\mu s}{1+\mu s\alpha}\alpha^{|Z|} \tag{3.26}$$

with $\mu = \mathrm{sign}(Z)$.

3.6 Results

3.6.1 Exact cumulant-generating function

Inserting the first passage quantities computed in Eq. (3.26) into the expression of the propagator with a single vacancy $\hat{\hat{p}}_Z(k,u)$, [Eq. (3.17)], we obtain

$$\hat{\hat{p}}_Z(k,u) = \frac{1}{u}\left[1 + \left(e^{i\mu k} - 1\right)\frac{2p_\mu}{1+\alpha}\alpha^{|Z|}\right]. \tag{3.27}$$

This immediately gives the solution for the cumulant-generating function [Eq. (3.11)],

$$\lim_{\rho_0\to 0}\frac{\hat{\psi}(k,u)}{\rho_0} = \frac{1}{u}\frac{2\alpha}{1-\alpha^2}\sum_{\mu=\pm 1} p_\mu(e^{i\mu k} - 1). \tag{3.28}$$

After some manipulation we find our final result in Laplace space,

$$\lim_{\rho_0\to 0}\frac{\hat{\psi}(k,u)}{\rho_0} = \frac{\cos k - 1 + is\sin k}{u^{3/2}\sqrt{2+u}}, \tag{3.29}$$

where the bias is $s = p_1 - p_{-1}$. And we are lucky that the Laplace transform can be inverted. We find successively that

$$\lim_{\rho_0\to 0}\frac{1}{\rho_0}\frac{\partial\psi(k,t)}{\partial t} = e^{-t}I_0(t)(\cos k - 1 + is\sin k), \tag{3.30}$$

$$\lim_{\rho_0\to 0}\frac{\psi(k,t)}{\rho_0} = te^{-t}[I_0(t) + I_1(t)](\cos k - 1 + is\sin k), \tag{3.31}$$

where I_0 and I_1 are modified Bessel functions of the first kind. This is our main result and to the best of our knowledge it has never been written like this before. This implies that we have the full time-dependence of the even (κ_{2n}) and odd (κ_{2n+1}) cumulants,

$$\lim_{\rho_0\to 0}\frac{\kappa_{2n}(t)}{\rho_0} = te^{-t}[I_0(t) + I_1(t)] \qquad \lim_{\rho_0\to 0}\frac{\kappa_{2n+1}(t)}{\rho_0} = s\,te^{-t}[I_0(t) + I_1(t)]. \tag{3.32}$$

The analytical results for the cumulants κ_2, κ_4, κ_6 and κ_8 of an unbiased TP are compared to numerical simulations on Fig. 3.4. The same is done for the cumulants κ_1, κ_2, κ_3 and κ_4 of a biased TP on Fig. 3.5. In both cases, an excellent agreement is found at high density at all times.

3.6.2 Short time and large time limit

At short time, we find that the cumulants obey

$$\lim_{\rho_0\to 0}\frac{\kappa_{2n}(t)}{\rho_0}\underset{t\to 0}{\sim} t \qquad\qquad \lim_{\rho_0\to 0}\frac{\kappa_{2n+1}(t)}{\rho_0}\underset{t\to 0}{\sim} st. \tag{3.33}$$

This means in particular that the variance κ_2 is diffusive, and that the displacement of a biased TP κ_1 is ballistic. These are the behaviors that can be intuitively expected.

At large time, we find that the cumulant-generating function satisfies

$$\lim_{\rho_0\to 0}\frac{\psi(k,t)}{\rho_0}=\sqrt{\frac{2t}{\pi}}(\cos k-1+is\sin k) \tag{3.34}$$

and the cumulants

$$\lim_{\rho_0\to 0}\frac{\kappa_{2n}(t)}{\rho_0}\underset{t\to\infty}{\sim}\sqrt{\frac{2t}{\pi}}, \qquad\qquad \lim_{\rho_0\to 0}\frac{\kappa_{2n+1}(t)}{\rho_0}\underset{t\to\infty}{\sim} s\sqrt{\frac{2t}{\pi}}. \tag{3.35}$$

The variance κ_2 is subdiffusive, and the displacement κ_1 is sub-ballistic. These expressions are in agreement with the literature [27, 28, 38].

3.6.3 Large deviation function

One can also compute the large deviation function $\phi(y)$ associated with a displacement Y of the TP. Using the Gärtner-Ellis theorem [59] linking the large deviation function to the cumulant-generating function [Eq. (3.34)] by a Legendre transform, we write

$$\mathbb{P}\left(Y=\rho_0\sqrt{\frac{2t}{\pi}}y\right)\asymp e^{-\rho_0\sqrt{\frac{2t}{\pi}}\phi(y)}, \tag{3.36}$$

$$\phi(y)=\sup_{q\in\mathbb{R}}\left[qy-(\cosh q-1+s\sinh q)\right]. \tag{3.37}$$

The symbol '$\asymp$' denotes asymptotic equivalence at exponential order when $t\to\infty$.

We solve the extremum over q and obtain $e^{\pm q}=\pm y+\sqrt{y^2+1-s^2}$, which gives us

$$\phi(y)=1-sy-\sqrt{y^2+1-s^2}+y\ln\left[y+\sqrt{y^2+1-s^2}\right]. \tag{3.38}$$

We will use this result in the next chapters.

3.7 Quenched initial conditions

In this last section, we consider a frozen initial disorder, also known in the literature as *quenched* disorder. The positions of the particles are assigned initially and one averages over multiple realizations of the evolution of the system. One then usually considers a "typical" initial condition by averaging over all the possible initial conditions at the end of the computation.

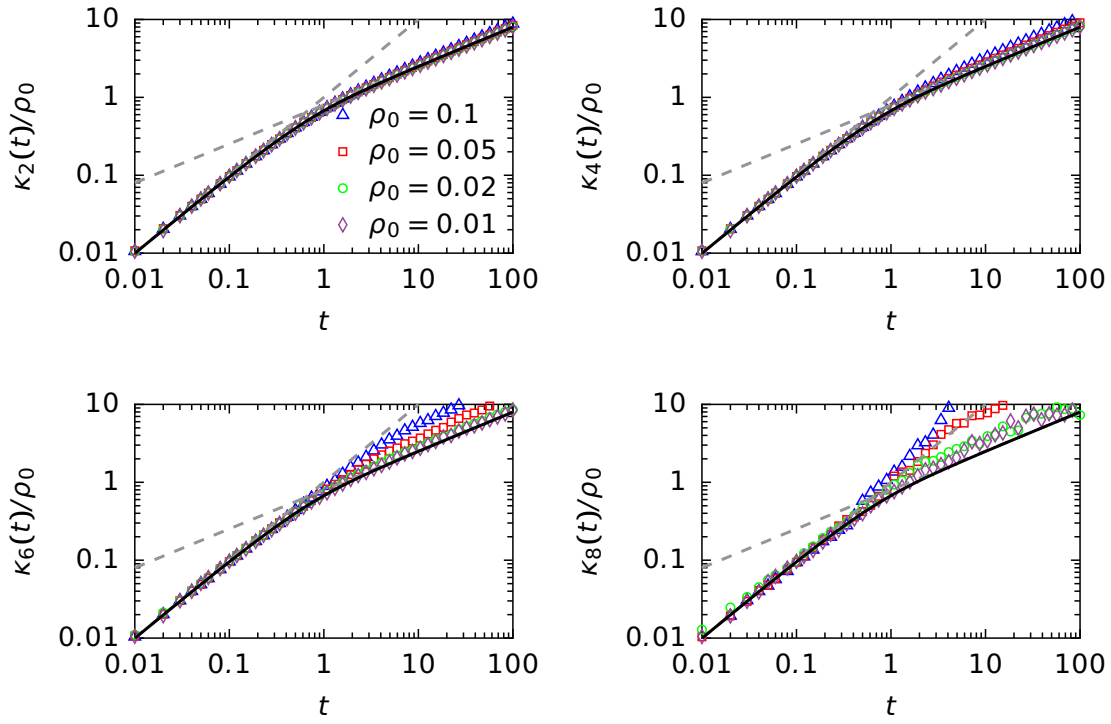

Figure 3.4: Time dependence of the cumulants κ_2, κ_4, κ_6 and κ_8 of an unbiased TP in the dense SEP ($\rho_0 = 0.1, 0.05, 0.02, 0.01$). The black line is the prediction from Eq. (3.32), the gray lines are the asymptotic regimes at short and large time. We note that the higher the order of the cumulant is, the lower ρ_0 should be in order to match the prediction.

3.7.1 Link with the single-vacancy case

We come back to the finite system with $\mathcal{N}$ sites and M vacancies considered in section 3.3. $P^{(t)}(Y|\{Z_j\})$ is the probability that the TP has a displacement Y at time t knowing that the M vacancies are initially at sites $\{Z_j\}$, and $\tilde{P}^{(t)}(k|\{Z_j\})$ is its Fourier transform. We define a cumulant-generating function conditioned on the initial positions of the vacancies,

$$\psi(k,t|\{Z_j\}) \equiv \log \tilde{P}^{(t)}(k|\{Z_j\}). \tag{3.39}$$

This object encapsulates the behavior of the system with given initial conditions. The quenched cumulant-generating function ψ_Q is then defined as the average of this quantity over the initial positions

$$\psi_Q(k,t) \equiv \frac{1}{(\mathcal{N}-1)^M} \sum_{Z_1,\dots,Z_M} \psi(k,t|\{Z_j\}). \tag{3.40}$$

We recall that at high density, $\rho_0 \equiv M/\mathcal{N} \to 0$, the propagator with M vacancies is expressed in terms of the one with a single vacancy [Eq. (3.7)]. We quickly find that the high density limit of the quenched cumulant-generating function reads

$$\lim_{\rho_0 \to 0} \frac{\psi_Q(k,t)}{\rho_0} = \sum_{Z \neq 0} \log \tilde{p}_Z^{(t)}(k). \tag{3.41}$$

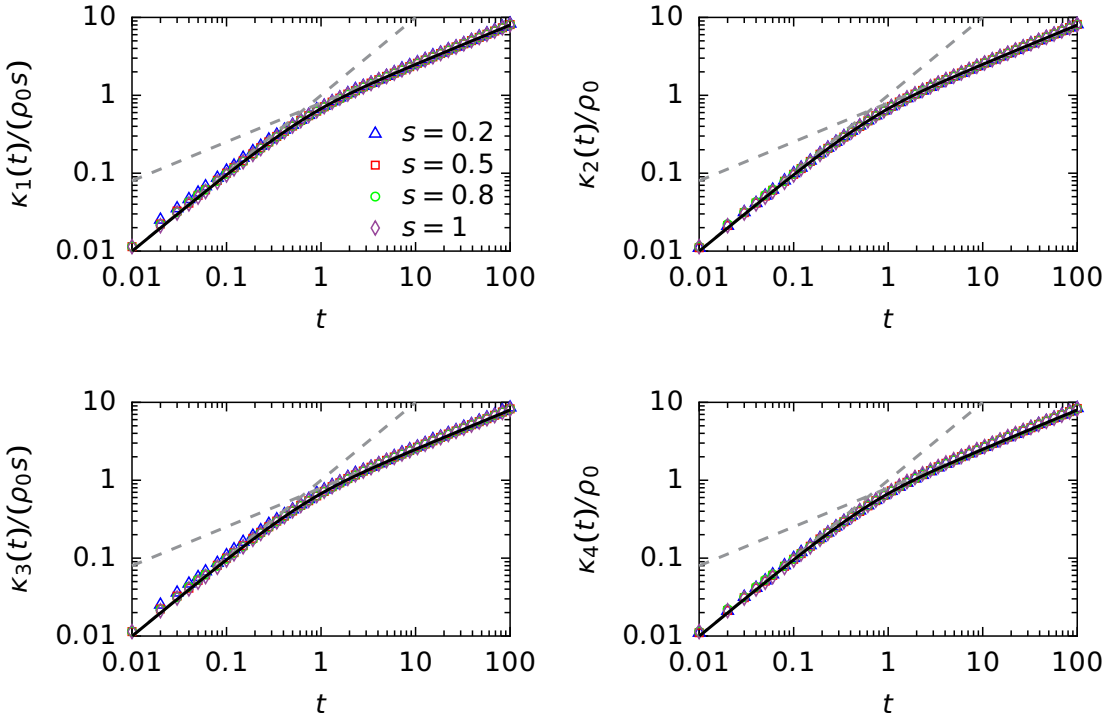

Figure 3.5: Time dependence of the cumulants κ_1, κ_2, κ_3 and κ_4 of a biased TP in the dense SEP ($\rho_0 = 0.02$). The values of the bias are $s = 0.2, 0.5, 0.8, 1$. The black line is the prediction from Eq. (3.32), the gray lines are the asymptotic regimes at short and large time.

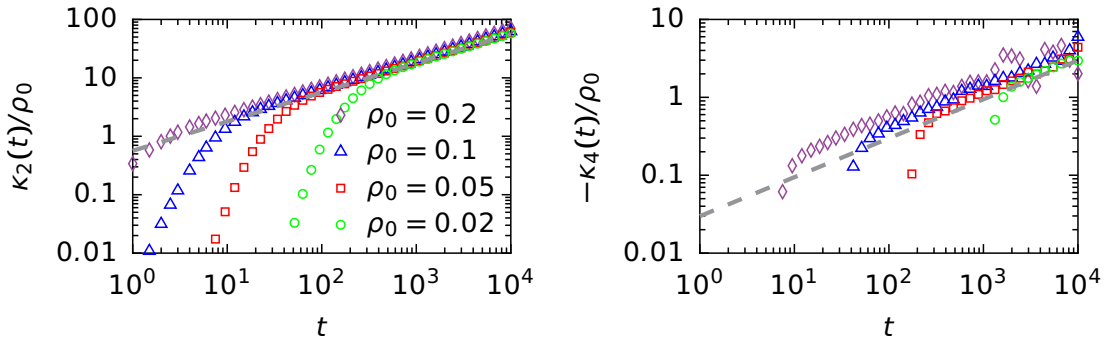

Figure 3.6: Time dependence of the cumulants κ_2 and κ_4 for deterministic initial conditions at high density (ρ_0 ranges from 0.02 to 0.2). The dashed gray lines are the predictions at large time for quenched initial conditions.

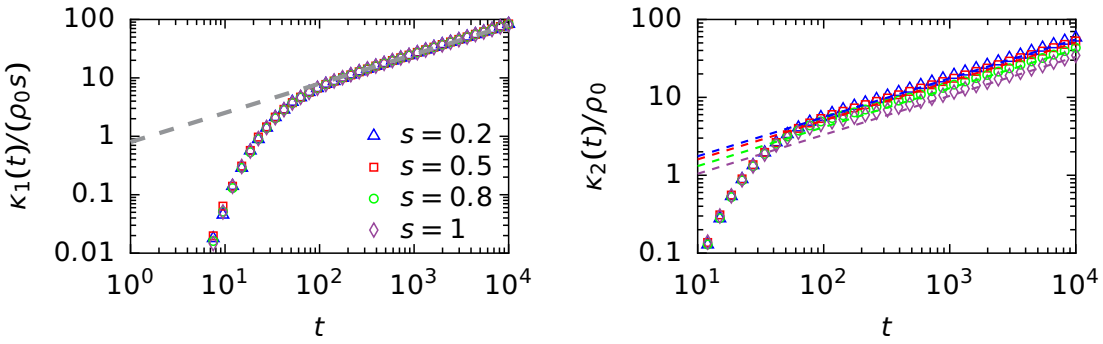

Figure 3.7: Time dependence of the first two cumulants κ_1 and κ_2 of a biased TP in the dense SEP ($\rho_0 = 0.05$) with deterministic initial conditions. The values of the bias are $s = 0.2, 0.5, 0.8, 1$. The dashed lines (gray on the left panel, colored on the right panel) are the large-time predictions from Eqs. (3.46) and(3.47).

3.7.2 Result at large time

The right-hand side of Eq. (3.41) does not involve a linear combination of the $\tilde{p}_Z^{(t)}(k)$. As a result, one cannot easily express the Laplace transform in time of the quenched cumulant-generating function in terms of the Laplace transform $\hat{\tilde{p}}_Z(k,u)$ given in Eq. (3.27). One needs to invert Eq. (3.27) to obtain an expression in time.

We use the limit $u \to 0$ with $u|Z|^2$ kept constant. This corresponds to the limit of large time $t \to \infty$ with $|Z|/\sqrt{t}$ constant. As $\alpha = 1 - \sqrt{2u} + \mathcal{O}(u)$, we write $\alpha^{|Z|} = e^{|Z| \ln \alpha} \underset{u\to 0}{\sim} e^{-|Z|\sqrt{2u}}$. From Eq. (3.27), this leads us to

$$\hat{\tilde{p}}_Z(k,u) \underset{u\to 0}{\sim} \frac{1}{u} + p_\mu \left(e^{i\mu k} - 1\right) \frac{e^{-|Z|\sqrt{2u}}}{u}. \tag{3.42}$$

This Laplace transform can be inverted, we obtain

$$\tilde{p}_Z^{(t)}(k) \underset{t\to\infty}{\sim} 1 + p_\mu \left(e^{i\mu k} - 1\right) \operatorname{erfc}\left(\frac{|Z|}{\sqrt{2t}}\right). \tag{3.43}$$

One obtains an intermediate result for the quenched cumulant-generating function [Eq. (3.41)],

$$\lim_{\rho_0 \to 0} \frac{\psi_Q(k,t)}{\rho_0} \underset{t\to\infty}{\sim} \sum_{Z=1}^{\infty} \sum_{\mu=\pm 1} \log\left[1 + p_\mu \left(e^{i\mu k} - 1\right) \operatorname{erfc}\left(\frac{|Z|}{\sqrt{2t}}\right)\right] \tag{3.44}$$

which by Riemann summation gives

$$\lim_{\rho_0 \to 0} \frac{\psi_Q(k,t)}{\rho_0} \underset{t\to\infty}{\sim} \sqrt{2t} \int_0^\infty dz \log\left[1 + p_1 \left(e^{ik} - 1\right) \operatorname{erfc} z\right] \left[1 + p_{-1} \left(e^{-ik} - 1\right) \operatorname{erfc} z\right]. \tag{3.45}$$

The first two cumulants can be computed exactly,

$$\lim_{\rho_0 \to 0} \frac{\kappa_1^Q(t)}{\rho_0} \underset{t\to\infty}{\sim} s\sqrt{\frac{2t}{\pi}}, \tag{3.46}$$

$$\lim_{\rho_0 \to 0} \frac{\kappa_2^Q(t)}{\rho_0} \underset{t\to\infty}{\sim} \sqrt{\frac{t}{\pi}} \left(1 + s^2(1 - \sqrt{2})\right). \tag{3.47}$$

We note that the displacement κ_1^Q is not modified by the initial conditions, consistently with the observations of Ref. [70]. On the contrary, the variance $\kappa_2^Q(t)$ is modified in two striking ways. First, contrary to the annealed initial conditions, the variance now depends on the bias s (it actually decreases with increased bias). And secondly, in the absence of bias ($s=0$), the scaling with time is $\sqrt{t/\pi}$ instead of $\sqrt{2t/\pi}$ in the annealed case. This $\sqrt{2}$ difference is well known and has been commented in the literature [35, 41]. It is a consequence of the fact that single-file systems have an infinite memory.

We performed simulations of the dense SEP with deterministic initial conditions: the vacancies are equally spaced initially. This configuration is the initial one for all simulations and the average is taken only over the evolution of the system. We show on Figs. 3.6 (no bias) and 3.7 (biased TP) that the large-time behavior of these simulations is well described by our approach.

3.7.3 Comments on the unbiased case

In the unbiased case ($p_1 = p_{-1} = 1/2$), Eq. (3.45) can be recast as

$$\lim_{\rho_0\to 0} \frac{\psi_Q(k,t)}{\rho_0} \underset{t\to\infty}{\sim} \sqrt{2t}\int_0^\infty dz \log\left[1-\sin^2\left(\frac{k}{2}\right)\operatorname{erfc} z \operatorname{erfc}(-z)\right]. \tag{3.48}$$

The first non-zero cumulants are

$$\lim_{\rho_0\to 0} \frac{\kappa_2^Q(t)}{\rho_0} \underset{t\to\infty}{\sim} \sqrt{\frac{t}{\pi}} \simeq 0.39894\sqrt{2t} \tag{3.49}$$

$$\lim_{\rho_0\to 0} \frac{\kappa_4^Q(t)}{\rho_0} \simeq -0.02109\sqrt{2t} \tag{3.50}$$

$$\lim_{\rho_0\to 0} \frac{\kappa_6^Q(t)}{\rho_0} \simeq 0.00893\sqrt{2t}. \tag{3.51}$$

These results are extremely similar to the ones found in the low-density limit (Brownian interacting particles) in Ref. [41]. Indeed the authors find

$$\psi_Q(k,t) \underset{\rho\to 0, t\to\infty}{\sim} \rho\sqrt{2t}\int_0^\infty dz \log\left[1-\sin^2\left(\frac{k}{2\rho}\right)\operatorname{erfc} z \operatorname{erfc}(-z)\right]. \tag{3.52}$$

Note that this similarity between the high and low density does not give insight into an arbitrary density. Indeed the fourth cumulant in the quenched setting has been computed at arbitrary density [47] and reads

$$\kappa_4^Q(t) = \frac{1-\rho}{\rho^3}\left[2(1-2\rho)^2\left(\frac{9}{\pi}\arctan\left(\frac{1}{2\sqrt{2}}\right)-1\right)+\rho(1-\rho)(4-3\sqrt{2})\right]\sqrt{\frac{t}{\pi}}. \tag{3.53}$$

This expression is much more complicated than the limit cases $\rho\to 0$ and $\rho\to 1$.

3.8 Conclusion

In this chapter, we saw that the probability law of the motion of a biased TP in the dense SEP can be computed by studying the motion of a single vacancy in the SEP [Eq. (3.11)]. The latter computation can be performed using standard results on random walks. We find the full time-dependence

of the cumulants of the position [Eq. (3.32)]. This interpolates between a linear dependence at short time (isolated particle) and a dependence as $t^{1/2}$ at large time which is characteristic of single file systems and corresponds to the results of Ref. [38]. Furthermore our approach extends to quenched initial conditions, and the large time quenched cumulant-generating function can be computed [Eq. (3.45)]. Our findings are backed by numerical simulations.

In the next two chapters, we show that our approach extends first to an arbitrary number of unbiased TPs in the dense SEP thus giving the full N-tag probability law; and then to two (and more) biased TPs, revealing collective effects.

Chapter 4

Dense symmetric exclusion process: N-tag probability law

Contents

4.1 Introduction

A tagged particle (TP) in the SEP, at position $X(t)$ exhibits anomalous behaviors. Its motion is subdiffusive [27] $\langle X(t)^2\rangle \propto \sqrt{t}$, instead of the usual diffusive scaling $\langle X(t)^2\rangle \propto t$. A closely related result is the consequence of a fluctuation dissipation principle: if the TP is (weakly) biased, its motion is sub-ballistic [42, 43] $\langle X(t)\rangle \propto \sqrt{t}$, instead of a ballistic scaling $\langle X(t)\rangle \propto t$. These peculiar behaviors stem from the strong geometrical constraints of the system: the particles of the SEP cannot bypass each other. This induces important spatial correlations in the system. Our goal is to characterize these correlations, and thus to go beyond single-TP observables and compute observables involving several TPs. So far, the only example of studies of correlation functions concerns models related to but different from the SEP. In the case of point-like hard-core particles on the line, which corresponds to the dilute limit of the SEP, a quantity related to the two-tag probability distribution has been computed explicitely [31]. The lowest order of

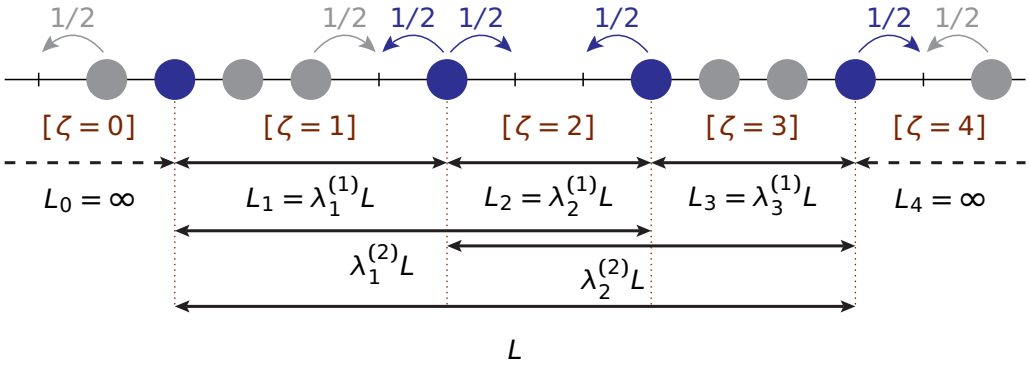

Figure 4.1: Symmetric exclusion process with 4 tagged particles (blue). The jump rates are $1/2$ for each allowed jump. The figure summarizes our notation for the initial distances between particles. The zones $\zeta = 0, 1, 2, 3, 4$ are also defined.

two-point correlation functions has also been derived for the random-average process [32–34], which displays features similar to the SEP. Finally, the SEP is sometimes mapped on an interface problem using a process called stochastic harmonic theory [30] leading to the Edwards-Wilkinson equation (see Appendix B for more details). This gives a Gaussian theory from which the lowest order two-point correlations can be extracted. Our goal is both to probe non-Gaussian behaviors and to study N-tag correlations.

In this chapter, we consider N tagged particles in the SEP (Fig. 4.1, $N = 4$) and study the full joint distribution of their displacements. We first give some important features at arbitrary density: we compute an equilibrium law for the distance between two TPs and show that this implies that the TPs have a coordinated motion at large time, moving as a single effective TP. This helps us understand the time scales of our problem. Secondly, we focus on the dense limit and use the vacancy-based approach introduced in the previous chapter to derive the full N-tag probability law of the problem. A major result is that the N-tag cumulants obey a universal scaling irrespective of the number of particles and the order of the cumulants. A time-dependent large deviation function is also obtained and enables us to obtain in particular the approach to the large time regime.

The results of this chapter have been published in [P3].

4.2 Large time behavior at arbitrary density

Our main result will be the characterization of the SEP in the high density limit. But before doing it, we obtain some important results that hold at arbitrary density. We first study the probability law of the distance between two TPs at equilibrium and obtain its expression. We then use this stationarity to show that at large time the TPs behave as a single one and identify the time regimes of the motion of the TPs.

4.2.1 Law of the distance between two particles

Let us consider two TPs in the SEP at density ρ, initially separated by a distance L. We focus on the distribution P_Δ of the distance Δ between the two TPs at large time. We will use extensively the fact that the SEP is an equilibrium system.

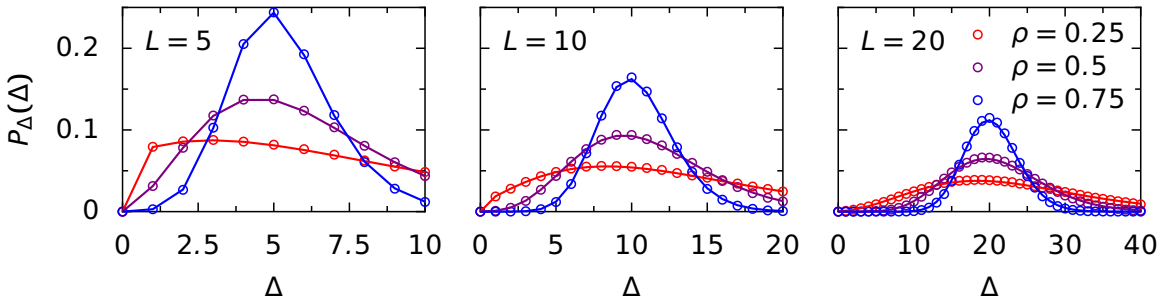

Figure 4.2: Probability law of the equilibrium distance Δ between two tagged particles in the SEP with its variation with the initial distance L (from left to right) and the average density ρ ($\rho = 0.25, 0.5, 0.75$ from red to blue). The circles are the results of numerical simulations at time $t = 2 \cdot 10^4$ (which we check is enough for convergence) and the lines are the prediction from Eq. (4.4).

The distance Δ is the sum of the number of particles and the number of vacancies between the TPs. The number k of particles is fixed initially and does not evolve; its probability law is denoted $P_{\text{part}}(k)$. On the other hand, the number m of vacancies fluctuates at equilibrium with a law $P_{\text{vac}}(m|k)$ that depends on k. As $\Delta = k + m + 1$, we can write

$$P_\Delta(\Delta) = \sum_{k=0}^{L-1} P_{\text{part}}(k) P_{\text{vac}}(\Delta - k - 1|k). \tag{4.1}$$

Initially there are $L-1$ sites between the TPs. Initially, they are all occupied independently with probability ρ. The law of k is thus binomial,

$$P_{\text{part}}(k) = \binom{L-1}{k} \rho^k (1-\rho)^{L-1-k}. \tag{4.2}$$

At equilibrium, we scan the sites between the two TPs, starting from the left TP and moving to the right. At each site, there is a probability ρ (independent of the other sites) of finding a particle. And by definition the $(k+1)$th particle is the right TP. The number of vacancies m is the number of times we failed to discover a particle. By definition, the number m of failures before $k+1$ successes is a negative binomial law written

$$P_{\text{vac}}(m|k) = \binom{m+k}{m} (1-\rho)^m \rho^{k+1}. \tag{4.3}$$

Finally, Eq. (4.1) leads to

$$P_\Delta(\Delta) = \sum_{k=0}^{L-1} \binom{L-1}{k} \binom{\Delta-1}{k} \rho^{2k+1} (1-\rho)^{L+\Delta-2k-2}. \tag{4.4}$$

This is the expression of the stationary law of the distance between two TPs initially separated by L. This exact expression is found to be in very good agreement with numerical simulations (Fig. 4.2).

Large deviation function

From Eq. (4.4), one derives the generating function

$$G_\Delta(z) \equiv \sum_{\Delta=1}^{\infty} P_\Delta(\Delta) z^\Delta = \left[\frac{\rho z}{1-(1-\rho)z}\right]\left[\frac{\rho^2 z}{1-(1-\rho)z} + 1 - \rho\right]^{L-1}. \tag{4.5}$$

For large initial distances, it scales as

$$\frac{1}{L}\ln G_\Delta(e^\nu) \xrightarrow[L\to\infty]{} \ln\left(\frac{\rho^2 e^\nu}{1-(1-\rho)e^\nu} + 1 - \rho\right) \equiv \psi_\Delta(\nu). \tag{4.6}$$

We define the variation of distance $D = \Delta - L$ and its probability law $P_{\rm dist}(D) = P_\Delta(L^* + \Delta)$. We apply the Gärtner-Ellis theorem of large deviations [59] and obtain

$$P_{\rm dist}(D = Ld) \asymp e^{-L\phi_D(d)}, \tag{4.7}$$

$$\phi_D(d) = \sup_{\nu\in\mathbb{R}}[(1+d) - \phi(\nu)] = \sup_{\nu\in\mathbb{R}}\left[\nu(1+d) - \ln\left(\frac{\rho^2}{e^{-\nu} - (1-\rho)} + 1 - \rho\right)\right]. \tag{4.8}$$

The symbol '$\asymp$' denotes asymptotic equivalence at exponential order when $L \to \infty$. ϕ_D is the large deviation function associated with the distance. We are especially interested in its expression in the high density limit $\rho = 1 - \rho_0$ with ρ_0 small. One checks that

$$\lim_{\rho_0\to 0} \frac{\phi_D(2\rho_0 u)}{2\rho_0} = \phi(u), \tag{4.9}$$

$$\phi(u) = 1 - \sqrt{1+u^2} + u\ln\left(u + \sqrt{1+u^2}\right). \tag{4.10}$$

Strikingly, ϕ is the same large-deviation function as the one of an unbiased TP at high density given by Eq. (3.36). We will check later that this expression is recovered from our high-density computations, and in numerical simulations [see Fig. 4.5c].

4.2.2 Cumulants at large time

Having derived the stationary law of the distance between two TPs, we now show what it implies for the time-evolution of the probability law of N TPs.

The positions of the N TPs at time t are denoted $X_1(t), \ldots, X_N(t)$ and their displacements are $Y_i(t) = X_i(t) - X_i^0$ with $X_i^0 = X_i(t=0)$. We define the cumulant-generating function as

$$\psi^{(t)}(\mathbf{k}) \equiv \ln\left\langle e^{i(k_1 Y_1 + \cdots + k_N Y_N)}\right\rangle \tag{4.11}$$

It generates the N-tag cumulants $\kappa^{(N)}_{p_1,\ldots,p_N}$ from the expansion in powers of $\mathbf{k}$,

$$\psi^{(t)}(\mathbf{k}) \equiv \sum_{p_1=0}^{\infty}\cdots\sum_{p_N=0}^{\infty} \frac{(ik_1)^{p_1}\ldots(ik_N)^{p_N}}{p_1!\ldots p_N!}\kappa^{(N)}_{p_1,\ldots,p_N}. \tag{4.12}$$

We give some examples: $\kappa^{(1)}_1 = \langle Y_1\rangle$, $\kappa^{(1)}_2 = \langle(\delta Y_1)^2\rangle$, $\kappa^{(2)}_{1,1} = \langle\delta Y_1\delta Y_2\rangle$, $\kappa^{(3)}_{1,1,1} = \langle\delta Y_1\delta Y_2\delta Y_3\rangle$, $\kappa^{(4)}_{1,1,1,1} = \langle\delta Y_1\delta Y_2\delta Y_3\delta Y_4\rangle - \langle\delta Y_1\delta Y_2\rangle\langle\delta Y_3\delta Y_4\rangle - \langle\delta Y_1\delta Y_3\rangle\langle\delta Y_2\delta Y_4\rangle - \langle\delta Y_1\delta Y_4\rangle\langle\delta Y_2\delta Y_3\rangle\ldots$ with $\delta Y_i = Y_i - \langle Y_i\rangle$. In particular, the cumulants of a single TP are $\kappa^{(1)}_p$ and at large time they satisfy

$$\kappa^{(1)}_p \underset{t\to\infty}{\sim} B_p(\rho)\sqrt{t} \tag{4.13}$$

with the coefficients $B_p(\rho)$ computed in Ref. [28].

In this subsection, we show that the large time behavior of the N-tag cumulants is identical to the one of the one-tag cumulants in the sense that

$$\lim_{t\to\infty} \frac{\kappa^{(N)}_{p_1,\dots,p_N}}{\sqrt{t}} = \lim_{t\to\infty} \frac{\kappa^{(1)}_{p_1+\cdots+p_N}}{\sqrt{t}} = B_{p_1+\cdots+p_N}(\rho). \tag{4.14}$$

Since the cumulants are linear combinations of the moments, it is enough to show that

$$A^{(N)}_{p_1,\dots,p_N} \equiv \langle Y_1^{p_1}\dots Y_N^{p_N}\rangle - \langle Y_1^{p_1+\cdots+p_N}\rangle = \mathscr{O}(t^{1/4}) \qquad \forall p_1,\dots,p_N \tag{4.15}$$

The key point is that while the moments of a TP scale as $t^{1/2}$, we saw in the previous subsection that the moments of the distance have a finite scaling at large time, that is to say[1]

$$\langle Y_1^p\rangle = \mathscr{O}\left(t^{1/2}\right) \quad \forall p\in\mathbb{N}, \qquad \langle (Y_i - Y_1)^p\rangle = \mathscr{O}\left(t^0\right) \quad \forall i\le N, \forall p\in\mathbb{N}. \tag{4.16}$$

We now give the proof of Eq. (4.15) using induction on N. The case $N=1$ is straightforward. Now, if Eq. (4.15) holds for a given N, let us prove that it holds for $N+1$. We show that $A^{(N+1)}_{p_1,\dots,p_N,q} = \mathscr{O}(t^{1/4})\ \forall q\ge 0$ by another induction on q. Indeed, for $q=0$ we have $A^{(N+1)}_{p_1,\dots,p_N,0} = A^{(N)}_{p_1,\dots,p_N} = \mathscr{O}(t^{1/4})$ from the inductive hypothesis on N. And if $A^{(N+1)}_{p_1,\dots,p_N,q'} = \mathscr{O}(t^{1/4})\ \forall q' < q$, we can write

$$A^{(N+1)}_{p_1,\dots,p_N,q} = \langle Y_1^{p_1}\dots Y_N^{p_N} Y_{N+1}^{q}\rangle - \langle Y_1^{p_1+\cdots+p_N+q}\rangle \tag{4.17}$$

$$= \langle Y_1^{p_1}\dots Y_N^{p_N}(Y_{N+1}-Y_1)^q\rangle - \sum_{r=1}^{q}\binom{q}{r}(-1)^r\left[\langle Y_1^{p_1+r}Y_2^{p_2}\dots Y_{N+1}^{q-r}\rangle - \langle Y_1^{p_1+\cdots+p_N+q}\rangle\right]. \tag{4.18}$$

The terms in the sum are of order $\mathscr{O}(t^{1/4})$ from the inductive hypothesis on q, and the first term can be bounded using the Cauchy-Schwarz inequality,

$$\left|\langle Y_1^{p_1}\dots Y_N^{p_N}(Y_{N+1}-Y_1)^q\rangle\right| \le \sqrt{\langle\left(Y_1^{p_1}\dots Y_N^{p_N}\right)^2\rangle\langle (Y_{N+1}-Y_1)^{2q}\rangle} = \sqrt{\mathscr{O}(t^{1/2})\mathscr{O}(t^0)} = \mathscr{O}(t^{1/4}). \tag{4.19}$$

This ends the proof of Eq. (4.15). We see that the key point is indeed the fact that the moments of the distance have a well-defined value at large time.

We stress that Eq. (4.14) has important consequences: it means that the large-time behavior of the N TPs is given by the one of a single TP. We now investigate the time regimes involved in the problem.

4.2.3 Time regimes

Our goal is to compute the full probability law of the displacements $\mathbb{P}(\{Y_i\})$. We remark that each initial length L_j (see Fig. 4.1) defines a diffusive time scale L_j^2. At short times, $t \ll L_j^2$ for all j, we expect the TPs to move independently from one another,

$$\mathbb{P}(\{Y_i\}) \underset{t\ll L_j^2}{\sim} \prod_{i=1}^{N} P_1(Y_i), \tag{4.20}$$

with P_1 the probability law of a single TP computed in Ref. [28] (see Appendix A).

[1] Actually, only the even moments (of a TP or of the distance) are non vanishing.

On the other hand, we saw that at large time the N TPs essentially behave as a single one. The N-tag cumulants are the same as the ones of any TP, or equivalently of the center of mass. In large-deviation form we are allowed to write

$$\mathbb{P}(\{Y_i = y_i\sqrt{t}\}) \asymp e^{-\sqrt{t}\Phi_1\left(\frac{y_1+\cdots+y_N}{N}\right)} \prod_{i=2}^{N} \delta(y_i - y_1), \tag{4.21}$$

where Φ_1 is the large-deviation function of a single TP computed in Ref. [28].

Naturally, one wants to derive the behavior between these two extremes, that is to say the behavior that happens for $t \sim L_j^2$. If we define the rescaled time $\tau = t/L^2$ and the relative distances $\lambda_j^{(1)} = L_j/L$ (see Fig. 4.1) we expect a large deviation principle of the type

$$\mathbb{P}(\{Y_i = y_i\sqrt{t}\}) \asymp e^{-\sqrt{t}K\left(\{y_i\},\tau,\{\lambda_j^{(1)}\}\right)} \tag{4.22}$$

with K to be determined.

From now on, we focus on the large density limit and unveil the behavior of the system at times $t \sim L^2$. We are able to obtain the function K involved in Eq. (4.22) and unveil a universal scaling form shared by the N-tag cumulants.

4.3 Framework at high density

We now study the dense limit of the SEP, at density $\rho \to 1$. The framework that we use is based on the study of the motion of the vacancies, it is an extension of section 3.3 to the case of N TPs. We follow the same steps. First we express the N-tag cumulant-generating function in terms of a propagator involving a single vacancy. Then, we express this propagator in terms of first passage quantities of a random walk. And finally, the latter quantities are computed from standard results.

4.3.1 From a single vacancy to the dense SEP

We first consider a system of size $\mathcal{N}$ with M vacancies (empty sites) initially at positions $Z_1, \ldots, Z_M$. We want an expression for the probability that the N TPs have displacements $\mathbf{Y} = (Y_1, \ldots, Y_N)$ at time t called $P^{(t)}(\mathbf{Y}|\{Z_j\})$. As we did in Eq. (3.4), this probability can be decomposed over displacements $\mathbf{Y}^j$ due to the j-th vacancy,

$$P^{(t)}(\mathbf{Y}|\{Z_j\}) = \sum_{\mathbf{Y}^1,\ldots,\mathbf{Y}^M} \delta_{\mathbf{Y},\mathbf{Y}^1+\cdots+\mathbf{Y}^M} \mathscr{P}^{(t)}(\{\mathbf{Y}^j\}|\{Z_j\}), \tag{4.23}$$

where $\mathscr{P}^{(t)}(\{\mathbf{Y}^j\}|\{Z_j\})$ is the probability that vacancies initially at sites Z_j induced displacements $\mathbf{Y}^j$ of the TPs. As in the previous chapter, we assume that in the high density limit, $\rho_0 = M/\mathcal{N} \to 0$ the motions of the vacancies are independent from one another and interact independently with the TPs. We state that this amounts to neglecting events of order $\mathcal{O}(\rho_0^2)$. We thus write

$$\mathscr{P}^{(t)}(\{\mathbf{Y}^j\}|\{Z_j\}) \underset{\rho_0\to 0}{\sim} \prod_{j=1}^{M} p_{Z_j}^{(t)}(\mathbf{Y}^j) \tag{4.24}$$

where $p_Z^{(t)}(\mathbf{Y})$ is the probability that a single vacancy initially at Z creates a displacement $\mathbf{Y}$ of the N TPs at time t. This is the key ingredient of our approach. Injecting into Eq. (4.23) and using

the Fourier transform

$$\tilde{P}^{(t)}(\mathbf{k}|\{Z_j\}) \equiv \sum_{\mathbf{Y}\in\mathbb{Z}^N} e^{i(k_1Y_1+\cdots+k_NY_N)}P^{(t)}(\mathbf{Y}|\{Z_j\}), \tag{4.25}$$

we obtain the decomposition

$$\tilde{P}^{(t)}(\mathbf{k}|\{Z_j\}) \underset{\rho_0\to 0}{\sim} \prod_{j=1}^{M} \tilde{p}_{Z_j}^{(t)}(\mathbf{k}). \tag{4.26}$$

At the same time, the annealed cumulant-generating function[2] is the logarithm of the Fourier transform of the probability law,

$$\psi^{(t)}(\mathbf{k}) \equiv \ln \tilde{P}^{(t)}(\mathbf{k}), \tag{4.27}$$

$$\tilde{P}^{(t)}(\mathbf{k}) \equiv \frac{1}{(\mathcal{N}-1)^M} \sum_{Z_1,\dots,Z_M\notin\{X_i^0\}} \tilde{P}^{(t)}(\mathbf{k}|\{Z_j\}), \tag{4.28}$$

where we perform an average over the initial conditions of the vacancies. The limit $\rho_0 = M/\mathcal{N} \to 0$ is then obtained as

$$\tilde{P}^{(t)}(\mathbf{k}) \underset{\rho_0\to 0}{\sim} \left[\frac{1}{\mathcal{N}-N}\sum_{Z\neq 0}\tilde{p}_Z^{(t)}(\mathbf{k})\right]^M = \left[1+\frac{1}{\mathcal{N}-N}\sum_{Z\neq 0}\left(\tilde{p}_Z^{(t)}(\mathbf{k})-1\right)\right]^M \tag{4.29}$$

$$\lim_{\rho_0\to 0}\frac{\psi^{(t)}(\mathbf{k})}{\rho_0} = \sum_{Z\notin\{X_i^0\}}\left(\tilde{p}_Z^{(t)}(\mathbf{k})-1\right). \tag{4.30}$$

This is the equivalent of Eq. (3.11) in the case of N TPs. Once again, the cumulant-generating function of the displacements at high density is expressed only in terms of the propagator of a single vacancy. This is a much simpler quantity and we now compute it.

4.3.2 Expression of the single-vacancy propagator

To express the single-vacancy propagator $p_Z^{(t)}(\mathbf{Y})$, a key definition is the one of the "adjacent sites", that is to say, the ones just next to a TP at the time that we consider. The adjacent site $\nu = +i$ is the site on the right of TP i (at position $X_i(t)+1$) while $\nu = -i$ is the site on the left of TP i (at position $X_i(t)-1$). The positions of the adjacent sites do evolve with time, but this is not a problem since we are only interested in the positions of the vacancies relatively to the TPs. In the following, Greek letters ν, μ, η always denote adjacent sites and the sums are done implicitely on the $2N$ sites $\nu = \pm 1, \cdots \pm N$. To quantify the displacements of the TPs, we define the vector $\mathbf{e}_\nu$ with $\nu = \pm i$ that has all components to 0 except the i-th that is ± 1: it corresponds to a displacement ± 1 of TP i. The conventions for the adjacent sites are summarized on Fig. 4.3.

Our last definition is $f_{\nu,Z}^{(t)}$, with $\nu = \pm i$. It is the probability that, starting from Z, the vacancy arrives for the first time on the position of one of the TPs at time t, this TP being TP i, and knowing that its last site was the adjacent site ν. This event induces a motion of TP i in the

[2] The quenched cumulant-generating function satisfies $\psi_Q(\mathbf{k},t)/\rho_0 \sim \sum_Z \log \tilde{p}_Z^{(t)}(\mathbf{k})$ (see section 3.7). As our results will be obtained in Laplace space (in time), this expression is hard to manipulate due to the non-linearity of the logarithm. The quenched case is left for future work.

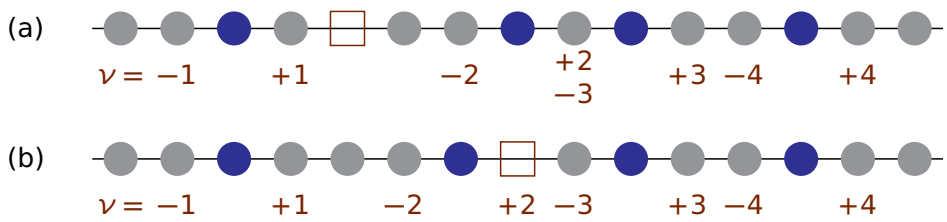

Figure 4.3: System with a single vacancy (brown square). The adjacent sites $\nu = \pm 1, \ldots, \pm 4$ are the sites next to the TPs. Between (a) and (b), the motion of the vacancy induced a motion of TP 2: the adjacent sites ± 2 also moved. Note that the motion of the vacancy makes the distances between TPs change; this is the reason why we introduce the parameter ζ (zone where the vacancy starts).

opposite direction (vector $\mathbf{e}_{-\nu}$). We can now partition the propagator $p_Z^{(t)}(\mathbf{Y})$ over the first event when one of the TPs is touched:

$$p_Z^{(t)}(\mathbf{Y}) = \delta_{\mathbf{Y},\mathbf{0}}\left(1 - \int_0^t d\tau \sum_\nu f_{\nu,Z}^{(\tau)}\right) + \int_0^t dt_1 \sum_\nu p_{-\nu}^{(t-t_1)}(\mathbf{Y} - \mathbf{e}_\nu) f_{\nu,Z}^{(t_1)}. \tag{4.31}$$

This is the analog of Eq. (3.12) in the case of N TPs. The reader might use this relation to understand better what our notations are. The first term corresponds to an absence of interaction between the vacancy and the TPs, and the second corresponds to a motion of one of the TPs due to an interaction. p_ν is an abuse of notation meaning that the vacancy starts from the adjacent site ν (we will make the same abuse of notation for $f_{\nu,\eta}$).

As we did in Eq. (3.12) for a single TP, we can now iterate the previous relation and decompose the motion of the TPs over all events. We write it for a vacancy that starts from the adjacent site η.

$$p_\eta^{(t)}(\mathbf{Y}) = \sum_{n=0}^{\infty} \sum_{\nu_1,\ldots,\nu_n} \delta_{\mathbf{Y},\sum_i \mathbf{e}_{\nu_i}} \int_0^\infty dt_1 \ldots dt_n \int_0^\infty d\tau\, \delta\left(t - \sum_{i=1}^n t_i - \tau\right) \times \left(1 - \sum_\mu f_{\mu,-\nu_n}^{(\tau)}\right) f_{\nu_n,-\nu_{n-1}}^{(t_n)} \ldots f_{\nu_2,-\nu_1}^{(t_2)} f_{\nu_1,\eta}^{(t_1)}, \tag{4.32}$$

with the convention $-\nu_0 = \eta$ if $n = 0$. We use the Fourier-transform in space and the Laplace transform in time,

$$\hat{\hat{p}}_Z(\mathbf{k},u) \equiv \sum_{Y_1,\ldots,Y_N=-\infty}^{\infty} e^{i(k_1 Y_1 + \cdots + k_N Y_N)} \int_0^\infty dt e^{-ut} p_Z^{(t)}(\mathbf{Y}). \tag{4.33}$$

Equations (4.31) and (4.32) then become

$$\hat{\hat{p}}_Z(\mathbf{k},u) = \frac{1}{u} + \sum_\nu \left[\hat{\hat{p}}_{-\nu}^{(\zeta)}(\mathbf{k},u) e^{i\mathbf{k}\cdot\mathbf{e}_\nu} - \frac{1}{u}\right] \hat{f}_{\nu,Z}(u), \tag{4.34}$$

$$\hat{\hat{p}}_\eta(\mathbf{k},u) = \frac{1}{u}\left\{\sum_{n=0}^{\infty} \sum_{\nu_n} \left(1 - \sum_\mu e^{-i\mathbf{k}\cdot\mathbf{e}_\mu} T_{\mu,\nu_n}(\mathbf{k},u)\right) [T(\mathbf{k},u)^n]_{\nu_n,\eta}\right\} \tag{4.35}$$

$$= \frac{1}{u}\left\{1 + \sum_\mu (1 - e^{-i\mathbf{k}\cdot\mathbf{e}_\mu}) \left[\frac{T}{1-T}\right]_{\mu,\eta}(\mathbf{k},u)\right\}. \tag{4.36}$$

We defined the $(2N \times 2N)$ matrix $T_{\mu,\nu}(\mathbf{k},u) = e^{i\mathbf{k}\cdot\mathbf{e}_\mu}\hat{f}_{\mu,-\nu}(u)$.

It now seems that we are done and can write the expression of the cumulant-generating function from Eq. (4.30). But there is one last subtlety to examine. When the vacancy interacts with a TP, the distance between two TPs changes by one unit[3]. However, the distance between two TPs to be considered in our computation is entirely set by the initial position of the vacancy. From Fig. 4.1, we define the zone $\zeta \in [0,N]$ in which the vacancy is initially situated: $\zeta = 0$ (resp. N) if it is on the left (resp. right) of all TPs, $\zeta = j$ if it is between TPs j and $j+1$. One realizes that the relevant distance between TPs j and $j+1$ is $L_j^{(\zeta)} = L_j + 1$ if $\zeta \neq j$ (the vacancy is added to the distance) and $L_j^{(j)} = L_j$ (the vacancy is already here). Quantities such as $f_{\mu,-\nu}$ and $T_{\mu,\nu}$ will depend on ζ by the intermediate of these relevant distances. In the following, for an adjacent site ν, we define $\zeta(\nu) = i$ if $\nu = +i$ and $\zeta(\nu) = i-1$ if $\nu = -i$ (the "zone" corresponding to site ν).

At the end of the day, the cumulant-generating function [Eq. (4.30)] can be expressed from Eqs. (4.34)-(4.36). We obtain

$$\lim_{\rho_0\to 0}\frac{\psi^{(t)}(\mathbf{k})}{\rho_0} = \frac{1}{u}\sum_\nu \left\{ (e^{i\mathbf{k}\cdot\mathbf{e}_\nu}-1) + e^{i\mathbf{k}\cdot\mathbf{e}_\nu}\sum_\mu (1-e^{-i\mathbf{k}\cdot\mathbf{e}_\mu})\left[\frac{T}{1-T}\right]_{\mu,-\nu}^{(\zeta(\nu))}(\mathbf{k},u)\right\} h_\nu(u), \tag{4.37}$$

$$h_\nu(u) = \sum_{Z\notin\{X_i^0\}} \hat{f}_{\nu,Z}(u). \tag{4.38}$$

Note that $\tilde{f}_{\nu,Z}$ is zero for all sites Z from which site ν cannot be reached. Hence, the sum in the expression of h_ν is only over the sites of the zone $\zeta(\nu)$ (see Fig. 4.1). Finally, the only quantities to compute are $\tilde{f}_{\mu,\nu}^{(\zeta)}(u)$ for all pair of adjacent sites, and $h_\nu(u)$ for all adjacent sites. We now compute them using standard results on random walks.

4.3.3 Expression of the quantities of interest

We first state the result of the first passage density of a walk with an absorbing site before computing $\tilde{f}_{\mu,\nu}^{(\zeta)}(u)$ and $h_\nu(u)$.

First passage density of a walk with an absorbing site. Let us consider a random walk on the discrete line. The probability density of being at site s at time t knowing that the walker was initially at site s_0 is denoted $P(s|s_0,t)$. Similarly, the probability of first passage at site s is denoted $F(s|s_0,t)$. It is easy to show [69] that the Laplace transforms of these two quantities satisfy $\hat{F}(s|s_0,u) = \hat{P}(s|s_0,u)/\hat{P}(s|s,u)$. We now consider the same walk with an absorbing site s_1: if the walker comes to s_1, it remains there forever. The probability (resp. first passage probability) of this modified walk is denoted $P_{s_1}^\dagger(s|s_0,t)$ (resp. $F_{s_1}^\dagger(s|s_0,t)$). Considering the first passage of the walker at s_1, one realizes [69] that $\hat{P}_{s_1}^\dagger(s|s_0,u) = \hat{P}(s|s_0,u) - \hat{P}(s|s_1,u)\hat{F}(s_1|s_0,u)$. At the end of the day, one obtains an expression for the first passage probability of the absorbing walk in terms of the first passage probability of the initial walk.

$$\hat{F}_{s_1}^\dagger(s|s_0,u) = \frac{\hat{P}_{s_1}^\dagger(s|s_0,u)}{\hat{P}_{s_1}^\dagger(s|s,u)} = \frac{\hat{P}(s|s_0,u)-\hat{P}(s|s_1,u)\hat{F}(s_1|s_0,u)}{\hat{P}(s|s,u)-\hat{P}(s|s_1,u)\hat{F}(s_1|s,u)} = \frac{\hat{F}(s|s_0,u)-\hat{F}(s|s_1,u)\hat{F}(s_1|s_0,u)}{1-\hat{F}(s|s_1,u)\hat{F}(s_1|s,u)} \tag{4.39}$$

[3] In the large time, large distance limit that we consider in the following, this effect plays no role. We still mention it for completeness.

As stated in subsection 3.5.1, the random walk that we consider for the vacancy is a Polya walk whose first passage density is given by

$$\hat{F}(s|s_0,u) = \alpha^{|s-s_0|}, \qquad \alpha = 1+u-\sqrt{u(2+u)}. \tag{4.40}$$

Expression of $\hat{f}_{\mu,\nu}$. The first-passage probability of touching TP 1 starting from site -1, or TP N from site $+N$ has the usual expression (no other TP can be touched).

$$\hat{f}_{-1,-1}(u) = \hat{f}_{N,N}(u) = \alpha \tag{4.41}$$

Then for $1 \le \mu \le N-1$, $\hat{f}_{\mu,\mu}$ is the first-passage probability of reaching TP μ without touching TP $\mu+1$ starting from site μ. One should understand that it is an application of Eq. (4.39) for $s=0$, $s_0=1$ and $s_1 = L_\mu$. By symmetry, $\hat{f}_{-(\mu+1),-(\mu+1)}$ has the same expression.

$$\hat{f}_{\mu,\mu} = \hat{f}_{-(\mu+1),-(\mu+1)} = \frac{\alpha - \alpha^{2L_\mu - 1}}{1-\alpha^{2L_\mu}} \tag{4.42}$$

Similarly, $\hat{f}_{\mu,-(\mu+1)}$ is the first-passage probability of reaching TP $\mu+1$ without touching TP μ starting from site μ. It corresponds to Eq. (4.39) with $s = L_\mu$, $s_0 = 1$ and $s_1 = 0$. By symmetry, $\hat{f}_{-(\mu+1),\mu}$ has the same expression.

$$\hat{f}_{\mu,-(\mu+1)} = \hat{f}_{-(\mu+1),\mu} = \frac{\alpha^{L_\mu - 1} - \alpha^{L_\mu+1}}{1-\alpha^{2L_\mu}} \tag{4.43}$$

The $\hat{f}_{\mu,\nu}$ corresponding to a pair (μ,ν) not mentioned above vanish because they correspond to situations that are impossible (another TP needs to be touched before the desired one).

Expression of h_ν. Finally, we need to compute the sums h_ν [Eq. (4.38)]. TP 1 can be touched from the left only for $Z<0$, in this case $\hat{f}_{-1,Z} = \alpha^{|Z|}$. The sum h_{-1}, which by symmetry is the same as h_{+N} is easy to compute,

$$h_{-1}(u) = h_{+N}(u) = \sum_{Z=-\infty}^{-1} \alpha^{Z'} = \frac{\alpha}{1-\alpha}. \tag{4.44}$$

For $1 \le \mu \le N-1$, $f_{\mu,\mu}$ and $f_{-(\mu+1),-(\mu+1)}$ are identical and correspond to a sum over all sites between TP μ and TP $\mu+1$: we number them $Z' = 1,\dots,L_\mu - 1$. The term for Z' corresponds to Eq. (4.39) with $s=0$, $s_0 = Z'$ and $s_1 = L_\mu$. We obtain

$$h_{+\mu}(u) = h_{-(\mu+1)}(u) = \sum_{Z'=1}^{L_\mu-1} \frac{\alpha^{Z'} - \alpha^{2L_\mu - Z'}}{1-2\alpha^{L_\mu}} = \frac{\alpha}{1-\alpha}\frac{(1-\alpha^{L_\mu})(1-\alpha^{L_\mu-1})}{1-\alpha^{2L_\mu}} \tag{4.45}$$

We remark that we recover Eq. (4.44) for $\mu = 0$ and N if we use the convention $L_0 = L_N = \infty$ (see Fig. 4.1).

Everything is now done to obtain the solution of the cumulant-generating function from Eq. (4.37).

4.4 Results at high density

In this section, we state the main results of the chapter. After writing the expression of the N-tag cumulant-generating function, we derive two important consequences: the universal scaling of the cumulants and the time-dependent large-deviation function.

4.4.1 Cumulant-generating function

We use a symbolic computation software (Mathematica) to inject the results of subsection 4.3.3 into the expression of the cumulant-generating function (4.37). We obtain,

$$\lim_{\rho_0\to 0}\frac{\hat{\psi}(\mathbf{k},u)}{\rho_0}=\frac{1}{u(1-\alpha^2)}\sum_{n=0}^{N-1}\sum_{i=1}^{N-n}\alpha^{\mathscr{L}_i^n}\Big\{2\alpha(1-\alpha^{L_{i-1}})(1-\alpha^{L_{i+n}})\cos(k_i+\cdots+k_{i+n}) \\ +(1-\alpha)Q_n(k_i,\ldots,k_{i+n})+C_{i,n}\Big\}. \quad (4.46)$$

$\alpha=1+u-\sqrt{u(2+u)}$, and $C_{i,n}$ are constants enforcing that the brackets vanish when $\mathbf{k}=\mathbf{0}$, so that $\hat{\psi}(\mathbf{k}=\mathbf{0})=0$. The sum of lengths $\mathscr{L}_i^n$ is given by

$$\mathscr{L}_i^n=L_i+\cdots+L_{i+n-1} \quad (4.47)$$

with the convention $L_0=L_N=\infty$ (see Fig. 4.1). And Q_n are terms that will not contribute to the asymptotic scaling, we write only the first two

$$Q_2(k_1,k_2)=\alpha^{L_1}\left(e^{ik_1}+e^{-ik_2}\right), \quad (4.48)$$

$$Q_3(k_1,k_2,k_3)=\alpha^{L_1}\left(e^{ik_1}+e^{-ik_2}\right)+\alpha^{L_2}\left(e^{ik_2}+e^{-ik_3}\right)+\alpha^{L_1+L_2}\left(e^{i(k_1+k_2)}+e^{-i(k_2+k_3)}+2\cos k_2\right). \quad (4.49)$$

We want to consider the limit of large time, that is to say the limit of Laplace parameter $u\to 0$. We rescale the Laplace variable u by setting $\tilde{u}=uL^2$ with $L=L_1+\cdots+L_N$ the initial distance between the extremal TPs. We consider the limit $u\to 0$ with $\tilde{u}$ kept constant. One notes that

$$\alpha^{\lambda L}\underset{u\to 0}{\sim}e^{-\lambda\sqrt{2\tilde{u}}} \quad (4.50)$$

so that when we keep only the dominant order, Eq. (4.46) simplifies into

$$\lim_{\rho_0\to 0}\frac{\hat{\psi}(\mathbf{k},u=L^2\tilde{u})}{\rho_0}\underset{u\to 0}{\sim}\frac{L^3}{\sqrt{2}\tilde{u}^{3/2}}\sum_{n=0}^{N-1}\sum_{i=1}^{N-n}\left(e^{-\sqrt{2\tilde{u}}\,\lambda_i^{(n)}}-e^{-\sqrt{2\tilde{u}}\,\lambda_{i-1}^{(n+1)}}-e^{-\sqrt{2\tilde{u}}\,\lambda_i^{(n+1)}}+e^{-\sqrt{2\tilde{u}}\,\lambda_{i-1}^{(n+2)}}\right) \\ \times(\cos(k_i+\cdots+k_{i+n})-1). \quad (4.51)$$

We defined $\lambda_i^{(n)}=\mathscr{L}_i^n/L=[L_i+\cdots+L_{i+n-1}]/L$ with $\lambda_i^{(0)}=0$ and the convention $L_0=L_N=+\infty$ (see Fig. 4.1). The following continuous inverse Laplace transform is known,

$$\hat{h}(u)=\frac{e^{-\lambda\sqrt{2u}}}{u^{3/2}}\Leftrightarrow h(t)=2\sqrt{\frac{t}{\pi}}g\left(\frac{\lambda}{\sqrt{2t}}\right), \quad (4.52)$$

$$g(w)=e^{-w^2}-\sqrt{\pi}\,w\,\mathrm{erfc}(w). \quad (4.53)$$

The function g corresponds to a Gaussian integrated twice (that is to say the integral of an error function). At the end of the day, Eq. (4.51) can be Laplace-inverted. The limit $u \to 0$ with $\tilde{u} = uL^2$ constant becomes a limit $t \to \infty$ with constant rescaled time $\tau = t/L^2$. Our final result is,

$$\lim_{\rho_0 \to 0} \frac{\psi^{(t)}(\mathbf{k})}{\rho_0} \underset{t\to\infty}{\sim} \sqrt{\frac{2t}{\pi}} \sum_{n=0}^{N-1} \sum_{i=1}^{N-n} \left[g\left(\frac{\lambda_i^{(n)}}{\sqrt{2\tau}}\right) - g\left(\frac{\lambda_{i-1}^{(n+1)}}{\sqrt{2\tau}}\right) - g\left(\frac{\lambda_i^{(n+1)}}{\sqrt{2\tau}}\right) + g\left(\frac{\lambda_{i-1}^{(n+2)}}{\sqrt{2\tau}}\right) \right] \times \left(\cos(k_i + \cdots + k_{i+n}) - 1\right). \quad (4.54)$$

This is the main result of this chapter. Even if we got rid of the very short time effects, we notice that this expression is still time-dependent, with the parameter $\tau = t/L^2$. We now state two important consequences of this result.

4.4.2 Universal scaling of the cumulants

The N-tag cumulants are obtained from the characteristic function [Eq. (4.12)]. For simplicity, we will focus on the ones involving all the N TPs, $\kappa^{(N)}_{p_1,\dots,p_N}$ with $p_i \neq 0$ for all i. Other cumulants can be obtained by tagging less particles[4]. Eq. (4.54) can be written as

$$\lim_{\rho_0 \to 0} \frac{\psi^{(t)}(\mathbf{k})}{\rho_0} \underset{t\to\infty}{\sim} \sqrt{\frac{2t}{\pi}} g\left(\frac{1}{\sqrt{2\tau}}\right) [\cos(k_1 + \cdots + k_N) - 1] + \dots \quad (4.55)$$

where the dots represent only cumulants involving less than N particles. All the odd cumulants $\kappa^{(N)}_{\text{odd}}(t) = \kappa^{(N)}_{p_1,\dots,p_N}$ with $p_1 + \cdots + p_N$ odd vanish as one expects for a system with no bias.

A striking feature is that all the even N-tag cumulants ($\kappa^{(N)}_{\text{even}}(t) = \kappa^{(N)}_{p_1,\dots,p_N}$ with $p_1 + \cdots + p_N$ even) are equal and satisfy the following universal scaling form

$$\lim_{\rho_0 \to 0} \frac{\kappa^{(N)}_{\text{even}}(t)}{\rho_0} = \sqrt{\frac{2t}{\pi}} g\left(\frac{1}{\sqrt{2\tau}}\right) + o(\sqrt{t}), \quad (4.56)$$

with g was defined in Eq. (4.53). This expression returns the expected large time behavior: as stated in Eq. (4.14), the N-tag cumulant eventually behaves as a one-tag cumulant (expression given in Eq. (3.35)). This prediction for arbitrary cumulants of an arbitrary number of TPs is in very good agreement with numerical simulations of the SEP (Fig. 4.4a, 2 to 4 TPs).

The scaling of Eq. (4.56) was known before for the correlation $\kappa^{(2)}_{1,1}$ between two TPs in two contexts. The first one is the Edwards-Wilkinson equation, which is seen as the Gaussian limit of the SEP at any density (see Appendix B for details); this equation indeed predicts [30] $\kappa^{(2)}_{1,1} = \kappa^{(2)}_2 g\left[(2\tau)^{-1/2}\right]$. Second, a similar scaling involving the function g and a rescaled time t/L^2 has been found for the correlation $\kappa^{(2)}_{1,1}$ of the random average process [33]. Note however that in our case, the scaling holds for arbitrary cumulants of an arbitrary number of TPs. It is also universal with respect to the initial positions of the TPs (at fixed total distance L). In particular, the only time-scale involved is $\tau = t/L^2$. The other time-scales t/L_j^2, with L_j the distances between two individual TPs, play no role. We however believe that it is a feature of high density and the arbitrary cumulants at arbitrary density should involve all the time scales.

[4] Note that tagging a particle that we do not look at is not neutral since it changes the initial conditions (the occupation of the given sites is imposed).

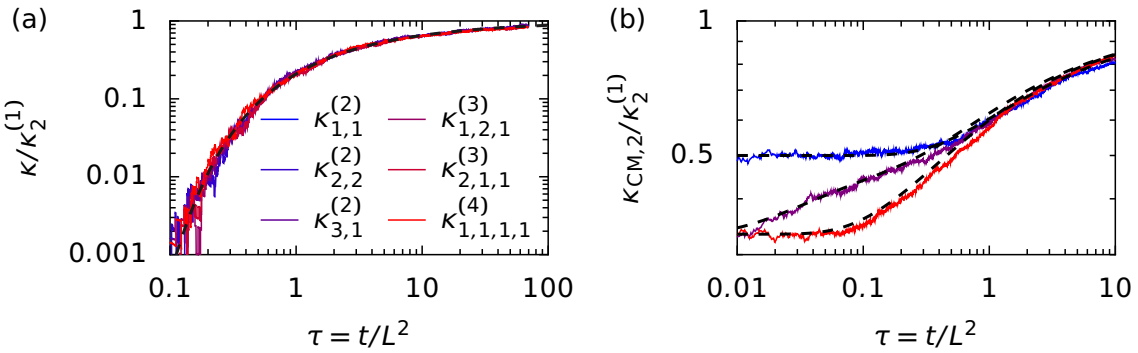

Figure 4.4: (a) Time evolution of various cumulants associated with 2 to 4 TPs, rescaled by the variance of a single TP, $\kappa_2^{(1)} = \rho_0\sqrt{2t/\pi}$. The colored lines are the results of numerical simulations with $\rho_0 = 0.002$ and initial total distance $L = 12$. The dashed black line is the universal prediction from Eq. (4.56). (b) Time evolution of the variance of the center of mass of 2 and 3 TPs ($\rho_0 = 0.002$, $L = 24$). From blue to red: 2 TPs, 3 TPs with $\lambda_1^{(1)} = 1/6$, 3 TPs with $\lambda_1^{(1)} = 1/2$. The dashed black lines are computed from Eq. (4.54).

While the N-tag cumulants are universal, the cumulants $\kappa_{CM,p}^{(N)}$ of the center of mass of N TPs, defined as

$$\psi^{(t)}\left(\frac{k}{N},\dots,\frac{k}{N}\right) \equiv \ln\left\langle e^{ik\left(\frac{Y_1+\cdots+Y_N}{N}\right)}\right\rangle \equiv \sum_{p=1}^{\infty}\frac{(ik)^p}{p!}\kappa_{CM,p}^{(N)}, \tag{4.57}$$

explicitely depend on the number of TPs and on their initial positions. One has to compute these cumulants directly from Eq. (4.54). This prediction is in very good agreement with the numerical simulations (Fig. 4.4b).

4.4.3 Time-dependent large deviation function

The last observable we want to look at is the N-tag large deviation function that is to say the generalization of Eq. (3.36) to the case of N tagged particles. First, we rewrite formally Eq. (4.54) as[5]

$$\psi(-i\mathbf{s},t) \equiv \ln\langle e^{\mathbf{s}\cdot\mathbf{Y}}\rangle \underset{t\to\infty}{\sim} \rho_0\sqrt{t}\,\chi(\mathbf{s},\tau), \tag{4.58}$$

$$\chi(\mathbf{s},\tau) = \sqrt{\frac{2}{\pi}}\sum_{n=0}^{N-1}\sum_{i=1}^{N-n}\left[g\left(\frac{\lambda_i^{(n)}}{\sqrt{2\tau}}\right) - g\left(\frac{\lambda_{i-1}^{(n+1)}}{\sqrt{2\tau}}\right) - g\left(\frac{\lambda_i^{(n+1)}}{\sqrt{2\tau}}\right) + g\left(\frac{\lambda_{i-1}^{(n+2)}}{\sqrt{2\tau}}\right)\right] \times\left[\cosh(s_i+\cdots+s_{i+n})-1\right]. \tag{4.59}$$

The Gärtner-Ellis theorem [59] states that a large deviation function for the probability law can be obtained as the Legendre transform of the rescaled characteristic function. In our case,

[5] A careful reader will note that we exchange the limits $\rho_0 \to 0$ and $t \to \infty$ without attempting to provide a justification.

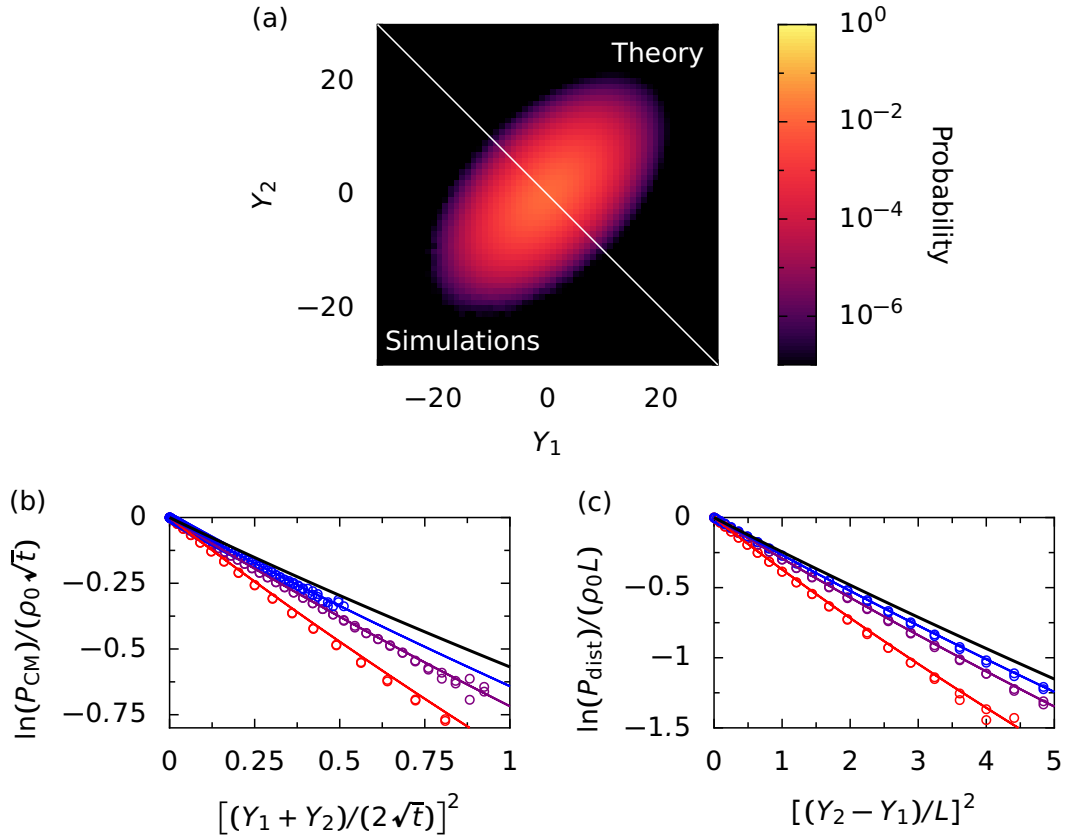

Figure 4.5: Numerical simulations relying on the dynamics of the vacancies for two TPs at parameters $\rho_0 = 0.01$ and $L = 10^3$. (a) Joint probability distribution of the displacements (Y_1, Y_2) at time $t = 5 \cdot 10^6$. Bottom left: simulations, top right: prediction from Eq. (4.60). (b) Rescaled marginal distribution of the displacement of the center of mass at times $t = 1 \cdot 10^6, 5 \cdot 10^6, 2 \cdot 10^7$ (recaled times $\tau = 1, 5, 20$, from red to blue). The colored circles come from the simulations while the colored lines are computed from Eq. (4.60). The black line is the asymptotic prediction from Eq. (4.62). (c) Rescaled marginal distribution of the distance at the same times as (b). The black line is the asymptotic prediction from Eq. (4.63). In (b) and (c), we took the square of the horizontal parameter for better readability and to see the deviations from gaussianity (straight lines).

we obtain the following expression for the joint probability distribution of the displacements.

$$\mathbb{P}\left(\{Y_i = \rho_0\sqrt{t}\,y_i\},\tau\right) \underset{t\to\infty}{\asymp} e^{-\rho_0\sqrt{t}K(\{y_i\},\tau)}, \tag{4.60}$$

$$K(\{y_i\},\tau) = \sup_{\mathbf{s}\in\mathbb{R}^N}\left[\sum_{i=1}^{N} s_i y_i - \chi(\mathbf{s},\tau)\right]. \tag{4.61}$$

$K(\{y_i\},\tau)$ is the N-tag large deviation function that depends on the rescaled time $\tau = t/L^2$. The symbol '$\asymp$' denotes asymptotic equivalence at exponential order. While the extremum could be written in terms of a set of implicit equations, this would not give more insight than numerically solving for the extremum. We perform numerical simulations relying on the random walks of the vacancies [6] and find a good agreement with our prediction for the joint probability law of two TPs at intermediate time (Fig. 4.5a).

In the case $N = 2$ TPs, it is especially interesting to look at the marginal distributions of the displacement of the center of mass $Y_{\mathrm{CM}} = (Y_1 + Y_2)/2$ and of the variation of distance $D = (Y_2 - Y_1)/2$. The large time limit ($\tau \to \infty$) of these two marginal laws can be computed, we obtain

$$\lim_{\tau\to\infty} P_{\mathrm{CM}}\left(Y_{\mathrm{CM}} = \rho_0\sqrt{\frac{2t}{\pi}}\,y\right) \asymp e^{-\rho_0\sqrt{\frac{2t}{\pi}}\phi(y)} \tag{4.62}$$

$$\lim_{\tau\to\infty} P_{\mathrm{dist}}\left(D = 2\rho_0 L d\right) \asymp e^{-2\rho_0 L\phi(d)} \tag{4.63}$$

with the large deviation function ϕ given by Eq. (4.10). These two results are consistent with the large deviation functions found previously for a single TP [Eq. (3.36)] and the distance [Eq. (4.9)]. Note that Eqs. (4.60)-(4.61), with respectively $s_2 = s_1 = s/2$ and $s_2 = -s_1 = s/2$ enable to quantify the deviations from these asymptotic laws at intermediate times. We check the predictions of these deviations in Fig. 4.5b-c and find a good agreement.

4.5 Conclusion

We started by showing that in the SEP at arbitrary density, the distance between two particles has an equilibrium probability distribution. This implies that an arbitrary number of tagged particles behave as a single one at large time, in the sense that the N-tag cumulants are equal to the single-tag cumulants [Eq. (4.14)]. The relevant timescales are the squares of the initial lengths between particles: below these the TPs are independent of one another, and above they move as a single one. We then determined the intermediate time regime in the high density limit. The method of Chap. 3 was extended to an arbitrary number of TPs. The N-tag cumulant-generating function was obtained [Eq. (4.54)]. Our main result is that all cumulants for an arbitrary number of TPs obey a universal scaling form involving only the initial distance between the extreme TPs [Eq. (4.56)]. Finally, we were also able to write the N-tag probability distribution in terms of a time-dependent large deviation function [Eq. (4.60)].

In the next chapter, we study the case of several biased tagged particles. The method is very similar but leads to much more tedious computations. We uncover collective effects between biased TPs that we call cooperativity and competition.

[6] Continuous-time simulations of the particles are too costly to obtain good statistics for rare events.

Chapter 5

Dense symmetric exclusion process: cooperativity and competition effects

Contents

5.1 Introduction

In the previous chapter, we provided the N-tag probability law of the dense symmetric exclusion process, which is an equilibrium system. But as we stated in Chap. 3, we are also interested in out-of-equilibrium effects that occur when one of the particles is biased. Known results for this situation are scarce and include notably the average displacement of the biased intruder [42, 43] and the higher-order cumulants in the dense limit (Ref. [38] and Chap. 3). In particular correlations in a system with a biased intruder were seldom looked at. A notable exception is the work done on the random average process [33, 34], in which two-tag observables were computed in the presence of a biased intruder. However, two-tag correlations have been shown to be crucial to check whether generalized fluctuation-dissipation relations hold for given initial conditions [35][1].

[1]The authors compare the displacement of an unbiased TP behind a biased TP to the correlations between these two TPs if they are both unbiased. The fluctuation-dissipation relation holds for equilibrium initial conditions but not for deterministic initial conditions that exhibit ageing. The method relies, among other things, on the Edwards-Wilkinson

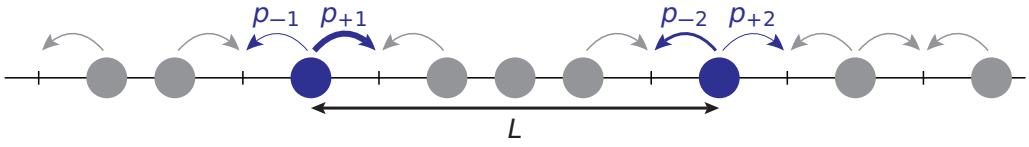

Figure 5.1: SEP with two biased TPs. The jump probabilities of TP i are $p_{\pm i} = (1 \pm s_i)/2$ where s_i are the biases. L denotes the initial distance between the TPs.

In this chapter, we investigate the probability law of two or more biased TPs in the dense SEP and bring to light striking collective effects mediated by the bath.

The system that we consider is shown on Fig. 5.1. Two biased tagged particles (TPs) are introduced in the SEP. Their jump rates to the left and right are respectively p_{-i} and p_{+i}, with $p_{+i}+p_{-i} = 1$. The biases are $s_i = 2p_{+i}-1$. We focus on the dense limit of the SEP already explored in the last two chapters and provide detailed computations leading to the full determination of the probability law of the displacements of the two TPs. The case of three or more TPs is tractable and very similar but the computations are heavier and rely a lot on a symbolic computation software.

We describe three main effects between the TPs; all of them are effects mediated by the bath (the other particles of the SEP). The first is bath-mediated binding: an arbitrary number of biased TPs move together at large time in the sense that the single-particle cumulants are equal to the ones of the center of mass, with the center of mass being described as a particle with an effective bias. Then, we study bath-mediated entrainment: when a single TP is biased we show that an unbiased TP follows it with a time-dependence that we describe. Finally, we study bath-mediated cooperativity and competition, that is to say the effects that two biased TPs in the SEP have over each other. In other words, what is the time-dependence of the cumulants before reaching the final state described by bath-mediated binding? Results for the motion of three TPs are presented at the end of this chapter (section 5.5).

The results of this chapter have been published in [P4].

5.2 Framework

We use the vacancy-based approach described in the previous two chapters. We see that the expression of the cumulant-generating function in terms of the properties of a single random walker is identical to the one found in the previous chapter. The difference is that, because of the biases, these properties have more complicated expressions. We state them and give the full result for the cumulant-generating function of two biased TPs.

5.2.1 Reminder of the previous chapter

In the previous chapter we studied N unbiased TPs in the dense SEP. In section 4.3, we showed that the cumulant-generating function of the TPs can be expressed in terms of the propagator of a single vacancy in the SEP [Eq. (4.30)]. The same reasoning holds for biased TPs and we write,

$$\psi^{(t)}(\mathbf{k}) \equiv \ln\left\langle e^{i(k_1 Y_1 + k_2 Y_2)}\right\rangle \tag{5.1}$$

$$\lim_{\rho_0 \to 0} \frac{\psi^{(t)}(\mathbf{k})}{\rho_0} = \sum_{Z \notin \{0,L\}} \left(\tilde{p}_Z^{(t)}(\mathbf{k}) - 1\right) \tag{5.2}$$

equation (Appendix B).

where $\tilde{p}_Z^{(t)}(\mathbf{k})$ is the Fourier transform of the probability of the displacements of the TPs if there is a single vacancy in the system, initially at Z. Moreover, following the computations of subsection 4.3.2, this probability can be expressed in terms of the first-passage propagators $f_{\nu,Z}$ associated with the motion towards an adjacent site and $f_{\mu,\nu}$ associated with the motion between two adjacent sites. We recall Eqs. (4.37)-(4.38),

$$\lim_{\rho_0\to 0}\frac{\psi^{(t)}(\mathbf{k})}{\rho_0}=\frac{1}{u}\sum_{\nu}\left\{(e^{i\mathbf{k}\cdot\mathbf{e}_\nu}-1)+e^{i\mathbf{k}\cdot\mathbf{e}_\nu}\sum_{\mu}(1-e^{-i\mathbf{k}\cdot\mathbf{e}_\mu})\left[\frac{T}{1-T}\right]^{(\zeta(\nu))}_{\mu,-\nu}(\mathbf{k},u)\right\}h_\nu(u), \tag{5.3}$$

$$h_\nu(u)=\sum_{Z\notin\{X_i^0\}}\hat{f}_{\nu,Z}(u), \tag{5.4}$$

with $T_{\mu,\nu}(\mathbf{k},u)=e^{i\mathbf{k}\cdot\mathbf{e}_\mu}\hat{f}_{\mu,-\nu}(u)$. The goal is now to compute the $\hat{f}_{\mu,-\nu}$ and h_ν in the case of biased TPs.

5.2.2 Computation of the first-passage probabilities

We restrict ourselves to the case of two TPs but the results easily extend to N TPs.

"Outside quantities"

When one starts from adjacent site -1, the only reachable adjacent site is -1 (the same holds for $+2$), $\hat{f}_{-1,-1}(u)$ and $\hat{f}_{2,2}(u)$ are identical to the case of a single biased TP given by Eq (3.26),

$$\hat{f}_{-1,-1}(u)=\alpha\frac{1-s_1}{1-s_1\alpha},\qquad\qquad \hat{f}_{2,2}(u)=\alpha\frac{1+s_2}{1+s_2\alpha}, \tag{5.5}$$

with $p_{\pm i}=(1\pm s_i)/2$. Similarly, the sums h_1 and h_{-1} are computed from Eq (3.26) by summing on Z from 1 to infinity,

$$h_{-1}(u)=\frac{\hat{f}_{-1,-1}(u)}{1-\alpha},\qquad\qquad h_2(u)=\frac{\hat{f}_{2,2}(u)}{1-\alpha}. \tag{5.6}$$

"Inside quantities"

We now compute the quantities related to sites $+1$ and -2. A TP starting from one of these sites may touch either of the two. We recall the expressions of $\hat{f}_{1,1}=f^{\mathrm{UB}}_{\mathrm{same}}$ and $\hat{f}_{1,-2}=f^{\mathrm{UB}}_{\mathrm{cross}}$ in the unbiased case [Eqs (4.42)-(4.43)],

$$\hat{f}^{\mathrm{UB}}_{\mathrm{same}}(u,L)=\frac{\alpha-\alpha^{2L-1}}{1-\alpha^{2L}},\qquad\qquad \hat{f}^{\mathrm{UB}}_{\mathrm{cross}}(u,L)=\frac{\alpha^{L-1}-\alpha^{L+1}}{1-\alpha^{2L}}. \tag{5.7}$$

As the TPs are biased, these expressions will be used for the sites next to the adjacent sites, that is to say for a distance $L-2$. Our computations are similar to the ones of Eq. (3.23) and the reader may re-read the arguments involved there. Starting from site $+1$, there are three solutions to touch TP 1: the walker immediately performs a jump to the left, or it first jumps to the right before coming back first to site 1 and finishing its motion on TP 1, or it first jumps to the right

before first touching site -2 and finishing its motion on TP 1. This leads us to the following decomposition for $f_{1,1}$,

$$\begin{aligned} f_{1,1}(t,L) = p_1 e^{-(p_1+1/2)t_0} &+ \int_0^t dt_0 \frac{1}{2} e^{-(p_1+1/2)t} \int_0^{t-t_0} dt_1 f^{\mathrm{UB}}_{\mathrm{same}}(t_1, L-2) f_{1,1}(t-t_0-t_1, L) \\ &+ \int_0^{t-t_0} dt_1 f^{\mathrm{UB}}_{\mathrm{cross}}(t_1, L-2) f_{-2,1}(t-t_0-t_1, L). \end{aligned} \tag{5.8}$$

In Laplace space, this gives

$$\hat{f}_{1,1}(u) = 2p_1U_1 + U_1 \hat{f}^{\mathrm{UB}}_{\mathrm{same}}(u, L-2)\hat{f}_{1,1}(u) + U_1 \hat{f}^{\mathrm{UB}}_{\mathrm{cross}}(u, L-2)\hat{f}_{1,-2}(u) \tag{5.9}$$

with $U_\nu = (2u + 2p_\nu + 1)^{-1}$. Similar arguments can be made for $\hat{f}_{1,-2}$, $\hat{f}_{-2,-2}$ and $\hat{f}_{-2,1}$, leading to the following system of 2×2 equations with 2×2 unknowns, where the unbiased quantities are taken for $L-2$.

$$\begin{cases} \left(U_1 \hat{f}^{\mathrm{UB}}_{\mathrm{same}} - 1\right)\hat{f}_{1,1} & + \left(U_1 \hat{f}^{\mathrm{UB}}_{\mathrm{cross}}\right)\hat{f}_{1,-2} & +2p_1U_1 & = 0 \\ \left(U_{-2} \hat{f}^{\mathrm{UB}}_{\mathrm{cross}}\right)\hat{f}_{1,1} & + \left(U_{-2} \hat{f}^{\mathrm{UB}}_{\mathrm{same}} - 1\right)\hat{f}_{1,-2} & & = 0 \\ \left(U_{-2} \hat{f}^{\mathrm{UB}}_{\mathrm{same}} - 1\right)\hat{f}_{-2,-2} & + \left(U_{-2} \hat{f}^{\mathrm{UB}}_{\mathrm{cross}}\right)\hat{f}_{-2,1} & +2p_{-2}U_{-2} & = 0 \\ \left(U_1 \hat{f}^{\mathrm{UB}}_{\mathrm{cross}}\right)\hat{f}_{-2,-2} & + \left(U_1 \hat{f}^{\mathrm{UB}}_{\mathrm{same}} - 1\right)\hat{f}_{-2,1} & & = 0 \end{cases} \tag{5.10}$$

The solution is

$$\begin{cases} \hat{f}_{1,1} &= \dfrac{2p_1U_1\left(1 - U_1 \hat{f}^{\mathrm{UB}}_{\mathrm{same}}\right)}{\left(1 - U_1 \hat{f}^{\mathrm{UB}}_{\mathrm{same}}\right)\left(1 - U_{-2} \hat{f}^{\mathrm{UB}}_{\mathrm{same}}\right) - U_1U_{-2}(\hat{f}^{\mathrm{UB}}_{\mathrm{cross}})^2} \\ \hat{f}_{1,-2} &= \dfrac{2p_1U_1U_{-2} \hat{f}^{\mathrm{UB}}_{\mathrm{cross}}}{\left(1 - U_1 \hat{f}^{\mathrm{UB}}_{\mathrm{same}}\right)\left(1 - U_{-2} \hat{f}^{\mathrm{UB}}_{\mathrm{same}}\right) - U_1U_{-2}(\hat{f}^{\mathrm{UB}}_{\mathrm{cross}})^2} \\ \hat{f}_{-2,-2} &= \dfrac{2p_{-2}U_{-2}\left(1 - U_{-2} \hat{f}^{\mathrm{UB}}_{\mathrm{same}}\right)}{\left(1 - U_1 \hat{f}^{\mathrm{UB}}_{\mathrm{same}}\right)\left(1 - U_{-2} \hat{f}^{\mathrm{UB}}_{\mathrm{same}}\right) - U_1U_{-2}(\hat{f}^{\mathrm{UB}}_{\mathrm{cross}})^2} \\ \hat{f}_{-2,1} &= \dfrac{2p_{-2}U_1U_{-2} \hat{f}^{\mathrm{UB}}_{\mathrm{cross}}}{\left(1 - U_1 \hat{f}^{\mathrm{UB}}_{\mathrm{same}}\right)\left(1 - U_{-2} \hat{f}^{\mathrm{UB}}_{\mathrm{same}}\right) - U_1U_{-2}(\hat{f}^{\mathrm{UB}}_{\mathrm{cross}})^2} \end{cases} . \tag{5.11}$$

Next, $\hat{f}_{1,Z}$ can be decomposed on the first adjacent site ($+1$ or -2) that is touched,

$$\hat{f}_{1,Z} = \hat{f}_{1,1}\hat{F}^{\dagger}_{L-1}(1|Z) + \hat{f}_{1,-2}\hat{F}^{\dagger}_{1}(L-1|Z) = \frac{\left(\alpha^{Z-1} - \alpha^{2L-Z-3}\right)\hat{f}_{1,1} + \left(\alpha^{L-Z-1} - \alpha^{L+Z-3}\right)\hat{f}_{1,-2}}{1-\alpha^{2(L-2)}} \tag{5.12}$$

, where $F^\dagger$ is given by Eq. (4.39). Finally, the sums h_1 and h_{-2} are expressed as

$$h_1(u) \equiv \sum_{Z=1}^{L-1} \hat{f}_{1,Z} = \frac{(1-\alpha^{L-2})(1-\alpha^{L-1})}{(1-\alpha)(1-\alpha^{2(L-2)})}\left(\hat{f}_{1,1} + \hat{f}_{1,-2}\right), \tag{5.13}$$

$$h_{-2}(u) \equiv \sum_{Z=1}^{L-1} \hat{f}_{-2,Z} = \frac{(1-\alpha^{L-2})(1-\alpha^{L-1})}{(1-\alpha)(1-\alpha^{2(L-2)})}\left(\hat{f}_{-2,-2} + \hat{f}_{-2,1}\right). \tag{5.14}$$

Equations (5.5), (5.6), (5.11), (5.13) and (5.14) provide all the quantities needed to compute the cumulant-generating function from Eq. (5.3).

5.3 Bath-mediated binding

Before examining in detail the case of $N = 2$ biased TPs, we put forward a striking result that holds for an arbitrary number of TPs[2]. We already saw in the previous chapter (subsection 4.2.2 and large time limit of Eq. (4.56)) that in the SEP with no biases, N TPs behave as a single one at large time. The same holds for N biased TPs in the dense SEP. We denote $Z = \sum_{j=1}^{N} Y_j/N$ the displacement of the center of mass. At large time, arbitrary N-tag cumulants are equal to the cumulants of Z,

$$\left\langle Y_1^{q_1} \dots Y_N^{q_N} \right\rangle_c \underset{t\to\infty}{\sim} \left\langle Z^{q_1+\dots+q_N} \right\rangle_c . \tag{5.15}$$

And the center of mass behaves as an effective particle with an effective bias S given by

$$S = \frac{\prod_{i=1}^{N}(1+s_i) - \prod_{i=1}^{N}(1-s_i)}{\prod_{i=1}^{N}(1+s_i) + \prod_{i=1}^{N}(1-s_i)}. \tag{5.16}$$

That is to say that the odd and even cumulants of Z at high density read

$$\lim_{\rho_0\to 0} \frac{\langle Z(t)^{2n}\rangle_c}{\rho_0} \underset{t\to\infty}{\sim} \lim_{\rho_0\to 0} \frac{\langle Z(t)^{2n+1}\rangle_c}{\rho_0 S} \underset{t\to\infty}{\sim} \sqrt{\frac{2t}{\pi}}. \tag{5.17}$$

(See (3.35) for the expression of the cumulants of a single biased particle.) The expression of the effective bias looks complicated at first sight. However it becomes much simpler if one associates a force f_j to each bias s_j using detailed balance[3],

$$e^{f_i} = \frac{1+s_i}{1-s_i} \qquad \Leftrightarrow \qquad s_i = \tanh\left(\frac{f_i}{2}\right). \tag{5.18}$$

In the same way, we define an effective force F from the effective bias S, which satisfies $S = \tanh(F/2)$. Eq. (5.16) is then rewritten as

$$F = \sum_{i=1}^{N} f_i. \tag{5.19}$$

The effective force on the center of mass is simply the sum of the forces on all the particles.

Eq. (5.15) holds for arbitrary cumulants, a special case is that the displacements of all the TPs are identical at large time,

$$\langle Y_1\rangle \underset{t\to\infty}{\sim} \dots \underset{t\to\infty}{\sim} \langle Y_N\rangle. \tag{5.20}$$

We will see in the next chapter that this result actually holds at an arbitrary density, assuming that the TPs do not separate from one another (at high density, particles never separate).

The bath mediating binding of arbitrary particles is a very important feature of the high-density SEP. At small times, the TPs are expected to move according to their own biases while at large time they move together with an effective bias. It is important to keep this fact in mind in the analysis of two biased TPs that comes now.

[2] We checked this result with Mathematica up to $N = 5$, we know that it holds in the unbiased system and we will see in the next chapter that it holds at arbitrary density for the first cumulant. We do not attempt to provide a clean proof but we are very confident that the result holds at arbitrary N.

[3] One considers a biased particle between two possible sites. The jump rates are $(1 \pm s_i)/2$. The difference in energy between the two states is defined as af_i/k_BT with a the lattice spacing and a Boltzmann weight is associated with this energy. Detailed balance, i.e. equality of the fluxes between the two sites, can then be written. Here we consider $a = 1$ and $k_BT = 1$.

5.4 Behavior of two biased tagged particles

5.4.1 Full result for two tagged particles

We now focus on the case of two TPs with biases s_1 and s_2, initially separated by a distance L (Fig. 5.1) and write the two-point cumulant-generating function. Although the result is a bit tedious to write, it is important to have the precise expressions for the analysis in the next subsections.

We use Eq. (5.3) along with the results of subsection 5.2.2 to obtain an expression for the cumulant-generating function via a symbolic computation software. From the previous chapter, we know that we should use a rescaled time $\tau = t/L^2$: the Laplace variable is written $u = \tilde{u}/L^2$ with u going to zero at constant $\tilde{u}$. The result reads

$$\lim_{\rho_0\to 0}\frac{\hat{\psi}(\mathbf{k}, u=\tilde{u}/L^2)}{\rho_0} = \frac{L^3}{\sqrt{2}\tilde{u}^{3/2}}\Big\{\hat{K}^{e,2}(\tilde{u})(\cos(k_1+k_2)-1)+\hat{K}^{o,2}(\tilde{u})\sin(k_1+k_2) + \sum_{i=1}^{2}\big[\hat{K}_i^{e,1}(\tilde{u})(\cos k_i - 1)+\hat{K}_i^{o,1}(\tilde{u})\sin k_i\big]\Big\}, \quad (5.21)$$

with functions $\hat{K}$ that we will give later. This is the analog of Eq. (4.51) for biased particles. The full structure in (k_1, k_2) is thus determined. One notes that $\hat{K}^{e,2}$ gives the even two-tag cumulants and $\hat{K}^{o,2}$ the odd two-tag cumulants. Similarly, $(\hat{K}_i^{e,1}+\hat{K}^{e,2})$ and $(\hat{K}_i^{o,1}+\hat{K}^{o,2})$ correspond respectively to the even and odd one-tag cumulants associated with TP i. The inverse Laplace transform gives the following structure in time,

$$\frac{1}{L}\lim_{\rho_0\to 0}\frac{\psi(\mathbf{k}, t=L^2\tau)}{\rho_0} = \sqrt{\frac{2\tau}{\pi}}\Big\{K^{e,2}(\tau)(\cos(k_1+k_2)-1)+K^{o,2}(\tau)\sin(k_1+k_2) + \sum_{i=1}^{2}\big[K_i^{e,1}(\tau)(\cos k_i - 1)+K_i^{o,1}(\tau)\sin k_i\big]\Big\}. \quad (5.22)$$

This is the analog of Eq. (4.54). Please note that $K(\tau)$ is related to but not equal to the inverse Laplace transform of $\hat{K}(\tilde{u})$. From the previous expression one can deduce all the cumulants ($i = 1, 2$), including those of the variation of distance $D = Y_2 - Y_1$.

$$\frac{\langle Y_1^j Y_2^{2n-j}\rangle_c}{\rho_0 L} = K^{e,2}(\tau)\sqrt{\frac{2\tau}{\pi}} \qquad \frac{\langle Y_1^j Y_2^{2n+1-j}\rangle_c}{\rho_0 L} = K^{o,2}(\tau)\sqrt{\frac{2\tau}{\pi}} \quad (5.23)$$

$$\frac{\langle Y_i^{2n}\rangle_c}{\rho_0 L} = [K^{e,2}(\tau)+K_i^{e,1}(\tau)]\sqrt{\frac{2\tau}{\pi}} \qquad \frac{\langle Y_i^{2n+1}\rangle_c}{\rho_0 L} = [K^{o,2}(\tau)+K_i^{o,1}(\tau)]\sqrt{\frac{2\tau}{\pi}} \quad (5.24)$$

$$\frac{\langle D^{2n}\rangle_c}{\rho_0 L} = [K_1^{e,1}(\tau)+K_2^{e,1}(\tau)]\sqrt{\frac{2\tau}{\pi}} \qquad \frac{\langle D^{2n+1}\rangle_c}{\rho_0 L} = [K_2^{o,1}(\tau)-K_1^{o,1}(\tau)]\sqrt{\frac{2\tau}{\pi}} \quad (5.25)$$

We notice that all the cumulants scale as the square root of (rescaled) time. To be fully explicit, we now give the expressions of the quantities $\hat{K}(\tilde{u})$ and $K(\tau)$ first in the case where a single particle is biased ($s_1 = 0, s_2 \neq 0$) and then in the general case of two biases ($s_1, s_2 \neq 0$). The Laplace space

quantities are first given.

	Case $s_1 = 0, s_2 \neq 0$	Case $s_1, s_2 \neq 0$
$\hat{K}^{e,2}(\tilde{u})$	v	$(1+s_1s_2)v/d_2$
$\hat{K}^{o,2}(\tilde{u})$	$s_2 v$	$(s_1+s_2)v/d_2$
$\hat{K}_1^{e,1}(\tilde{u})$	$(1-v)(1+s_2v)$	$(1-v)(1+s_2v)/d_2$
$\hat{K}_1^{o,1}(\tilde{u})$	0	$s_1(1-v)(1+s_2v)/d_2$
$\hat{K}_2^{e,1}(\tilde{u})$	$1-v$	$(1-v)(1-s_1v)/d_2$
$\hat{K}_2^{o,1}(\tilde{u})$	$s_2(1-v)$	$s_2(1-v)(1-s_1v)/d_2$,

with $v = e^{-\sqrt{2\tilde{u}}}$ and $d_2 = 1+s_1s_2v^2$. And then, the time-dependent quantities.

	Case $s_1 = 0, s_2 \neq 0$	Case $s_1, s_2 \neq 0$
$K^{e,2}(\tau)$	$g_1(\tau)$	$G_{0,s_1s_2,0}(\tau)$
$K^{o,2}(\tau)$	$s_2 g_1(\tau)$	$G_{0,s_1+s_2,0}(\tau)$
$K_1^{e,1}(\tau)$	$1+(s_2-1)g_1(\tau)-s_2g_2(\tau)$	$G_{1,s_2-1,-s_2}(\tau)$
$K_1^{o,1}(\tau)$	0	$G_{s_1,s_1(s_2-1),-s_1s_2}(\tau)$
$K_2^{e,1}(\tau)$	$1-g_1(\tau)$	$G_{1,-s_1-1,s_1}(\tau)$
$K_2^{o,1}(\tau)$	$s_2(1-g_1(\tau))$	$G_{s_2,-s_2(1+s_2),s_1s_2}(\tau)$

The function g is the one we already encountered in the absence of bias and the functions $G_{\alpha,\beta,\gamma}$ are infinite sums of g taken with different arguments.

$$g(u) = e^{-u^2} - \sqrt{\pi}u \operatorname{erfc} u \tag{5.26}$$

$$g_n(\tau) = g(n/\sqrt{2\tau}) \tag{5.27}$$

$$G_{\alpha,\beta,\gamma}(\tau) = \sum_{n=0}^{\infty} (-s_1s_2)^n \left[\alpha g_{2n}(\tau) + \beta g_{2n+1}(\tau) + \gamma g_{2n+2}(\tau)\right] \tag{5.28}$$

The time evolution of the cumulants is given by Eqs. (5.23), (5.24). We note that at small τ, $G_{\alpha,\beta,\gamma} = \alpha$ while at large τ, $G_{\alpha,\beta,\gamma} = (\alpha+\beta+\gamma)/(1+s_1s_2)$. For instance, the odd cumulants of TP 1, and in particular its displacement, are given by $(K_1^{o,1}+K^{o,2})$ which corresponds to $(\alpha,\beta,\gamma) = (s_1, s_1s_2+s_2, -s_1s_2)$. This implies the following behaviors at short and large times,

$$\lim_{\rho_0\to 0} \frac{\langle Y_1^{2p+1}\rangle}{\rho_0} \underset{t\ll L^2}{\sim} s_1\sqrt{\frac{2t}{\pi}}, \qquad \lim_{\rho_0\to 0} \frac{\langle Y_1^{2p+1}\rangle}{\rho_0} \underset{t\gg L^2}{\sim} \frac{s_1+s_2}{1+s_1s_2}\sqrt{\frac{2t}{\pi}}. \tag{5.29}$$

This is in full agreement with the bath-mediated binding that we described in the previous section.

We should say a few words about the probability law of the distance between the two TPs. At intermediate time, it is fully characterized by the cumulants given in Eq. (5.25). And at large time, one obtains a stationary distribution characterized by

$$\frac{\langle D^{2n}\rangle_c}{\rho_0 L} \underset{t\to\infty}{\sim} \frac{2+s_2-s_1}{1+s_1s_2}, \qquad \frac{\langle D^{2n+1}\rangle_c}{\rho_0 L} \underset{t\to\infty}{\sim} \frac{s_2-s_1-2s_1s_2}{1+s_1s_2}. \tag{5.30}$$

Having put forward the analytical results, we now investigate the two cases of one and two biased particles and describe the behavior of the system.

5.4.2 Bath-mediated entrainment

We first look at the case of a single biased TP ($s_2 \neq 0$) followed by an unbiased TP ($s_1 = 0$), initially at a distance L (see Figure 5.2, top). This corresponds to the perturbation induced by a biased tracer in a quiescent medium. The behavior of TP 2 is given by the single-TP results [Eq. (3.35)] and the one of TP 1 is computed from Eq. (5.24).

$$\lim_{\rho_0\to 0} \frac{\langle Y_2^{2p+1}(t)\rangle_c}{\rho_0} \underset{t\to\infty}{\sim} s_2 \sqrt{\frac{2t}{\pi}}, \qquad \lim_{\rho_0\to 0} \frac{\langle Y_2^{2p}(t)\rangle_c}{\rho_0} \underset{t\to\infty}{\sim} \sqrt{\frac{2t}{\pi}}, \tag{5.31}$$

$$\lim_{\rho_0\to 0} \frac{\langle Y_1^{2p+1}(t)\rangle_c}{\rho_0} \underset{t\to\infty}{\sim} s_2 \sqrt{\frac{2t}{\pi}} g\left(\frac{L}{\sqrt{2t}}\right), \tag{5.32}$$

$$\lim_{\rho_0\to 0} \frac{\langle Y_1^{2p}(t)\rangle_c}{\rho_0} \underset{t\to\infty}{\sim} \sqrt{\frac{2t}{\pi}} \left[1 + s_2 g\left(\frac{L}{\sqrt{2t}}\right) - s_2 g\left(\frac{2L}{\sqrt{2t}}\right)\right]. \tag{5.33}$$

The behavior of the unbiased TP (TP 1) is very interesting. We recover that the cumulants of TP 1 are identical to those of TP 2 at large time $t \gg L^2$, a fact that we already know from bath-mediated binding. But we also get the time evolution of these cumulants over the time scale L^2. The intermediate-time behavior of the average displacement, and other odd cumulants of TP 1, is given by the same function g involved in the correlation of two unbiased TPs, Eq. (4.56). A consequence of that is the existence of the generalized fluctuation-dissipation relation,

$$\lim_{f_2\to 0} \frac{2\langle Y_1(f_1 = 0, f_2)\rangle}{f_2} = \langle Y_1 Y_2\rangle_c (f_1 = f_2 = 0), \tag{5.34}$$

with $f_i = \tanh(s_i/2)$ the forces that we introduced before. The behavior of an unbiased TP following a TP with a small bias is related to the correlations of the TPs if none of them is biased. This relation has been shown to hold in the opposite limit of a dilute SEP ($\rho \to 0$) [35] with equilibrium initial conditions.

The variance of TP 1 and the other even cumulants are remarkable in that while they depend on the bias s_2 at intermediate time, this dependence disappears at large time. The first two cumulants of both TPs are compared to numerical simulations in Fig. 5.2a-b and a very good agreement is found.

We also look at the dynamics of the two-TP cumulants. The even ones $\kappa^e = \langle Y_1^p Y_2^q\rangle_c$ with $p+q$ even are all equal and so are the odd ones $\kappa^o = \langle Y_1^p Y_2^q\rangle_c$ with $p+q$ odd ($p, q \geq 1$). Their expressions are deduced from Eq. (5.23),

$$\lim_{\rho_0\to 0} \frac{\kappa^e(t)}{\rho_0} = \lim_{\rho_0\to 0} \frac{\kappa^o(t)}{\rho_0 s_2} = \sqrt{\frac{2t}{\pi}} g\left(\frac{L}{\sqrt{2t}}\right). \tag{5.35}$$

A comparison with numerical simulations is done in Fig. 5.2c. It is remarkable that the even cumulants are unchanged in the presence of a single bias (Eq. (4.56) is the expression without any bias). The expression of the odd cumulants is also simple and is identical to the one of the cumulants of TP1. We note that both the expression of the two-point correlation function (5.35) and of the average displacement of the unbiased TP (5.33) are very similar to those obtained in the random average process [32, 33], which points towards their universality.

A last observable is the law of the distance between the two TPs which is computed from Eq (5.25). The law at intermediate time, and the asymptotic distribution at large time, are shown on Fig. 5.2d to be in very good agreement with numerical simulations.

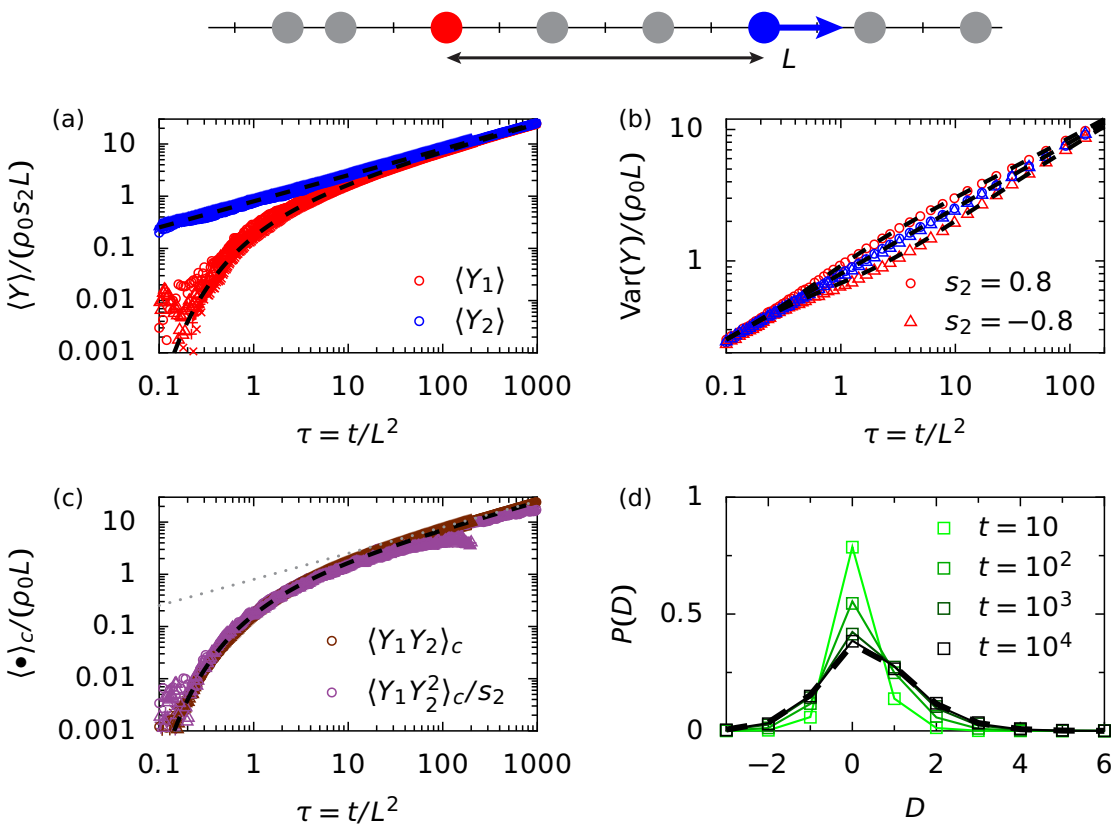

Figure 5.2: Bath-mediated entrainment. Only the right TP is biased. The fraction of vacancies is $\rho_0 = 0.01$. (a) Average displacements Y_1 (red) and Y_2 (blue) are a function of rescaled time. Different symbols correspond to $L = 10, 50$ and $s_2 = -0.2, 0.8$. The dashed black lines are the predictions from Eqs. (5.31) and (5.32). (b) Variances of the displacement of TP 1 (red) and TP 2 (blue) for $L = 10$, $s_2 = 0.8$ (circle) and $s_2 = -0.8$ (triangles). The dashed black lines are the predictions from Eqs. (5.31) and (5.33). (c) Rescaled cumulants $\langle Y_1 Y_2\rangle_c$ (brown) and $\langle Y_1 Y_2\rangle_c$ (purple) for the same parameters as (a). The dashed black line is the prediction from Eq. (5.35). (d) Probability law of the variation of distance $D = Y_2 - Y_1$ at times $10, 10^2, 10^3, 10^4$ (green to black) for $L = 10$, $s_2 = 0.8$ and $\rho_0 = 0.05$. The squares come from the simulations, the colored lines are predictions computed from Eq. (5.25) and the dashed black line is the asymptotic prediction at large time [Eq. (5.30)].

5.4.3 Bath-mediated cooperativity and competition

We now turn to the general case in which both TPs are biased (see Figure 5.3, top), with biases s_1 and s_2. We show that depending on the relative signs of the biases, the TPs may either "cooperate" or "compete". The dynamics of effective interactions between the TPs can be analyzed by introducing the rescaled instantaneous velocities

$$A_j(t) = \frac{\sqrt{2\pi t}}{\rho_0} \frac{d\langle Y_j \rangle}{dt}. \tag{5.36}$$

The interest of this quantity lies in the bath-mediated binding that we uncovered in Eq. (5.17). At short times, the TPs move according to their own biases while at large time they move together with an effective bias. This implies that the rescaled instantaneous velocities have the following limits,

$$A_j(t) \underset{t \ll L^2}{\sim} s_j \qquad\qquad A_j(t) \underset{t \gg L^2}{\sim} S = \frac{s_1 + s_2}{1 + s_1 s_2}. \tag{5.37}$$

Moreover, the full time dependence is obtained from Eqs. (5.24) and (5.28) and reads

$$A_1(t) = H_{s_1, s_2(1+s_1), -s_1 s_2}\left(\frac{L}{\sqrt{2t}}\right), \qquad A_2(t) = H_{s_2, s_1(1-s_2), s_1 s_2}\left(\frac{L}{\sqrt{2t}}\right) \tag{5.38}$$

with

$$H_{\alpha,\beta,\gamma}(u) = \sum_{n=0}^{\infty} (-s_1 s_2)^n \left\{ \alpha e^{-[2nu]^2} + \beta e^{-[(2n+1)u]^2} + \gamma e^{-[(2n+2)u]^2} \right\}. \tag{5.39}$$

The rescaled velocities computed in numerical simulations are plotted on Fig. 5.3 for two situations. In (a i), the two TPs have same-sign biases and they cooperate. At large time, they move together faster than any of the two would do if it were alone, in agreement with the bath-mediated effect we described before. Note that such an accelerated dynamics has been numerically observed in two-dimensional systems [71]. At intermediate times, we also unveil an overshoot of the rescaled velocity of the trailing TP. On Fig. 5.3 (a ii), we show the case of opposite biases in which the TPs compete, and the most biased one "wins" at large time. The dynamics is well described by our approach and we note that the velocity of the less biased TP changes sign at a given time t^* (gray square). We come back to this effect at the end of this subsection.

As always, it is crucial to characterize the two-TP cumulants, the even and odd ones $\kappa^e = \langle Y_1^p Y_2^q \rangle_c$ and $\kappa^o = \langle Y_1^p Y_2^q \rangle_c$ with $p+q$ respectively even and odd. The even ones are all equal and so are the odd ones. They are computed from Eq. (5.23) and we find

$$\lim_{\rho_0 \to 0} \frac{\kappa^e(t)}{\rho_0} = \lim_{\rho_0 \to 0} \frac{\kappa^o(t)}{\rho_0 S} = \sqrt{\frac{2t}{\pi}} g^\dagger\left(\frac{L}{\sqrt{2t}}\right), \tag{5.40}$$

$$g^\dagger(u) = (1 + s_1 s_2) \sum_{n=0}^{\infty} (-s_1 s_2)^n g([2n+1]u), \tag{5.41}$$

with g given by Eq. (5.26). While the structure is similar to the case of a single bias [Eq. (5.35)], we note that the scaling function has changed and now depends on the biases. Two-point cumulants, as well as variances, are plotted on Fig. 5.3 (b i) and (b ii).

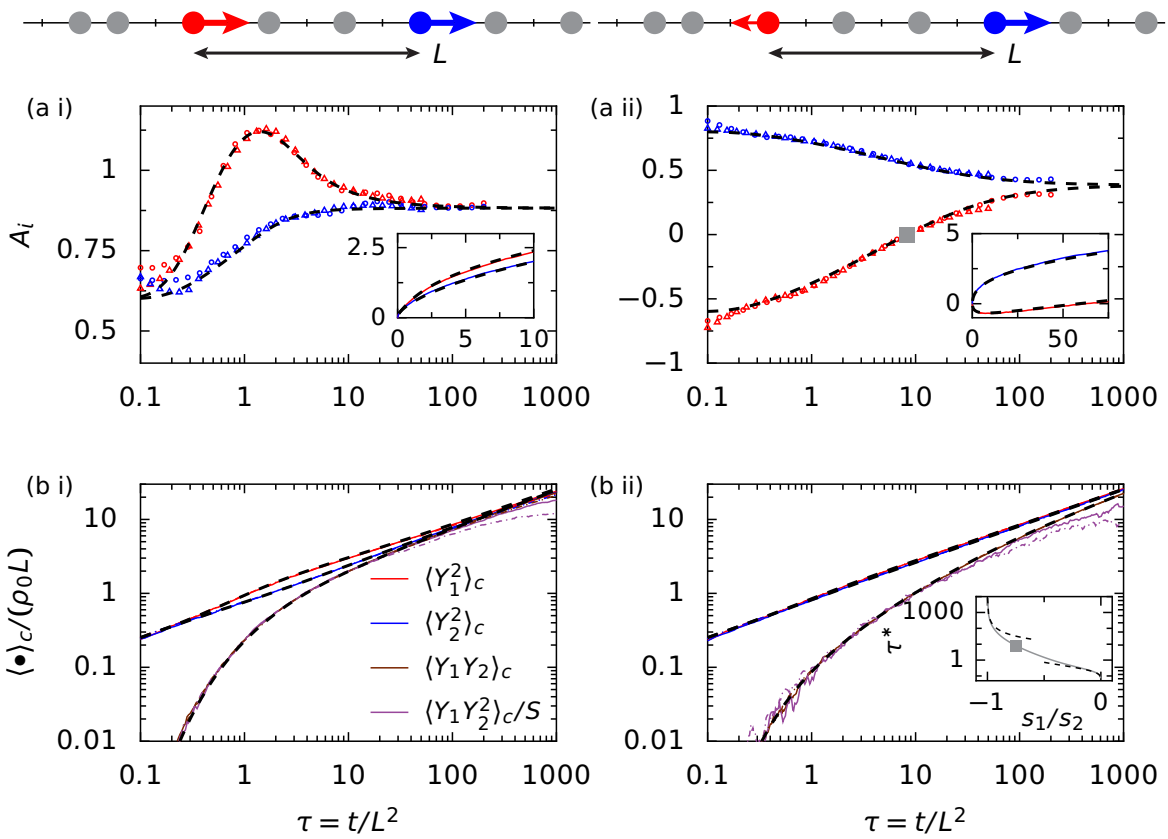

Figure 5.3: Cooperativity and competition ($\rho_0 = 0.01$). Left, (a i) and (b i), two TPs moving with identical biases $s_1 = s_2 = 0.8$. Right, (a ii) and (b ii), two TPs moving with biases in opposite directions $s_1 = -0.6$ and $s_2 = 0.8$. The rescaled velocities A_i [Eq. (5.36)] are plotted in (a i) and (a ii) for two distances $L = 50$ (circles) and 200 (triangles). The insets show the average displacements $\langle Y_i\rangle/(\rho_0 L)$ as a function of the rescaled time τ. At short time the rescaled velocities are s_1 and s_2 while at large time they have the common value $S = (s_1+s_2)/(1+s_1 s_2)$. The dashed black lines are the predictions from Eq. (5.38). The variances $\langle Y_i^2\rangle_c$ and the cumulants $\langle Y_1 Y_2\rangle_c$ and $\langle Y_1 Y_2^2\rangle_c$ are plotted in (b i) and (b ii) with the dashed black lines being the predictions from Eqs. (5.24) and (5.40). In the right figures, (a ii) and (b ii), the velocity changes sign at a rescaled time τ^* corresponding to the gray square in (a ii) and in the inset of (b ii). The inset of (b ii) is the prediction for the U-turn time τ^* as a function of s_1/s_2 for $s_2 = 0.8$ with dashed black lines showing the asymptotic behaviors.

U-turn time

We consider two TPs with biases $s_2 > 0$ and $-s_2 < s_1 < 0$ (Fig. 5.3, right) and characterize the U-turn time t^* of TP 1, that is to say the time at which its velocity changes sign. The rescaled U-turn time $\tau^* = t/L^2$ is the point at which $A_1(\tau)$ given by Eq. (5.38) vanishes, that is to say the solution of

$$H_{s_1,s_2(1+s_1),-s_1s_2}(1/\sqrt{2\tau^*}) = 0, \tag{5.42}$$

with H given in Eq. (5.39). This equation should be solved numerically in the general case but we can give explicitely the limit $s_1/s_2 \to 0$ and $s_1/s_2 \to -1$.

When s_1/s_2 is small, τ^* is small so $(\tau^*)^{-1/2}$ is large. We can keep only the first two terms in the sum:

$$A_1(\tau^*) \approx s_1 + s_2(1+s_1)e^{-\frac{1}{2\tau^*}} \approx s_1 + s_2 e^{-\frac{1}{2\tau^*}} = 0 \tag{5.43}$$

$$\tau^* \underset{s_1/s_2\to 0}{\sim} \left[2\ln\left(\frac{s_2}{-s_1}\right)\right]^{-1}. \tag{5.44}$$

And when s_1/s_2 approaches -1, we write $s_1 = -s_2(1-\epsilon)$ with $\epsilon \ll 1$ and look for τ^* satisfying $(2\tau^*)^{-1} = \eta\epsilon$ with η depending only on s_2. The expansion of $A_1(\tau^*)$ at order ϵ gives

$$A_1(\tau^*) \approx \epsilon\left\{\frac{s_2}{1-s_2^2} - \eta\frac{s_2(1+s_2)}{(1-s_2)^2}\right\} = 0. \tag{5.45}$$

This eventually leads to

$$\tau^* \underset{s_1/s_2\to -1}{\sim} \left[\frac{(1+s_2)^2}{2(1-s_2)}\right]\frac{1}{1+\frac{s_1}{s_2}}. \tag{5.46}$$

The numerical resolution of the implicit equation (5.42) for the U-turn time, as well as the asymptots (5.44) and (5.46) are shown in the inset of Fig. 5.3 (b ii).

5.5 Extension to three tagged particles

To conclude this chapter, we study the case of three TPs with biases s_1, s_2, s_3. We denote $L_1 = X_2^0 - X_1^0$ and $L_2 = X_3^0 - X_2^0$ and $L = L_1 + L_2$ the initial distance between the TPs. The method is very similar to the case of two TPs. Most computations are done with the help of Mathematica.

The explicit result for the Laplace transform of the cumulant-generating function, in terms of the rescaled variable $\tilde{u} = uL^2$ is

$$\begin{aligned}\lim_{\rho_0\to 0}\frac{\hat{\psi}(\mathbf{k}, u=\tilde{u}/L^2)}{\rho_0} = \frac{L^3}{\sqrt{2}\tilde{u}^{3/2}}\Big\{&\hat{K}^{e,3}(\tilde{u})(\cos(k_1+k_2+k_3)-1) + \hat{K}^{o,3}(\tilde{u})\sin(k_1+k_2+k_3)\\ &+\sum_{i=1}^{2}\left[\hat{K}^{e,2}_{i,i+1}(\tilde{u})(\cos(k_i+k_{i+1})-1) + \hat{K}^{o,1}_{i,i+1}(\tilde{u})\sin(k_i+k_{i+1})\right]\\ &+\sum_{i=1}^{3}\left[\hat{K}^{e,1}_{i}(\tilde{u})(\cos k_i - 1) + \hat{K}^{o,1}_{i}(\tilde{u})\sin k_i\right]\Big\}.\end{aligned} \tag{5.47}$$

One notes that the structure is very similar to the one without biases [Eq (4.51)], with the addition of sine terms that correspond to the odd cumulants. The quantities $\hat{K}^{\alpha,n}$, that are related to the

cumulants, read

$$\hat{K}^{\alpha,n}(\tilde{u}) = \frac{\sum_{a,b=0}^{2} Q^{\alpha,n}(a,b) v_1^a v_2^b}{1 + s_1 s_2 v_1^2 + s_2 s_3 v_2^2 + s_1 s_3 v_1^2 v_2^2} \tag{5.48}$$

with $v_1 = e^{-(L_1/L)\sqrt{2\tilde{u}}}, v_2 = e^{-(L_2/L)\sqrt{2\tilde{u}}}$. For completeness, we give the twelve 3×3 matrices Q of coefficients.

$$Q^{e,3} = (1 + s_1 s_2 + s_2 s_3 + s_1 s_3) \begin{pmatrix} 0 & 0 & 0 \\ 0 & 1 & 0 \\ 0 & 0 & 0 \end{pmatrix} \qquad Q^{o,3} = \frac{s_1 + s_2 + s_3 + s_1 s_2 s_3}{1 + s_1 s_2 + s_2 s_3 + s_1 s_3} Q^{e,3} \tag{5.49}$$

$$Q^{e,2}_{1,2} = (1 + s_1 s_2) \begin{pmatrix} 0 & 0 & 0 \\ 1 & s_3 - 1 & -s_3 \\ 0 & 0 & 0 \end{pmatrix} \qquad Q^{o,2}_{1,2} = \frac{s_1 + s_2}{1 + s_1 s_2} Q^{2,e}_{1,2} \tag{5.50}$$

$$Q^{e,2}_{2,3} = (1 + s_2 s_3) \begin{pmatrix} 0 & 1 & 0 \\ 0 & -1 - s_1 & 0 \\ 0 & s_1 & 0 \end{pmatrix} \qquad Q^{o,2}_{2,3} = \frac{s_2 + s_3}{1 + s_2 s_3} Q^{2,e}_{2,3} \tag{5.51}$$

$$Q^{e,1}_1 = \begin{pmatrix} 1 & 0 & s_2 s_3 \\ s_2 - 1 & 0 & s_3(1 - s_2) \\ -s_2 & 0 & -s_3 \end{pmatrix} \qquad Q^{o,1}_1 = s_1 Q^{1,e}_1 \tag{5.52}$$

$$Q^{e,1}_2 = \begin{pmatrix} 1 & s_3 - 1 & -s_3 \\ -1 - s_1 & 1 + s_1 - s_3 - s_1 s_3 & s_3(1 + s_1) \\ s_1 & s_1(s_3 - 1) & -s_1 s_3 \end{pmatrix} \qquad Q^{o,1}_2 = s_2 Q^{1,e}_2 \tag{5.53}$$

$$Q^{e,1}_3 = \begin{pmatrix} 1 & -1 - s_2 & s_2 \\ 0 & 0 & 0 \\ s_1 s_2 & -s1(1 + s_2) & s_1 \end{pmatrix} \qquad Q^{o,1}_3 = s_3 Q^{1,e}_3 \tag{5.54}$$

One remarks that $Q^o = S Q^e$ with S the effective bias for the TPs that are involved [Eq. (5.16)]. The Laplace transform (5.47) can be inverted numerically to obtain the time evolution of the cumulants. We show on Fig. 5.4 that the dynamics on three TPs with different biases that we observe in numerical simulations is highly non-trivial and is very well described by our approach.

One notices that the sum of all the coefficients of the matrices Q^1 and Q^2 is zero. This means that for $\tilde{u} \to 0$, (5.47) simplifies into

$$\lim_{\rho_0 \to 0} \frac{\hat{\psi}(\mathbf{k}, u)}{\rho_0} \underset{u \to 0}{\sim} \frac{1}{\sqrt{2} u^3} \left\{ \cos(k_1 + k_2 + k_3) - 1 + \frac{s_1 + s_2 + s_3 + s_1 s_2 s_3}{1 + s_1 s_2 + s_1 s_3 + s_2 s_3} \sin(k_1 + k_2 + k_3) \right\}. \tag{5.55}$$

The interpretation is that at large time, the three TPs move together as a single effective TP with effective bias $S = \frac{s_1 + s_2 + s_3 + s_1 s_2 s_3}{1 + s_1 s_2 + s_1 s_3 + s_2 s_3}$. This is exactly the bath-mediated binding effect that we described in section 5.3.

We do not attempt to write the full result for N TPs with arbitrary biases $(s_1, \ldots, s_N)$. But the structure in $\mathbf{k}$ is quite clear: the generalization of Eq. (5.47) (which is by the way the generalization of Eq.(4.51)) reads

$$\lim_{\rho_0 \to 0} \frac{\hat{\psi}(\mathbf{k}, \tilde{u})}{\rho_0} = \frac{L^3}{\sqrt{2} \tilde{u}^{3/2}} \sum_{n=0}^{N-1} \sum_{i=1}^{N-n} \left[\hat{K}^e_{i,n}(\tilde{u}) (\cos(k_i + \cdots + k_{i+n}) - 1) + \hat{K}^o_{i,n}(\tilde{u}) \sin(k_i + \cdots + k_{i+n}) \right] \tag{5.56}$$

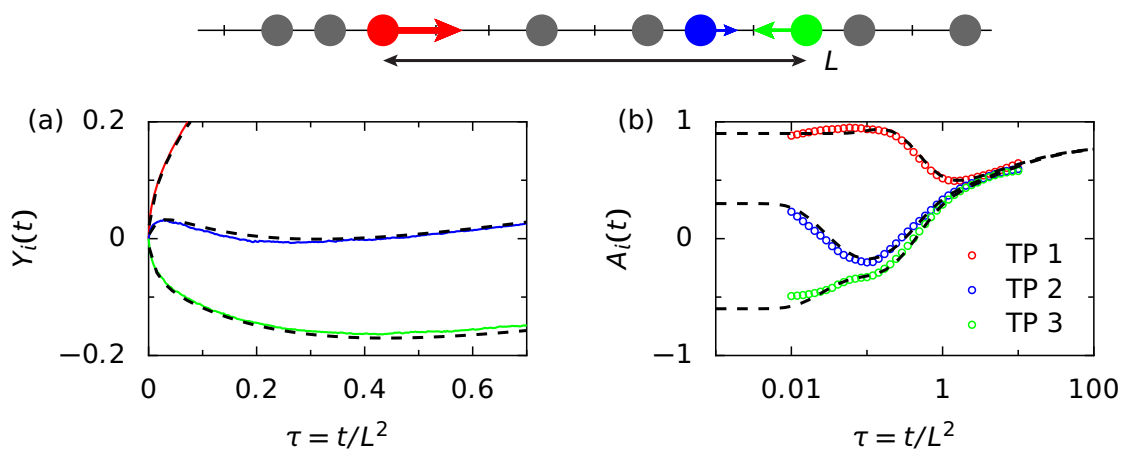

Figure 5.4: Displacements of three TPs with biases $s_1 = 0.9, s_2 = 0.3$ and $s_3 = -0.6$ with initial total distance $L = X_3^0 - X_1^0 = 60$ and $X_2^0 - X_1^0 = 45$. The fraction of vacancies is $\rho_0 = 0.01$. The colored lines and circles correspond to numerical simulations while the dashed black lines are the theoretical predictions coming from the inversion of Eq. (5.47). (a) Displacements of the TPs with respect to rescaled time. (b) Rescaled velocities [Eq. (5.36)] of the TPs. The dynamics of the TPs is highly non-trivial and is well captured by our approach. For instance, the second TP first moves to right according to its own bias, then it moves to the left because of TP 3, and finally it moves to the right at large time when all TPs move together.

The expressions of $\hat{K}_{i,n}^{\alpha}$ are generalizations of Eq. (5.48). The result when $u \ll L^{-2}$, which corresponds to very large times (larger than the square of all the distances involved), is

$$\lim_{\rho_0 \to 0} \frac{\hat{\psi}(\mathbf{k}, u)}{\rho_0} \underset{u \to 0}{\sim} \frac{1}{\sqrt{2} u^3} \left\{ \cos\left(\sum_{i=1}^{N} k_i \right) - 1 + S \sin\left(\sum_{i=1}^{N} k_i \right) \right\}. \tag{5.57}$$

As we explained in section 5.3, this means that all the TPs behave as a single one at large time. The effective bias S is given by Eq. (5.16).

5.6 Conclusion

We studied the case of biased tagged particles in the dense SEP. Our main result is that all the TPs move as a single one at large time [Eq. (5.15)], we call this effect bath-mediated binding. The effective TP undergoes an effective force which is the sum of the forces on all the TPs. We unveil the intermediate time behavior of two biased TPs. First, in the case of a single bias, the unbiased particle follows the biased one. The time dependence that we describe leads to a generalized fluctuation-dissipation relation. Then, in the case of two biases, we uncover a cooperativity effect if the biases have the same sign, and a competition effect when they have opposite signs. The dynamics is non-trivial and well described by our approach. Finally, we showed that results can also be obtained for three particles with arbitrary biases.

The bath mediated effect that we described is striking but we now show that it is a feature of the high density limit. At intermediate density, we shall develop an hydrodynamic approach and uncover an unbinding transition. Below a certain force the TPs remain bound but at high force they move apart from one another.

Chapter 6

Unbinding transition in single-file systems

Contents

6.1 Introduction

In the previous chapter, we studied biased intruders in the high density SEP. We derived the full probability law of two biased tagged particles. Among other effects, we uncovered bath-mediated binding, that is to say that biased TPs move together at large time. All single-tag cumulants are

equal as stated in Eq. (5.17). A natural question is: what happens at arbitrary density? Do biased TPs still move together at large time, even if the system is not dense? Or can they separate in a certain regime? Our approach to answer these questions will be completely different from the one we used at high density.

While computing full N-tag probability laws at arbitrary density seems out of reach, we can still focus on the displacements of the particles (first cumulants). The known solution for the displacement of a single TP in the SEP [42, 43] involves hydrodynamic equations for the density field of the system. We first rephrase these equations in a language that should be familiar to physicists: advection-diffusion equation, no-flux boundary conditions and force balance. We check that the equations return the displacement of a single biased TP.

Next, we show that our hydrodynamic approach extends to the case of two biased TPs, first in the case of opposite biases, then for arbitrary biases. The crucial result is that, depending on the magnitude of the drive the two TPs may either remain at finite distance at large time, or separate from one another with time dependence $t^{1/2}$. This is a sharp transition that we call the unbinding transition. We characterize the critical forcing and show that the transition is associated with the divergence of a quantity (final distance between TPs) when approached from below, and to another quantity (distance over square-root of time) that becomes non-zero only above the transition with a critical exponent that we give. The critical regime is shown to be associated with a distance between particles scaling with time as $t^{1/4}$. We also compute the phase diagram associated with the forces on the TPs. Furthermore, the description extends to an arbitrary number of biased TPs and we show that the TPs either remain all bound or separate into two groups.

Last but not least, the unbinding transition is not specific to the symmetric exclusion process: it is observable in arbitrary single-file systems with a critical force related to the equilibrium pressure of the system. We focus numerically on two models that have been shown to be relevant in experiments with colloidal systems: the gas of hard rods [9] and the gas of pointlike particles with dipole-dipole interactions [10]. The transition does occur at the predicted point. The unbinding transition is thus robust and should be observable in experiments.

The results of this chapter have been published in [P2].

6.2 Hydrodynamic equations

We consider the same system as in the previous chapter: an arbitrary number of biased TPs in the SEP, but this time at arbitrary density. We introduce the characteristic time τ of the particles (previously we considered $\tau = 1$). The particles of the bath have jump rates $1/(2\tau)$ to the left and to the right, and the i-th tagged particle has rates p_{+i}/τ for a jump to the right and p_{-i}/τ for a jump to the left (Fig. 6.1a). The novelty is that we adopt a continuous description. The particles of the bath are described by a density field $\rho(x,t)$ where x is the position in space and t is the time (Fig. 6.1b). The average density is now denoted ρ_∞. We consider only the average positions of the TPs (over both the initial conditions for the bath and the evolution of the system) that we denote $\bar{X}_i(t) \equiv \langle X_i(t) \rangle$. Higher-order cumulants are the subject of the next chapter.

We will describe the system by three hydrodynamic equations: a diffusion equation for the density field; no flux boundary conditions at the positions of the TPs; and an equation linking the displacement of a TP to the density field. Our approach is similar to the ones adopted in Refs. [42, 43]. Note that in the next chapter, we will extend this approach to so-called generalized profiles.

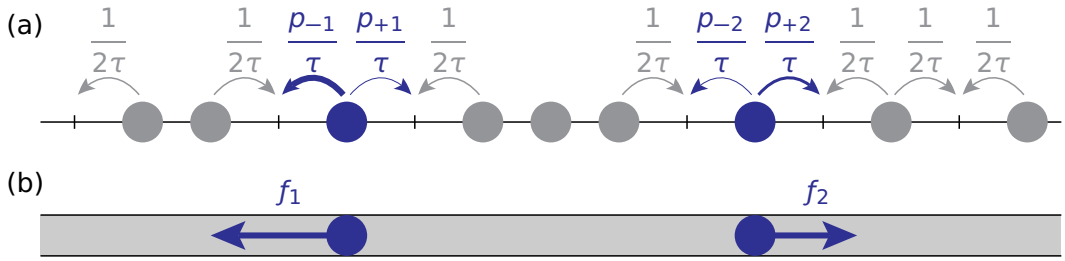

Figure 6.1: (a) Symmetric exclusion process with two biased TPs. The time constant for jumps is denoted τ and the lattice step is a. (b) Description in terms of a continuous medium (gray) characterized by a density $\rho(x,t)$. The forces on the TPs are given by detailed balance: $e^{af_i/(k_BT)} = p_{+i}/p_{-i}$.

6.2.1 Density field

In the SEP, the dynamics of the bath is known to be diffusive. The diffusion coefficient is $D = a^2/2\tau$ where a is the step of the lattice and τ the typical time for jumps. The density field satisfies

$$\frac{\partial \rho}{\partial t}(x,t) = D\frac{\partial^2 \rho}{\partial x^2}(x,t). \tag{6.1}$$

It is instructive to write the density field in the referential frame of the TP i. We write,

$$\rho_i^*(x,t) = \rho(\bar{X}_i(t) + x, t) \tag{6.2}$$

where $\bar{X}_i(t)$ is the (average) position of TP i. The change of variables leads to

$$\frac{\partial \rho_i^*}{\partial t}(x,t) = D\frac{\partial^2 \rho_i^*}{\partial x^2}(x,t) + V_i\frac{\partial \rho_i^*}{\partial x}(x,t) = -\frac{\partial J_i^*}{\partial x}(x,t), \tag{6.3}$$

$$J_i^*(x,t) = -D\frac{\partial \rho_i^*}{\partial x}(x,t) - V_i\rho_i^*(x,t), \tag{6.4}$$

where $V_i = \frac{d\bar{X}_i}{dt}$ is the (average) velocity of TP i. J_i^* is the current in the referential frame of the TP.

6.2.2 Boundary condition on a tagged particle

The TPs act on the density field as walls. In the reference frame of a TP, the flux vanishes at the position of the TP. This means that,

$$J_i^*(0^\pm) = 0, \tag{6.5}$$

$$D\frac{\partial \rho_i^*}{\partial x}(0^\pm, t) = -V\rho^*(0^\pm). \tag{6.6}$$

The cases $x = 0^+$ and $x = 0^-$ need to be considered independently as the density may be discontinuous at the position of a TP.

6.2.3 Displacement of a tagged particle

Our last equation is about the velocity V_i of a TP. The jumps of TP i to the right happen with rate p_{+i} and are performed only if the site directly to the right is empty. This happens with probability $(1-\rho(\bar{X}_i^+,t))$. And *mutatis mutandis* for jumps to the left. Consequently, the velocity of TP i can be expressed as

$$V_i \equiv \frac{d\bar{X}_i(t)}{dt} = p_{+i}\left[1-\rho(\bar{X}_i^+,t)\right] - p_{-i}\left[1-\rho(\bar{X}_i^-,t)\right]. \tag{6.7}$$

6.2.4 Displacement at large time and pressure of the SEP

At large time, as seen in the previous chapter, the displacements will be sub-ballistic: $\bar{X}_i(t) \propto \sqrt{t}$. This means that the velocities V_i vanish at large time. Thus, Eq. (6.7) becomes

$$\frac{1-\rho(\bar{X}_i^+,t)}{1-\rho(\bar{X}_i^-,t)} = \frac{p_{-i}}{p_{+i}}. \tag{6.8}$$

Considering jumps between two neighboring sites, we can associate energies with the two positions. Using detailed balance, we are able to define a force f_i from the jump rate. f_i satisfies

$$\frac{p_{+i}}{p_{-i}} = \exp\left(\frac{af_i}{k_BT}\right), \tag{6.9}$$

where a is the step of the lattice and T the temperature.

A simple computation in the microcanonical ensemble[1] shows that the equilibrium pressure of the SEP is given by

$$P(\rho) = -\frac{k_BT}{a}\log(1-\rho). \tag{6.10}$$

This leads us to rewrite Eq. (6.8) as

$$P(\rho(\bar{X}_i^+)) - P(\rho(\bar{X}_i^-)) = f_i. \tag{6.11}$$

This is a force balance: the difference between the pressure applied on the right and the one applied on the left is equal to the force on the particle. This mechanical equilibrium holds only because the velocity of a TP vanishes at large time.

6.3 Single driven particle

Let us now study the case of a single particle. We will recover the results of Refs. [42, 43] for the displacement of a biased particle in the SEP at arbitrary density.

6.3.1 Self-similar equations

We make the assumption that the density field in the referential frame of the TP has a diffusive self-similar scaling and write,

$$\rho_1^*(x,t) = \phi\left(\frac{x}{\sqrt{4Dt}}\right). \tag{6.12}$$

[1] For a finite SEP of length L and step a with N particles, the number of available states is $\Omega(N,L) = \binom{L/a}{N}$, the entropy is $S(N,L) = k_B \ln\Omega(N,L)$ and finally the pressure is $P = T\left.\frac{\partial S}{\partial L}\right|_N$. The density is $\rho = aN/L$.

Looking at the diffusion equation (6.3), we find that the proper scaling for the velocity $V_1(t)$ is $t^{-1/2}$. We write,

$$V_1(t) = A\sqrt{\frac{D}{t}} \tag{6.13}$$

with A a constant which depends only on the average density ρ_∞. The bulk equation (6.3) and the boundary equation (6.6) become

$$\phi''(u) + 2(u+A)\phi'(u) = 0, \tag{6.14}$$

$$\phi'(0^\pm) = -2A\phi(0^\pm). \tag{6.15}$$

6.3.2 Resolution

The integration of the bulk equation (6.14) gives

$$\phi'(u) = \phi'(0)e^{A^2}e^{-(u+A)^2}. \tag{6.16}$$

We integrate a second time, separating $u > 0$ and $u < 0$. We use the fact that the density goes to ρ_∞ at large distance and we remember the boundary equation (6.15).

$$\phi(u \gtrless 0) = \rho_\infty \mp \phi'(0^\pm)\frac{\sqrt{\pi}}{2}e^{A^2}\operatorname{erfc}(\pm(u+A)) \tag{6.17}$$

$$= \rho_\infty \pm A\phi(0^\pm)\sqrt{\pi}e^{A^2}\operatorname{erfc}(\pm(u+A)) \tag{6.18}$$

This solution for $u = 0^\pm$ can be written as

$$\phi(0^\pm) = \rho_\infty g(\pm A) \tag{6.19}$$

$$g(A) = \frac{1}{1-\sqrt{\pi}Ae^{A^2}\operatorname{erfc}A}, \tag{6.20}$$

finally giving the solution for the scaled density profile $\phi(u)$ in terms of A,

$$\phi(u \gtrless 0) = \rho_\infty + \rho_\infty \frac{\sqrt{\pi}Ae^{A^2}\operatorname{erfc}(\pm(u+A))}{1 \mp \sqrt{\pi}Ae^{A^2}\operatorname{erfc}(\pm A)}. \tag{6.21}$$

We recall that the density in front of and behind the TPs satisfies Eq. (6.8) at large time. We thus obtain the following implicit equation for A,

$$\frac{1-\rho_\infty g(A)}{1-\rho_\infty g(-A)} = \exp\left(-\frac{af}{k_BT}\right). \tag{6.22}$$

The large time behavior of the position of the TP is $\bar{X}_1(t) = 2A\sqrt{Dt}$. This solution is the one found in Refs. [42, 43]. We note that there is no explicit formula.

6.3.3 Results at small force or high density

At small force, or at high density, the displacement is very small (i.e. $A \ll 1$). The function g can be expanded as $g(A) \approx 1 + \sqrt{\pi}A$. Taking the logarithm of Eq. (6.22), one obtains

$$-2\sqrt{\pi}\frac{\rho_\infty}{1-\rho_\infty}A = -\frac{af}{k_BT}. \tag{6.23}$$

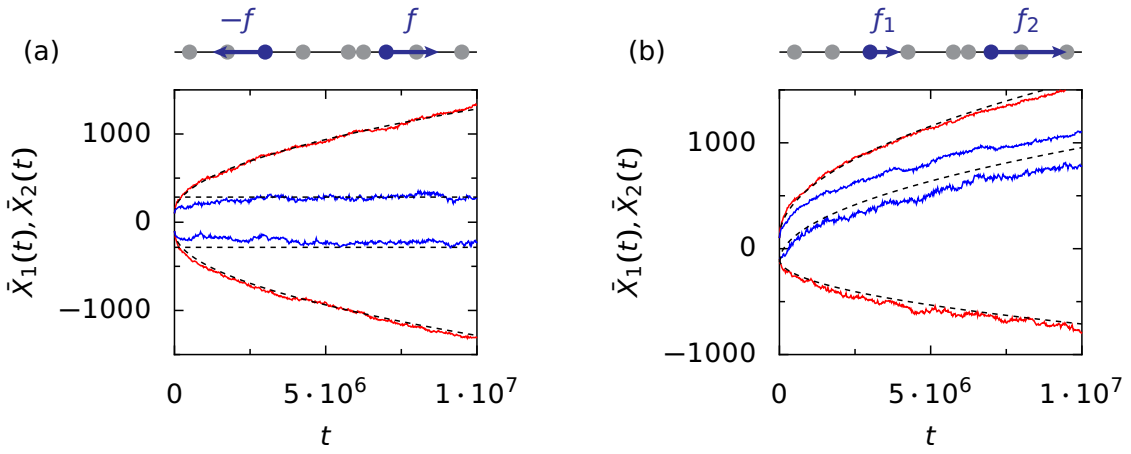

Figure 6.2: Numerical results for the positions $X_1(t)$ and $X_2(t)$ of two biased TPs in the SEP at density $\rho_\infty = 0.5$. The blue curves correspond to forces for which the TPs remain bound while the red curves correspond to an unbound situation. The dashed black lines are the theoretical predictions from Eqs. (6.28), (6.32), (6.46), (6.51). (a) Opposite forces $f_2 = -f_1 = f$. Blue: $f = 0.5$. Red: $f = 1.5$. (b) Arbitrary forces f_1 and f_2. Blue: $f_1 = 0, f_2 = 1$ (prediction only on the asymptotic scaling). Red: $f_1 = -1, f_2 = 2$.

And finally, we obtain an explicit expression in the limit considered:

$$\bar{X}_1(t) \underset{t\to\infty}{\sim} \frac{1-\rho_\infty}{\rho_\infty} \frac{af}{k_B T} \sqrt{\frac{Dt}{\pi}}. \tag{6.24}$$

In particular, this is consistent with the high-density result found in Ref. [38].

The case of a single driven TP contains all the ingredients that we will use to study the case of multiple driven TPs: in particular the equation of state (6.10) that leads to the force balance (6.11), and the expression of the density in front of and behind a TP moving as $\sqrt{t}$ [Eq. (6.19)].

6.4 Two particles driven by opposite forces

6.4.1 Qualitative behaviors

In this section, we study the central case of this chapter on the unbinding transition. We look at two TPs biased in opposite directions by equal magnitude forces: $f_2 = -f_1 = f > 0$. Initially, the TPs are separated by a distance L. On Fig. 6.2a, we show numerically that for a small force f, the two TPs remain at a finite distance at large time while for a large force f they eventually separate and move apart from one another.

We now investigate this unbinding transition. We characterize the bound regime (f small), the unbound regime (f large), give the expression of the critical force f_c and characterize the critical regime ($f = f_c$). We will see that the bound regime corresponds to a force balance [Eq. (6.11)] that can be satisfied without net motions of the TPs and with homogeneous density profiles. On the other hand, the unbound regime corresponds to TPs moving as $\sqrt{t}$ and creating non-stationary density profiles in front of them.

6.4.2 Bound regime and critical force

We first investigate the case where the TPs remain at a constant distance at large time. The number of particles between the two TPs is fixed, at large time the density between the two TPs becomes uniform and we call it ρ_{in}. The density outside the TPs is ρ_∞, it is also uniform. We saw previously that the velocity equation becomes the force balance (6.11) at large time. We write it for the TP on the right (by symmetry, the same is given by the other TP) and obtain

$$P(\rho_\infty) - P(\rho_{\text{in}}) = f. \tag{6.25}$$

One notes that as $P(\rho_{\text{in}}) > 0$, this force balance can only hold for $f < P(\rho_\infty)$. This immediately gives the critical force

$$f_c = P(\rho_\infty) = -\frac{k_B T}{a} \log(1-\rho_\infty). \tag{6.26}$$

The critical force is the pressure of the bath at density ρ_∞. The interpretation is that for forces below this pressure, the bath can "retain" the TPs while above this pressure it cannot. An important remark is that in the high density regime $\rho_\infty \to 1$ studied in the previous chapter, the critical force diverges. As we saw, there is no transition in this regime and the TPs always remain bound. This is interpreted by the fact that the bath can always exert a high enough pressure for the TPs to stay together. For a density $\rho_\infty < 1$, Eq. (6.26) gives the maximum force under which the TPs remain bound.

In the bound regime, for the SEP, the force balance (6.25) gives the expression of ρ_{in},

$$\rho_{\text{in}} = 1 - \exp\left(-\frac{a[P(\rho_\infty) - f]}{k_B T}\right). \tag{6.27}$$

And the final distance between the TPs is expressed by using the conservation of the number of particles,

$$\frac{\bar{X}_2^\infty - \bar{X}_1^\infty}{L} = \frac{\rho_\infty}{\rho_{\text{in}}} = \frac{\rho_\infty}{1 - \exp\left(-\frac{a[P(\rho_\infty)-f]}{k_B T}\right)}, \tag{6.28}$$

with L the initial distance between the TPs. This expression is used for the prediction of Fig. 6.3a at $f = 0.5$ and for the theoretical expression of Fig. 6.3b for $f < P(\rho_\infty)$.

When f becomes close to $P(\rho_\infty)$, ρ_{in} is small so $P(\rho_{\text{in}}) \simeq P'(0)\rho_{\text{in}}$ and the final distance becomes,

$$\frac{\bar{X}_2^\infty - \bar{X}_1^\infty}{L} = \frac{\rho_\infty}{\rho_{\text{in}}} \underset{f \to P(\rho_\infty)^-}{\sim} \frac{\rho_\infty P'(0)}{P(\rho_\infty) - f} \tag{6.29}$$

where $P'(0) = k_B T/a$ corresponds to the ideal gas result. In other words the approach of the transition is associated with a divergence of the final distance between the TPs as $(f_c - f)^{-1}$ (see Fig. 6.3b).

6.4.3 Unbound regime

On the other hand, when $f > P(\rho_\infty)$, we expect the TPs to move apart from one another symmetrically, with a time scaling similar to a single driven TP [Eq. (6.13)],

$$\bar{X}_2(t) \underset{t\to\infty}{\sim} -\bar{X}_1(t) \underset{t\to\infty}{\sim} A\sqrt{4Dt}. \tag{6.30}$$

The density in front of TP 2 is then given by Eqs. (6.19)-(6.20),

$$\rho(\bar{X}_2^+) = \rho_\infty g(A). \tag{6.31}$$

As the TPs separate, the density inbetween them vanishes, $\rho(X_2^+) = 0$. Finally, the force balance (6.11) gives an implicit equation for A,

$$P(\rho_\infty g(A)) = f. \tag{6.32}$$

This implicit equation provides the prediction at $f = 1.5$ in Fig. 6.3a and the theoretical expression in Fig. 6.3b for $f > P(\rho_\infty)$. When the force is close to the critical force, the prefactor A is small, so $g(A) \simeq 1 + \sqrt{\pi}A$ and $P(\rho_\infty g(A)) - P(\rho_\infty) \simeq \sqrt{\pi}AP'(\rho_\infty)$. This gives,

$$A = \frac{\bar{X}_2(t)}{\sqrt{4Dt}} \underset{f \to P(\rho_\infty)^-}{\sim} \frac{1}{\sqrt{\pi}} \frac{f - P(\rho_\infty)}{P'(\rho_\infty)} \tag{6.33}$$

with $P'(\rho_\infty) = k_B T/[a(1-\rho_\infty)]$. In other words, A vanishes at the transition as $A \propto [f - P(\rho_\infty)]$ (see Fig. 6.3b).

6.4.4 Critical regime

We now study the critical regime $f = P(\rho_\infty)$ and try to obtain the expression of the displacement $\bar{X}_2(t)$. As $\bar{X}_2(t) \sim t^0$ below the transition and $\bar{X}_2(t) \sim t^{1/2}$ above the transition, we may assume that at the transition $\bar{X}_2(t) = Ct^\gamma$ with $0 < \gamma < 1/2$. Our goal is to determine the exponent γ and the prefactor C.

The starting point of our analysis is the force balance (6.11) that still applies here because the velocity $V_2 \sim t^{\gamma-1}$ vanishes at large times. We write

$$P(\rho_\infty) = P(\rho_+) - P(\rho_-), \tag{6.34}$$

with $P(\bar{X}_2^-) = \rho_-$, $P(\bar{X}_2^+) = \rho_+$ and $f_2 = P(\rho_\infty)$. The quantities to compute are ρ_- and ρ_+. Since the TPs do separate ($\gamma > 0$), the density between them vanishes at large time, that is to say $\rho_-(t) \ll 1$. On the other hand, since the prefactor A in Eq. (6.31) vanishes at the approach of the transition, the density field in front of TP 2 is only weakly modified, $\rho_+(t) = \rho_\infty + \delta\rho_+(t)$ with $\delta\rho_+(t) \ll 1$. We introduce the small parameters that we just saw in Eq. (6.34) and find

$$P'(0)\rho_-(t) = P'(\rho_\infty)\delta\rho_+(t). \tag{6.35}$$

The precise determination of $\rho_-(t)$ and $\delta\rho_+(t)$ will give us both the scaling and the prefactor of the behavior of $\bar{X}_2(t) = Ct^\gamma$. Writing the conservation of the number of particles between the TPs, we readily obtain

$$\frac{\rho_-(t)}{\rho_\infty} = \frac{L}{X_2(t) - X_1(t)} \simeq \frac{L}{2C} t^{-\gamma}. \tag{6.36}$$

The determination of $\rho_+(t)$ is less straightforward. We need to go back to Eqs. (6.3) and (6.6) for the density field $\rho_2^*(x,t)$ in the referential frame of TP 2. Since the velocity is assumed to decay faster than $t^{-1/2}$, the term $V_2\partial_x\rho_2^*$ is negligible in the diffusion equation. And as we said before, $\rho_2^*(0^+,t) \simeq \rho_\infty$. The equations to be considered are

$$\frac{\partial\rho_2^*}{\partial t}(x,t) = D\frac{\partial^2\rho_2^*}{\partial x^2}(x,t), \tag{6.37}$$

$$D\frac{\partial\rho_2^*}{\partial t}(0^+,t) = -\rho_\infty V_2(t). \tag{6.38}$$

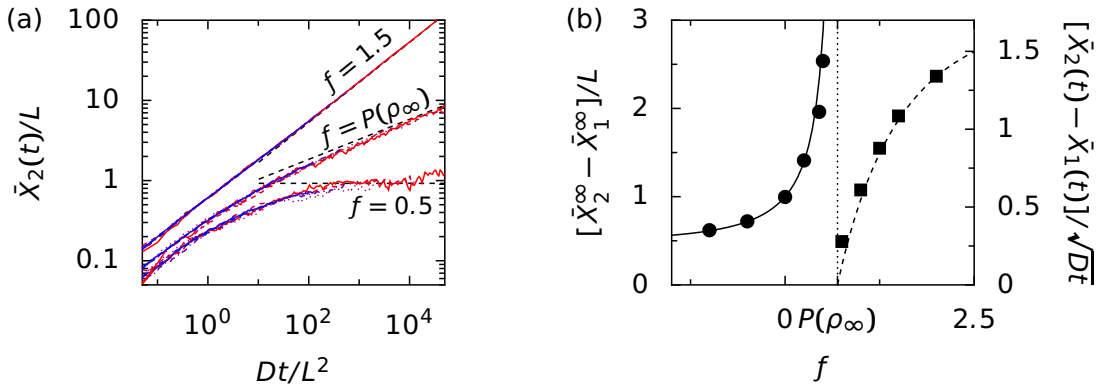

Figure 6.3: Opposite forces $f_2 = -f_1 = f$ at density $\rho_\infty = 0.5$. (a) Caracterization of the displacement average $\bar{X}_2(t)$ in the three regimes: bound ($f = 0.5$), critical ($f = P(\rho_\infty) \approx 0.69$) and unbound ($f = 1.5$). From red to blue, $L = 10, 20, 50, 100, 200, 500$. The average is performed on about 50 simulations with the same parameters. The dashed black lines are the predictions from Eqs. (6.28), (6.32), (6.42). (b) Final distance between the TPs below the transition (left), and separation above the transition (right). The circles and squares are the results of numerical simulations. The lines are the predictions from Eqs. (6.28), (6.32).

This is a diffusion equation for the half line $x > 0$ with an injection $\rho_\infty V_2$ at the origin. The solution is expressed in terms of the Green function of the problem,

$$\rho_2^*(x,t) = \rho_\infty + \rho_\infty \int_0^t V_2(t')G(x,t-t'), \tag{6.39}$$

$$G(x,t) = \frac{1}{\sqrt{\pi D t}} e^{-\frac{x^2}{4Dt}}. \tag{6.40}$$

As $V_2(t) = d\bar{X}_2/dt = \gamma C t^{\gamma-1}$, the density in front of the TP is $\rho_+(t) = \rho_2^*(0^+,t)$,

$$\rho_+(t) = \frac{\gamma C \rho_\infty}{\sqrt{\pi D}} \int_0^t \frac{t'^\gamma dt'}{\sqrt{t-t'}} = \frac{\gamma C b_\gamma \rho_\infty}{\sqrt{\pi D}} t^{\gamma-1/2} \tag{6.41}$$

with $b_\gamma = B(1/2,\gamma)$ where B is the beta function. This is the result we needed.

We now inject Eqs. (6.36) and (6.41) into Eq. (6.35). This gives $-\gamma = \gamma - 1/2$ that is to say $\gamma = 1/4$ which is between 0 and 1/2 as expected. The prefactor C is also computed from this equation. At the end of the day, the average displacement under the critical force is

$$\bar{X}_2(t) \underset{t\to\infty}{\sim} \sqrt{\frac{2\sqrt{\pi}}{b_{1/4}}} \sqrt{\frac{P'(0)L}{P'(\rho_\infty)}} (Dt)^{1/4} \simeq 0.82 \sqrt{\frac{P'(0)L}{P'(\rho_\infty)}} (Dt)^{1/4}. \tag{6.42}$$

The $t^{1/4}$ dependence and the prefactor are in agreement with numerical simulations (Fig. 6.3a).

6.5 Two particles driven by arbitrary forces

The unbinding transition is also observed in numerical simulations for arbitrary forces f_1 and f_2 as shown on Fig. 6.2. We now characterize the bound and unbound regimes and obtain a phase diagram (Fig. 6.5).

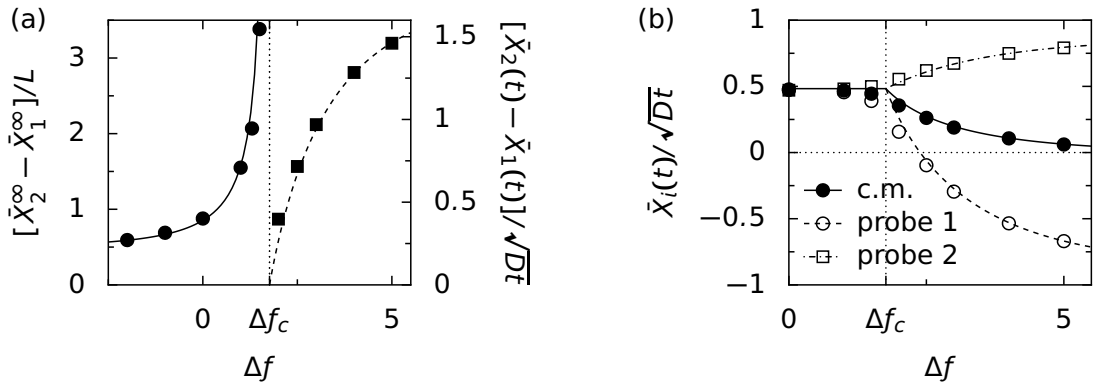

Figure 6.4: Arbitrary forces on two TPs with constant sum $F = f_1 + f_2$. The critical difference of forces $\Delta f_c = f_2^c - f_1^c$ is given by Eq. (6.48). (a) Separation of the TPs below and above the transition. Left: final distance, right: prefactor of the separation. The symbols come from numerical simulations while the lines are the theoretical prediction from Eqs (6.47) and (6.51). (b) Motion of the two TPs and of the center of mass (c.m.). The symbols are the numerical simulations and the lines: are the predictions.

6.5.1 Bound regime

We first assume that the TPs move together. Their scalings at large time are identical and are given by Eq. (6.13),

$$\bar{X}_1(t) \underset{t\to\infty}{\sim} \bar{X}_2(t) \underset{t\to\infty}{\sim} A\sqrt{4Dt}, \tag{6.43}$$

with A to be determined. We write the force balances [Eq (6.11)] for the two TPs,

$$P(\rho_{\text{in}}) - P(\rho_\infty g(-A)) = f_1, \tag{6.44}$$
$$P(\rho_\infty g(A)) - P(\rho_{\text{in}}) = f_2, \tag{6.45}$$

and we sum them into

$$P(\rho_\infty g(A)) - P(\rho_\infty g(-A)) = f_1 + f_2 = F. \tag{6.46}$$

We see that this corresponds to the implicit equation (6.22) for a single TP driven by a force $F = f_1 + f_2$. The two TPs thus behave as a single TP with an effective force being the sum of the two forces. The solution for the prefactor A common to the two TPs is given by the resolution of Eq. (6.46). Once A is known, the density ρ_{in} and the final distance between the TPs are determined as

$$P(\rho_{\text{in}}) = P(\rho_\infty g(A)) - f_2 \qquad \frac{\bar{X}_2^\infty - \bar{X}_1^\infty}{L} = \frac{\rho_\infty}{\rho_{\text{in}}}, \tag{6.47}$$

with L the initial distance between the TPs. A comparison with numerical results is given in Fig. 6.4. The final distance between the TPs diverges at the approach of the transition.

6.5.2 Transition and phase diagram

To investigate the onset of the transition, we consider a total sum of forces $F = f_1 + f_2$ and vary the difference $\Delta f = f_2 - f_1$. The coefficient A thus remains constant. The transition happens when the force balance (6.44) is broken ($P(\rho_{\text{in}}) < 0$ is impossible) that is to say $f_1 < -P(\rho_\infty g(-A))$.

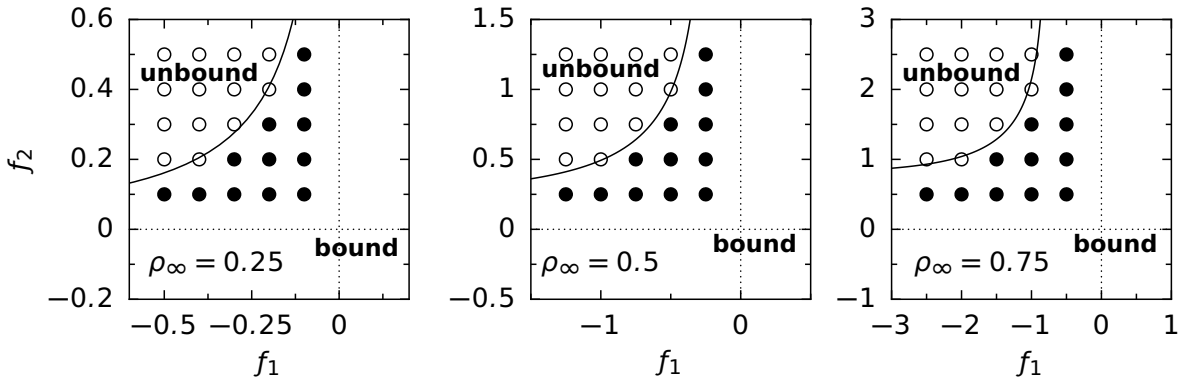

Figure 6.5: Phase diagrams at densities $\rho_\infty = 0.25, 0.5, 0.75$ (left to right). The numerical simulations leading to a bound configuration are denoted by filled circles and the unbound configurations correspond to open circles. The black line is the theoretical boundary from Eq. (6.48).

Equivalently, since $f_1 + f_2$ is constant, this corresponds to the point at which Eq (6.45) is broken, which means $f_2 > P(\rho_\infty g(A))$. In particular an unbound configuration always corresponds to $f_1 < 0$ and $f_2 > 0$: if the forces have the same sign, the TPs are bound. The critical difference of forces at constant $F = f_1 + f_2$ is

$$\Delta f_c(F) = P(\rho_\infty g(A(F))) + P(\rho_\infty g(-A(F))), \tag{6.48}$$

with $A(F)$ given by Eq (6.46).

From this relation, one can build a phase diagram in the plane (f_1, f_2) to predict if the TPs are bound or unbound. This is done in Fig. 6.5 and checked against numerical simulations.

6.5.3 Unbound regime

Let us now consider that the TPs unbind at large time, that is to say their positions satisfy,

$$\bar{X}_1(t) \underset{t\to\infty}{\sim} A_1\sqrt{4Dt}, \qquad \bar{X}_2(t) \underset{t\to\infty}{\sim} A_2\sqrt{4Dt}, \tag{6.49}$$

with $A_1 < A_2$. The density between the TPs vanishes, $\rho_{\text{in}} = 0$. The outside quantities are given by Eqs. (6.19)-(6.20),

$$\rho(\bar{X}_1^-) = \rho_\infty g(-A_1), \qquad \rho(\bar{X}_2^+) = \rho_\infty g(A_2). \tag{6.50}$$

The force balances for the two TPs thus read,

$$-P(\rho_\infty g(-A_1)) = f_1, \qquad P(\rho_\infty g(A_2)) = f_2. \tag{6.51}$$

These are the implicit equations giving the coefficients A_1 and A_2. The predictions, compared to numerical simulations, are plotted in Fig. 6.4. We remark that the motion of the center of mass vanishes at large difference of forces.

6.6 Arbitrary number of driven particles

Our approach extends to the case of an arbitrary number N of TPs driven by forces $f_1, \ldots, f_N$. As in the case of two TPs, we observe two possibilities: the TPs either stay together (Fig. 6.6a) or separate into two groups (Fig. 6.6b).

Let us explain why there can be at most two groups if all forces are non zero. Imagine TP i seeing its left neighbor TP $i-1$ moving to the left and its right neighbor TP $i+1$ moving to the right (with time dependence $t^{1/2}$). The density vanishes both on the left and on the right of TP i. If the force f_i is non zero, the TP thus moves ballistically in the direction of the force until it catches up with one of its two neighbors. In a configuration where the leftmost TP moves as $t^{1/2}$ to the left and the rightmost TP as $t^{1/2}$ to the right, all TPs will move with one of the two, except non-driven TPs that happen to be between the two groups.

The question now is whether there is one or two groups of TPs. To answer this, we consider the set of effective forces (F_1^i, F_2^i) with

$$F_1^i = \sum_{j=1}^{i} f_j \qquad\qquad F_2^i = \sum_{j=i+1}^{N} f_j \tag{6.52}$$

for $1 \leq i < N$. This corresponds to separating the TPs in two groups $(1,\dots,i)$ and $(i+1,\dots,N)$. One then puts the points (F_1^i, F_2^i) in the phase diagram (Fig. 6.5) as shown on Fig. 6.6c. If all the points lie in the bound region, the TPs stay together (Fig. 6.6c). Realizing that the densities between the TPs are homogeneous at large time and summing the force balances, we obtain the implicit equation for the displacement coefficient,

$$\bar{X}_1(t) \underset{t\to\infty}{\sim} \dots \underset{t\to\infty}{\sim} \bar{X}_N(t) \underset{t\to\infty}{\sim} A\sqrt{4Dt}, \tag{6.53}$$

$$P(\rho_\infty g(A)) - P(\rho_\infty g(-A)) = F = \sum_{i=1}^{N} f_i. \tag{6.54}$$

If one or more points are in the unbound regime of the phase diagram, the system separates for the most unstable point that is to say the largest $\Delta F^i = F_2^i - F_1^i$ (Fig. 6.6b). In this case, the density between the two groups vanishes at large time, and the prefactors A_1 and A_2 are given by

$$\bar{X}_1(t) \underset{t\to\infty}{\sim} \dots \underset{t\to\infty}{\sim} \bar{X}_i(t) \underset{t\to\infty}{\sim} A_1\sqrt{4Dt} \tag{6.55}$$

$$\bar{X}_{i+1}(t) \underset{t\to\infty}{\sim} \dots \underset{t\to\infty}{\sim} \bar{X}_N(t) \underset{t\to\infty}{\sim} A_2\sqrt{4Dt} \tag{6.56}$$

and satisfy

$$-P(\rho_\infty g(-A_1)) = F_1^i, \qquad\qquad P(\rho_\infty g(A_2)) = F_2^i. \tag{6.57}$$

These two implicit equations give the prefactors for the motions of the two TPs.

6.7 Continuous systems

The approach that we developed for the SEP relies on the force balance (6.11). Actually, this force balance is not specific to the SEP and can be written for any single-file system. Let us consider a generic system with a density field $\rho(x,t)$ and an intruder at position $\bar{X}(t)$ driven by a force f. Since the velocity still vanishes at large time ($\bar{X}(t) \propto t^{1/2}$), we may write

$$P(\rho(\bar{X}_1)) - P(\rho(\bar{X}^-)) = f. \tag{6.58}$$

$P(\rho)$ is the equilibrium pressure of the system at density ρ, that is to say the equation of state. For the SEP, it is given by Eq. (6.10). Our analysis of the unbinding transition applies. In the

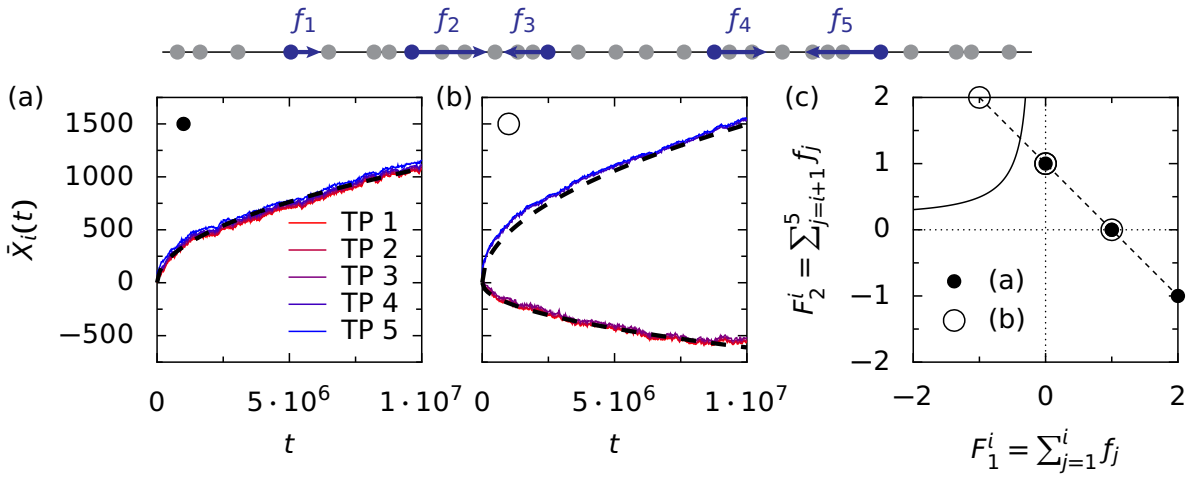

Figure 6.6: Five TPs submitted to arbitrary forces at density $\rho_\infty = 0.5$. (a) and (b) Simulations (colored lines) and predictions (dashed black lines) in two configurations. (a) At forces $(1,1,-1,-1,1)$, the TPs all move together. (b) At forces $(1,-1,-1,1,1)$, the TPs separate into two groups. (c) Phase diagram at $\rho = 0.5$. All the divisions of case (a) — corresponding to panel (a) — are in the bound regime while one division of case (b) is in the unbound regime (TPs (1, 2, 3) and TPs (4, 5)). This implies that the TPs stay together in case (a) and separate in case (b).

case of two TPs with opposite forces we predict a transition at a force $f_c = P(\rho_\infty)$ where ρ_∞ is the average density of the system. In the following we also generalize the other equations, in particular the diffusion equation of the density field.

We focus on two models of continuous single-file systems that were shown to be relevant in experiments. The first one is the gas of hard rods, also known as Tonks gas [66] in which Brownian rods of size a are placed on a line and cannot overlap each other. This model has been shown to be in quantitative agreement with diffusion experiments in a quasi-one-dimensional colloidal suspension [9]. The pressure of the hard rod gas is known to be given [66] by

$$P_{\mathrm{HR}}(\rho) = \frac{k_B T \rho}{1 - a\rho}. \tag{6.59}$$

As expected, the pressure diverges at the density a^{-1} at which no space remains.

The second model is the one of point-like diffusive particles interacting via a repulsive dipole-dipole interaction given by the potential $U(r) = A/r^3$. This corresponds to the experiments of Ref. [10] of paramagnetic colloids in a magnetic field. The pressure of this gas is not known. However, at low density one can perform a virial expansion [20] leading to

$$P_{\mathrm{dip}}(\rho) \simeq k_B T \rho \left[1 + 1.35 a\rho + 1.40 (a\rho)^2\right], \tag{6.60}$$

with the characteristic scale of the interaction $a = [A/(k_B T)]^{1/3}$.

We consider two TPs driven away from one another by antisymmetric forces $f_2 = -f_1 = f$ as we did in section 6.4. For both models, we predict an unbinding transition at a critical force $f_c = P(\rho_\infty)$ with ρ_∞ the average density of the system. Below the critical force, the particles remain at a finite distance at large time, while above the critical force they move in opposite directions as $\sqrt{t}$. We check this in numerical simulations in Fig. 6.7.

In the bound regime, the final distance between the two TPs is still given by the conservation of the number of particles between the TPs,

$$\frac{\bar{X}_2^\infty - \bar{X}_1^\infty}{L} = \frac{\rho_\infty}{\rho_{\text{in}}} \tag{6.61}$$

with L the initial distance between the TPs. ρ_{in} is the density between the TPs, it satisfies the force balance $P(\rho_{\text{in}}) = P(\rho_\infty) - f$. For the Tonks gas, $\rho_{\text{in}} = [a + k_B T/(P(\rho_\infty) - f)]^{-1}$. At the approach of the transition, the final distance diverges as

$$\frac{\bar{X}_2^\infty - \bar{X}_1^\infty}{L} \underset{f \to P(\rho_\infty)^-}{\sim} \frac{\rho_\infty P'(0)}{P(\rho_\infty) - f}. \tag{6.62}$$

The characterization of the unbound regime runs into the difficulty that the diffusion coefficient of continuous models is density-dependent. The diffusion equation for the density field $\rho(x,t)$ reads

$$\frac{\partial \rho}{\partial t}(x,t) = \frac{\partial}{\partial x}\left[D(\rho(x,t)) \frac{\partial \rho}{\partial x}(x,t) \right], \tag{6.63}$$

with $D(\rho)$ the diffusion coefficient at density ρ. In the absence of hydrodynamic interactions, it is given by

$$D(\rho) = \kappa_0 P'(\rho), \tag{6.64}$$

with κ_0 the mobility of the particles [9]. We thus only consider small displacements $\bar{X}/\sqrt{t} \ll 1$ for which the density field is only weakly perturbed. In this case, we write $D(\rho) \simeq D(\rho_\infty)$. Eq. (6.33) obtained for the SEP is still valid, the displacement of TP 2 is given by

$$\bar{X}_2(t) \underset{t \to \infty}{\sim} \frac{f - P(\rho_\infty)}{P'(\rho_\infty)} \sqrt{\frac{4D(\rho_\infty)t}{\pi}}. \tag{6.65}$$

Last, in the critical case, the density field is indeed weakly perturbed. Eq. (6.42) holds with $D = D(\rho_\infty)$. The predictions of the three regimes are compared in Fig. 6.7 for the two models considered.

6.8 Conclusion

We developed an hydrodynamic approach of the density field of the SEP. It is based on three equations: a diffusion equation for the density field, a no-flux boundary condition at the position of the TPs, and an equation linking the displacement of the TP to the density field. At large time, the last one turns into a force balance. We used this approach to investigate the behavior of two TPs driven apart from one another and unveiled an unbinding transition: at small forces the TPs stay at a constant distance from one another while at large forces they separate and move as $t^{1/2}$. The critical force is the equilibrium pressure of the bath and the critical regime is characterized by a behavior in $t^{1/4}$. The approach works for arbitrary forces and we found a phase diagram. Furthermore, in the case of an arbitrary number of driven TPs, we found that there are at most two groups of TPs moving together. Importantly, our approach extends to arbitrary single-file systems. The critical force is still the equilibrium pressure of the bath, and we checked that the predicted unbinding transition occurs in numerical simulations. We are thus confident that this transition should be observable in experimental systems, e.g. colloids.

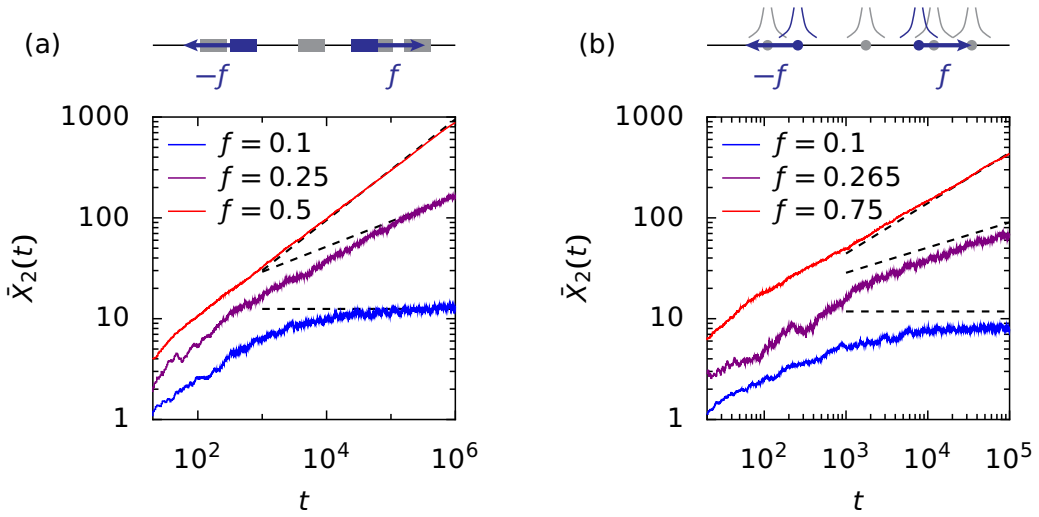

Figure 6.7: Simulations of continuous systems. (a) Hard rods. (b) Dipole-dipole interactions ($1/r^3$). The density is $\rho_\infty = 0.2$ for both graphs and the forces on the two TPs are antisymmetric. The results for the displacement of the right TP are given in the three regimes below, at and above the critical force ($P(\rho_\infty) = 0.2$ in (a) and $P(\rho_\infty) \simeq 0.265$ in (b)). The dashed lines are the theoretical predictions given in section 6.7.

An important point of this chapter is that the average displacement of a TP $\bar{X}(t)$ is coupled with the deterministic density field $\rho(x,t)$. Hence, an hydrodynamic description of the field gives the behavior of the average displacement. In the next chapter, we show that this can be extended to higher-order cumulants of the displacement. They are coupled with what we call generalized profiles that is to say correlations between the fluctuating density field and the displacement. Deriving hydrodynamic equations for these generalized profiles thus gives hope to compute arbitrary cumulants of the SEP.

Chapter 7

Symmetric exclusion process: single-tag observables from generalized profiles

Contents

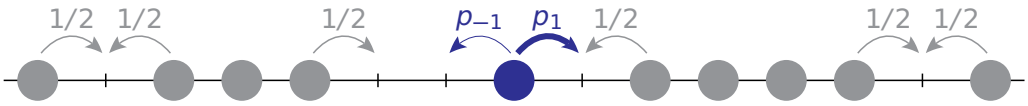

Figure 7.1: Symmetric exclusion process with one biaised particle (blue). The bias on the particle is $s = p_1 - p_{-1}$.

7.1 Introduction

Predicting the properties of a TP in the SEP beyond the variance (at any density) is an important challenge for which only few methods are available. The only method giving the full solution [28, 29] is quite convoluted and is based on Bethe Ansatz results for the ASEP (see Appendix A). Another method giving the second and fourth cumulants of the SEP [45, 47] is the so-called macroscopic fluctuation theory (MFT). It starts from the fluctuating hydrodynamics equations first derived by Spohn [46] and expands them using a path-integral formalism. A strength of this method is that it allows to get rid of the microscopic details of the system and to have an hydrodynamic formalism focusing from the start on the observables at large time and large distance. However, the fact that the position of a tagged particle is obtained only implicitly in terms of the density field seems to make the computations tedious: they have not been performed above the fourth cumulant.

In this section, we build upon the framework of the previous chapter and extend it to compute the cumulant-generating function. The profiles become generalized profiles, and the average displacement is replaced by the characteristic function. As before, the tagged particle is coupled with the density field of the bath: we adopt a Lagrangian description for this particle. And the bath is considered in the reference frame of the TP: this is similar to an Eulerian specification for a flow field. This difference of description between the TP and the bath seems to us natural for the study of single-tag observables of the SEP. Our approach starts from the master equation of the problem [37, 46] and is exact. But in the general case, the equations are not closed. The challenge is thus to find the regimes in which the equations are or can be closed.

We first recall the master equation of the SEP and use it to derive exact microscopic equations. We then look at large distance and large time and obtain exact hydrodynamic equations. These equations can be solved exactly for the lowest-order cumulants at any density, and for all cumulants in the limits of both high and low density. Finally, we show that the approach extends to arbitrary single-file processes for which we compute the variance of a particle. This topic of this chapter is still under work. The presentation may be quite technical but it should not distract the reader from the main point which is that we build a new approach based on generalized profiles that gives the probability law of an intruder as a byproduct.

7.2 Master equation for the SEP with one tagged particle

We consider the usual symmetric exclusion process. Particles jump to the left and to the right with rates $1/2$ with exclusion. We introduce a tagged particle (TP) with asymmetric jump rates: p_1 to the right and p_{-1} to the left (Fig. 7.1). The TP is initially at the origin, and its position at time t is denoted X_t. We define the occupation $\eta_r(t)$ of each site $r \in \mathbb{Z}$ of the line at time t as $\eta_r(t) = 1$ if the site is occupied and $\eta_r(t) = 0$ if the site is empty. The system is entirely determined by its configuration $(X, \underline{\eta})$ with $\underline{\eta} = \{\eta_r\}_{r\in\mathbb{Z}}$. We now show that the rules enforced on the system lead

naturally to a master equation, already derived in Refs. [37, 46].

We denote $P(X,\underline{\eta},t)$ the probability that the system is in the configuration $(X,\underline{\eta})$ at time t. During a small time interval Δt, this configuration can change for two reasons.

- A bath particle performs a jump to the left or to the right. This happens with probability $\Delta t/2$. We call $\underline{\eta}^{r,+}$ the configuration $\underline{\eta}$ in which the occupations of sites r and $r+1$ are exchanged. One realizes that all the possible jumps of the bath particles correspond to exchanges between configurations $\underline{\eta}$ and $\underline{\eta}^{r,+}$, for $r \neq X, X-1$. Indeed these configurations are different only if exactly one of the two sites is occupied: this corresponds to an allowed jump.
- The TP jumps to the left (probability $p_{-1}\Delta t$) or to the right (probability $p_1\Delta t$). This happens only if the site of arrival is empty, that is to say if $1-\eta_{X\pm1}=1$.

One can then write the following equation for the evolution of the system between t and $t+\Delta t$.

$$P(X,\underline{\eta},t+\Delta t)-P(X,\underline{\eta},t)=\sum_{r\neq X,X-1}\frac{\Delta t}{2}\Big[P(X,\underline{\eta}^{r,+},t)-P(X,\underline{\eta},t)\Big] + \Delta t\sum_{\mu=\pm1}p_\mu\Delta t\Big\{(1-\eta_X)P(X-\mu,\underline{\eta},t)-(1-\eta_{X+\mu})P(X,\underline{\eta},t)\Big\} \quad (7.1)$$

The first term corresponds to the diffusion of the bath, and the second to the motion of the TP. Finally, the master equation verified by our system is

$$\partial_t P(X,\underline{\eta},t)=\frac{1}{2}\sum_{r\neq X,X-1}\Big[P(X,\underline{\eta}^{r,+},t)-P(X,\underline{\eta},t)\Big] + \sum_{\mu=\pm1}p_\mu\Big\{(1-\eta_X)P(X-\mu,\underline{\eta},t)-(1-\eta_{X+\mu})P(X,\underline{\eta},t)\Big\}. \quad (7.2)$$

This master equation will be crucial for the derivations of microscopic equations for integrated quantities, such as $\langle X_t\rangle$ or $\langle\eta_r\rangle$. Doing so is the goal of the next section.

7.3 Exact microscopic equations

7.3.1 Definitions

The first key observable is the cumulant-generating function $\psi(\lambda,t)$ of the position X_t of the TP,

$$\psi(\lambda,t)\equiv\ln\left\langle e^{\lambda X_t}\right\rangle. \quad (7.3)$$

We changed variable $\lambda=iu$ compared to the previous chapters. The expansion in powers of λ gives the cumulants of the position,

$$\psi(\lambda,t)=\sum_{n=0}^{\infty}\frac{\lambda^n}{n!}\kappa_n(t). \quad (7.4)$$

The first cumulants read $\kappa_1=\langle X_t\rangle$, $\kappa_2=\langle(\delta X_t)^2\rangle$, $\kappa_3=\langle(\delta X_t)^3\rangle$, $\kappa_4=\langle(\delta X_t)^4\rangle-3\langle(\delta X_t)^2\rangle$ with $\delta X_t=X_t-\langle X_t\rangle$.

The second observable is the generalized profile $\tilde{w}_r(\lambda,t)$ in the reference frame of the TP defined as

$$\tilde{w}_r(\lambda,t) \equiv \frac{\langle \eta_{X_t+r} e^{\lambda X_t}\rangle}{\langle e^{\lambda X_t}\rangle}. \tag{7.5}$$

Its expansion in powers of λ gives the joint cumulants of X_t and η_{X_t+r}.

$$\tilde{w}_r(\lambda,t) = \sum_{n=0}^{\infty} \frac{\lambda^n}{n!} \langle \eta_{X_t+r} (X_t)^n\rangle_c \equiv k_r + \lambda \tilde{g}_r + \frac{\lambda^2}{2}\tilde{h}_r + \frac{\lambda^3}{6}\tilde{m}_r + \dots \tag{7.6}$$

with the first orders given by $k_r = \langle \eta_{X_t+r}\rangle$, $\tilde{g}_r = \langle \delta\eta_{X_t+r}\delta X_t\rangle$, $\tilde{h}_r = \left\langle \delta\eta_{X_t+r}(\delta X_t)^2\right\rangle$, $\tilde{m}_r = \left\langle \delta\eta_{X_t+r}(\delta X_t)^3\right\rangle - 3\left\langle \delta\eta_{X_t+r}\delta X_t\right\rangle\left\langle (\delta X_t)^2\right\rangle$, with $\delta\eta_{X_t+r} = \eta_{X_t+r} - \langle \eta_{X_t+r}\rangle$. The order 0, k_r is simply the profile in the reference frame of the TP, the higher order are generalizations involving the displacement of the TP.

The definition of $\tilde{w}_r$ (7.5) may look unfamiliar. However, one can write the two-point characteristic function

$$\ln\left\langle e^{\lambda X_t + \alpha \eta_{X_t+r}}\right\rangle = \ln\left\langle e^{\lambda X_t}\right\rangle + \alpha \frac{\langle \eta_{X_t+r} e^{\lambda X_t}\rangle}{\langle e^{\lambda X_t}\rangle} + \mathcal{O}(\alpha^2) = \psi(\lambda,t) + \alpha\tilde{w}_r(\lambda,t) + \mathcal{O}(\alpha^2). \tag{7.7}$$

$\tilde{w}_r$ is the first order in α of this characteristic function. Since $\eta^2_{X_t+r} = \eta_{X_t+r}$, this first order encodes all the couplings between η_{X_t+r} and X_t.

7.3.2 Equation for the cumulant-generating function

We want to obtain an equation for the cumulant-generating function $\psi(\lambda,t)$ [Eq. (7.3)] from the master equation (7.2). We start by computing the time derivative of the moment-generating function $\langle e^{\lambda X_t}\rangle$ from the master equation.

$$\partial_t \langle e^{\lambda X_t}\rangle \equiv \sum_{X,\underline{\eta}} e^{\lambda X} \partial_t P(X,\underline{\eta}) \tag{7.8}$$

$$= \sum_{\mu=\pm1} p_\mu \sum_{X,\underline{\eta}} \left\{ (1-\eta_X) P(X-\mu,\underline{\eta},t) e^{\mu\lambda} e^{\lambda(X-\mu)} - (1-\eta_{X+\mu}) P(X,\underline{\eta},t) e^{\lambda X}\right\} \tag{7.9}$$

$$= \sum_{\mu=\pm1} p_\mu (e^{\mu\lambda}-1)\left\langle (1-\eta_{X+\mu}) e^{\lambda X_t}\right\rangle \tag{7.10}$$

The summation is performed on all positions X and all configurations $\underline{\eta}$. The "diffusive" term of the master equation vanishes by reordering the summation on $\underline{\eta}$ and the "TP" term is expressed via a shift $X \mapsto X+\mu$. The time derivative of $\psi(\lambda,t) = \ln\langle e^{\lambda X_t}\rangle$ then follows

$$\partial_t \psi = \frac{\partial_t \langle e^{\lambda X_t}\rangle}{\langle e^{\lambda X_t}\rangle} = p_1(e^\lambda - 1)(1-\tilde{w}_1) + p_{-1}(e^{-\lambda}-1)(1-\tilde{w}_{-1}), \tag{7.11}$$

with $\tilde{w}_r$ defined in Eq. (7.5). This is an exact equation which links the time derivative of the cumulant-generating function to the values of the generalized profiles $\tilde{w}_r$ at sites ±1 with respect to the TP. At order λ, one recovers the velocity equation,

$$\partial_t \langle X_t\rangle = p_1(1-k_1) - p_{-1}(1-k_{-1}) \tag{7.12}$$

with $k_r = \langle \eta_{X_t+r}\rangle$. This exact equation intuitively means that the velocity is equal to the rate of allowed jump to the right minus the rate of allowed jump to the left.

7.3.3 Equation for the generalized profiles

We define $w_r = \langle \eta_{X_t+r} e^{\lambda X_t} \rangle$, such that $\tilde{w}_r = w_r / \langle e^{\lambda X_t} \rangle$. A rather tedious computation from the master equation (7.2) gives,

$$\partial_t w_r \equiv \sum_{X,\underline{\eta}} \eta_{X+r} e^{\lambda X} \partial_t P(X, \underline{\eta}) \tag{7.13}$$

$$= \frac{1}{2} \sum_{\mu} (1 - \delta_{r,-\mu}) \nabla_\mu w_r + \sum_{\mu} p_\mu \left\{ e^{\mu\lambda} \left\langle (1 - \eta_{X_t+\mu}) \eta_{X_t+r+\mu} e^{\lambda X_t} \right\rangle - \left\langle (1 - \eta_{X_t+\mu}) \eta_{X_t+r} e^{\lambda X_t} \right\rangle \right\} \tag{7.14}$$

with $\nabla_\mu w_r = w_{r+\mu} - w_r$ and the convention $\eta_{X_t} = 0$. The first term comes from the "diffusive" term of the master equation, and the second term from the "TP" term. Importantly, one notices that this is not a closed equation on w_r: it involves the correlations $\langle \eta_{X_t+\mu} \eta_{X_t+r} e^{\lambda X_t} \rangle$.

The time derivative of the generalized profiles $\tilde{w}_r$ can be computed as

$$\partial_t \tilde{w}_r = \frac{\partial_t w_r}{\langle e^{\lambda X_t} \rangle} - \tilde{w}_r \partial_t \psi, \tag{7.15}$$

with $\partial_t \psi$ given by Eq. (7.11). The result is

$$\partial_t \tilde{w}_r = \frac{1}{2} \sum_{\mu} (1 - \delta_{r,-\mu}) \nabla_\mu \tilde{w}_r + \sum_{\mu} p_\mu \left\{ e^{\mu\lambda} \tilde{C}_{\mu,r+\mu} - \tilde{C}_{\mu,r} - (e^{\mu\lambda} - 1)(1 - \tilde{w}_\mu) \tilde{w}_r \right\}, \tag{7.16}$$

$$\tilde{C}_{\mu,r}(\lambda, t) \equiv \frac{\left\langle (1 - \eta_{X_t+\mu}) \eta_{X_t+r} e^{\lambda X_t} \right\rangle}{\langle e^{\lambda X_t} \rangle}. \tag{7.17}$$

Eq. (7.16) is not a closed equation since it involves the correlations $\tilde{C}_{\mu,r}$. Moreover, it appears unattractive at first sight. We now put forward a rewriting of the correlations that we claim to be relevant and that should clarify the situation.

7.3.4 Decoupling approach

We first write the key expression of our approach that we call a "decoupling approach". Then, we derive the new equations. Finally, we try to get some insight into what this decoupling approach means.

The key point is to define new correlations $f_{\mu,r}$ as

$$f_{\mu,r}(\lambda, t) \equiv \begin{cases} \tilde{C}_{\mu,r} - (1 - \tilde{w}_\mu) \tilde{w}_{r-\mu} & \text{if } \mu r > 0 \\ \tilde{C}_{\mu,r} - (1 - \tilde{w}_\mu) \tilde{w}_r & \text{if } \mu r < 0 \end{cases} \tag{7.18}$$

with the convention $\tilde{w}_0 = 0$. We note that the subtracted term is asymmetric depending on the relative signs of μ and r. Our insight is that $f_{\mu,r}$ should vanish in some limit cases that we detail in the following.

Introducing the expression into Eq. (7.16), we obtain the following equation

$$\partial_t \tilde{w}_r = \frac{1}{2} \sum_{\mu} (1 - \delta_{r,-\mu}) \nabla_\mu \tilde{w}_r - B_\nu \nabla_{-\nu} \tilde{w}_r + \sum_{\mu} p_\mu \left\{ e^{\mu\lambda} f_{\mu,r+\mu} - f_{\mu,r} \right\}, \tag{7.19}$$

with ν the sign of r and B_ν a (time-dependent) coefficient closely linked to the time-derivative of the cumulant-generating function [Eq. (7.11)],

$$B_\nu(\lambda,t) \equiv p_\nu(1-\tilde{w}_\nu) - p_{-\nu}e^{-\nu\lambda}(1-\tilde{w}_{-\nu}) = \frac{\partial_t\psi}{e^{\nu\lambda}-1}. \tag{7.20}$$

In particular B_ν has the same time dependence as $\partial_t\psi$. Eq. (7.19) is the central equation of this chapter. Before detailing its implications, we offer some insight into Eq. (7.18).

Remark. When we introduced our decoupling approach, we had in mind the profiles $\langle\eta_{X_t+r}\rangle$ and the order $\lambda^{(0)}$ of the correlations $f_{\mu,r}$ that we call $f^{(0)}_{\mu,r}$. We remind the reader of the fact that η_r can take only two values: 0 and 1. Let us analyze what it means to have a vanishing correlation $f^{(0)}_{1,r}$.

$$0 = f^{(0)}_{1,r} \equiv \langle(1-\eta_{X+1})\eta_{X+r}\rangle - \langle 1-\eta_{X+1}\rangle\langle\eta_{X+r-1}\rangle \tag{7.21}$$

$$\iff \mathbb{P}[(\eta_{X+1}=0)\cap(\eta_{X+r}=1)] = \mathbb{P}[\eta_{X+1}=0]\,\mathbb{P}[\eta_{X+r-1}=1] \tag{7.22}$$

$$\iff \mathbb{P}[\eta_{X+r}=1|\eta_{X+1}=0] = \mathbb{P}[\eta_{X+r-1}=1] \tag{7.23}$$

The probability that site r with respect to the TP is occupied knowing that site 1 is empty is equal to the probability that site $r-1$ is occupied. In particular, one checks that this holds if the law of the distance between successive particles follows a geometric distribution. This is valid for the SEP at equilibrium because the density follows a product measure [72]. For the case of a biased intruder, $f^{(0)}_{1,r}$ quantifies the deviation from this relation. And $f_{\mu,r}$ at any order in λ investigates how the couplings of the displacement X_t with the field modify this relation.

7.3.5 Final equations

We now summarize the four equations that we found and will investigate in the following.

$$\partial_t\tilde{w}_r = \frac{1}{2}\Delta\tilde{w}_r - B_\nu\nabla_{-\nu}\tilde{w}_r + \sum_\mu p_\mu\left\{e^{\mu\lambda}f_{\mu,r+\mu} - f_{\mu,r}\right\} \tag{7.24}$$

$$\partial_t\tilde{w}_\mu = \frac{1}{2}\nabla_\mu\tilde{w}_\mu + B_\mu\tilde{w}_\mu + p_\mu e^{\mu\lambda}f_{\mu,2\mu} - p_{-\mu}f_{-\mu,\mu} \tag{7.25}$$

$$\lim_{r\to\pm\infty}\tilde{w}_r = \rho \tag{7.26}$$

$$\partial_t\psi = p_1(e^\lambda-1)(1-\tilde{w}_1) + p_{-1}(e^{-\lambda}-1)(1-\tilde{w}_{-1}) \tag{7.27}$$

with $\nabla_\nu\tilde{w}_r = \tilde{w}_{r+\nu} - \tilde{w}_r$ and $\Delta\tilde{w}_r = \tilde{w}_{r+1} + \tilde{w}_{r-1} - 2\tilde{w}_r$. The coefficient B_ν is linked to $\partial_t\psi$ by $B_\nu = \partial_t\psi/(e^{\nu\lambda}-1)$. The correlations $f_{\mu,r}$ are defined in Eq. (7.18).

Let us emphasize the meaning of the different equations. Eq. (7.24) is the bulk equation for the generalized profiles. It is valid for $r \neq \pm 1$, and $\nu = \pm 1$ denotes the sign of r. It is remarkable that the generalized velocity $\partial_t\psi$ is involved (by the coefficient B_ν). Eq. (7.25) is the boundary equation, it details what happens at sites $\mu = \pm 1$. Eq. (7.26) is the large distance behavior: the generalized profiles defined by Eq. (7.5) should converge at large distance to the average density ρ of the system. Finally, Eq. (7.27) links the generalized velocity (derivative of the cumulant-generating function) to the generalized profiles at sites ± 1.

The system of equations (7.24)-(7.27) is exact, but it is not closed since it involves the correlations $f_{\mu,r}$. One would require a closure relation on these correlations to solve the system. In the following, we will show that in some limit cases, such a relation is either unnecessary ($f_{\mu,r} \sim 0$) or can be explicitly provided.

7.4 Exact hydrodynamic equations

The goal of this section is to study the equations (7.24)-(7.27) in the large time limit $t \to \infty$, with a diffusive scaling $r \sim \sqrt{t}$ on the positions. We first write the time scalings of the different functions involved. Then we derive the hydrodynamic (large time and large distance) equations. And finally, we show that at order 0 we recover the hydrodynamic equation for the profile that we studied in Chap 6.

7.4.1 Scalings

From the previous chapters, we know that in the SEP, the cumulant-generating function $\psi(\lambda, t)$ scales as $\sqrt{t}$. We write

$$\partial_t \psi(\lambda, t) = \frac{A(\lambda)}{\sqrt{2t}} + \mathcal{O}(t^{-1}). \tag{7.28}$$

This immediately implies the following time scalings of $B_{\pm 1}$,

$$B_\mu(\lambda, t) = \mu \frac{b_\mu(\lambda)}{\sqrt{2t}} + \mathcal{O}(t^{-1}) \tag{7.29}$$

with $b_\mu(\lambda) = \mu A(\lambda)/(e^{\mu\lambda} - 1)$. The sign μ is a convention adapted to the equations that we will derive.

From our intuition from Chap 6, and numerical simulations, we state that the profiles $\tilde{w}_r$ follow a diffusive scaling at large time,

$$\tilde{w}_r(\lambda, t) = \rho + \Phi\left(\frac{r}{\sqrt{2t}}, \lambda\right) + \mathcal{O}(t^{-1/2}). \tag{7.30}$$

From Eq. (7.26), $\lim_{v \to \pm\infty} \Phi(v, t) = 0$.

One has the insight that the correlations $f_{\mu,r}(\lambda, t)$ also need to satisfy a diffusive scale $r \sim \sqrt{t}$. In numerical simulations, we see that there is no term of order t^0 and that the first term is of order $t^{-1/2}$. We write the following expansion,

$$f_{\mu,r}(\lambda, t) = \frac{1}{\sqrt{t}} F_\mu\left(\frac{r}{\sqrt{2t}}, \lambda\right) + \frac{1}{t} G_\mu\left(\frac{r}{\sqrt{2t}}, \lambda\right) + \mathcal{O}(t^{-3/2}). \tag{7.31}$$

Now that we have the scaling forms, we can study Eqs. (7.24)-(7.27) in this limit.

7.4.2 Derivation of the equations

We separate the relations into two categories, those which come from a vanishing quantity, and the hydrodynamic equations.

Vanishing quantities. From the scalings of Eqs. (7.28)-(7.30), we see that the left-hand side of Eq. (7.27) scales as $t^{-1/2}$ while the right-hand side scales as t^0. At large time, this imposes the relation

$$p_1(e^\lambda - 1)[1 - \rho - \Phi(0^+)] + p_{-1}(e^{-\lambda} - 1)[1 - \rho - \Phi(0^-)] = 0. \tag{7.32}$$

This is a generalization of the "force balance" written in Chap 6.

Similarly, the left-hand side of Eq. (7.24) scales as t^{-1}, while the right-hand side has a term of order $t^{-1/2}$ that must be vanishing. This imposes,

$$p_1(e^{\lambda}-1)F_1(v)+p_{-1}(e^{-\lambda}-1)F_{-1}(v)=0, \tag{7.33}$$

$$p_{-1}F_{-1}(v)=p_1e^{\lambda}F_1(v). \tag{7.34}$$

This symmetry relation, similar in spirit to Eq. (7.32), is one of the major advantages of the definition of $f_{\mu,r}$ [Eq. (7.18)].

Hydrodynamic equations. We can now write the scaling limit of the bulk equation (7.24) from the scalings (7.30)-(7.31).

$$-v\Phi'(v)=\frac{1}{2}\Phi''(v)+b_\mu\Phi'(v)+\sum_\mu \mu p_\mu e^{\mu\lambda}F'_\mu(v)+\sum_\mu p_\mu(e^{\mu\lambda}-1)G_\mu(v) \tag{7.35}$$

Note that the second order in time of the development of $f_{\mu,r}$ is needed.

Similarly, the boundary equation (7.25) gives

$$0=\frac{\mu}{2}\Phi'(0^\mu)+\mu b_\mu[\rho+\Phi(0^\mu)]. \tag{7.36}$$

It is striking that the correlation terms vanish because of the symmetry (7.34).

Finally we can write the large-time and large-distance equations, that we call the hydrodynamic equations. They correspond to Eqs. (7.24)-(7.27) at large time.

$$\Phi''(v)+2(v+b_\mu)\Phi'(v)+2p_1(e^{\lambda}-1)F'_1(v)+2\sum_\mu p_\mu(e^{\mu\lambda}-1)G_\mu(v)=0, \tag{7.37}$$

$$\Phi'(0^\mu)+2b_\mu[\rho+\Phi(0^\mu)]=0, \tag{7.38}$$

$$\lim_{v\to\pm\infty}\Phi(v)=0, \tag{7.39}$$

$$p_1(e^{\lambda}-1)[1-\rho-\Phi(0^+)]+p_{-1}(e^{-\lambda}-1)[1-\rho-\Phi(0^-)]=0. \tag{7.40}$$

We used the symmetry relation (7.34) in the bulk equation. These equations are exact. Solving them requires a closure relation on $F_\mu(v)$ and $G_\mu(v)$.

That being said, at the order λ^0, one realizes that the correlations play no role at all. And if there is no bias ($p_1=p_{-1}=1/2$), the equations at order λ^1 also do not involve correlations. We now investigate the equations obtained in these two cases and the solution they give.

7.5 Lowest orders

We expand the generalized profiles in power of λ, $\Phi(v,\lambda)=\Phi_0(v)+\lambda\Phi_1(v)+\mathcal{O}(\lambda^2)$. Φ_0 is the large time and large distance limit of the profiles $k_r=\langle\eta_{X_t+r}\rangle$, and Φ_1 the limit shape of the first order profiles $\tilde{g}_r=\langle\eta_{X_t+r}X_t\rangle-\langle\eta_{X_t+r}\rangle\langle X_t\rangle$. We focus on the equations obtained for Φ_0 from Eqs. (7.37)-(7.40), and then those for Φ_1 in the absence of bias.

7.5.1 Density profile (order 0)

Remarkably, at order λ^0, the bulk equation (7.37) does not involve the correlations,

$$\Phi_0''(v)+2(v+A_0)\Phi_0'(v)=0 \tag{7.41}$$

with

$$A_0 = b_\mu^{(0)} = \frac{\partial_t \langle X \rangle}{\sqrt{2t}}. \tag{7.42}$$

Furthermore, the boundary equation (7.38) and the velocity equation (7.40) give

$$\Phi_0'(0^\mu) + 2A_0[\rho + \Phi_0(0^\mu)] = 0, \tag{7.43}$$

$$p_1\left[1-\rho-\Phi_0(0^+)\right] + p_{-1}\left[1-\rho-\Phi_0(0^-)\right] = 0. \tag{7.44}$$

We realize that Eqs. (7.41), (7.43) and (7.44) are those that we studied in chapter 6 on the unbinding transition [Eqs. (6.14), (6.15) and (6.7) with $\Phi_0 = \phi - \rho$]. Their solution is given in subsection 6.3.2 and reads

$$\Phi_0(v \gtrless 0) = \rho \frac{\sqrt{\pi} A_0 e^{A_0^2} \operatorname{erfc}(\pm(v + A_0))}{1 \mp \sqrt{\pi} A_0 e^{A_0^2} \operatorname{erfc}(\pm A_0)}. \tag{7.45}$$

Finally, $\langle X(t) \rangle = A_0 \sqrt{2t}$ with A_0 satisfying the implicit equation

$$\frac{1-\rho g(A_0)}{1-\rho g(-A_0)} = \frac{p_{-1}}{p_1} \tag{7.46}$$

with $g(A_0) = \left[1 - \sqrt{\pi} A_0 e^{A_0^2} \operatorname{erfc} A_0\right]^{-1}$. This solution is the known solution of Refs. [42, 43]. As we showed in the previous chapter, it is the basis of our analysis of the unbinding transition.

Symmetric TP in a step density profile

Remarkably our approach extends to a step density profile. Let us consider that initially, $\langle \eta_{X_0+r} \rangle (t = 0) = \rho_\pm$ for $r \gtrless 0$. This is the configuration studied by Imamura and coworkers [28, 29]. In this case, it is not hard to show that one can define

$$\tilde{w}_r(t) \underset{t\to\infty}{\sim} \rho_v + \Phi\left(\frac{r}{\sqrt{2t}}\right) \tag{7.47}$$

with $v = \operatorname{sign}(r)$, and that the boundary equation (7.38) and velocity equation (7.40) become

$$\Phi'(0^\mu) + 2b_\mu[\rho_\mu + \Phi(0^\mu)] = 0, \tag{7.48}$$

$$p_1(e^\lambda - 1)[1 - \rho_+ - \Phi(0^+)] + p_{-1}(e^{-\lambda} - 1)[1 - \rho_- - \Phi(0^-)] = 0. \tag{7.49}$$

The bulk equation (7.37) and the large distance limit (7.39) are left unchanged.

Solving the equations at order λ^0, one obtains successively,

$$\Phi_0(v \gtrless 0) = \pm A_0[\rho_\pm + \Phi_0(0^\pm)]\sqrt{\pi} e^{A^2} \operatorname{erfc}(\pm(v + A_0)), \tag{7.50}$$

$$\rho_\pm + \Phi_0(0^\pm) = \rho_\pm g(\pm A_0), \tag{7.51}$$

$$g(A_0) = \frac{1}{1 - \sqrt{\pi} A_0 e^{A_0^2} \operatorname{erfc} A_0}. \tag{7.52}$$

We consider the velocity equation (7.49) at order λ^0 and we restrict ourselves to the symmetric case $p_1 = p_{-1} = 1/2$,

$$\rho_+ g(A_0) - \rho_- g(-A_0) = 0. \tag{7.53}$$

Finally, using the relation $\operatorname{erfc}(-x) = 2 - \operatorname{erfc} x$, we obtain the following implicit equation on A_0,

$$2A_0\rho_+ = (\rho_- - \rho_+)\left[\frac{e^{-A_0^2}}{\sqrt{\pi}} - A_0 \operatorname{erfc} A_0\right]. \tag{7.54}$$

The average position of the TP is $\langle X(t)\rangle = A_0\sqrt{2t}$. As expected, this result is the one obtained in Ref. [28]. Additionally, our approach gives the profile in the reference frame of the TP, $\langle \eta_{X_t+r}\rangle(t) \sim \rho_v + \Phi_0(r/\sqrt{2t})$ with

$$\Phi_0(v \gtrless 0) = \frac{\pm\sqrt{\pi}A_0 e^{A_0^2}\operatorname{erfc}[\pm(v+A_0)]}{1 \mp \sqrt{\pi}A_0 e^{A_0^2}\operatorname{erfc}(\pm A_0)}. \tag{7.55}$$

Note that hydrodynamic equations similar to ours were already provided in Ref. [43] in the case of an arbitrary initial density profile.

7.5.2 First order without bias

In this subsection, we assume that the TP is unbiased: $p_1 = p_{-1} = 1/2$. Let us expand the correlations [Eq. (7.18)] in powers of λ: $f_{\mu,r}(\lambda,t) = f^{(0)}_{\mu,r}(t) + \lambda f^{(1)}_{\mu,r}(t) + \dots$, and similarly $F_\mu(v,\lambda) = F^{(0)}_\mu(v) + \lambda F^{(1)}_\mu(v) + \dots$ and $G_\mu(v,\lambda) = G^{(0)}_\mu(v) + \lambda G^{(1)}_\mu(v) + \dots$.

It has been shown that the product measures are invariant measures for the SEP [72]. This means that starting from the equilibrium state (annealed initial conditions), the average density is $\langle \eta_i(t)\rangle = \rho$ and the equal time correlations between occupations vanish: $\langle \eta_i(t)\eta_j(t)\rangle = \langle \eta_i(t)\rangle\langle \eta_j(t)\rangle = \rho^2$ for arbitrary $i \neq j$ at arbitrary time. From the definition (7.18), this implies $f^{(0)}_{\mu,r}(t) = 0$ and thus $F^{(0)}_\mu(v) = G^{(0)}_\mu(v) = 0$. This has the remarkable consequence that the bulk equation (7.37) in the hydrodynamic limit can be written exactly at order λ without any correlation term,

$$\Phi_1''(v) + 2v\Phi_1'(v) = 0. \tag{7.56}$$

We used the fact that in the symmetric case, $\langle X(t)\rangle = 0$ thus $b^{(0)}_\mu = 0$. We remark that the exact microscopic equation (7.24) at order λ involves $f^{(1)}_{\mu,r}$ (the correlation between $\eta_{X+\mu}$, η_{X+r} and X) which does not vanish. The microscopic equation at order 1 is not closed.

We now define the variance $\kappa_2(t)$ and its rescaling at large time $\hat{\kappa}_2$,

$$\kappa_2(t) \equiv \langle X^2(t)\rangle - \langle X(t)\rangle^2 \underset{t\to\infty}{\sim} \hat{\kappa}_2\sqrt{2t}. \tag{7.57}$$

One checks that the order 1 of b_μ is $b^{(1)}_\mu = \hat{\kappa}_2/2$. The boundary equation (7.38) at order λ reads

$$\Phi_1'(0^\pm) + \rho\hat{\kappa}_2 = 0. \tag{7.58}$$

And the velocity equation (7.39), expanded at order λ^2 gives

$$\Phi_1(0^+) - \Phi_1(0^-) = 1 - \rho. \tag{7.59}$$

We are now ready to obtain the solution for $\Phi_1(v)$ and $\hat{\kappa}_2$. Equations (7.56) and (7.58), with the addition of the large distance limit [Eq. (7.39)] give

$$\Phi_1(v \gtrless 0) = \mp\frac{\sqrt{\pi}}{2}\Phi_1'(0^\pm)\operatorname{erfc}(\pm v) = \pm\frac{\sqrt{\pi}}{2}\rho\hat{\kappa}_2\operatorname{erfc}(\pm v). \tag{7.60}$$

As $\Phi_1(v) = -\Phi_1(-v)$, Eq. (7.59) gives $\Phi(0^+) = -\Phi(0^-) = (1-\rho)/2$.

Finally the order 1 profiles, defined as

$$\left\langle \eta_{X_t+r} X_t \right\rangle - \left\langle \eta_{X_t+r} \right\rangle \langle X_t \rangle \underset{t\to\infty}{\sim} \Phi_1\left(\frac{r}{\sqrt{2t}}\right) \tag{7.61}$$

are given by

$$\Phi_1(v \gtrless 0) = \pm\frac{1-\rho}{2}\,\mathrm{erfc}(\pm v), \tag{7.62}$$

and the variance is,

$$\hat{\kappa}_2 = \frac{1-\rho}{\rho}\frac{1}{\sqrt{\pi}}, \qquad\qquad \kappa_2 = \frac{1-\rho}{\rho}\sqrt{\frac{2t}{\pi}}. \tag{7.63}$$

This last result is the well-known result first found by Arratia [27]. To the best of our knowledge, the order 1 profiles have not been investigated before. The result of Eq. (7.62), which can be checked in numerical simulations, is new.

A natural question is whether similar results exist at higher orders. We now show that it is indeed the case in both the limits of high and low density.

7.6 High density

7.6.1 Scalings and equations

In the high density limit $\rho \to 1$, the cumulant-generating function is expected to scale as $(1-\rho)$. We write

$$\psi(\lambda,t) \underset{\rho\to1}{\sim} (1-\rho)\check{\psi}(\lambda,t), \qquad B_\mu(\lambda,t) \underset{\rho\to1}{\sim} (1-\rho)\check{B}_\mu(\lambda,t) = (1-\rho)\frac{\partial_t\check{\psi}(\lambda,t)}{e^{\mu\lambda}-1}, \tag{7.64}$$

with $\check{\psi}$ and $\check{B}_\mu$ independent of the density ρ.

The fluctuations of occupation $\delta\eta_r = \eta_r - \langle\eta_r\rangle$ also scale as $(1-\rho)$. Thus, the generalized profiles $\tilde{w}_r$ scale as $(1-\rho)$ while the correlations $f_{\mu,r}$ (between $\eta_{X+\mu}$ and η_{X+r}) scale as $(1-\rho)^2$.

$$\tilde{w}_r \underset{\rho\to1}{\sim} \rho + (1-\rho)\check{w}_r = 1 + (1-\rho)(\check{w}_r - 1), \tag{7.65}$$

$$f_{\mu,r} = \mathcal{O}[(1-\rho)^2]. \tag{7.66}$$

When all the scalings are written, the microscopic equations (7.24)-(7.27) become a closed system independent of ρ,

$$\partial_t\check{w}_r = \frac{1}{2}\Delta\check{w}_r \tag{7.67}$$

$$\partial_t\check{w}_\mu = \frac{1}{2}\nabla_\mu\check{w}_\mu + \check{B}_\nu(t) \tag{7.68}$$

$$\lim_{r\to\pm\infty}\check{w}_r = 0 \tag{7.69}$$

$$\partial_t\check{\psi} = p_1(e^\lambda - 1)(1-\check{w}_1) + p_{-1}(e^{-\lambda}-1)(1-\check{w}_{-1}). \tag{7.70}$$

7.6.2 Microscopic solution

We define the Laplace transform

$$\check{w}_r(u) = \int_0^\infty e^{-ut} w_r(t) dt. \tag{7.71}$$

The bulk and boundary equations become,

$$\frac{1}{2}[\check{w}_{r+1}(u) + \check{w}_{r-1}(u)] - (1+u)\check{w}_r(u) = 0 \tag{7.72}$$

$$\frac{1}{2}\check{w}_{2\nu}(u) - \left(\frac{1}{2}+u\right)\check{w}_\nu(s) + \nu \check{B}_\nu(u) = 0. \tag{7.73}$$

The equation $\alpha^2 - 2(1+u)\alpha + 1 = 0$ has two solutions, but only one satisfies the condition $\alpha^r \underset{r\to\infty}{\to} 0$ imposed by Eq. (7.69). The solution of Eq. (7.72) is

$$\check{w}_r(u) = \gamma_\mu(u)\alpha^{|r|}, \tag{7.74}$$

$$\alpha = 1 + u - \sqrt{(1+u)^2 - 1}, \tag{7.75}$$

where μ is the sign of r. Injecting this expression into the boundary equation (7.73), we obtain (recall that $\alpha^2 - 2(1+u)\alpha + 1 = 0$)

$$\gamma_\mu(u) = \frac{2\check{B}_\mu(u)}{(1+2u)\alpha - \alpha^2} = \frac{2\check{B}_\mu(u)}{1-\alpha} = \frac{2}{1-\alpha}\frac{(\partial_t \check{\psi})(u)}{e^{\mu\lambda}-1}. \tag{7.76}$$

We finally use the velocity equation (7.70) and obtain

$$(\partial_t \check{\psi})(u) = \frac{1}{u}\left[p_1(e^\lambda - 1) + p_{-1}(e^{-\lambda} - 1)\right] - \frac{2(p_1 + p_{-1})\alpha}{1-\alpha}(\partial_t \check{\psi})(u), \tag{7.77}$$

$$(\partial_t \check{\psi})(u) = \frac{1}{u}\frac{1-\alpha}{1+\alpha}[\cosh\lambda - 1 + is\sinh\lambda] = \frac{1}{\sqrt{u(2+u)}}[\cosh\lambda - 1 + is\sinh\lambda], \tag{7.78}$$

with the bias $s = p_1 - p_{-1}$. This expression can be inverted into

$$\partial_t \check{\psi}(t) = e^{-t} I_0(t)[\cosh\lambda - 1 + is\sinh\lambda]. \tag{7.79}$$

We have recovered, by a completely different method, the full solution found by the vacancy approach in Eq. (3.30). As expected, the large time limit is

$$\partial_t \check{\psi}(t) \underset{t\to\infty}{\sim} \frac{1}{\sqrt{2\pi t}}[\cosh\lambda - 1 + is\sinh\lambda]. \tag{7.80}$$

We also obtain the full solution for the generalized profiles $\check{w}_r$,

$$\check{w}_r(u) = \frac{1}{u}\frac{2}{1+\alpha}\left[p_\nu - e^{-\nu\lambda}p_{-\nu}\right]\alpha^{|r|}. \tag{7.81}$$

The small u behavior at constant $r\sqrt{u}$ gives the large time behavior at constant $r/\sqrt{t}$,

$$\check{w}_r(u) \underset{u\to 0}{\sim} \left[p_\nu - e^{-\nu\lambda}p_{-\nu}\right]\frac{e^{-|r|\sqrt{2u}}}{u} \tag{7.82}$$

$$w_r(t) \underset{t\to\infty}{\sim} \left[p_\nu - e^{-\nu\lambda}p_{-\nu}\right]\operatorname{erfc}\left(\frac{|r|}{\sqrt{2t}}\right). \tag{7.83}$$

As expected, the orders λ^0 and λ^1 are consistent with the results at arbitrary density found above. The first three orders of the profiles are checked against numerical simulations in Fig. 7.2

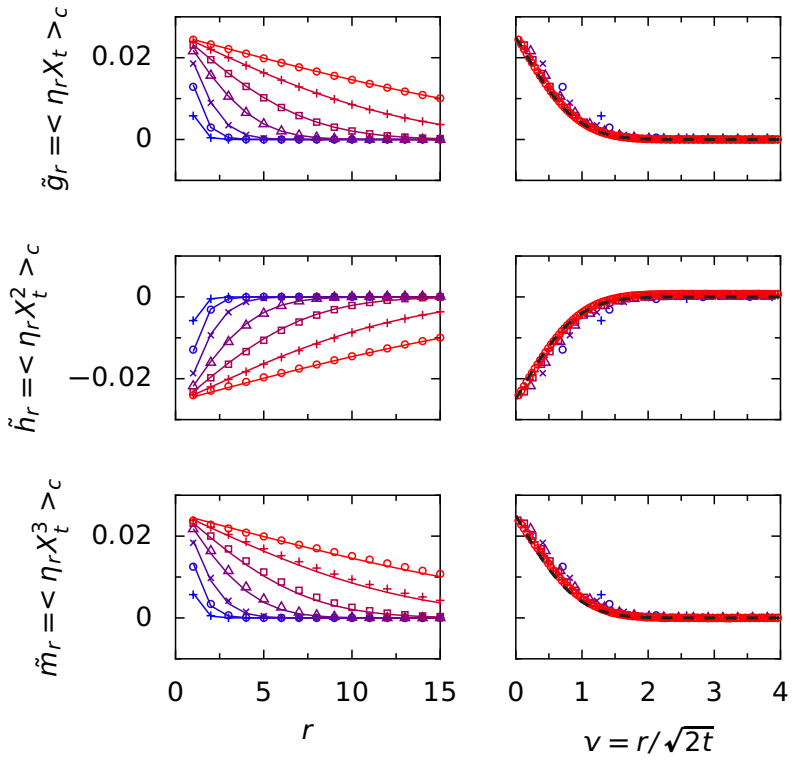

Figure 7.2: Generalized profiles of the symmetric high density SEP ($\rho = 0.95$). The symbols correspond to numerical simulations at times $t = 0.3, 1, 3, 10, 30, 100, 300$ (blue to red). Left: non-rescaled profiles compared to the numerical inversion of Eq. (7.81) (colored lines). Right: rescaled profiles compared to the prediction from Eq. (7.83) (dashed black line).

7.7 Low density limit

7.7.1 Scalings and equations

At first sight, the low density limit ($\rho \to 0$) is harder to define than the high density limit. The reason for that is that it corresponds to a continuous limit. It only makes sense with a rescaling of both space and time: we consider the limit $\rho \to 0$ at constant rescaled position z and constant rescaled time τ with

$$z = \rho r, \qquad \tau = \rho^2 t. \tag{7.84}$$

Note that z is a continuous variable. Since space is rescaled, the displacement of the TP should be considered as $X_t = \hat{X}_t/\rho$, with $\hat{X}_t$ constant. The factors $e^{\lambda X_t}$ of the generating functions should thus be written $e^{\hat{\lambda}\hat{X}_t}$: the limit of low density is taken at constant rescaled generating parameter

$$\hat{\lambda} = \frac{\lambda}{\rho}. \tag{7.85}$$

We can immediately write the scaling limit of the cumulant-generating function $\psi(\lambda, t) = \ln\langle e^{\lambda X_t}\rangle$,

$$\psi(\lambda, t) \underset{\rho\to 0}{\sim} \hat{\psi}\left(\hat{\lambda} = \frac{\lambda}{\rho}, \tau = \rho^2 t\right), \tag{7.86}$$

with $\hat{\psi}$ independent of ρ. The parameters B_μ involved in the equation become

$$B_\mu(\lambda,t) \equiv \frac{\partial_t \psi}{e^{\mu\lambda}-1} \underset{\rho\to 0}{\sim} \frac{\rho^2 \partial_\tau \hat{\psi}}{\mu\rho\hat{\lambda}} = \mu\rho \hat{B}(\hat{\lambda},\tau) \tag{7.87}$$

with $B(\hat{\lambda},\tau) = \partial_\tau\hat{\psi}(\hat{\lambda},\tau)/\hat{\lambda}$. We want to consider the general case of a biased TP with jump probabilities $p_\nu = 1 \pm \nu s$ where $-1 \le s \le 1$ is the bias. The displacement of a unique particle on a discrete line scales as $X_t \sim st$. In the continuous limit, we expect a scaling $\hat{X}_\tau \sim S\tau$ with $\hat{X} = \rho X$ and $\tau = \rho^2 t$. This means that in the low density limit, the bias should scale with the density as

$$s \underset{\rho\to 0}{\sim} \rho S. \tag{7.88}$$

S is an unbounded force in the continuous limit.

Let us now investigate the scalings of $\tilde{w}_r$ defined in Eq. (7.5) and $f_{\mu,r}$ defined in Eq. (7.18). At low density, we expect the fluctuations of occupation to scale like the density, $\delta\eta_r = \eta_r - \langle\eta_r\rangle \propto \rho$. One checks that such fluctuations are involved once in $\tilde{w}_r$ and twice in $f_{\mu,r}$. This leads us to the following scalings,

$$\tilde{w}_r(\lambda,t) \underset{\rho\to 0}{\sim} \rho \hat{W}\left(\hat{\lambda} = \frac{\lambda}{\rho}, z = \rho r, \tau = \rho^2 t\right) \tag{7.89}$$

$$f_{\mu,r}(\lambda,t) \underset{\rho\to 0}{\sim} \rho^2 \hat{\mathscr{F}}_\mu\left(\hat{\lambda} = \frac{\lambda}{\rho}, z = \rho r, \tau = \rho^2 t\right) \tag{7.90}$$

with $\hat{W}$ and $\hat{\mathscr{F}}_\mu$ independent of ρ.

Once the scalings are stated, the equations (7.24)-(7.27) can be written in the limit $\rho \to 0$, in the symmetric case $p_1 = p_{-1} = 1/2$. The bulk equation (7.24) scales as ρ^3, the boundary equation (7.25) and the velocity equation (7.27) both scale as ρ^2. We remark that the bias is not directly involved in the bulk and boundary equations. The continuous equations in the low-density limit are

$$\partial_\tau \hat{W}(\hat{\lambda},z,\tau) = \frac{1}{2}\partial_z^2 \hat{W} + \hat{B}\partial_z \hat{W} + \frac{1}{2}\left\{\partial_z \hat{\mathscr{F}}_1 - \partial_z \hat{\mathscr{F}}_{-1} + \hat{\lambda}\left(\hat{\mathscr{F}}_1 - \hat{\mathscr{F}}_{-1}\right)\right\}, \tag{7.91}$$

$$0 = \frac{1}{2}\partial_z \hat{W}(\lambda,0^\mu,\tau) + \hat{B}\hat{W}(0^\mu) + \frac{1}{2}\left(\hat{\mathscr{F}}_1(0^\mu) - \hat{\mathscr{F}}_{-1}(0^\mu)\right), \tag{7.92}$$

$$\lim_{z\to\pm\infty} \hat{W}(\hat{\lambda},z,\tau) = 1, \tag{7.93}$$

$$\partial_\tau \hat{\psi}(\hat{\lambda},\tau) = \frac{1}{2}\hat{\lambda}^2 - \frac{1}{2}\hat{\lambda}\left[\hat{W}(\lambda,0^+,\tau) - \hat{W}(\lambda,0^-,\tau)\right] + \hat{\lambda}S. \tag{7.94}$$

As usual, this set of equations is not closed and we need an expression for the correlations $\hat{\mathscr{F}}_\mu$. We will see in the following that we are able to solve this issue at large time in the symmetric case.

7.7.2 Large time behavior

We now write the large time scalings ($\tau \to \infty$) of the quantities involved in Eqs. (7.91)-(7.94). They are a particular case of the expressions of subsection 7.4.1. The time derivative of the cumulant-generating function, and the quantity $\hat{B}$ obey

$$\partial_\tau \psi(\hat{\lambda},\tau) \underset{\tau\to\infty}{\sim} \frac{\hat{A}(\hat{\lambda})}{\sqrt{2t}} \qquad\qquad \hat{B}(\hat{\lambda},\tau) = \frac{\partial_\tau \psi(\hat{\lambda},\tau)}{\hat{\lambda}} \underset{\tau\to\infty}{\sim} \frac{\beta(\hat{\lambda})}{\sqrt{2t}}. \tag{7.95}$$

The generalized profiles $\hat{W}$ and the correlations $\hat{\mathscr{F}}_\mu$ obey

$$\hat{W}(\hat{\lambda},z,\tau) = 1 + \hat{\Phi}\left(\hat{\lambda}, \frac{z}{\sqrt{2\tau}}\right) + \mathcal{O}(\tau^{-1/2}) \tag{7.96}$$

$$\hat{\mathscr{F}}_\mu(\hat{\lambda},z,\tau) = \frac{1}{\sqrt{\tau}}\hat{F}_\mu\left(\hat{\lambda}, \frac{z}{\sqrt{2\tau}}\right) + \frac{1}{\tau}\hat{G}_\mu\left(\hat{\lambda}, \frac{z}{\sqrt{2\tau}}\right) + \mathcal{O}(\tau^{-3/2}). \tag{7.97}$$

We remark that the scaling variable can be written in the original set of variables, $v = z/\sqrt{2\tau} = r/\sqrt{2t}$. Another important remark is that the "symmetry relation" (7.34) still holds and gives in this particular case ($\lambda = \rho\hat{\lambda}$),

$$\hat{F}_1(\hat{\lambda}, v) = \hat{F}_{-1}(\hat{\lambda}, v). \tag{7.98}$$

The large time limit of Eqs (7.91)-(7.94) can now be stated. It is a particular case of Eqs. (7.37)-(7.40).

$$\hat{\Phi}''(v) + 2(v+\beta)\hat{\Phi}'(v) + \hat{\lambda}\left[\hat{G}_1(v) - \hat{G}_{-1}(v)\right] = 0, \tag{7.99}$$

$$\hat{\Phi}'(0^\mu) + 2\beta\left[1 + \hat{\Phi}(0^\mu)\right] = 0, \tag{7.100}$$

$$\lim_{v\to\pm\infty} \Phi(v) = 0, \tag{7.101}$$

$$\hat{\Phi}(0^+) - \hat{\Phi}(0^-) = \hat{\lambda} + 2S. \tag{7.102}$$

Surprisingly, the leading order of $\hat{\mathscr{F}}_\mu$ disappears. The only remaining correlation is $\hat{G}_1 - \hat{G}_{-1}$. We now provide a closure relation on this term when $S = 0$ and show that it leads to the known result for the cumulant-generating function.

7.7.3 Closure relation and solution in the symmetric case

We consider the case of an unbiased particle ($S = 0$) and we put forward the following closure relation

$$\hat{G}_1(\hat{\lambda}, v) - \hat{G}_{-1}(\hat{\lambda}, v) = 2\frac{d\beta}{d\hat{\lambda}}\hat{\Phi}'(v). \tag{7.103}$$

We are able to check this relation numerically at the first two lowest orders in $\hat{\lambda}$ (Fig. 7.4). Even though we have no simple interpretation for the moment, we claim that this closure relation gives the correct result both for the cumulant-generating function and for the generalized profiles.

The immediate implication is that Eq. (7.99) becomes closed,

$$\hat{\Phi}''(v) + 2(v+\xi)\hat{\Phi}'(v) = 0, \tag{7.104}$$

with ξ the (rescaled) derivative of the cumulant-generating function with respect to its parameter,

$$\xi \equiv \beta + \hat{\lambda}\frac{d\beta}{d\hat{\lambda}} = \frac{d}{d\hat{\lambda}}(\hat{\lambda}\beta) = \frac{1}{\sqrt{2\tau}}\frac{d\hat{\psi}(\hat{\lambda},\tau)}{d\hat{\lambda}}. \tag{7.105}$$

Now, the equations (7.104), (7.100) and (7.101) can be solved without much difficulty and one obtains

$$\hat{\Phi}(v \gtrless 0) = \frac{\pm\beta}{\pi^{-1/2}e^{-\xi^2} \mp \beta\,\mathrm{erfc}(\pm\xi)}\,\mathrm{erfc}(\pm(v+\xi)). \tag{7.106}$$

And finally, Eq. (7.102), with $S = 0$, leads us to an implicit equation for β and ξ,

$$\beta\left(\frac{\mathrm{erfc}(\xi)}{\pi^{-1/2}e^{-\xi^2} - \beta\,\mathrm{erfc}(\xi)} + \frac{\mathrm{erfc}(-\xi)}{\pi^{-1/2}e^{-\xi^2} + \beta\,\mathrm{erfc}(-\xi)}\right) = \hat{\lambda}. \tag{7.107}$$

Since β and ξ are expressed in terms of the cumulant-generating function, the latter is now fully characterized. More precisely, we define the cumulants κ_n and the rescaled cumulants $\hat{\kappa}_n$ as

$$\psi(\lambda,t) \equiv \sum_{n=1}^{\infty} \frac{\lambda^n}{n!}\kappa_n(t) \qquad\qquad \hat{\psi}(\hat{\lambda},\tau) \equiv \sum_{n=1}^{\infty} \frac{\hat{\lambda}^n}{n!}\hat{\kappa}_n\sqrt{2\tau}. \tag{7.108}$$

Since the two expressions are equal, we have $\kappa_n(t) = \rho^{1-n}\hat{\kappa}_n\sqrt{2t}$. From their definitions, the expansions of β and ξ in powers of $\hat{\lambda}$ also give the rescaled cumulants,

$$\beta \equiv \frac{1}{\sqrt{2\tau}}\frac{\hat{\psi}(\hat{\lambda},\tau)}{\hat{\lambda}} = \sum_{n=0}^{\infty}\frac{\hat{\lambda}^n}{(n+1)!}\hat{\kappa}_{n+1}, \qquad \xi \equiv \frac{1}{\sqrt{2\tau}}\frac{d\hat{\psi}(\hat{\lambda},\tau)}{d\hat{\lambda}} = \sum_{n=0}^{\infty}\frac{\hat{\lambda}^n}{n!}\hat{\kappa}_{n+1}. \tag{7.109}$$

These expressions can be injected into Eq (7.107) to obtain the cumulants order by order,

$$\hat{\kappa}_2 = \frac{1}{\sqrt{\pi}}, \qquad\qquad \hat{\kappa}_4 = \frac{3(4-\pi)}{\pi^{3/2}}, \tag{7.110}$$

$$\hat{\kappa}_6 = \frac{15(68-30\pi+3\pi^2)}{\pi^{5/2}}, \qquad \hat{\kappa}_8 = \frac{21(10912-6840\pi+1320\pi^2-75\pi^3)}{\pi^{7/2}}. \tag{7.111}$$

The cumulants are $\kappa_n(t) = \rho^{1-n}\hat{\kappa}_n\sqrt{2t}$. These are exactly the coefficients known in the literature for interacting point-like particles on a line [41, 44, 45], a model which is equivalent to the low density SEP.

Furthermore, a lengthy and tricky computation shows that Eq. (7.107) is equivalent to the parametrization obtained by Sadhu and Derrida [41]:

$$\lambda = \frac{\rho}{2}\left(\sqrt{h(-\xi)}-\sqrt{h(\xi)}\right)\left[\frac{\operatorname{erfc}(\xi)}{\sqrt{h(\xi)}}+\frac{\operatorname{erfc}(-\xi)}{\sqrt{h(-\xi)}}\right] \tag{7.112}$$

$$\psi(\lambda,t) = \sqrt{2t}\frac{\rho}{4}\left(\sqrt{h(\xi)}-\sqrt{h(-\xi)}\right)^2\left[\operatorname{erfc}(\xi)\sqrt{\frac{h(-\xi)}{h(\xi)}}+\operatorname{erfc}(-\xi)\sqrt{\frac{h(\xi)}{h(-\xi)}}\right] \tag{7.113}$$

with $h(\xi) = \int_{\xi}^{\infty} dy\,\operatorname{erfc}(y)$. The first equation is an implicit equation on ξ (which is the same quantity as in our approach) and the second one gives the expression of the cumulant-generating function.

At the end of the day, we have found a new approach that starts from the master equation and we offered a closure relation. This approach enables us to recover the known results for the cumulants of the low density SEP. But importantly, we also obtain expressions for the generalized profiles,

$$\tilde{w}_r(\lambda,t) \equiv \sum_{n=0}^{\infty}\frac{\lambda^n}{n!}\langle \eta_{X_t+r}(X_t)^n\rangle_c \underset{\substack{\rho\to 0\\ t\to\infty}}{\sim} \rho\hat{\Phi}\left(\hat{\lambda}=\frac{\lambda}{\rho}, \nu=\frac{r}{\sqrt{2t}}\right) \equiv \sum_{n=0}^{\infty}\frac{\lambda^n}{n!}\rho^{1-n}\hat{\Phi}^{(n)}(\nu) \tag{7.114}$$

where $\langle\bullet\rangle_c$ is a multi-variable cumulant. From Eq. (7.106), the lowest orders are

$$\hat{\Phi}^{(1)}(\nu) = \frac{1}{2}\operatorname{erfc}\nu, \tag{7.115}$$

$$\hat{\Phi}^{(2)}(\nu) = \frac{1}{2}\operatorname{erfc}\nu - 2\frac{e^{-\nu^2}}{\pi}, \tag{7.116}$$

$$\hat{\Phi}^{(3)}(\nu) = \frac{3}{\pi^{3/2}}\left[(2\nu-\sqrt{\pi})e^{-\nu^2}+\sqrt{\pi}\operatorname{erfc}\nu\right], \tag{7.117}$$

$$\hat{\Phi}^{(4)}(\nu) = -\frac{1}{2\pi^2}\left[(128-24\pi+24\sqrt{\pi}\nu+32\nu^2)e^{-\nu^2}+3\pi(\pi-8)\operatorname{erfc}\nu\right]. \tag{7.118}$$

We are able to check these expressions in numerical simulations.

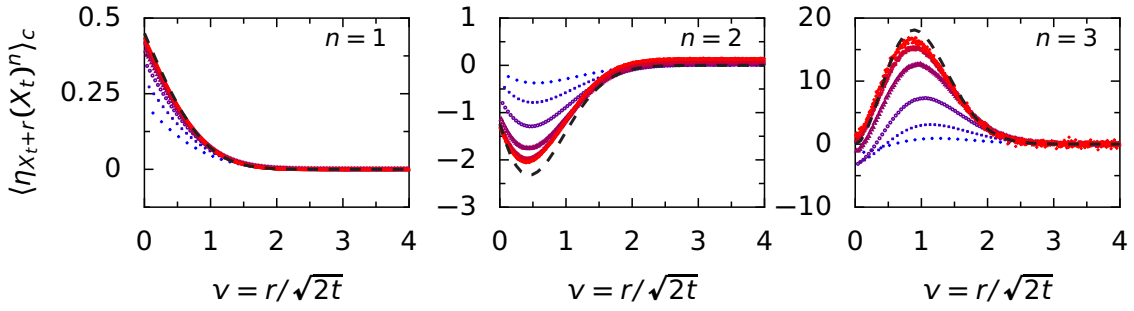

Figure 7.3: Rescaled generalized profiles of the low density SEP ($\rho = 0.1$). The cumulants come from the expansion (7.114). The symbols are the results of numerical simulations at $t = 30, 100, 300, 1000, 3000, 10000$ (blue to red). The dashed black lines are the predictions from Eqs. (7.115)-(7.117) with a correcting factor $1-\rho = 0.9$. We indeed expect such a factor to hold at arbitrary density for the profiles, in the same way that it holds for the cumulants [28]. The density $\rho = 0.1$ is a compromise to have a reasonable time scale for convergence $t_{\text{conv}} \sim \rho^{-2}$. The simulation corresponds to a system of size 5000 (500 particles), 10^9 repetitions were performed.

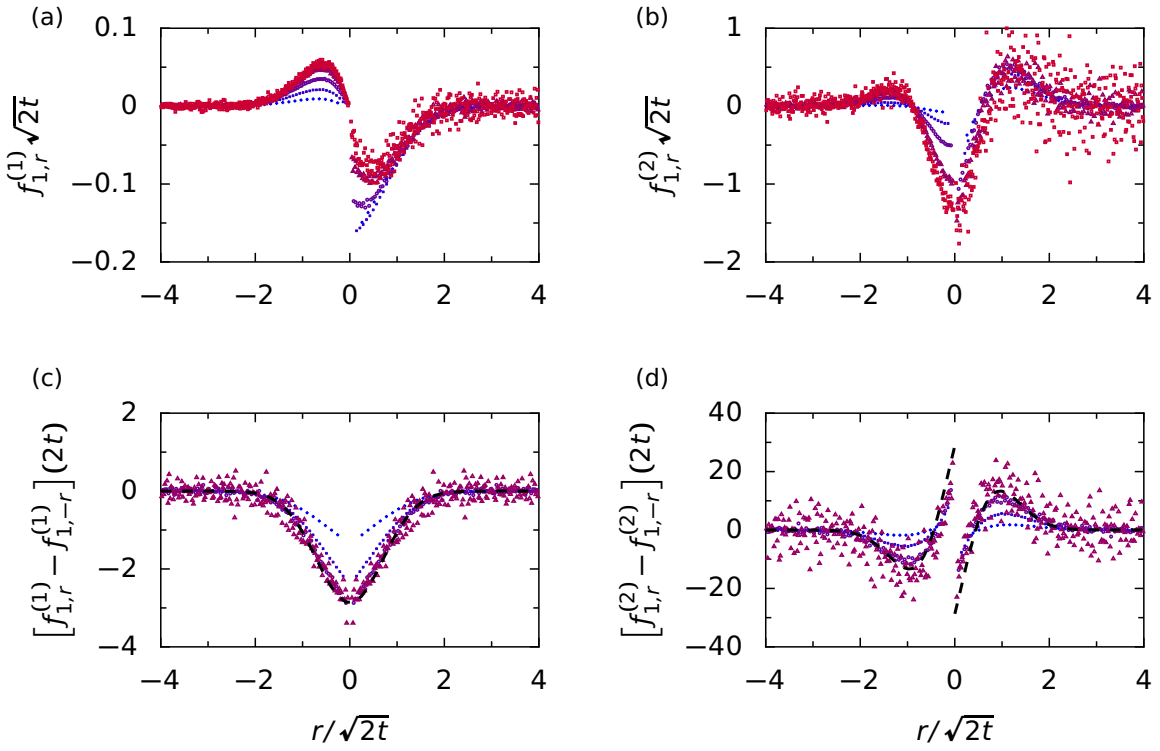

Figure 7.4: Correlations of the low density SEP, $f_{\mu,r}(\lambda, t) = \lambda f^{(1)}_{\mu,r}(t) + (\lambda^2/2) f^{(2)}_{\mu,r}(t) + \ldots$ [Eq. (7.18)]. The parameters, including the times corresponding to the colors, are the same as Fig. 7.3. (a) and (b) Rescaled first and second orders of the correlations. Since $f_{1,r}(\lambda) = f_{-1,-r}(-\lambda)$, the symmetry relation (7.98) is verified numerically at large time ((anti-)symmetry between $v > 0$ and $v < 0$). (c) and (d) Rescaled difference $f_{1,r} - f_{1,r}$ for the first and second orders. From the symmetry (7.98) this difference is of order t^{-1}. The dashed black lines are the predictions corresponding to the closure relation (7.103) with the second cumulant given by Eq. (7.110) and the profiles by Eqs. (7.115)-(7.116) (with the $1-\rho$ prefactor used in Fig. 7.3).

7.8 Variance of generic single-file processes

Let us now turn to generic single-file processes. We say a few words about the fluctuating hydrodynamics framework, first introduced by Spohn [46] and used for instance in Refs. [45,47]. Any single-file system may be described at large distance and large time by two coefficients only, the diffusion coefficient $D(\rho)$ and the mobility $\sigma(\rho)$. These coefficients may be computed from the microscopic details [46] and are related to fluxes at the macroscopic level. For the SEP, the diffusion coefficient is $D(\rho)=1/2$ and the mobility is $\sigma(\rho)=\rho(1-\rho)$. The fluctuating hydrodynamics equation for the density field $\rho(x,t)$ at large distance and large time is

$$\frac{\partial \rho}{\partial t}(x,t)=\frac{\partial}{\partial x}\Big[D(\rho)\rho(x,t)+\sqrt{\sigma(\rho)}\eta(x,t)\Big] \tag{7.119}$$

where $\eta(x,t)$ is a local unitary Gaussian noise. The position X_t of a tagged particle initially at the origin is expressed implicitly using the conservation of the number of particles on the right:

$$\int_{X_t}^{\infty} dx\rho(x,t)=\int_0^{\infty} dx\rho(x,0). \tag{7.120}$$

We now suggest that our approach of subsection 7.5.2 can be extended for a generic single-file system characterized by its diffusion coefficient and its mobility. We focus on a single TP which is not biased. We define the generalized profile of order 1 as the correlation between the displacement of the TP and the density field in the reference frame of the TP,

$$\tilde{g}(x,t)\equiv\langle\rho(X_t+x)X_t\rangle-\langle\rho(X_t+x)\rangle\langle X_t\rangle. \tag{7.121}$$

At large time, this profile is assumed to scale as

$$\tilde{g}(x,t)\underset{t\to\infty}{\sim}\Phi_1\left(\frac{x}{\sqrt{2t}}\right). \tag{7.122}$$

Without attempting to provide a rigorous derivation, we postulate that Φ_1 follows the hydrodynamic equations below, that are similar to Eqs. (7.37)-(7.40).

$$D(\bar{\rho})\Phi_1''(v)+v\Phi_1(v)=0, \tag{7.123}$$
$$D(\bar{\rho})\Phi_1'(0^{\pm})=-\bar{\rho}\hat{\kappa}_2, \tag{7.124}$$
$$\Phi_1(\pm\infty)=0, \tag{7.125}$$
$$\Phi_1(0^+)-\Phi_1(0^-)=\frac{\sigma(\bar{\rho})}{2\bar{\rho}D(\bar{\rho})}, \tag{7.126}$$

with $\bar{\rho}$ the average density of the system, and $\hat{\kappa}_2=\langle X_t^2\rangle/\sqrt{2t}$. By symmetry, the last equation gives $\Phi_1(0^+)=-\Phi_1(0^-)=\sigma(\bar{\rho})/(4\bar{\rho}D(\bar{\rho}))$. The solution of the bulk and boundary equations is

$$\Phi_1(v\gtrless 0)=\mp\sqrt{\frac{\pi D(\bar{\rho})}{2}}\Phi_1'(0^{\pm})\operatorname{erfc}\left(\frac{\pm v}{\sqrt{2D(\bar{\rho})}}\right)=\pm\sqrt{\frac{\pi D(\bar{\rho})}{2}}\rho\hat{\kappa}_2\operatorname{erfc}\left(\frac{\pm v}{\sqrt{2D(\bar{\rho})}}\right). \tag{7.127}$$

Finally, from the value of $\Phi_1(0^{\pm})$, the profile reads

$$\Phi_1(v\gtrless 0)=\pm\frac{\sigma(\bar{\rho})}{4\bar{\rho}D(\bar{\rho})}\operatorname{erfc}\left(\frac{\pm v}{\sqrt{2D(\bar{\rho})}}\right) \tag{7.128}$$

and the solution for the variance is found to be

$$\langle X_t^2 \rangle = \hat{\kappa}_2 \sqrt{2t} = \frac{\sigma(\bar{\rho})}{\bar{\rho}^2} \sqrt{\frac{t}{\pi D(\bar{\rho})}}. \tag{7.129}$$

This result is the known result of Ref. [45] for the variance of a generic single-file system.

Further work should attempt to make sense rigorously of the hydrodynamic equations (7.123)-(7.126) for the profiles of order 1. Another interesting point would be to generalize the full hydrodynamic equations (7.37)-(7.40) (at all orders) to generic single-file systems.

7.9 Conclusion

Obtaining the probability law of a tagged particle in the SEP at arbitrary density, or in a given single-file system, is a hard problem that has been tackled so far using macroscopic fluctuation theory [45,47] or Bethe Ansatz methods [28,29]. In this chapter, we introduced a new approach relying on generalized density profiles, that is to say correlations between the displacement of the TP and the density field in the reference frame of the TP. The interest of these generalized profiles lies in the fact that their values around the origin give the cumulant-generating function of the displacement of the TP [Eq. (7.11)]. Moreover, starting from the master equation of the problem, one can derive a bulk and a boundary equations for the generalized profiles. These equations are not closed and involve higher order correlations. We used a decoupling approach to write these correlations in a way that creates an "advection" term in the equations with a coefficient B_μ closely related to the cumulant-generating function. In some limit cases, the remaining correlations, called $f_{\mu,r}$, either vanish or can be determined. In addition to the microscopic equation, we also wrote exact hydrodynamic equations valid at large distance and large time that immediately focus on the anomalous large-time features.

The first cases in which the correlations vanish are the lowest orders of the generalized profiles. For the density profile related to a biased TP, we recover (and prove) the equations that were studied in the previous chapter and that give the displacement of the TP. For an unbiased TP, the correlations involved for the order 1 of the profiles also vanish and we recover the well-known result for the variance of the SEP at arbitrary density. A case that can be solved completely is the SEP at high density: the correlations vanish at all orders at any time and we obtain the cumulant-generating function derived in Chap. 3. The low-density case can also be solved by postulating a closure relation at large time. We recover the known result for the cumulant-generating function and obtain analytical expression for the generalized profiles at all orders. Finally, one can postulate generic hydrodynamic equations for the order 1 profiles of single-file systems. These equations enable to recover the variance of an arbitrary single-file system.

We believe that the approach introduced in this chapter can be the starting point of further studies. It would be interesting to investigate the meaning and the justification of several points, namely the decoupling approach and the closure relation found at low density. Another goal would be to find the expressions of the generalized profiles that are associated with the generating function of a TP in the SEP found by Imamura, Sasamoto and Mallick [28,29]. The extension to generic single-file systems also needs further work (justification, and equations at higher orders). Finally, it would be interesting to investigate if our approach also extends to the problem of several TPs studied in the previous chapters.

Part II

Correlations of driven and active bidimensional systems

Introduction

The first part of this thesis was dedicated to the study of correlations in single-file systems and in particular in the SEP. We highlighted the fact that such observables give us key insights into the anomalous behavior of such systems in which the motion of any given particle is highly dependent on what the others do. The importance of correlations is of course not limited to one-dimensional systems. Indeed a large part of liquid theory [1] is dedicated to the characterization of the pair correlation function $g(r)$. This function has the advantage of being experimentally measurable and can be related to macroscopic observables such as the compressibility and the pressure. We will see in this part that such correlation functions can also be used to characterize out-of-equilibrium systems where particles are driven.

The two major cases that we consider are driven binary mixtures (DBMs) in which two species of particles are driven in opposite directions by an electric field, and active Brownian particles (ABPs) that self-propel along their orientation, which is diffusive. In both cases, we will see that the correlation function becomes anisotropic: one writes $g(x_\parallel, \mathbf{x}_\perp)$ with $x_\parallel$ and $\mathbf{x}_\perp$ the directions respectively parallel and perpendicular to the motion of the particles. Two questions arise. What is the spatial structure of the correlations? And how do the correlations decay at large distance? The spatial structure is a key indicator of the collective effects in the system. For DBMs we show that the structure is an indication of "laning": particles of the same species tend to align with each other. And for ABPs, we uncovered a striking winged shape at high activity. The matter of the decay of the correlations is well known in equilibrium statistical physics for phase transitions [20]. For instance the correlation $C(r, T)$ of the Ising model at temperature T decays exponentially with a correlation length ξ below (or above) the critical temperature while it exhibits a scale-free power-law decay at the critical temperature

$$C_{\text{Ising}}(r, T \neq T_c) \propto e^{-r/\xi}, \qquad C_{\text{Ising}}(r, T = T_c) \propto r^{-d+2-\eta}.$$

These two scalings are typical of what one could call normal (exponential) and anomalous (algebraic) behaviors of the correlation function. In the two driven systems that are considered, we will uncover interesting power-law decays of the correlations. Moreover, we will see that these anomalous decays are associated with scaling forms in the structure of the correlations $g(x_\parallel, \mathbf{x}_\perp)$.

The starting point of our approach is the Dean equation [58], an exact equation for the density field of pairwise interacting particles. As it is non-linear and involves multiplicative noise, it is difficult to deal with. But we will see that it can be linearized around a homogeneous density profile. This gives results valid in a weak-interaction limit and we will see that some of these results can be generalized to arbitrary interactions.

In Chapter 8, we introduce our framework for a passive liquid. We derive the Dean equation [58] for the density field and linearize it around a homogeneous density. This enables us to obtain an expression for the pair correlation $g(r)$. This expression is identical to the one obtained with the well-known random phase approximation [1].

Chapter 9 focuses on a first instance of out-of-equilibrium system: a driven binary mixture in which particles belonging to two different species are driven in opposite directions by an external electric field. A Dean equation can be computed and linearized. This gives anisotropic pair correlations, both intra-species and inter-species, that are quantitatively correct in a regime of weak interactions. Our main finding is that these pair correlations satisfy a scaling form which has a diffusive scaling and is associated with a power-law decay in the direction of the drive. Numerical simulations show that these scalings and the associated function still hold outside of the validity regime of our theory.

The next instance of out-of-equilibrium system is active Brownian particles (ABPs), a paradigmatic model of active matter that we study in Chapter 10. These interacting particles self-propel at a constant velocity along their orientation and undergo both translational and rotational diffusion. As in the previous chapter, a Dean equation is computed and linearized. In addition to this weak interaction limit, we focus on a dilute system. This enables us to obtain a linear equation satisfied by the two-point position-orientation correlation functions. A numerical resolution of this equation is in agreement with the numerical simulations. At high activity, a striking non-trivial winged structure is observed for the correlations. Furthermore the equation leads to analytical results in the three limits of small velocity, rotational diffusion and transitional diffusion. Strikingly the two limits of high activity (low rotational diffusion and low translation diffusion) give rise to two distinct scaling forms for the correlations that both describe a type of wings and agree with the numerical simulations.

Finally, Chapter 11 is dedicated to the experiments performed in Takeuchi laboratory in the University of Tokyo. Electrophoretic Janus particles, which are a good experimental realization of active Brownian particles are created and observed with a microscope equipped with a camera. The experimental pair correlation functions are computed and the winged structure characteristic of the high activity regime are observed. Although a quantitative agreement is out-of-reach, these findings prove that the theory developed in Chapter 10 gives a very good insight into the system.

Chapter 8

Framework for a passive liquid

Contents

8.1 Introduction

The aim of statistical physics is, if we quote the title of a standard textbook by Balian [22], to go "From Microphysics to Macrophysics"[1]. That is to say to explain the macroscopic properties of a system from its microscopic statistics or laws of motion. Standard examples for classical and quantum interacting systems, and the study of phase transitions can be found in classic textbooks [20–23]. Historically, the focus was put on the limit cases of solid and gas states. Solids in which a strong potential energy maintains the atoms in a crystalline structure, are usually approached first as an assembly of independent quantum harmonic oscillators (Einstein model), with the addition of the Debye approximation at low temperature (Ref. [21], complément III.E). Deviations, in particular due to the crystalline structure, are computed with respect to this reference state. On the other hand, in gases it is the kinetic energy that is dominant, and in first approximation the interactions are neglected, leading to the well-known ideal gas [20, 21]. A possible refinement is to derive the van der Waals equation from carefully chosen approximations (Ref. [23], 5.3) from which one may explain the liquid-gas transition. A more general approach

[1] Original French title: *Du microscopique au macroscopique*.

is to perform an expansion at small density ρ known as the virial expansion [1, 20, 23] in which the pressure P is found to be given by

$$\frac{P}{k_B T} = \rho + B_2(T)\rho^2 + B_3(T)\rho^3 + \dots \tag{8.1}$$

where the coefficients B_n can be expressed in terms of the pair potential $V(r)$.

Liquid theory, in which roughly speaking, kinetic and potential energy have the same order of magnitude, remained a challenge for a long time[2]. A key point was to obtain a quantitative prediction for the pair correlation $g(r)$ of a given liquid. The remarkable book by Hansen and McDonald presents the advances in the domain [1]. Most of the framework is based on a density field theory of which we give some crumbs in Appendix C. The virial expansion and other diagramatic expansions are relevant. But important cases include carefully drafted closure relations such as the random-phase approximation (RPA, see Appendix C), or the Percus-Yevick approximation that is successful for strong repulsive short-range potentials.

The approach of Hansen and McDonald (Ref. [1], chap 2), based on statistical ensembles, holds for equilibrium systems. To compute the correlations in an out-of-equilibrium system (or to compute time correlations of equilibrium systems), one needs to start from the microscopic dynamics of the system. In this chapter, we follow the approach of Dean [58] and derive an exact stochastic equation for the density field of a liquid system. The price to pay for the exactness of the Dean equation is that it is non-linear and involves a multiplicative noise. Both problems can be removed by resorting to an approximation of linearization. We show that this approximation gives a prediction for the pair correlations that is identical to the RPA.

A crucial point to keep in mind is that we will see in the next chapters that our approach extends for out-of-equilibrium systems, something that is unreachable by usual density functional theory.

8.2 Exact Dean equation for interacting passive particles

8.2.1 Coupled Langevin equations

We follow closely the original derivation of Dean [58] of a stochastic equation for the density field of interacting particles, starting from microscopic equations. We consider a fluid composed of N identical particles in dimension d (in this section, the reader may assume that $d = 3$). Particle i is at position $\mathbf{X}_i(t)$ at time t and is subjected to several effects listed below.

- Particles are subjected to thermal noise. We model it by a Gaussian white noise with a diffusion constant D_0. Formally, N d-dimensional independent Gaussian noises $\{\boldsymbol{\eta}_i(t)\}_{i=1}^N$ are associated with the particles and their first two moments are given by

$$\langle \eta_i^\mu(t) \rangle = 0, \tag{8.2}$$
$$\langle \eta_i^\mu(t)\eta_j^\nu(t') \rangle = 2D_0\delta_{i,j}\delta^{\mu,\nu}\delta(t-t'), \tag{8.3}$$

  where i, j are particle indices, $\mu, \nu \in \{1, \dots, d\}$ denote spatial coordinates, $\delta_{i,j}$ and $\delta^{\mu,\nu}$ are Kronecker deltas and $\delta(t)$ is the Dirac delta function.

[2] And at that time the LPTMC was called LPTL (Laboratoire de Physique Théorique des Liquides).

- Particles interact with each other via an arbitrary spatial potential $V(\mathbf{x}) = V(\|\mathbf{x}\|)$ that is assumed to be isotropic and to satisfy $\nabla V(\mathbf{0}) = 0$. The total interaction energy of the system is

$$E_{\text{int}} = \sum_{i=1}^{N} \sum_{j=1}^{i-1} V(\mathbf{X}_i - \mathbf{X}_j) \tag{8.4}$$

  and the force acting on particle i is $(-\nabla_i E_{\text{int}})$, with ∇_i the gradient with respect to $\mathbf{X}_i$.

- For completeness, we consider an external forcing field $\varphi(\mathbf{x})$ that varies in space but is the same for all particles and is independent of time. The resulting force on particle i is $(-\nabla_i \varphi(\mathbf{X}_i))$. We will drop this term in the next section.

- For simplicity, the mobility (velocity to force ratio) is set to 1 for all the particles.

At the end of the day, the time evolution of the positions $\{\mathbf{X}_i(t)\}$ of the particles is given by the following N coupled Langevin equations.

$$\frac{d\mathbf{X}_i}{dt} = -\sum_{j=1}^{N} \nabla_i V(\mathbf{X}_i(t) - \mathbf{X}_j(t)) - \nabla_i \varphi(\mathbf{X}_i) + \boldsymbol{\eta}_i(t) \tag{8.5}$$

We used the assumption $\nabla V(\mathbf{0}) = 0$ to include the term i in the sum. The equations (8.5) are the basis for numerical simulations of the system.

For the following computation it is convenient to use stochastic calculus within the Itô formalism [73]. Defining the Wiener process $\mathbf{B}_i(t)$ as

$$\mathbf{B}_i(t) = \int_0^t \boldsymbol{\eta}_i(t) dt, \tag{8.6}$$

we are able to rewrite Eq. (8.5) in terms of differential elements,

$$d\mathbf{X}_i = -\left(\sum_{j=1}^{N} \nabla_i V(\mathbf{X}_i(t) - \mathbf{X}_j(t)) + \nabla_i \varphi(\mathbf{X}_i) \right) dt + d\mathbf{B}_i, \tag{8.7}$$

$$(d\mathbf{X}_i)^2 = (d\mathbf{B}_i)^2 = 2D_0 dt. \tag{8.8}$$

8.2.2 Derivation of the Dean equation

A key step is to define the local fluctuating density $\rho(\mathbf{x}, t)$ of the fluid at position $\mathbf{x}$ at time t. We write $\rho(\mathbf{x}, t)$ as the sum of localized densities $\rho_i(\mathbf{x}, t)$ associated with each particle,

$$\rho(\mathbf{x}, t) \equiv \sum_{i=1}^{N} \rho_i(\mathbf{x}, t), \qquad \rho_i(\mathbf{x}, t) \equiv \delta(\mathbf{X}_i(t) - \mathbf{x}). \tag{8.9}$$

$\delta(\mathbf{x})$ is the Dirac delta function. Our goal is to compute the time evolution of $\rho(\mathbf{x}, t)$. Using the theory of distributions, we consider a test function f that is smooth and decays fastly. We can write

$$f(\mathbf{X}_i(t)) = \int d\mathbf{x} f(\mathbf{x}) \rho_i(\mathbf{x}, t). \tag{8.10}$$

Moreover, the Itô formula [73] reads

$$df(\mathbf{X}_i) = \nabla f \cdot d\mathbf{X}_i + \frac{1}{2}\nabla^2 f (d\mathbf{X}_i)^2 \tag{8.11}$$

with the gradient and Laplacian terms

$$[\nabla f](\mathbf{X}_i(t)) = \int d\mathbf{x}[\nabla f(\mathbf{x})]\rho_i(\mathbf{x},t), \qquad [\nabla^2 f](\mathbf{X}_i(t)) = \int d\mathbf{x}[\nabla^2 f(\mathbf{x})]\rho_i(\mathbf{x},t). \tag{8.12}$$

Using Eqs. (8.7), (8.8) and (8.11), we obtain

$$\frac{d}{dt}f(\mathbf{X}_i(t)) = \int d\mathbf{x}\,\rho_i(\mathbf{x},t)\left\{\nabla f \cdot \left(-\sum_{j=1}^{N}\nabla V(\mathbf{x}-\mathbf{X}_j(t)) - \nabla\varphi(\mathbf{x}) + \boldsymbol{\eta}_i(t)\right) + D_0\nabla^2 f\right\}, \tag{8.13}$$

and after some integrations by parts,

$$\frac{d}{dt}f(\mathbf{X}_i(t)) = \int d\mathbf{x}\, f(\mathbf{x},t)\left\{\nabla\left[\rho_i(\mathbf{x},t)\left(\sum_{j=1}^{N}\nabla V(\mathbf{x}-\mathbf{X}_j(t)) + \nabla\varphi(\mathbf{x})\right)\right] - \nabla[\rho_i(\mathbf{x},t)\boldsymbol{\eta}_i(t)] + D_0\nabla^2\rho_i(\mathbf{x},t)\right\}. \tag{8.14}$$

On the other hand, we can simply differentiate ρ with respect to time in the integral.

$$\frac{d}{dt}f(\mathbf{X}_i(t)) = \int d\mathbf{x}\, f(\mathbf{x})\frac{\partial\rho_i}{\partial t}(\mathbf{x},t). \tag{8.15}$$

As f is an arbitrary test function, we obtain an equality between distributions,

$$\frac{\partial\rho_i}{\partial t} = \nabla\left[\rho_i(\mathbf{x},t)\left(\sum_{j=1}^{N}\nabla V(\mathbf{x}-\mathbf{X}_j(t)) + \nabla\varphi(\mathbf{x})\right)\right] - \nabla[\rho_i(\mathbf{x},t)\boldsymbol{\eta}_i(t)] + D_0\nabla^2\rho_i(\mathbf{x},t). \tag{8.16}$$

One notes that using the definition of $\rho(\mathbf{x})$,

$$\sum_{j=1}^{N}\nabla V(\mathbf{x}-\mathbf{X}_j(t)) = \int d\mathbf{y}\rho(\mathbf{y})\nabla V(\mathbf{x}-\mathbf{y}) = (\nabla V * \rho)(\mathbf{x}) = \nabla(V*\rho)(\mathbf{x}) \tag{8.17}$$

with '$*$' denoting the spatial convolution. We can now sum over i and obtain

$$\frac{\partial\rho}{\partial t} = \nabla\left[\rho(\mathbf{x},t)\nabla(V*\rho)(\mathbf{x},t) + \rho(\mathbf{x},t)\nabla\varphi(\mathbf{x})\right] + D_0\nabla^2\rho(\mathbf{x},t) - \sum_{i=1}^{N}\nabla[\rho_i(\mathbf{x},t)\boldsymbol{\eta}_i(t)]. \tag{8.18}$$

We define a global Gaussian noise field $\boldsymbol{\eta}(\mathbf{x},t)$ satisfying $\langle\boldsymbol{\eta}(\mathbf{x},t)\rangle = 0$ and

$$\langle\eta^\alpha(\mathbf{x},t)\eta^\beta(\mathbf{x}',t')\rangle = 2D_0\delta^{\alpha,\beta}\delta(\mathbf{x}-\mathbf{x}')\delta(t-t'). \tag{8.19}$$

Dean remarked [58] that $\left[-\sum_{i=1}^{N}\rho_i(\mathbf{x},t)\boldsymbol{\eta}_i(t)\right]$ is a Gaussian noise that has the same moments as $\left[\rho(\mathbf{x},t)^{1/2}\boldsymbol{\eta}(\mathbf{x},t)\right]$. We can substitute one noise for the other. At the end of the day, we obtain the so-called Dean equation that we choose to write as a conservation equation for the field ρ,

$$\frac{\partial\rho}{\partial t} = -\nabla\cdot\mathbf{J}(\mathbf{x},t), \tag{8.20}$$

$$\mathbf{J}(\mathbf{x},t) = -D_0\nabla\rho(\mathbf{x},t) - \rho(\mathbf{x},t)\nabla(V*\rho)(\mathbf{x},t) - \rho(\mathbf{x},t)\nabla\varphi(\mathbf{x}) + \rho(\mathbf{x},t)^{1/2}\boldsymbol{\eta}(\mathbf{x},t), \tag{8.21}$$

$$\langle\boldsymbol{\eta}(\mathbf{x},t)\boldsymbol{\eta}(\mathbf{x}',t')\rangle = 2D_0\delta(\mathbf{x}-\mathbf{x}')\delta(t-t'). \tag{8.22}$$

This equation is the starting point of our approach. Although we will not use this form in the following, we remark that the flux $\mathbf{J}(\mathbf{x})$ can be written in terms of a functional $H[\rho]$ of the density,

$$\mathbf{J}(\mathbf{x}) = -\rho(\mathbf{x})\nabla\frac{\delta H[\rho]}{\delta\rho(\mathbf{x})} + \rho(\mathbf{x})^{1/2}\boldsymbol{\eta}(\mathbf{x}), \tag{8.23}$$

$$H[\rho] = D_0\int d\mathbf{x}\,\rho(\mathbf{x})\log\rho(\mathbf{x}) + \frac{1}{2}\int d\mathbf{x}\,d\mathbf{y}\,\rho(\mathbf{x})V(\mathbf{x}-\mathbf{y})\rho(\mathbf{y}) + \int d\mathbf{x}\,\rho(\mathbf{x})\varphi(\mathbf{x}). \tag{8.24}$$

The Dean equation (8.20) is exact but the price to pay for this consists in two major technical difficulties. The first one concerns the multiplicative noise ($\sqrt{\rho}\boldsymbol{\eta}$). Although it is well defined in the Itô framework this noise is hard to handle. The second and perhaps more important problem is that the term $\rho\nabla[V*\rho]$ is non-linear in the density. This implies that marginal laws for the density profile, the two-point correlations, etc. all involve higher-order correlations. This hierarchy of equations, that is expected for usual liquids, cannot be closed without resorting to an approximation.

8.2.3 Hierarchy of equations

We define the average density profile $\bar{\rho}(\mathbf{x},t) = \langle\rho(\mathbf{x},t)\rangle$. From the Dean equation (8.20), it satisfies the equation

$$\frac{\partial\bar{\rho}}{\partial t} = D_0\nabla^2\bar{\rho} + \nabla\left[\nabla\varphi(\mathbf{x})\bar{\rho}(\mathbf{x})\right] + \nabla\int d\mathbf{y}\,\nabla V(\mathbf{x}-\mathbf{y})C_e(\mathbf{x},\mathbf{y},t) \tag{8.25}$$

which is not closed as it involves the two-point correlations $C_e(\mathbf{x},\mathbf{y},t) = \langle\rho(\mathbf{x},t)\rho(\mathbf{y},t)\rangle$. Similarly, using the Itô convention and the symmetry $\mathbf{x}\leftrightarrow\mathbf{y}$, these two-point correlations satisfy

$$\frac{\partial C_e(\mathbf{x},\mathbf{y})}{\partial t} = 2D_0\nabla_{\mathbf{x}}^2\left[C_e(\mathbf{x},\mathbf{y}) - \delta(\mathbf{x}-\mathbf{y})\bar{\rho}(\mathbf{x})\right] + \nabla_{\mathbf{x}}\left[\nabla\varphi(\mathbf{x})C_e(\mathbf{x},\mathbf{y})\right] + \nabla_{\mathbf{y}}\left[\nabla\varphi(\mathbf{y})C_e(\mathbf{x},\mathbf{y})\right]$$
$$+ 2\nabla_{\mathbf{x}}\int d\mathbf{z}\,\nabla_{\mathbf{x}}V(\mathbf{x}-\mathbf{z})\left\langle\rho(\mathbf{x})\rho(\mathbf{y})\rho(\mathbf{z})\right\rangle. \tag{8.26}$$

This equation is also not closed since it involves the three-point correlation function. In fact a hierarchy of equations can be generated and the derivative of the n-point correlation involves the $(n+1)$-point correlation. This is very similar to the BBGKY hierarchy in usual density field theory [1, 20].

We shall now put forward our approximation of linearization of the Dean equation. This will enable us to obtain a linear equation with additive noise for which the equations of the correlations will be closed.

8.3 Linearization of the Dean equation

8.3.1 Linear limit

We pointed out that the Dean equation is non-linear, with multiplicative noise. Here, we simplify the problem by linearizing around an homogeneous and constant density $\bar{\rho}$. We write the density field as

$$\rho(\mathbf{x},t) \equiv \bar{\rho} + \bar{\rho}^{1/2}\phi(\mathbf{x},t). \tag{8.27}$$

Our equations will be considered in the large density regime $\bar{\rho} \to \infty$. We wrote that the fluctuations scale as $\bar{\rho}^{1/2}$, so that there are no density-dependent factors in Eq. (8.29). From now on, we assume that there is no external field[3]: $\varphi(\mathbf{x}) = 0$.

The scalings in $\bar{\rho}$ in Eq. (8.20) need to be consistent. This leads us to consider an interaction potential $V(\mathbf{x})$ that decays with the density $\bar{\rho}$ as

$$V(\mathbf{x}) \equiv D_0 \frac{v(\mathbf{x})}{\bar{\rho}}. \tag{8.28}$$

The diffusion coefficient D_0 is here so that $v(\mathbf{x})$ describes the ratio of the potential over the temperature, which is physically relevant.

Ultimately, the limit we consider is a limit of *large density*, $\bar{\rho} \to \infty$, at constant $v(\mathbf{x})$ that is to say *small interactions* ($V \to 0$). The reader may draw a parallel with the well-known Curie-Weiss model for interacting spins. In this mean-field limit of the Ising model, all spins interact with each other – as it is the case for our particles at very high density. And the coupling constant decays with the number of spins – as does our potential with increased density. A consequence of the linear limit is that the field $\rho(\mathbf{x},t)$ becomes Gaussian: we can also call it a *Gaussian limit*.

8.3.2 Linearized Dean equation

Introducing Eqs. (8.27) and (8.28) into the Dean equation (8.20) and keeping only the terms of order $\bar{\rho}^{1/2}$, one obtains the following equation.

$$\frac{\partial \phi}{\partial t}(\mathbf{x},t) = D_0\nabla^2\phi(\mathbf{x},t) + D_0\nabla^2[v * \phi](\mathbf{x},t) - \nabla\cdot\boldsymbol{\eta}(\mathbf{x},t), \tag{8.29}$$

$$\langle \boldsymbol{\eta}(\mathbf{x},t)\boldsymbol{\eta}(\mathbf{x}',t')\rangle = 2D_0\delta(\mathbf{x}-\mathbf{x}')\delta(t-t'). \tag{8.30}$$

This is the linearized Dean equation from which we will derive the correlations. The Gaussian noise $\boldsymbol{\eta}$ is the same as before, but it now appears as an additive noise. Furthermore, the equation is now linear in ϕ. One notes that ϕ is a Gaussian field. We build on this remark below.

We define the Fourier transform $\tilde{f}(\mathbf{k})$ of a function $f(\mathbf{x})$ as

$$\tilde{f}(\mathbf{k}) = \int d\mathbf{x} e^{-i\mathbf{k}\cdot\mathbf{x}} f(\mathbf{x}), \qquad f(\mathbf{x}) = \frac{1}{(2\pi)^d}\int d\mathbf{k} e^{i\mathbf{k}\cdot\mathbf{x}}\tilde{f}(\mathbf{k}). \tag{8.31}$$

We write Eq (8.29) in Fourier space,

$$\frac{\partial \tilde{\phi}}{\partial t}(\mathbf{k},t) = -k^2 D_0[1+\tilde{v}(\mathbf{k})]\tilde{\phi}(\mathbf{k},t) + \tilde{\xi}(\mathbf{k},t), \tag{8.32}$$

with $\xi(\mathbf{k},t)$ a Gaussian noise of vanishing average and of correlation

$$\langle \tilde{\xi}(\mathbf{k},t)\tilde{\xi}(\mathbf{k}',t')\rangle = 2(2\pi)^d D_0 k^2 \delta(\mathbf{k}+\mathbf{k}')\delta(t-t'). \tag{8.33}$$

[3] The linearization around an homogeneous density is not adapted to the problem with an external field. One should try to linearize around the non-interacting profile $\bar{\rho}\exp(-\varphi(\mathbf{x})/D_0)$.

8.3.3 Correlations

The field $\phi(\mathbf{x})$ satisfies the linear equation with additive noise (8.29). It is a Gaussian field, hence it is fully characterized by its average $\langle\phi(\mathbf{x},t)\rangle = 0$, and its correlations $\langle\phi(\mathbf{x},t)\phi(\mathbf{x}',t')\rangle$.

Convergence to equilibrium. In Fourier space, the equation on the average reads

$$\frac{\partial\langle\tilde{\phi}(\mathbf{k},t)\rangle}{\partial t} = -D_0k^2[1+\tilde{v}(\mathbf{k})]\langle\tilde{\phi}(\mathbf{k},t)\rangle. \tag{8.34}$$

The equilibrium solution is $\langle\tilde{\phi}(\mathbf{k},t)\rangle_{\rm eq} = 0$, giving $\langle\phi(\mathbf{x},t)\rangle = 0$. On average, the fluctuations of density vanish, which is what we expect. If we start from an inhomogeneous density field, we see that the convergence towards equilibrium of a given wave vector $\mathbf{k}$ is associated with a decay rate $k^2D_0[1+\tilde{v}(\mathbf{k})] = k^2[D_0+\bar{\rho}\tilde{V}(\mathbf{k})]$.

Equal-time correlations. Let us look at the equal-time two-point correlations $\mathscr{C}(\mathbf{x},\mathbf{x}',t) = \langle\phi(\mathbf{x},t)\phi(\mathbf{x}',t)\rangle$. We study the evolution of its Fourier transform $\tilde{\mathscr{C}}(\mathbf{k},\mathbf{k}',t)$ during a time step Δt using the Itô formalism.

$$\tilde{\mathscr{C}}(\mathbf{k},\mathbf{k}',t+\Delta t) = \tilde{\mathscr{C}}(\mathbf{k},\mathbf{k}',t) + \langle\delta\tilde{\phi}(\mathbf{k},t)\tilde{\phi}(\mathbf{k}',t)\rangle + \langle\tilde{\phi}(\mathbf{k},t)\delta\tilde{\phi}(\mathbf{k}',t)\rangle + \langle\delta\tilde{\phi}(\mathbf{k},t)\delta\tilde{\phi}(\mathbf{k}',t)\rangle, \tag{8.35}$$

where $\delta\tilde{\phi}(\mathbf{k},t)$ is the change of $\tilde{\phi}(\mathbf{k},t)$ during Δt. The computation yields

$$\langle\delta\tilde{\phi}(\mathbf{k},t)\tilde{\phi}(\mathbf{k}',t)\rangle = -k^2\Delta t D_0[1+\tilde{v}(\mathbf{k})]\tilde{\mathscr{C}}(\mathbf{k},\mathbf{k}',t), \tag{8.36}$$

$$\langle\delta\tilde{\phi}(\mathbf{k},t)\delta\tilde{\phi}(\mathbf{k}',t)\rangle = \langle\tilde{\xi}(\mathbf{k},t)\tilde{\xi}(\mathbf{k}',t)\rangle\Delta t = 2(2\pi)^d D_0k^2\delta(\mathbf{k}+\mathbf{k}')\Delta t. \tag{8.37}$$

We deduce that the time evolution of $\tilde{\mathscr{C}}$ is governed by

$$\partial_t\tilde{\mathscr{C}}(\mathbf{k},\mathbf{k}',t) = -\left[\mathbf{k}^2D_0(1+\tilde{v}(\mathbf{k})) + \mathbf{k}'^2D_0(1+\tilde{v}(\mathbf{k}'))\right]\tilde{\mathscr{C}} + 2(2\pi)^d D_0k^2\delta(\mathbf{k}+\mathbf{k}'). \tag{8.38}$$

This closed equation corresponds to the linearized version of Eq. (8.26).

We use the invariance by translation and write the pair correlations in terms of the usual function $h(\mathbf{x})$ [1],

$$h(\mathbf{x},t) = \frac{\langle\rho(\mathbf{0},t)\rho(\mathbf{x},t)\rangle - \bar{\rho}\delta(\mathbf{x})}{\bar{\rho}^2} - 1 = \frac{\mathscr{C}(\mathbf{0},\mathbf{x},t) - \delta(\mathbf{x})}{\bar{\rho}}. \tag{8.39}$$

The $\delta(\mathbf{x})$ term corresponds to the correlation of a given particle with itself. In Fourier space,

$$\tilde{h}(\mathbf{k},t) = \frac{1}{\bar{\rho}}\left(\frac{\tilde{\mathscr{C}}(\mathbf{k},-\mathbf{k},t)}{(2\pi)^d} - 1\right), \tag{8.40}$$

so that the time evolution and the equilibrium solutions are

$$\partial_t\tilde{h}(\mathbf{k},t) = -2k^2\left([D_0+\bar{\rho}\tilde{V}(\mathbf{k})]\tilde{h}(\mathbf{k},t) + \tilde{V}(\mathbf{k})\right), \tag{8.41}$$

$$\tilde{h}_{\rm eq}(\mathbf{k}) = \frac{-\tilde{V}(\mathbf{k})}{D_0+\bar{\rho}\tilde{V}(\mathbf{k})}. \tag{8.42}$$

This result for the pair correlations is the one obtained in liquid theory [1] using the so-called Random-Phase Approximation (RPA), which is also a mean-field approximation. In Appendix C, we detail the steps leading to Eq. (8.42) from the RPA applied to liquid theory.

Two-time correlations. For a complete characterization of the Gaussian process, we define the two-time correlations

$$h_\tau(\mathbf{x},\tau) \equiv \frac{\langle \rho(\mathbf{0},0)\rho(\mathbf{x},\tau)\rangle}{\bar{\rho}^2} - \frac{\delta(\mathbf{x})\delta(\tau)}{\rho} - 1, \tag{8.43}$$

where we assume that the system is equilibrated at time 0. One shows that the time evolution of the Fourier transform is given by

$$\partial_\tau \tilde{h}_\tau(\mathbf{k},\tau) = -D_0 k^2[1+\tilde{v}(\mathbf{k})]\tilde{h}_\tau(\mathbf{k},\tau). \tag{8.44}$$

Using the equilibrium solution at $\tau = 0$, the solution is

$$h_\tau(\mathbf{k},\tau) = \tilde{h}_{\text{eq}}(\mathbf{k}) e^{-D_0 k^2[1+\tilde{v}(\mathbf{k})]\tau} = \frac{-\tilde{V}(\mathbf{k})}{D_0 + \bar{\rho}\tilde{V}(\mathbf{k})} e^{-k^2[D_0+\bar{\rho}\tilde{V}(\mathbf{k})]\tau}. \tag{8.45}$$

Each mode decays with the rate associated with the convergence to equilibrium.

8.3.4 Numerical simulations

Our result for the pair correlation function can be checked against numerical simulations of the coupled Langevin equations (8.5) (without external field) using Brownian dynamics. We use the following isotropic soft-sphere potential,

$$V(\mathbf{x}) = \begin{cases} \frac{\epsilon}{2}(a - \|\mathbf{x}\|)^2 & \text{if } \|\mathbf{x}\| < a \\ 0 & \text{otherwise.} \end{cases} \tag{8.46}$$

This is the potential we will use throughout Part II, it is convenient for several reasons. The fact that it has a finite range allows one to implement efficient simulations (the computation of the interactions has a complexity scaling linearly with the number of particles). It is also a bounded potential which enables us to probe both the weak-interaction and strong-interaction limits. Furthermore, the Fourier transform of $V(\mathbf{x})$ can be expressed analytically in dimensions 2 and 3 and is also finite. The expressions for $a = \epsilon = 1$ are

$$\tilde{V}_{2D}(\mathbf{k}) = \frac{\pi}{k^2}\left[\pi J_1(k)H_0(k) - \pi J_0(k)H_1(k) - 2J_2(k)\right], \tag{8.47}$$

$$\tilde{V}_{3D}(\mathbf{k}) = \frac{4\pi}{k^5}(2k + k\cos k - 3\sin k), \tag{8.48}$$

where J_n and H_n are respectively Bessel and Struke functions. The values at 0 are $\tilde{V}_{2D}(0) = \pi/12$, $\tilde{V}_{3D}(0) = \pi/15$.

We work in a dimensionless system of units by setting $\epsilon = 1$, $a = 1$ and the mobility to 1. At high enough density, the pair correlation function is described quantitatively by the theoretical expression of Eq. (8.42) as shown on Fig. 8.1.

8.3.5 Compressibility and pressure

In a statistical approach, the pressure P is defined as a derivative of the free energy of the system with respect to the volume V. It corresponds both to the thermodynamic pressure and to the

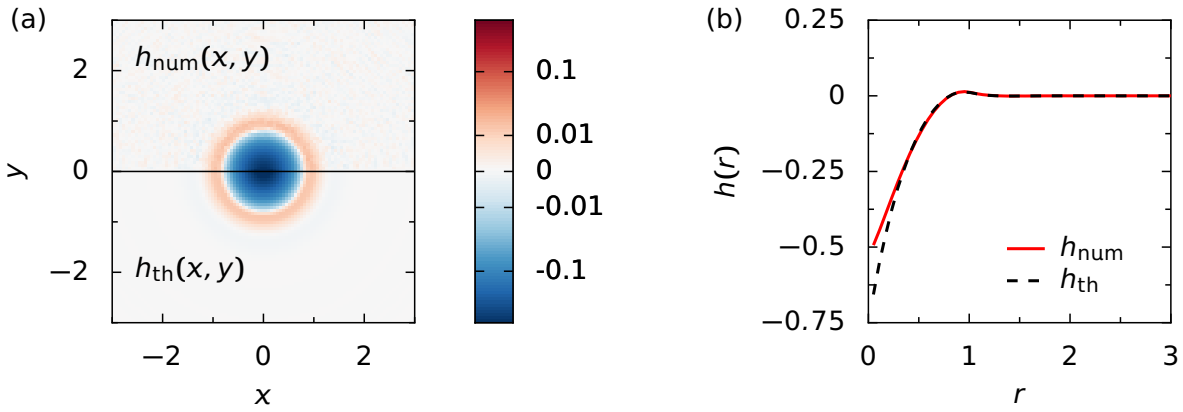

Figure 8.1: Pair correlation function of soft spheres in dimension 2 at density $\bar{\rho} = 2$, with diffusion coefficient $D_0 = 0.5$. (a) $h(\mathbf{x})$ from the simulations (top, 2000 particles) and from the theory from Eq. (8.42) (bottom). (b) Radial component of $h(\mathbf{x}) = h(\|\mathbf{x}\|)$ (red: simulations, black: theory).

pressure applied on the boundaries of a box. The isothermal compressibility χ_T is the thermodynamic quantity quantifying the relative variation of volume associated with a change of pressure at constant temperature,

$$\chi_T \equiv -\frac{1}{V}\left.\frac{\partial V}{\partial P}\right|_T. \tag{8.49}$$

Remarkable results of liquid theory state that both the isothermal compressibility and the pressure can be expressed in terms of the pair correlation $h(\mathbf{r})$ as[4]

$$\bar{\rho} k_B T \chi_T = 1 + \bar{\rho} \int d\mathbf{r}\, h(\mathbf{r}), \tag{8.50}$$

$$\frac{P}{k_B T} = \bar{\rho} - \frac{\bar{\rho}^2}{2d k_B T} \int d\mathbf{r}\, r \frac{dV}{dr} h(\mathbf{r}). \tag{8.51}$$

See for instance Ref. [1], Eqs. (2.5.22) and (2.6.12); or Ref. [20], Eq. (7.21) and Exercise 7.1. One notes that, contrary to the pressure, the expression of the compressibility does not involve the shape of the potential. This opens the door to an experimental estimate of the compressibility from the measurement of the pair correlation function[5]. Note that the pressure equation holds only because we consider pairwise interactions (for three body interactions we would need three-point correlations and so on). This is also be true for the similar expressions that we derive in the next chapters for the effective mobility in binary mixtures and the effective velocity of ABPs .

Let us now see what are the expressions obtained from Eqs. (8.50) and (8.51) in our linearized framework (which gives the results of the RPA approximation). We note that, from the Einstein relation with the mobility set to unity, the diffusion coefficient is $D_0 = k_B T$. The compressibility equation (8.50) involves only the Fourier transform at the origin $\tilde{h}(0)$. From Eq. (8.42), we obtain

$$\bar{\rho} k_B T \chi_T = \left(1 + \frac{\bar{\rho}\tilde{V}(0)}{k_B T}\right)^{-1}. \tag{8.52}$$

[4]The potential $V(\mathbf{r}) = V(r)$ is assumed to be isotropic so that $\int d\mathbf{r}\, r \frac{dV}{dr} = 0$. One can put either $h(\mathbf{r})$ or $g(\mathbf{r})$ in the pressure equation.

[5]The structure factor, which is the Fourier transform of the pair correlations, can be measured by neutron scattering.

The correction compared to non-interacting particles is given by the ratio of the "average strength" of interactions $\bar{\rho}\int d\mathbf{r}\, V(\mathbf{r})$ over the temperature.

In the same spirit, the pressure equation (8.51) can be rewritten in Fourier space. From Eq. (8.42), we obtain

$$\frac{P}{k_B T} = \bar{\rho} + \frac{1}{2d}\int \frac{d\mathbf{k}}{(2\pi)^d}\left(\frac{\bar{\rho}\tilde{V}(\mathbf{k})}{k_B T}\right)\left(\frac{\bar{\rho}\tilde{W}(\mathbf{k})}{k_B T}\right)\left(1+\frac{\bar{\rho}\tilde{V}(\mathbf{k})}{k_B T}\right)^{-1} \tag{8.53}$$

where $\tilde{W}(\mathbf{k})$ is the d-dimensional Fourier transform of $r\frac{dV}{dr}$. The correction to the ideal gas is expressed in terms of the ratio of the potential and the temperature $\bar{\rho}\tilde{V}(\mathbf{k})/(k_B T)$.

8.4 Conclusion

The goal of this chapter was to introduce the framework used in the next two chapters, in the simple case of a passive liquid. We derived the Dean equation and showed that it is hard to deal with it as it is. In particular, it gives rise to a hierarchy of equations for the correlation functions. What can be done is to linearize it around an homogeneous density profile. The equations then become linear and the density field becomes Gaussian. The pair correlations can be computed and one recovers the result of the random phase approximation of liquid theory. This prediction is in quantitative agreement with numerical simulations of dense soft spheres.

In the next two chapters, the framework is extended to two out-of-equilibrium systems: driven binary mixtures and active Brownian particles.

Chapter 9

Binary mixture

Contents

9.1 Introduction

In the previous chapter, we introduced a framework based on a linearization of the Dean equation. This enabled us to recover a well-known approximation of liquid theory. We now reveal the full strength of our approach, namely that it can be extended to out-of-equilibrium systems. Indeed previous studies used a similar framework to probe several systems with external forces: a single driven intruder in a quiescent bath [24], an electrolytic solution in which corrections to the conductivity are computed [2], and a system made of two parallel plates with charged particles in which attractive Casimir forces are evidenced [25]. In this chapter, we aim at characterizing

the correlations in a binary mixture of driven particles (Fig. 9.1). A fraction of the particles are driven by an external force while the others are not driven. Or alternatively, the populations of particles are driven in opposite directions.

This is very reminiscent of pedestrian crowds moving oppositely in a corridor in which collective behavior emerges as people self-organize in lanes moving in a given direction [16]. Understanding such processes is crucial to understand how to design buildings that can be evacuated as fast as possible [15]. The formation of lanes is a robust feature of systems of oppositely driven agents. In physics experiments, it was shown to occur for instance in driven oppositely charged colloids [48] as well as in plasmas [49]. The nature of laning is still debated theoretically, even with very simple dynamics. A German group first concluded, using numerical simulations, that there was a phase transition between a disordered state at small forces and a 'laned' state at high forces [50]. But ten years later, with increased computational power, they discovered that there was only a smooth crossover between the two regimes [51]: the lanes were shown to be of finite size with an exponential scaling with respect to the force. Other numerical simulations in a confined system (narrow channel) concluded that there was a reentrant laning transition in such a system [74]. An effort to obtain theoretical results was made in Ref. [60] by using a numerical integration of a closure of the many-body Smoluchowski equation. A good agreement was found with numerical simulations, in particular the strong anisotropy of the pair correlation functions. The authors argue that the correlations decay as a power-law along the direction of the force (with an exponent between 1 and 2) and that this divergence may be related to a true phase transition (no characteristic length). However their approach is limited to small forces and they argue that more work should be done to characterize the decay of the correlations.

In this chapter, we use the framework introduced previously to characterize analytically the correlations of driven binary mixtures with arbitrary forcing. We indeed find that they decay algebraically along the force, with an exponent $3/2$ in dimension 2 (exponent $(d+1)/2$ in dimension d). This exponent is associated with a scaling function which is related to a diffusion equation. This scaling function is shown to be robust and holds for numerical simulations outside of the validity regime of our approximation, for dilute and hard particles. A by-product of our approach is the computation of the effective mobility of the particles.

The results of this chapter have been published in [P1].

9.2 Theoretical approach

9.2.1 Coupled Langevin equations for driven systems

We consider a system similar to subsection 8.2.1 with external forces applied on the particles.

N particles in dimension d have positions $\{\mathbf{X}_i(t)\}$ at time t. They undergo thermal noise with diffusion constant D_0: $\boldsymbol{\eta}_i(t)$ is a Gaussian white noise having zero average and correlation

$$\langle \eta_i^\mu(t)\eta_j^\nu(t')\rangle = 2D_0\delta_{i,j}\delta^{\mu,\nu}\delta(t-t'). \tag{9.1}$$

The interaction between particles is modeled by an isotropic pair potential $V(\mathbf{x}) = V(\|\mathbf{x}\|)$. As before, the mobility is set to one.

The novelty is that each particle belongs to one of q species. All particles of species $\alpha \in \{1,\dots,q\}$ undergo the same external force $\mathbf{F}_\alpha$. The species of particle i is denoted $\alpha_i \in \{1,\dots,q\}$.

The setup that we have in mind is $q = 2$ with $\mathbf{F}_1 = \mathbf{F}$ and $\mathbf{F}_2 = \mathbf{0}$: this corresponds to an external (electric) field to which only some of the particles are sensitive. A sketch of the system is provided in Fig. 9.1. Alternatively, one may take $\mathbf{F}_1 = \mathbf{F}$ and $\mathbf{F}_2 = -\mathbf{F}$, a setup in which particles

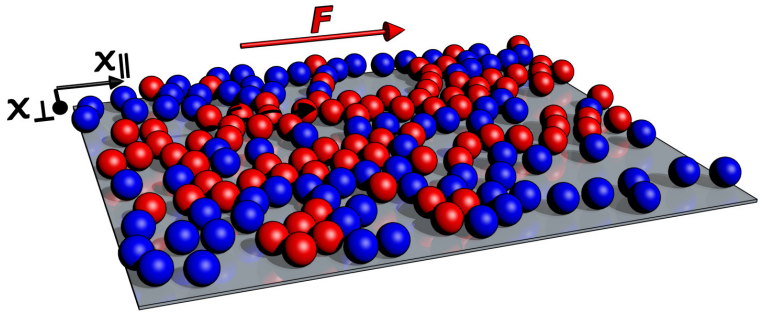

Figure 9.1: Picture of the binary mixture we consider. Red particles (species 1) are driven to the right by a force $\mathbf{F}_1 = \mathbf{F} = F\mathbf{x}_\parallel$ while the blue ones (species two) are not driven $\mathbf{F}_2 = \mathbf{0}$. All particles are diffusive and interact via a pairwise potential.

are driven in opposite directions, e.g. because they have opposite charges. But one should note that our theoretical framework also applies to a variety of other setups, for instance $q = 2$ with $\mathbf{F}_1 = F\mathbf{e}_x$ and $\mathbf{F}_2 = F\mathbf{e}_y$, or $q = 3$ with $\mathbf{F}_1 = \mathbf{F}$, $\mathbf{F}_2 = -\mathbf{F}$ and $\mathbf{F}_3 = \mathbf{0}$. Actually, for two species we will show that only the difference of forces $\mathbf{F}_1 - \mathbf{F}_2$ matters[1].

The coupled Langevin equations that we consider are

$$\frac{d\mathbf{X}_i}{dt} = \mathbf{F}_{\alpha_i} - \sum_{j\neq i} \nabla_i V(\mathbf{X}_i(t) - \mathbf{X}_j(t)) + \boldsymbol{\eta}_i(t). \tag{9.2}$$

The main remark is that because of the forces, the system is out of equilibrium. Nevertheless, it admits a steady state, and it is this steady state that we want to characterize. Our approach relies on obtaining equations for the density fields of each species.

9.2.2 Exact Dean equation

Our first step is to define a local fluctuating density for each species α,

$$\rho_\alpha(\mathbf{x}, t) \equiv \sum_{i\in\mathscr{T}_\alpha} \delta(\mathbf{X}_i(t) - \mathbf{x}) \tag{9.3}$$

where $\mathscr{T}_\alpha$ is the set of particles belonging to species α. The average over space of $\rho_\alpha(\mathbf{x})$ is denoted $\bar{\rho}_\alpha$. The total average density is $\bar{\rho} = \sum_\alpha \bar{\rho}_\alpha$, and we define the fraction of particles α as $\tau_\alpha = \bar{\rho}_\alpha/\bar{\rho}$. Starting from Eq. (9.2), we can adapt the derivation of subsection 8.2.2 to separate the density fields ρ_α that undergo respective forces $\nabla\phi = \mathbf{F}_\alpha$ and are coupled by the pair potential $V(\mathbf{x})$. We obtain the following set of Dean equations for the fluctuating densities ρ_α,

$$\frac{\partial \rho_\alpha}{\partial t} = -\nabla\cdot\mathbf{J}_\alpha(\mathbf{x}, t), \tag{9.4}$$

$$\mathbf{J}_\alpha(\mathbf{x}, t) = -D_0\nabla\rho_\alpha(\mathbf{x}, t) + \rho_\alpha\mathbf{F}_\alpha - \rho_\alpha(\mathbf{x}, t)\sum_{\beta=1}^{q}\nabla(V * \rho_\beta)(\mathbf{x}, t) + \rho_\alpha(\mathbf{x}, t)^{1/2}\boldsymbol{\eta}_\alpha(\mathbf{x}, t). \tag{9.5}$$

$\{\boldsymbol{\eta}_\alpha\}$ are q independent Gaussian white noises having zero average and correlations

$$\langle\boldsymbol{\eta}_\alpha(\mathbf{x}, t)\boldsymbol{\eta}_\beta(\mathbf{x}', t')\rangle = 2D_0\delta_{\alpha,\beta}\delta(\mathbf{x} - \mathbf{x}')\delta(t - t'). \tag{9.6}$$

[1] As a side remark, the authors of Ref. [75] showed that diagonal patterns emerge for populations driven in perpendicular directions on a lattice. These diagonals correspond to the direction "$\mathbf{F}_1 - \mathbf{F}_2$".

As pointed out in the previous chapter, the Dean equations are exact, but very hard to tackle as they are non-linear with multiplicative noise. We shall resort to a linearization approximation to obtain analytical results.

9.2.3 Linearized Dean equation

Our approximation, which we detailed in the previous chapter, consists in linearizing around homogeneous and constant densities $\bar{\rho}_\alpha$ for all species.

$$\rho_\alpha(\mathbf{x},t) \equiv \bar{\rho}_\alpha + \bar{\rho}_\alpha^{1/2}\phi_\alpha(\mathbf{x},t). \tag{9.7}$$

$\bar{\rho}_\alpha$ is assumed to be large, and we check afterwards that ϕ_α is of order 1.

Keeping only the leading order terms, we obtain the following linearized Dean equations,

$$\frac{\partial \phi_\alpha}{\partial t}(\mathbf{x},t) = D_0\nabla^2\phi_\alpha(\mathbf{x},t) - \mathbf{F}_\alpha\cdot\nabla\phi_\alpha + D_0\sum_\beta(\tau_\alpha\tau_\beta)^{1/2}\nabla^2[v*\phi_\beta](\mathbf{x},t) - \nabla\cdot\boldsymbol{\eta}_\alpha(\mathbf{x},t), \tag{9.8}$$

$$\langle\boldsymbol{\eta}_\alpha(\mathbf{x},t)\boldsymbol{\eta}_\beta(\mathbf{x}',t')\rangle = 2D_0\delta_{\alpha,\beta}\delta(\mathbf{x}-\mathbf{x}')\delta(t-t'). \tag{9.9}$$

In Fourier space, they read

$$\frac{\partial\tilde{\phi}}{\partial t}(\mathbf{k},t) = -D_0k^2\sum_\beta\tilde{A}_{\alpha,\beta}(\mathbf{k})\tilde{\phi}_\alpha(\mathbf{k},t) + \tilde{\xi}_\alpha, \tag{9.10}$$

with the $q\times q$ matrix $\tilde{A}$ having components defined by

$$A_{\alpha,\beta}(\mathbf{k}) = \delta_{\alpha,\beta}\left(1 + i\frac{\mathbf{f}_\alpha\cdot\mathbf{k}}{k^2}\right) + \sqrt{\tau_\alpha\tau_\beta}\tilde{v}(k). \tag{9.11}$$

$\mathbf{f}_\alpha = \mathbf{F}_\alpha/D_0$ is the Péclet number associated with a species. In Fourier space, the correlations of the Gaussian white noises $\tilde{\xi}_\alpha$ are

$$\langle\tilde{\xi}_\alpha(\mathbf{k},t)\tilde{\xi}_\beta(\mathbf{k}',t')\rangle = 2(2\pi)^d D_0k^2\delta_{\alpha,\beta}\delta(\mathbf{k}+\mathbf{k}')\delta(t-t'). \tag{9.12}$$

Now having a linear equation, we are able to obtain analytical results for key observables. We first focus on the correlation functions of the system and derive a scaling form. Then, we obtain insights into the effective mobility of the particles which characterizes the opposition to the motion of a particle due to the particles of other species.

9.3 Correlation functions

9.3.1 Definition

The correlation function $h_{\alpha,\beta}$ characterizes the relative disposition of particles of species α and β. If a particle β is at the origin, where are the particles α? We use the invariance by translation and define

$$h_{\alpha,\beta}(\mathbf{x}) = \left\langle\left(\frac{\rho_\alpha(\mathbf{x})}{\bar{\rho}_\alpha} - 1\right)\left(\frac{\rho_\beta(\mathbf{0})}{\bar{\rho}_\beta} - 1\right)\right\rangle - \delta_{\alpha,\beta}\frac{\delta(\mathbf{x})}{\bar{\rho}_\alpha}. \tag{9.13}$$

$\bar{\rho}_\alpha$ is the average density of species α. The last term subtracts the self-contribution of a given particle.

For the analysis of the linearized Dean equations (9.8), it will be also useful to define

$$C_{\alpha,\beta}(\mathbf{x}) = \left\langle \phi_\alpha(\mathbf{x})\phi_\beta(\mathbf{0})\right\rangle, \tag{9.14}$$

which is related to $h_{\alpha,\beta}$ by

$$h_{\alpha,\beta}(\mathbf{x}) = [C_{\alpha,\beta}(\mathbf{x}) - \delta_{\alpha,\beta}\delta(\mathbf{x})]/\sqrt{\bar\rho_\alpha\bar\rho_\beta}. \tag{9.15}$$

9.3.2 Linear equation

We analyze the variation of $C_{\alpha,\beta}(\mathbf{k},t)$ between times t and $t+\delta t$ using Itô calculus as we did in subsection 8.3.3. The linearized Dean equation (9.8) leads to the following time evolution for the matrix $C(\mathbf{k},t) \equiv \left(C_{\alpha,\beta}(\mathbf{k},t)\right)_{\alpha,\beta}$,

$$\partial_t \tilde C(\mathbf{k},t) = D_0 k^2\left[2\mathbb{I} - \tilde A(\mathbf{k})\tilde C(\mathbf{k},t) - \tilde C(\mathbf{k},t)\tilde A^*(\mathbf{k})\right], \tag{9.16}$$

with A defined in Eq. (9.11) and '$*$' denoting the complex conjugate. We used the property $A(-\mathbf{k}) = A^*(\mathbf{k})$. We focus on the stationary solution $C^{\text{stat}}(\mathbf{k},t)$, it satisfies the linear equation

$$\tilde A(\mathbf{k})\tilde C^{\text{stat}}(\mathbf{k},t) + \tilde C^{\text{stat}}(\mathbf{k},t)\tilde A^*(\mathbf{k}) = 2\mathbb{I}. \tag{9.17}$$

This is a set of q^2 linear equations for the variables $\left(C^{\text{stat}}_{\alpha,\beta}\right)_{\alpha,\beta=1,\dots,q}$[2]. For $1 \le \alpha,\beta \le q$,

$$\left[2 + i\frac{\mathbf{k}\cdot(\mathbf{f}_\alpha - \mathbf{f}_\beta)}{k^2}\right]\tilde C^{\text{stat}}_{\alpha,\beta}(\mathbf{k}) + \tilde\nu(\mathbf{k})\sum_{\gamma=1}^{q}\left(\sqrt{\tau_\alpha\tau_\gamma}C^{\text{stat}}_{\gamma,\beta}(\mathbf{k}) + C^{\text{stat}}_{\alpha,\gamma}(\mathbf{k})\sqrt{\tau_\gamma\tau_\beta}\right) = 2\delta_{\alpha,\beta}. \tag{9.18}$$

One can use a symbolic computation software to solve for this set of equations. We now give the result in two specific cases: passive particles ($\mathbf{f}_\alpha = 0$), and two species ($q = 2$).

9.3.3 Resolution

From now on, we consider only the equilibrium correlation functions, we drop the superscript 'stat': $C = C^{\text{stat}}$. We first focus on the trivial case of passive particles that amounts to our study in the previous chapter. Then, we investigate the case of two species, for which we will obtain our main results.

Passive interacting species

At equilibrium, when all the forces are equal to zero, the matrix A writes

$$A_{\alpha,\beta}(\mathbf{k}) = \delta_{\alpha,\beta} + \sqrt{\tau_\alpha\tau_\beta}\tilde\nu(\mathbf{k}) \tag{9.19}$$

$$A(\mathbf{k}) = \mathbb{I} + \tilde\nu(\mathbf{k})|T\rangle\langle T|. \tag{9.20}$$

We define the unit vector $|T\rangle = (\sqrt{\tau_1},\dots,\sqrt{\tau_p})^T$ using quantum mechanics notations for simplicity. Any orthogonal basis $(|T\rangle,\dots)$ is an eigenbasis of A. As A is real, the equation (9.17) admits a simple solution: $\tilde C$ is the inverse of A,

$$\tilde C(\mathbf{k}) = A^{-1}(\mathbf{k}) = \mathbb{I} - \frac{\tilde\nu(\mathbf{k})}{1+\tilde\nu(\mathbf{k})}|T\rangle\langle T|. \tag{9.21}$$

[2] Using the symmetry $\tilde C^{\text{stat}}_{\beta,\alpha} = (\tilde C^{\text{stat}}_{\alpha,\beta})^*$, there are only $q(q+1)/2$ independent equations.

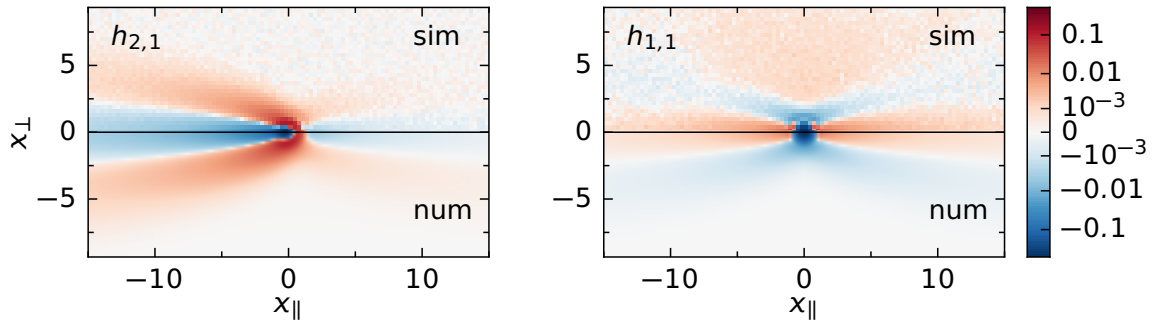

Figure 9.2: Pair correlation functions $h_{2,1}$ and $h_{1,1}$ in dimension 2. The parameters are $\bar{\rho} = 2, D_0 = 0.2, F = 4$ and the fractions of particles are $\tau_1 = \tau_2 = 0.5$. Throughout this chapter the pair potential is the soft-sphere potential $V(r) = (1-r)^2/2$ for $r < 1$. The top panel shows the results of the numerical simulations ($N = 8 \cdot 10^4$ particles). The bottom panel is the numerical inversion of Eq. (9.29).

That is to say,

$$\tilde{C}_{\alpha,\beta}(\mathbf{k}) = \delta_{\alpha,\beta} - \frac{\sqrt{\tau_\alpha \tau_\beta}\tilde{v}(\mathbf{k})}{1+\tilde{v}(\mathbf{k})}. \tag{9.22}$$

Using Eq. (9.15), we obtain the pair correlations $h_{\alpha,\beta}$: for all α and β,

$$\tilde{h}_{\alpha,\beta}(\mathbf{k}) = \frac{-\tilde{V}(\mathbf{k})}{D_0 + \bar{\rho}\tilde{V}(\mathbf{k})}. \tag{9.23}$$

The pair correlation is independent of the species considered and is the equilibrium result we found for passive particles [Eq. (8.42)].

Two driven species

When we turn on the forces, the matrix A [Eq. (9.11)] is no longer a real matrix. Furthermore, the terms $\delta_{\alpha,\beta}\mathbf{k}\cdot\mathbf{f}_\alpha$ and $\sqrt{\tau_\alpha\tau_\beta}$ cannot be diagonalized in the same basis. We have no choice but to solve the set of linear equations (9.18). For $q = 2$ species, it reads

$$\begin{cases} 2(1+\tau_1\tilde{v})\tilde{C}_{1,1} + \sqrt{\tau_1\tau_2}\tilde{v}(\tilde{C}_{1,2}+\tilde{C}_{2,1}) = & 2 \\ \left(2+\tilde{v}+i\frac{\mathbf{k}\cdot(\mathbf{f}_1-\mathbf{f}_2)}{k^2}\right)\tilde{C}_{1,2} + \sqrt{\tau_1\tau_2}\tilde{v}(\tilde{C}_{1,1}+\tilde{C}_{2,2}) = & 0 \\ \left(2+\tilde{v}-i\frac{\mathbf{k}\cdot(\mathbf{f}_1-\mathbf{f}_2)}{k^2}\right)\tilde{C}_{2,1} + \sqrt{\tau_1\tau_2}\tilde{v}(\tilde{C}_{1,1}+\tilde{C}_{2,2}) = & 0 \\ 2(1+\tau_2\tilde{v})\tilde{C}_{2,2} + \sqrt{\tau_1\tau_2}\tilde{v}(\tilde{C}_{1,2}+\tilde{C}_{2,1}) = & 2. \end{cases} \tag{9.24}$$

A crucial point is that the forces $\mathbf{f}_1$ and $\mathbf{f}_2$ appear only as the difference $\mathbf{f}_1 - \mathbf{f}_2$. We define

$$\Delta f = \|\mathbf{f}_1 - \mathbf{f}_2\| \tag{9.25}$$

$$k_\parallel = \frac{\mathbf{k}\cdot(\mathbf{f}_1-\mathbf{f}_2)}{\|\mathbf{f}_1-\mathbf{f}_2\|} \tag{9.26}$$

$$\mathbf{k}_\perp = \mathbf{k} - \frac{\mathbf{k}\cdot(\mathbf{f}_1-\mathbf{f}_2)}{\|\mathbf{f}_1-\mathbf{f}_2\|} \tag{9.27}$$

so that $\mathbf{k}\cdot(\mathbf{f}_1-\mathbf{f}_2) = k_\parallel \Delta f$. $k_\parallel$ is the component of $\mathbf{k}$ parallel to the direction of the difference of forces.

The system (9.24) can be solved by hand, or with a computer algebra system. It yields

$$\tilde{C} = \left[(1+\tilde{\nu})(2+\tilde{\nu})^2 + (1+\tau_1\tilde{\nu})(1+\tau_2\tilde{\nu})\frac{k_\parallel^2\Delta f^2}{k^4}\right]^{-1} \begin{pmatrix} (1+\tau_2\tilde{\nu})\left[(2+\tilde{\nu})^2 + \frac{k_\parallel^2\Delta f^2}{k^4}\right] & -\sqrt{\tau_1\tau_2}\tilde{\nu}(2+\tilde{\nu})\left(2+\tilde{\nu}-i\frac{k_\parallel\Delta f}{k^2}\right) \\ -\sqrt{\tau_1\tau_2}\tilde{\nu}(2+\tilde{\nu})\left(2+\tilde{\nu}+i\frac{k_\parallel\Delta f}{k^2}\right) & (1+\tau_1\tilde{\nu})\left[(2+\tilde{\nu})^2 + \frac{k_\parallel^2\Delta f^2}{k^4}\right] \end{pmatrix}. \quad (9.28)$$

This can be recast in terms of pair correlation functions [Eq. (9.15)].

$$\tilde{h} = \frac{-\tilde{\nu}}{\bar{\rho}}\left[(1+\tilde{\nu})(2+\tilde{\nu})^2 + (1+\tau_1\tilde{\nu})(1+\tau_2\tilde{\nu})\frac{k_\parallel^2\Delta f^2}{k^4}\right]^{-1} \left\{(2+\tilde{\nu})^2\mathbb{I} + \begin{pmatrix} (1+\tau_2\tilde{\nu})\frac{k_\parallel^2\Delta f^2}{k^4} & -(2+\tilde{\nu})i\frac{k_\parallel\Delta f}{k^2} \\ (2+\tilde{\nu})i\frac{k_\parallel\Delta f}{k^2} & (1+\tau_1\tilde{\nu})\frac{k_\parallel^2\Delta f^2}{k^4} \end{pmatrix}\right\}. \quad (9.29)$$

The inverse Fourier transform of this result can be performed numerically. We find a very good agreement with data from simulations (Figs. 9.2 and 9.4). The cross-species correlations $h_{2,1}$ are negative in the longitudinal direction ($x_\parallel < 0$) while the inter-species correlations $h_{1,1}$ are positive along this direction. This shows a tendency of the particles to align with others of the same species and to anti-align with particles of a different species.

Vanishing fraction of driven particles

An interesting special case is when there are only few biased particles in a bath of unbiased particles. This corresponds to $\mathbf{f}_2 = \mathbf{0}$ (thus $\Delta f = f_1$) with $\tau_1 \to 0$ (thus $\tau_2 \to 1$). In this case, one is mostly interested in the cross correlations $h_{2,1}$. They read

$$\tilde{h}_{2,1} = \frac{-\tilde{\nu}}{\bar{\rho}(1+\tilde{\nu})}\frac{(2+\tilde{\nu})\left[(2+\tilde{\nu})+i\frac{k_\parallel\Delta f}{k^2}\right]}{(2+\tilde{\nu})^2+\frac{k_\parallel^2\Delta f^2}{k^4}} = \frac{1}{\bar{\rho}}\left(\frac{2+\tilde{\nu}}{1+\tilde{\nu}}\right)\frac{-k^2\tilde{\nu}}{(2+\tilde{\nu})k^2 - ik_\parallel\Delta f}. \quad (9.30)$$

In Ref. [24], the authors studied the profile induced by a unique driven intruder using the same approach as us. Their result [Eq. (55)] has the same structure as Eq. (9.30). The only difference is the factor $(2+\tilde{\nu})/(1+\tilde{\nu})$ that comes from the fact that their observable (the profile) and ours (the pair correlation) are different even in the absence of forces.

9.4 Long distance scaling of the correlations

9.4.1 Soft short-range potential

We assume that the integral over space of the potential V is finite,

$$\left|\int d\mathbf{r}\, V(\mathbf{r})\right| < \infty. \quad (9.31)$$

Physically, this means that V is both (a) short-ranged and (b) soft. (a) The potential should have a finite range ($V(\mathbf{r}) = 0$ for $\|\mathbf{r}\| > a$), an exponential decay at large distance, or a fast algebraic decay $V(\mathbf{r}) \underset{r\to\infty}{\sim} r^{-\alpha}$ with $\alpha > d$ (d is the dimension of the physical space). In particular, the results that we will derive do not hold for long-range potentials such as electrostatic interactions [2]. (b) The potential should have a finite value at $r = 0$, or diverge slower than r^{-d}. This excludes hard potentials, such as the Lennard-Jones potential, for which no weak-interaction limit can be defined. Note however that we will see that some of our large-distance results hold for hard particles, in which case such potentials may be considered.

In the following, we will denote

$$\nu_0 = \frac{\bar\rho}{D_0}\int d\mathbf{r}\, V(\mathbf{r}) = \frac{\bar\rho \tilde V(\mathbf{0})}{D_0} \tag{9.32}$$

the rescaled integral of the potential over space.

9.4.2 Discontinuity at small wave number

We now turn back to the correlations in a driven binary mixture [Eq. (9.29)] and we look for a scaling form at large distance, that is to say small wave number $\mathbf{k}$. In agreement with the previous paragraph, we make the substitution $\tilde v(\mathbf{k}) \mapsto \nu_0$ which corresponds to the limit $\mathbf{k} \to \mathbf{0}$.

The correlations between species $h_{2,1}$, and within the same species $h_{1,1}$ thus read

$$\tilde h_{2,1} = -A\frac{\alpha k^2(\alpha k^2 + ik_\parallel \Delta f)}{\alpha^2 k^4 + \beta^2 k_\parallel^2 \Delta f^2}, \qquad \tilde h_{1,1} = A\frac{\alpha^2 k^4 + \gamma_2^2 k_\parallel^2 \Delta f^2}{\alpha^2 k^4 + \beta^2 k_\parallel^2 \Delta f^2} \tag{9.33}$$

with $k^2 = k_\parallel^2 + \mathbf{k}_\perp^2$ [Eqs. (9.26), (9.27)] and the numerical factors are

$$A = \frac{\nu_0}{\bar\rho(1+\nu_0)}, \qquad \gamma_2 = (1+\tau_2\nu_0)^{1/2}, \qquad \alpha = 2+\nu_0, \qquad \beta = \left(1 + \frac{\tau_1\tau_2\nu_0^2}{1+\nu_0}\right)^{1/2}. \tag{9.34}$$

As $h_{1,2}$ and $h_{2,2}$ have the same phenomenology than $h_{2,1}$ and $h_{1,1}$, we do not consider them.

One soon realizes that the limits $k_\parallel \to 0$ and $\mathbf{k}_\perp \to 0$ either do not commute ($\tilde h_{1,1}$) or lead to different scalings ($\tilde h_{2,1}$), namely

$$\tilde h_{2,1}(k_\parallel = 0, \mathbf{k}_\perp) \underset{\mathbf{k}_\perp\to 0}{\sim} -A\mathbf{k}_\perp^2, \qquad \tilde h_{2,1}(k_\parallel, \mathbf{k}_\perp = 0) \underset{k_\parallel\to 0}{\sim} \frac{-i\alpha A}{\beta^2\Delta f}k_\parallel, \tag{9.35}$$

$$\tilde h_{1,1}(k_\parallel = 0, \mathbf{k}_\perp) \underset{\mathbf{k}_\perp\to 0}{\sim} A, \qquad \tilde h_{1,1}(k_\parallel, \mathbf{k}_\perp = 0) \underset{k_\parallel\to 0}{\sim} A\frac{\gamma_2^2}{\beta^2}. \tag{9.36}$$

This non-commutativity of the limits when $\mathbf{k} \to \mathbf{0}$ hints at a slow decay of the correlations at large distance. Indeed a fast (exponential) decay would imply a regularity of the Fourier transform at the origin. The regime of small $\mathbf{k}$ is linked to the large-distance regime in real space, we thus expect the behavior at large distance to be dominated by the singularity around $\mathbf{k} = \mathbf{0}$ that we now characterize.

Looking at the limits of $\tilde h_{2,1}$, one sees that the following "balance" should hold when $\mathbf{k} \to \mathbf{0}$: $k_\parallel \sim \mathbf{k}_\perp^2$. We keep only the singular part of the correlations, the one that is responsible for the

singularity at the origin. We write $\mathbf{k}^2 = k_\parallel^2 + \mathbf{k}_\perp^2 \simeq \mathbf{k}_\perp^2$ and obtain

$$\tilde{h}^s_{2,1}(k_\parallel, \mathbf{k}_\perp) = -A\frac{\alpha \mathbf{k}_\perp^2(\alpha \mathbf{k}_\perp^2 + ik_\parallel \Delta f)}{\alpha^2 \mathbf{k}_\perp^4 + \beta^2 k_\parallel^2 \Delta f^2}, \qquad \tilde{h}^s_{1,1} = A\frac{\alpha^2 \mathbf{k}_\perp^4 + \gamma_2^2 k_\parallel^2 \Delta f^2}{\alpha^2 \mathbf{k}_\perp^4 + \beta^2 k_\parallel^2 \Delta f^2}. \tag{9.37}$$

We prefer to recast these expressions under the equivalent formulations below.

$$\tilde{h}^s_{2,1}(k_\parallel, \mathbf{k}_\perp) = -\frac{A\alpha}{2\beta \Delta f}\left[(1-\beta^{-1})G(k_\parallel, k_\perp) + (1+\beta^{-1})G(-k_\parallel, k_\perp)\right] \tag{9.38}$$

$$\tilde{h}^s_{1,1}(k_\parallel, \mathbf{k}_\perp) = \frac{A}{\beta^2}\left\{\gamma_2^2 + \alpha^2(\beta^2 - \gamma_2^2)\left[\tilde{G}(k_\parallel, k_\perp) + \tilde{G}(-k_\parallel, k_\perp)\right]\right\} \tag{9.39}$$

$$\tilde{G}(k_\parallel, \mathbf{k}_\perp) = \frac{-\mathbf{k}_\perp^2}{\frac{D}{2}\mathbf{k}_\perp^2 + ik_\parallel} \tag{9.40}$$

The coefficient D, that will later be interpreted as a diffusion coefficient is

$$D = \frac{2\alpha}{\beta \Delta f}. \tag{9.41}$$

We now give the space dependence of the function $G(k_\parallel, \mathbf{k}_\perp)$ that will lead to a scaling form for the correlations.

9.4.3 Scaling form

All we need is to compute the inverse Fourier transform of $\tilde{G}(k_\parallel, \mathbf{k}_\perp)$. We first define the coordinates respectively parallel and perpendicular to the direction of the difference of forces[3],

$$x_\parallel = \frac{\mathbf{r}\cdot(\mathbf{F}_1 - \mathbf{F}_2)}{\|\mathbf{F}_1 - \mathbf{F}_2\|}, \qquad \mathbf{x}_\perp = \mathbf{r} - \frac{\mathbf{r}\cdot(\mathbf{F}_1 - \mathbf{F}_2)}{\|\mathbf{F}_1 - \mathbf{F}_2\|}. \tag{9.42}$$

Using the residue theorem first, and then a Gaussian integral, we compute the inverse Fourier transform of Eq. (9.40).

$$G(x_\parallel, \mathbf{x}_\perp) = \int \frac{d\mathbf{k}_\perp}{(2\pi)^{d-1}} e^{i\mathbf{x}_\perp \cdot \mathbf{k}_\perp}(-\mathbf{k}_\perp^2) \int_{-\infty}^{\infty} \frac{dk_\parallel}{2\pi} \frac{e^{ix_\parallel k_\parallel}}{\frac{D}{2}\mathbf{k}_\perp^2 + ik_\parallel} \tag{9.43}$$

$$= \Theta(x_\parallel) \int \frac{d\mathbf{k}_\perp}{(2\pi)^{d-1}} e^{i\mathbf{x}_\perp \cdot \mathbf{k}_\perp}(-\mathbf{k}_\perp^2) e^{-\frac{1}{2}Dx_\parallel \mathbf{k}_\perp^2} \tag{9.44}$$

$$G(x_\parallel, \mathbf{x}_\perp) = \frac{\Theta(x_\parallel)}{(2\pi)^{\frac{d-1}{2}}}\left[Dx_\parallel\right]^{-\frac{d+1}{2}} g\left(\frac{\mathbf{x}_\perp}{\sqrt{D|x_\parallel|}}\right) \tag{9.45}$$

where Θ is the Heaviside step function, D is given by Eq. (9.41), and the function g is the second derivative of a Gaussian,

$$g(\mathbf{u}) = \nabla_{\mathbf{u}}^2\left(e^{-\mathbf{u}^2/2}\right) = (\mathbf{u}^2 - d + 1)e^{-\mathbf{u}^2/2}. \tag{9.46}$$

We note that G is the solution of the diffusion equation

$$\begin{cases} \frac{\partial G}{\partial x_\parallel}(x_\parallel, \mathbf{x}_\perp) = \frac{D}{2}\nabla_\perp^2 G(x_\parallel, \mathbf{x}_\perp) \\ G(x_\parallel = 0, \mathbf{x}_\perp) = \nabla_\perp^2 \delta(\mathbf{x}_\perp) \end{cases} \tag{9.47}$$

[3] One should actually choose a coordinate system $\mathbf{r} = (x_1, \ldots, x_d)$ such that $x_\parallel = x_1$, $\mathbf{x}_\perp = (x_2, \ldots, x_d)$.

for $x_\parallel \geq 0$. This diffusion equation induces the scalings $\mathbf{x}_\perp/x_\parallel$ and $x_\parallel^{-(d+1)/2}$. We will come back later on the intuitive meaning of this equation.

We have argued that the large-distance behavior of the correlations stems from their singular parts [Eqs. (9.38) and (9.39)]. Now, from Eq. (9.45), we are able to write the scaling form obeyed by the correlations at large distance, which is the main result of this chapter.

$$h_{\alpha,\beta}(\mathbf{x}) \underset{x_\parallel\to\pm\infty}{\sim} h^s_{\alpha,\beta}(\mathbf{x}) \underset{x_\parallel\to\pm\infty}{\sim} \frac{H^\pm_{\alpha,\beta}}{|x_\parallel|^{\frac{d+1}{2}}} g\left(\frac{\mathbf{x}_\perp}{\sqrt{D|x_\parallel|}}\right). \tag{9.48}$$

'+' corresponds to the wake in front of a particles while '−' is the wake behind it. The prefactors scale with the forces as $\Delta f^{\frac{d-1}{2}}$,

$$H^-_{2,1} = \frac{1}{\bar\rho}\frac{\nu_0\beta^{\frac{d-1}{2}}(1+\beta^{-1})}{2^{d+1}\pi^{\frac{d-1}{2}}(1+\nu_0)(2+\nu_0)^{\frac{d-1}{2}}}\Delta f^{\frac{d-1}{2}}, \tag{9.49}$$

$$H^+_{2,1} = \frac{1}{\bar\rho}\frac{\nu_0\beta^{\frac{d-1}{2}}(1-\beta^{-1})}{2^{d+1}\pi^{\frac{d-1}{2}}(1+\nu_0)(2+\nu_0)^{\frac{d-1}{2}}}\Delta f^{\frac{d-1}{2}}, \tag{9.50}$$

$$H^+_{1,1} = H^-_{1,1} = -\frac{1}{\bar\rho}\frac{(1-\tau_1)\nu_0^2[1+(1-\tau_1)\nu_0]\beta^{\frac{d-5}{2}}}{2^{d+1}\pi^{\frac{d-1}{2}}(1+\nu_0)(2+\nu_0)^{\frac{d-1}{2}}}\Delta f^{\frac{d-1}{2}}. \tag{9.51}$$

The profile has an algebraic (power-law) decay in the longitudinal direction, but decays exponentially in the transverse direction. This behavior can be probed in numerical simulations by analyzing cuts at a constant $x_\parallel$. We find a very good agreement on Fig. 9.3, we stress that there is no free parameter in our prediction.

As a side remark, we note that when $\tau_2 \to 0$, we have $H^\pm_{2,1} = 0$ and $H^+_{2,1} = 0$. The only algebraic effect is a wake in the cross correlations for $x_\parallel < 0$. This corresponds to the case of a unique driven intruder studied in Ref. [24].

9.4.4 Numerical simulations

To check our findings, we performed numerical simulations of stochastic molecular dynamics in dimension 2. N particles of two species are placed uniformly at random in a periodic box of size $L = \sqrt{N/\bar\rho}$ where $\bar\rho$ is the density. Particles are separated into two species: species 1 undergoes a force $F_1 > 0$ (to the right) while species 2 is not driven ($F_2 = 0$). We use the following soft-sphere potential,

$$V(\mathbf{x}) = \begin{cases} \frac{1}{2}(1-\|\mathbf{x}\|)^2 & \text{if } \|\mathbf{x}\| \leq 1 \\ 0 & \text{otherwise} \end{cases} \tag{9.52}$$

where both the particle radius and the strength of the potential are set to 1. The evolution of the system is simulated according to the Langevin equations (9.2) using a constant time step Δt. The noises $\boldsymbol{\eta}_i$ are simulated by drawing Gaussian numbers of variance $2D_0\Delta t$ at each step.

After a certain time (of the order of 2), the system reaches its stationary state and we start to measure the correlation functions by using bins of resolution 0.1. More details are given in the supplementary materials of [P1]. The comparison of the correlations with the inverse Fourier transform of Eq. (9.29) is shown in Fig. 9.2. And the scaling form of the cuts [Eq. (9.48)] is checked in Fig. 9.3. Both show a very good agreement of our theory with numerical simulations at a high density $\bar\rho = 2$.

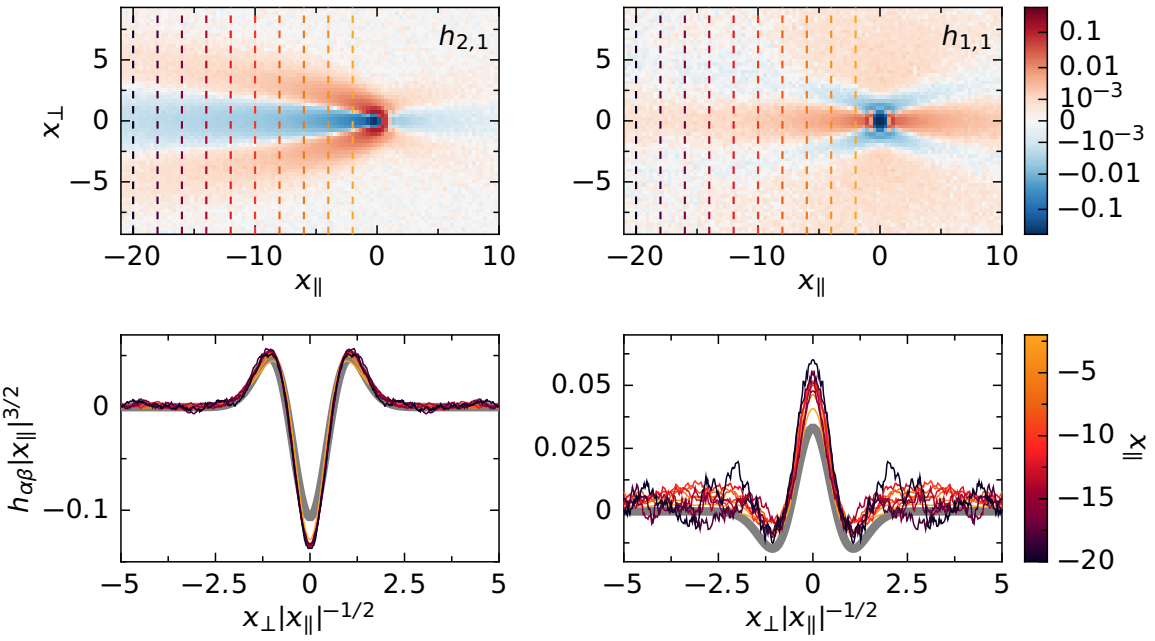

Figure 9.3: Scaling form for the pair correlation functions $h_{2,1}$ and $h_{1,1}$. Top: simulation data of Fig. 9.2 ($\bar{\rho} = 2, D_0 = 0.2, F = 4, \tau_1 = \tau_2 = 0.5$), the dashed lines correspond to the cuts shown in the bottom. Bottom: rescaled cuts of the correlations. The gray line corresponds to the prediction from Eq. (9.48) without any ajusted factor.

Simulations in dimension 3 were also performed. Results are shown in Fig. 9.4. They are consistent with our findings: the comparison with the numerical inverse Fourier transform is good and the collapse of $h_{2,1}$ is convincing. To obtain a better agreement between the simulations and the theory one should perform larger-scale simulations. The number of particles ($N = 10^4$ at a density $\bar{\rho} = 1$) induces a system size $L \approx 22$ which is comparable to our range of observation, so finite-size effects play a role.

9.4.5 Universality of the scaling form

Simulations outside the validity regime of the approach

When the linearization of the Dean equation is valid (high density, weak interactions), we found analytically that the correlations obey a scaling form at large distance

$$h^{\pm}_{\alpha,\beta}(x_\parallel, \mathbf{x}_\perp) \underset{x_\parallel \to \pm\infty}{\sim} \frac{H_{\alpha,\beta}}{|x_\parallel|^{\frac{d+1}{2}}} g\left(\frac{\mathbf{x}_\perp}{\sqrt{D|x_\parallel|}}\right), \tag{9.53}$$

$$g(\mathbf{u}) = \nabla^2_{\mathbf{u}}\left(e^{-\mathbf{u}^2/2}\right) = (\mathbf{u}^2 - d + 1)e^{-\mathbf{u}^2/2}, \tag{9.54}$$

where d is the dimension and g is the second derivative of a Gaussian [Eq. (9.46)]. Furthermore, we obtained expressions for the prefactors D and $H^{\pm}_{\alpha_\beta}$.

A natural question to ask is whether the scaling form (9.53) still holds outside of the validity regime of our approach. To check this, we perform numerical simulations of dilute particles with hard interactions [Fig. 9.5]. The correlations $h_{2,1}$ and $h_{1,1}$ look qualitatively very similar to the

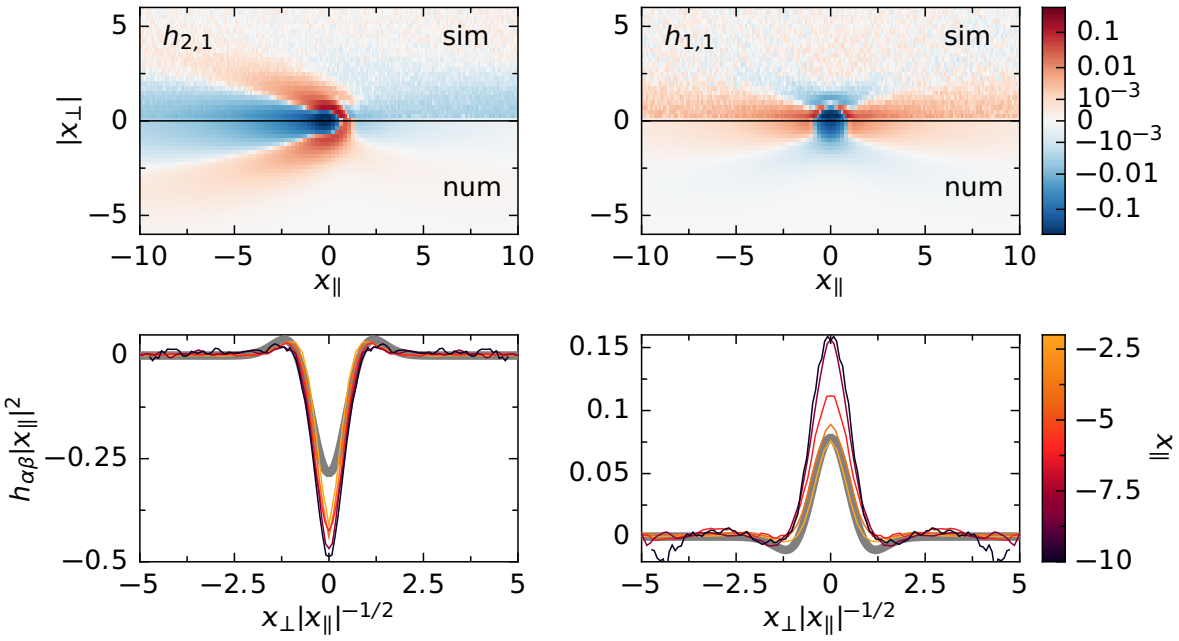

Figure 9.4: Pair correlation functions $h_{2,1}$ and $h_{1,1}$ in dimension 3. The parameters are $\bar{\rho} = 1, D_0 = 0.1, F = 2$ and the fractions of particles are $\tau_1 = \tau_2 = 0.5$. Top: the upper panel shows the results of the numerical simulations ($N = 1 \cdot 10^4$ particles). The lower panel is the numerical inversion of Eq. (9.29). Bottom: rescaled cuts of the correlation functions. The gray line corresponds to the prediction from Eq. (9.48) without any ajusted factor. Unfortunately, the system size is too small to obtain good results (length : $(N/\bar{\rho})^{1/3} \approx 22$).

ones obtained in the dense and soft regime that we studied previously. Moreover, using cuts at fixed $x_\parallel$, we observe that we obtain a collapse with the exponents predicted by Eq. (9.53) and the scaling function g. The width and the height are ajusted by hand. The width is found to be identical for $h_{2,1}$ and $h_{1,1}$.

Qualitative argument

This suggested universality of the scaling form is remarkable. We shall now suggest a simple explanation based on the diffusion equation (9.47). Let us consider a unique point-like intruder driven at a constant speed $\mathbf{U}_1 = U_1 \mathbf{e}_\parallel$ in a quiescent diffusive bath of initial density $\bar{\rho}$. This is a toy model for a vanishing fraction of driven particles ($\tau_1 \to 0$, force $\mathbf{F}_1$) with the other particles not submitted to any force ($\mathbf{F}_2 = \mathbf{0}$). The position of the intruder is given by $X_\parallel = U_1 t$ and $\mathbf{X}_\perp = \mathbf{0}$. The density in front of the intruder is left unperturbed: $\rho(x_\parallel > X_\parallel, \mathbf{x}_\perp) = \bar{\rho}$.

The key point is the perturbation induced by the intruder at $x_\parallel = X_\parallel$. It needs to be local (the intruder is point-like), radially symmetric (dependant only on the norm $\|\mathbf{x}_\perp\|$) and most importantly conservative: if the field represents particles, those that are pushed away by the intruder need to be somewhere else (on the sides of the intruder). The perturbation that satisfies these conditions is the second derivative of a Dirac function. $\rho(x_\parallel = X_\parallel^-, \mathbf{x}_\perp) - \bar{\rho} = A \nabla_\perp^2 \delta(\mathbf{x}_\perp)$. One checks that this corresponds to a depletion at $\mathbf{x}_\perp = 0$ and an accumulation of particles at $\|\mathbf{x}_\perp\| = 0^+$.

The density field obeys a diffusion equation $\partial_t \rho = D^* \nabla^2 \rho$. As a consequence, the density field

in the referential frame of the intruder, $\rho^*(x_\parallel, \mathbf{x}_\perp) \equiv \rho(X_\parallel + x_\parallel, \mathbf{x}_\perp)$ reaches a time-independent stationary state satisfying

$$0 = D^* \left(\partial_\parallel^2 + \nabla_\perp^2\right) \rho^*(x_\parallel, \mathbf{x}_\perp) + U_1 \partial_\parallel \rho^*(x_\parallel, \mathbf{x}_\perp). \tag{9.55}$$

ρ^* is the analog of $h_{2,1}$ in our minimal model. We are interested in scalings at large distance: one notices that we should have $\nabla_\perp^2 \sim \partial_\parallel$. Since at large distance, the lowest order of derivatives should dominate, we neglect the diffusion in the parallel direction and write

$$-\partial_\parallel \rho^*(x_\parallel, \mathbf{x}_\perp) \approx \frac{D^*}{U_1} \nabla_\perp^2 \rho^*(x_\parallel, \mathbf{x}_\perp), \tag{9.56}$$

with the boundary condition at $x_\parallel = 0^-$,

$$\rho^*(x_\parallel = 0^-, \mathbf{x}_\perp) - \bar{\rho} = A \nabla_\perp^2 \delta(\mathbf{x}_\perp). \tag{9.57}$$

Eqs. (9.56) and (9.56) correspond to the diffusion equation (9.47) that we obtained previously. Its solution is indeed the scaling form

$$\rho^*(x_\parallel < 0, \mathbf{x}_\perp) \sim \frac{1}{|x_\parallel|^{\frac{d+1}{2}}} g\left(\sqrt{\frac{U_1}{2D^*}} \frac{\mathbf{x}_\perp}{\sqrt{|x_\parallel|}}\right). \tag{9.58}$$

The factor $\mathbf{x}_\perp / \sqrt{|x_\parallel|}$ is the usual self-similar ratio for diffusion. The decay exponent $|x_\parallel|^{\frac{d+1}{2}}$ stems from the second derivative of a Dirac function as initial condition. The reader is perhaps more familiar with the exponent $|x_\parallel|^{\frac{d-1}{2}}$ associated with a Dirac initial condition. Similarly the shape g, second derivative of a Gaussian, is the analog of the Gaussian function associated with a Dirac initial condition.

To summarize, we found the scaling form (9.53) with minimal ingredients. Our argument explains well the scaling of $h_{2,1}$ for $x_\parallel < 0$. In reality, we considered a non-vanishing fraction of particles driven at constant force (instead of constant velocity), and the reference particle is also diffusing. All these differences affect only the prefactors involved. The scaling for $h_{1,1}$ can be thought of as correlations between the same species mediated by inter-species correlations. And the scaling of $h_{2,1}$ for $x_\parallel > 0$ is due to the fact that particles "align": what is seen is the wake created by the other particles of the same species.

Note on a model of active binary mixtures

Finally, let us note that Bain and Bartolo studied a model of active binary mixtures in dimension two [76] (our system could be called "passive binary mixtures"). Each point-like particle has an orientation which defines its direction of motion at constant speed, and wants to move towards either the left or the right. Particles interact via pairwise repulsive torques. In this system, the authors found a phase transition between two states: an homogeneous state and a phase separated state. The phase separated state is argued to be specific of activity. But a striking feature is that the correlations in the homogeneous state between left-moving and right-moving particles $g_{lr}(x_\parallel, x_\perp)$, and between particles of the same kind $g_{ll}(x_\parallel, x_\perp)$, obey the scaling form: $g_{\alpha,\beta}(x_\parallel, x_\perp) \sim x_\parallel^{-3/2} \mathscr{C}\left(x_\perp / x_\parallel^{1/2}\right)$. This behavior is very similar to Eq. (9.53). It is striking that the scaling exponents that we found can be reproduced in a purely deterministic active model with no temperature.

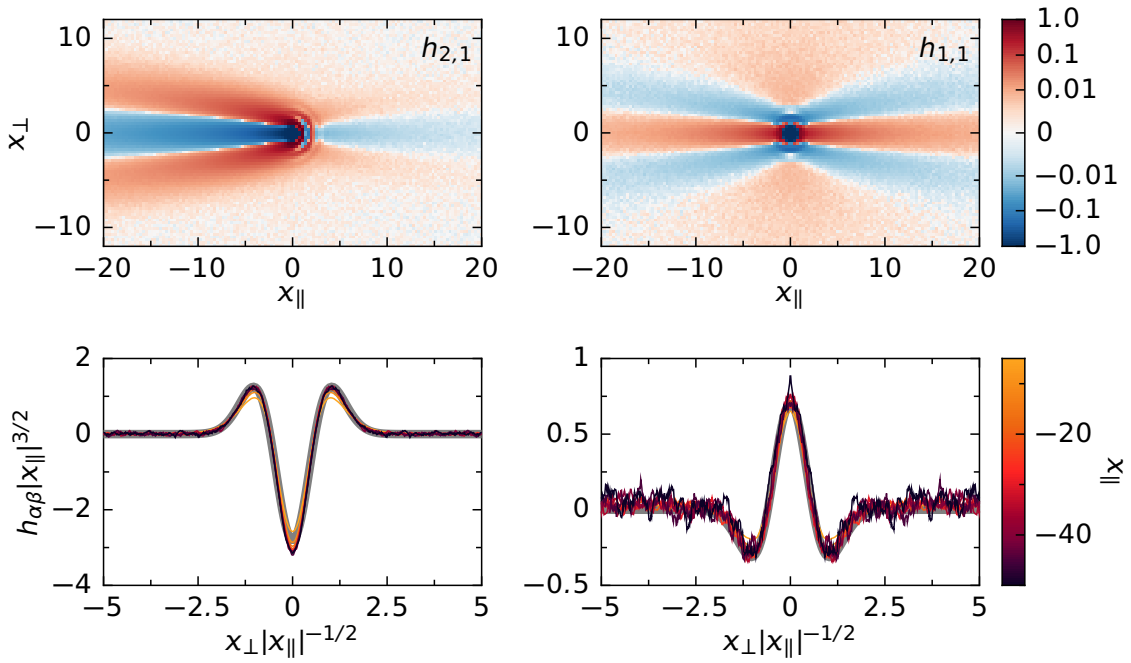

Figure 9.5: Pair correlation functions in dimension 2 for dilute and hard particles. The parameters are $\bar{\rho} = 0.2$, $T = 0.001$, $F = 0.02$, $\tau_1 = \tau_2 = 0.5$. Top: correlation functions from the simulations. Bottom: rescaled cuts of the correlations at constant $x_\parallel$ using the exponents from Eq. (9.48). The gray curves correspond to the scaling function (9.40) with adjusted horizontal and vertical factors. The agreement is perfect: this hints at a universality of the scaling form that we found.

9.5 Effective mobility

9.5.1 Definition

We consider the Langevin equation (9.2) in the case of $q = 2$ species with only the first one undergoing a force: $\mathbf{F}_1 \neq \mathbf{0}$, $\mathbf{F}_2 = \mathbf{0}$. The average velocity $\mathbf{V}_1$ of particles of species 1 is defined as

$$\mathbf{V}_1 \equiv \frac{1}{N_1} \sum_{i \in \mathscr{T}_1} \langle \mathbf{X}_i \rangle. \tag{9.59}$$

By symmetry, it has to be in the direction of the force $\mathbf{F}_1$. We call the proportionality coefficient κ_{eff} the effective mobility,

$$\mathbf{V}_1 \equiv \kappa_{\text{eff}} \mathbf{F}_1. \tag{9.60}$$

The effective mobility quantifies the hindering of the motion of a particle due to the presence of the other particles. In the absence of interactions (potential $V(\mathbf{x}) = 0$), it is simply the mobility, we previously set it to one: $\kappa_{\text{eff}} = 1$. In an electrolytic solution, the effective mobility is closely linked to the conductivity of the solution [2].

The velocity $\mathbf{V}_1$ can be computed from the Langevin equation (9.2),

$$\mathbf{V}_1 = \mathbf{F}_1 - \frac{1}{N_1} \left\langle \sum_{i \in \mathscr{T}_1} \sum_{j \neq i} \nabla_i V(\mathbf{X}_i(t) - \mathbf{X}_j(t)) \right\rangle. \tag{9.61}$$

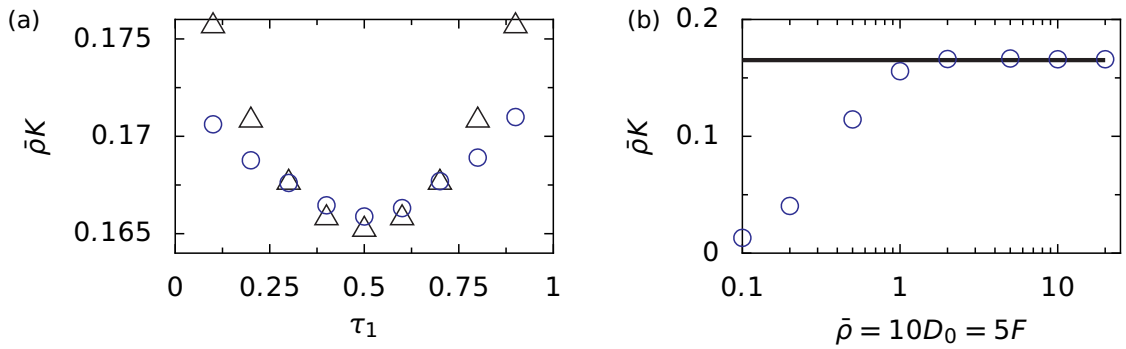

Figure 9.6: Mobility $\kappa_{\text{eff}} = 1 - \tau_2 K$. (a) Value of K for $\bar{\rho} = 2$, $D_0 = 0.2$, $F = 4$ as a function for the proportion of driven particles τ_1. The blue circles correspond to simulations, while the black triangles are the predictions from Eq. (9.69). (b) We choose to impose $\bar{\rho} = 10D_0 = 5F$ with $\tau_1 = 0.5$, so that our prediction for $\bar{\rho}K$ is constant [Eq. (9.69)]; it corresponds to the black line. The blue circles are the values corresponding to numerical simulations for various densities. We see that our approach leads to quantitative results at high density.

This can be projected along the direction of the force and leads to

$$\kappa_{\text{eff}} = 1 - \frac{1}{N_1 F_1} \left\langle \sum_{i \in \mathscr{T}_1} \sum_{j \neq i} \partial_{\parallel} V(\mathbf{X}_i(t) - \mathbf{X}_j(t)) \right\rangle . \tag{9.62}$$

$\partial_{\parallel}$ denotes the derivative along the direction of the force. The absence of interactions ($V = 0$) indeed gives $\kappa_{\text{eff}} = 1$. We shall now see that the term involving the potential can be expressed exactly in terms of the correlations.

9.5.2 Link with the correlation functions

Remembering the definition of the densities [Eq. (9.3)] and using the invariance by translation, one transforms Eq. (9.62) into

$$\kappa_{\text{eff}} = 1 - \frac{1}{\bar{\rho}_1 F_1} \int d\mathbf{x}\, \partial_{\parallel} V(\mathbf{x}) \left\langle \rho_1(\mathbf{x}) \rho_1(\mathbf{0}) + \rho_1(\mathbf{x}) \rho_2(\mathbf{0}) \right\rangle . \tag{9.63}$$

And, from the definition of $h_{\alpha,\beta}$ [Eq. (9.13)], we have

$$\langle \rho_\alpha(\mathbf{x}) \rho_\beta(\mathbf{0}) \rangle = \bar{\rho}_\alpha \bar{\rho}_\beta \left[1 + h_{\alpha,\beta} \right] + \bar{\rho}_\beta \delta_{\alpha,\beta} \delta(\mathbf{x}). \tag{9.64}$$

We inject this into the expression of κ_{eff}. We use the facts that $\partial_{\parallel} V(\mathbf{0}) = 0$ and that $\partial_{\parallel} V(\mathbf{x}) h_{1,1}(\mathbf{x})$ is an even function (particles of the same species do not slow down each other). Our final relation is

$$\kappa_{\text{eff}} = 1 - \frac{\bar{\rho}_2}{F_1} \int d\mathbf{x}\, \partial_{\parallel} V(\mathbf{x}) h_{1,2}(\mathbf{x}). \tag{9.65}$$

Let us stress that this is an exact relation between the effective mobility and the cross-correlations $h_{1,2}$. It is an analog, for binary mixtures, of the pressure equation (8.51) that we studied in the

case of passive liquids. We prefer to rewrite it as

$$\kappa_{\text{eff}} = 1 - \tau_2 K, \tag{9.66}$$

$$K = \frac{\bar{\rho}}{F_1} \int d\mathbf{x}\, \partial_{\parallel} V(\mathbf{x}) h_{1,2}(\mathbf{x}). \tag{9.67}$$

τ_2 is the fraction of non-driven particles hindering the motion of the others, and it can be shown (see [P1]) that K is symmetric with respect to the fraction of driven particles: $K(\tau_1, \tau_2 = 1-\tau_1) = K(\tau_2, \tau_1)$. Note that K can also be written as an integral in Fourier space,

$$K = -\frac{\bar{\rho}}{F_1} \int \frac{d\mathbf{k}}{(2\pi)^d} i k_{\parallel} \tilde{V}(\mathbf{k}) \tilde{h}_{1,2}(\mathbf{k}). \tag{9.68}$$

9.5.3 Linearized approximation

We use our results for the correlations in the linearized approximation (9.29) and inject them into (9.66). We obtain $\kappa_{\text{eff}} = 1 - \tau_2 K$ with

$$K = \frac{1}{\bar{\rho}} \int \frac{d\mathbf{k}}{(2\pi)^d} \frac{\tilde{\nu}^2 (2+\tilde{\nu}) k_{\parallel}^2 k^2}{(1+\tilde{\nu})(2+\tilde{\nu})^2 + (1+\tau_1\tilde{\nu})(1+\tau_2\tilde{\nu}) \frac{k_{\parallel}^2 f^2}{k^4}}, \tag{9.69}$$

and $f = F/D_0$. This expression can be integrated numerically and compared to numerical simulations (Fig. 9.6). In subsection 8.3.1, we explained that our approximation is valid for a dense system with weak interactions, $\bar{\rho} \to \infty$ with $\bar{\rho} V(\mathbf{x})$ constant. In numerical simulations, the potential strength is set to one: the regime of weak interactions corresponds to large D_0 and F (with constant F/D_0). For this reason, in Fig. 9.6b we choose $\bar{\rho}/D_0$ constant and F/D_0 constant with $\bar{\rho}$ that varies. With this, $\bar{\rho}K$ remains constant. We are able to check that we obtain a quantitative agreement between the theory and the simulations in the right end of Fig. 9.6b, this corresponds indeed to the regime of high density and weak interactions. This figure justifies our choice of density $\bar{\rho} = 2$ in the other figures. Fig. 9.6a finally shows that a correct dependence of the mobility on the tracers' fraction is predicted by our approach in its validity regime (even if some discrepancies are observed).

9.6 Conclusion

In this chapter, we studied a driven binary mixture: a system where some particles are driven by an external field and some are not (or equivalently, are driven in the opposite direction). We used the framework based on the linearized Dean equation that we introduced in the previous chapter. It gives us access to the pair correlations in a regime of weak interactions (that corresponds in this case to a high density). We uncovered a universal scaling form satisfied by both the inter-species and the intra-species correlations. The scaling form is associated with an algebraic decay ($x_{\parallel}^{-(d+1)/2}$) along the drive and with a diffusive scaling in the perpendicular direction. It can be explained by simple arguments and was found to hold in numerical simulations outside of the validity regime of our approach. Finally, we computed the effective mobility of the particles and showed that it gives quantitative results in the validity regime of the linearization.

While the study of linear perturbations around an homogeneous profile will not give a definitive answer on the existence of a laning transition, we can nevertheless make a few comments.

The most simple one is that particles of the same species are positively correlated along the drive, while particles of different species are negatively correlated in this direction. Hence, there is some kind of "laning". One strength of our approach is that it holds for arbitrary forces (and not only small forces). And nothing in our results hints that a transition may occur at a given force. This is in agreement with simulations of very large systems [51] that point towards a smooth crossover towards lanes. Moreover, we do find a power-law decay of the correlations along the drive as was hinted at in Ref. [60] but this does not seem to be associated with a phase transition. These long-range correlations hold for any external force (and not at a given critical point).

In the next chapter, we study a different system, in the field of active matter: active Brownian particles.

Chapter 10

Active Brownian particles

Contents

10.1 Introduction

In the previous chapter, we studied the pair correlations of an out-of-equilibrium system composed of particles driven by an external electric field. We uncovered a power-law decay associated with a scaling form. We now focus on a paradigmatic model of active matter: active Brownian particles

(ABPs) and conduct a similar analysis that will lead us to exhibit similar scaling forms in some limit regimes.

Let us recall a few things about active matter, a field that has received a lot of attention in the past twenty years. In some out-of-equilibrium systems, such as driven binary mixtures considered previously, energy is injected at large scale via an external potential. On the contrary, in active matter systems, energy is injected at the scale of the particles: this means that each particle has its own motor which enables it to self-propel. Usual examples in the living world include flocks of birds [18], herds of sheeps [19] and crowds of humans [17] at the macroscopic scale; and bacteria [11–13] and microtubules [14] at the microscopic scale. In all these systems, the main goal is to understand how a collective dynamics emerges from local rules governing the motion of individuals. To get a better insight into this issue, various experimental model systems have been introduced to study active matter in laboratory under controlled conditions. In Chapter 11, we will compare our theoretical results to experiments of electrophoretic Janus particles [77–80]. Other examples of artificial active matter systems include catalytic Janus particles [81–83], Quincke rollers [84, 85], vibrated polar disks [86] and interacting hexbugs [87].

Active matter systems are very diverse and so are their theoretical descriptions. Broadly speaking one distinguishes between systems with and without alignment. One of the most popular models that incorporate alignment is the Vicsek model [88] in which self-propelled point-like particles align with their neighbors (with noise). This model exhibits a transition towards ordered collective motion and shows giant number fluctuations in this ordered phase [89]. It is a paradigmatic model of active polar liquids, which can be described at large scale by Toner and Tu hydrodynamics [61, 62]. Note that alignment effects are not always explicit and can also take the form of velocity-orientation couplings [87, 90]. On the other hand, some systems do not show alignment and their collective effects are a mere consequence of self-propulsion. Two models of such systems, that were shown to be closely related [91, 92], are active Brownian particles (ABPs) described below, and run-and-tumble particles that move at constant speed in a constant direction with reorientations happening at exponentially distributed times. These models show an effective attraction between particles leading to a phase separation that we describe below.

The central model of this chapter is active Brownian particles (see Fig. 10.1). Each particle is embedded with an orientation and moves at constant velocity along it. Moreover, the orientation is diffusive and a translational noise is added to the position of the particle. The propagator of an isolated particle is known in dimensions 2 and 3 [93, 94], but the most characteristic behaviors occur for interacting ABPs. At high activity (large velocity), it has been shown that the system spontaneously separates into two phases of large and small density [52]. This phenomenon is called motility-induced phase separation (MIPS) and is a very important feature of the system. The pressure of ABPs has been shown to be a state function [95] and this fact has been used recently to compute the phase diagram (density versus activity) of active Brownian hard spheres [53]. This bridges the gap between melting (passive hard spheres) and MIPS (highly active hard spheres). The homogeneous phase of ABPs has received comparatively few attention so far. Nevertheless, focusing on dilute and soft ABPs we will show that this phase is very different from an equilibrium liquid.

Our main goal is the computation of the pair correlations of soft ABPs, and in particular of their spatial structure. Some studies approximate the activity as a colored noise and switch to the model of active Ornstein-Uhlenbeck particles for which the velocity autocorrelation decays exponentially [54, 55, 96]. This approach gives the angular average of the pair correlations but crucially misses the spatial structure. A second framework consists in starting from the many-body Smoluchowski equation, writing a closure relation and solving numerically the nonlinear

equations obtained [56,57,97]. This provides quantitative results for the effective velocity (which is linked to the correlations) but does not characterize analytically the pair correlations.

In this chapter, we use the method introduced previously (linearization of the Dean equation) to obtain analytical results for the pair correlations of dilute and soft active Brownian particles. We derive a closed equation satisfied by these correlations and solve it in the three limits of low activity, low rotational diffusion and low translational diffusion. The first one is associated with an exponential decay, but the other two limits reveal scaling forms striking both in their overall shape (structure with wings) and in their decay exponents. Overall, the picture can be unified on a phase diagram (Fig. 10.6) which enables us to predict the structure of the correlations for a given set of parameters.

The results of this chapter have been published in [P5].

10.2 Theoretical approach

10.2.1 Coupled Langevin equations for active Brownian particles

We consider interacting active Brownian particles in dimension 2 (see Fig. 10.1). Each particle is characterized by a couple position-orientation $(\mathbf{X}_i, \Theta_i)$. Due to an internal mechanism, particles move with a velocity of constant norm U and direction given by the orientation. This orientation is assumed to be diffusive with a rotational diffusion constant D_r. We also consider translational diffusion with a diffusion constant D_0. As in the two previous chapters, particles interact via a pair potential $V(\mathbf{r})$ that we assume to be isotropic. The positions $\mathbf{X}_i$ and the orientations Θ_i obey the following coupled Langevin equations.

$$\frac{d\mathbf{X}_i}{dt} = U\hat{\mathbf{e}}_{\Theta_i(t)} - \sum_{j\neq i} \nabla_i V(\mathbf{X}_i(t) - \mathbf{X}_j(t)) + \boldsymbol{\eta}_i(t), \tag{10.1}$$

$$\frac{d\Theta_i}{dt} = \nu_i, \tag{10.2}$$

where $\hat{\mathbf{e}}_\theta$ is the unit vector making an angle θ with the horizontal axis. The noises $\boldsymbol{\eta}$ and ν are Gaussian white noises with zero average and correlations

$$\langle \eta_i^\alpha(t)\eta_j^\beta(t')\rangle = 2D_0\delta_{i,j}\delta^{\alpha,\beta}\delta(t-t'), \tag{10.3}$$

$$\langle \nu_i(t)\nu_j(t')\rangle = 2D_r\delta_{i,j}\delta(t-t'). \tag{10.4}$$

Remark: arbitrary dimension

We chose to consider a system in dimension 2 but nothing prevents us from studying an arbitrary dimension d (in particular $d = 3$). In this case, the orientation $\hat{\mathbf{e}}_\theta$ is replaced by a vector $\hat{\mathbf{s}}$ living on $\mathscr{S}$, the unit sphere embedded in d-dimensional space. One should make the following substitutions in the computations that come later.

- The orientation becomes a Brownian process on the sphere $\mathscr{S}$.
- 2π factors are replaced by $|\mathscr{S}|$, the area of the sphere $\mathscr{S}$.
- The first (resp. second) derivative with respect to θ becomes the gradient $\nabla_{\mathscr{S}}$ (resp. the Laplacian $\nabla^2_{\mathscr{S}}$) on the sphere $\mathscr{S}$.

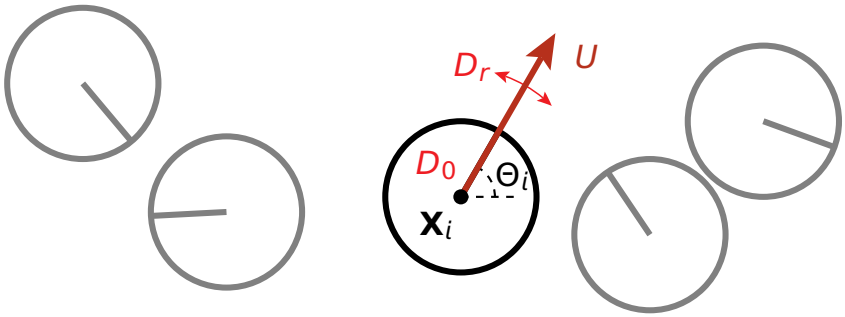

Figure 10.1: Sketch of active Brownian particles. A given particle is at position $\mathbf{X}_i$ and has an orientation Θ_i. It moves at velocity U along its orientation and undergoes rotational and translational diffusion with respective coefficients D_r and D_0. The particles interact by a pair potential $V(\mathbf{r})$.

- Fourier series are generalized into spherical harmonics which are the eigenvectors of the Laplacian $\nabla^2_{\mathscr{S}}$. The lowest eigenvectors (equivalent to the order 1 of Fourier series) are the vectors of the unit sphere: for $\hat{\mathbf{s}} \in \mathscr{S}$, $\nabla^2_{\mathscr{S}}\hat{\mathbf{s}} = -(d-1)\hat{\mathbf{s}}$. There are d linearly independent unit vectors, those of the canonical basis.

10.2.2 Exact Dean equation

We define the density $f(\mathbf{x},\theta,t)$ in the phase space $(\mathbf{x},\theta)$ as

$$f(\mathbf{x},\theta,t) = \sum_{i=1}^{N}\sum_{m=-\infty}^{\infty} f_i(\mathbf{x},\theta+2m\pi,t) \tag{10.5}$$

with the individual densities

$$f_i(\mathbf{x},\theta,t) = \delta(\mathbf{X}_i(t)-\mathbf{x})\delta(\Theta_i(t)-\theta). \tag{10.6}$$

We consider a smooth and fastly decaying test function $\varphi(\mathbf{r},\theta)$. By definition of f_i,

$$\varphi(\mathbf{X}_i(t),\Theta_i(t)) = \int d\mathbf{r}\int_{-\infty}^{\infty} d\theta f_i(\mathbf{r},\theta,t)\varphi(\mathbf{r},\theta). \tag{10.7}$$

Then, the time derivative of $\varphi(\mathbf{X}_i(t),\Theta_i(t))$ can be written in two different ways:

$$\frac{d}{dt}\varphi(\mathbf{X}_i(t),\Theta_i(t)) = \int d\mathbf{x}\int_{-\infty}^{\infty} d\theta \frac{\partial f_i}{\partial t}(\mathbf{x},\theta,t)\varphi(\mathbf{x},\theta) \tag{10.8}$$

$$= \int d\mathbf{x}\int_{-\infty}^{\infty} d\theta f_i(\mathbf{x},\theta,t)(dt)^{-1}d\varphi(\mathbf{x},\theta). \tag{10.9}$$

The differential $d\varphi$ is given by the Itô formula [73],

$$d\varphi = \nabla\varphi\cdot d\mathbf{X}_i + \frac{\partial\varphi}{\partial\theta}d\Theta_i + \frac{1}{2}\nabla^2\varphi(d\mathbf{X}_i)^2 + \frac{1}{2}\frac{\partial^2\varphi}{\partial\theta^2}d\Theta_i^2 + \frac{\partial}{\partial\theta}\nabla\varphi\cdot d\mathbf{X}_i d\Theta_i \tag{10.10}$$

$$= \nabla\varphi\cdot\left\{-\nabla_i\sum_j V(\mathbf{X}_i-\mathbf{X}_j) + U\hat{\mathbf{e}}_{\Theta_i}\right\}dt + D_0 dt\nabla^2\varphi + D_r dt\frac{\partial^2\varphi}{\partial\theta^2}. \tag{10.11}$$

The differentials $d\mathbf{X}_i$ and $d\Theta_i$ are computed from Eqs. (10.1) and (10.2) (we assumed $\nabla V(\mathbf{0}) = \mathbf{0}$). Performing the necessary integrations by parts and recalling that the function φ is arbitrary, one obtains

$$\frac{\partial f_i}{\partial t} = D_0 \nabla^2 f_i + D_r \frac{\partial^2 f_i}{\partial^2 \theta} + \nabla \left(f_i \sum_{j=1}^{N} \nabla V(\mathbf{x} - \mathbf{X}_j(t)) \right) - U \mathbf{e}_\theta \cdot \nabla f_i - \sqrt{2D_0} \nabla f_i \cdot \boldsymbol{\eta}_i - \sqrt{2D_r} \frac{\partial}{\partial \theta} (f_i \nu_i). \tag{10.12}$$

Using Eq. (10.5) and rearranging the noises like Dean [58], we finally obtain the following Dean equation for $f(\mathbf{x}, \theta, t)$,

$$\frac{\partial}{\partial t} f(\mathbf{x}, \theta, t) = -\nabla \mathbf{J}(\mathbf{x}, \theta, t) - \frac{\partial}{\partial \theta} K(\mathbf{x}, \theta, t). \tag{10.13}$$

$\mathbf{J}$ and K are currents reflecting the conservation of the number of particles. They read

$$\begin{aligned} \mathbf{J}(\mathbf{x}, \theta, t) = &-D_0 \nabla f(\mathbf{x}, \theta, t) - f(\mathbf{x}, \theta, t) \int_0^{2\pi} d\theta (\nabla V * f)(\mathbf{x}, \theta, t) + f(\mathbf{x}, \theta, t) U \hat{\mathbf{e}}_\theta \\ &- f^{1/2}(\mathbf{x}, \theta, t) \boldsymbol{\eta}(\mathbf{x}, \theta, t) \end{aligned} \tag{10.14}$$

$$K(\mathbf{x}, \theta, t) = -D_r \frac{\partial}{\partial \theta} f(\mathbf{x}, \theta, t) - f^{1/2}(\mathbf{x}, \theta, t) \nu(\mathbf{x}, \theta, t). \tag{10.15}$$

As usual, the spatial convolution is $(f * g)(\mathbf{x}) = \int d\mathbf{x}' f(\mathbf{x}') g(\mathbf{x} - \mathbf{x}')$. $\boldsymbol{\eta}$ and ν are Gaussian white noises with zero average and correlations

$$\langle \eta^\alpha(\mathbf{x}, \theta, t) \eta^\beta(\mathbf{x}', \theta', t') \rangle = 2D_0 \delta^{\alpha\beta} \delta(\mathbf{x} - \mathbf{x}') \delta(\theta - \theta') \delta(t - t'), \tag{10.16}$$

$$\langle \nu(\mathbf{x}, \theta, t) \nu(\mathbf{x}', \theta', t') \rangle = 2D_r \delta(\mathbf{x} - \mathbf{x}') \delta(\theta - \theta') \delta(t - t'). \tag{10.17}$$

10.2.3 Linearized Dean equation

As usual, the Dean equation is non linear with multiplicative noise. We linearize it around an homogeneous profile as done in the previous chapters. Let us denote $\bar{\rho}$ the average density of particles. One sees that the average over space of $f(\mathbf{x}, \theta, t)$ is $\bar{\rho}/(2\pi)$. The linearization reads

$$f(\mathbf{r}, \theta, t) = \frac{\bar{\rho}}{2\pi} + \sqrt{\frac{\bar{\rho}}{2\pi}} \phi(\mathbf{r}, \theta, t). \tag{10.18}$$

The field ϕ is assumed to be of order 1 in $\bar{\rho}$. We also scale the potential with $\bar{\rho}$ and write

$$V(\mathbf{r}) \equiv \frac{v(\mathbf{r})}{\bar{\rho}}. \tag{10.19}$$

At the lowest order, the Dean equation (10.12) becomes linear with additive noise.

$$\frac{\partial \phi}{\partial t} = \left[D_0 \nabla^2 + D_r \frac{\partial^2}{\partial \theta^2} - U \hat{\mathbf{e}}_\theta \cdot \nabla \right] \phi + \frac{1}{2\pi} \int_0^{2\pi} d\theta' (\nabla^2 v * \phi)(\theta') + \nabla \cdot \boldsymbol{\eta} + \frac{\partial \nu}{\partial \theta}. \tag{10.20}$$

We define the Fourier transform $\tilde{\phi}(\mathbf{k}, \theta, t) = \int d\mathbf{x} e^{-i\mathbf{k}\cdot\mathbf{x}} \phi(\mathbf{x}, \theta, t)$ and obtain

$$\frac{\partial \tilde{\phi}}{\partial t} = \left[-D_0 k^2 + D_r \partial_\theta^2 - iU\mathbf{k} \cdot \hat{\mathbf{e}}_\theta \right] \tilde{\phi} - \frac{k^2 \tilde{v}(\mathbf{k})}{2\pi} \int_0^{2\pi} d\theta' \tilde{\phi}(\mathbf{k}, \theta') + \tilde{\boldsymbol{\eta}}(\mathbf{k}, \theta) + \partial_\theta \tilde{\nu}. \tag{10.21}$$

In Fourier space, the noises have the following covariances

$$\langle \tilde{\eta}(\mathbf{k}, \theta, t) \tilde{\eta}(\mathbf{k}', \theta', t') \rangle = 2(2\pi)^2 D_0 k^2 \delta(\mathbf{k} + \mathbf{k}') \delta(\theta - \theta') \delta(t - t') \tag{10.22}$$

$$\langle \tilde{\nu}(\mathbf{k}, \theta, t) \tilde{\nu}(\mathbf{k}, \theta, t) \rangle = 2(2\pi)^2 D_r \delta(\mathbf{k} + \mathbf{k}') \delta(\theta - \theta') \delta(t - t'). \tag{10.23}$$

10.3 Correlations

10.3.1 Definitions

Our system is invariant by translation, we define the correlation of the density field f between point $(\mathbf{0},\theta)$ and point $(\mathbf{r},\theta')$ as

$$C(\mathbf{r},\theta,\theta') \equiv \frac{\left\langle f(\mathbf{0},\theta) f(\mathbf{r},\theta')\right\rangle}{[\bar{\rho}/(2\pi)]^2} - \frac{\delta(\mathbf{r})\delta(\theta-\theta')}{\bar{\rho}/(2\pi)} - 1. \tag{10.24}$$

The second term is the correlation of a given particle with itself and the third is the $r \to \infty$ limit. By rotational invariance, all the information is contained in $C(\mathbf{r},0,\theta')$. Our key observable will be the integration of this function with respect to θ'.

$$B(\mathbf{r}) = \frac{1}{2\pi}\int_0^{2\pi} C(\mathbf{r},0,\theta')d\theta'. \tag{10.25}$$

Intuitively $B(\mathbf{r})$ is the density seen by a given particle in its reference frame. One should note that with our convention, the correlations without self-propulsion ($U=0$, passive system) read

$$C(\mathbf{r}) = B(\mathbf{r}) = h(\mathbf{r}) \tag{10.26}$$

with the usual definition of the pair correlation $h(\mathbf{r})$.

Due to our definition of the linearized Dean equation, it is also useful to define the correlation of the field ϕ between coordinates $(\mathbf{r}_1,\theta_1)$ and $(\mathbf{r}_2,\theta_2)$,

$$\mathscr{C}(\mathbf{r}_1,\mathbf{r}_2,\theta_1,\theta_2,t) \equiv \langle \phi(\mathbf{r}_1,\theta_1,t)\phi(\mathbf{r}_2,\theta_2,t)\rangle. \tag{10.27}$$

$C(\mathbf{r},\theta,\theta')$ is then given by

$$C(\mathbf{r},\theta,\theta',t) = \frac{1}{\bar{\rho}}\left\{\mathscr{C}(\mathbf{0},\mathbf{r},\theta,\theta',t) - \delta(\mathbf{r})\delta(\theta-\theta')\right\}. \tag{10.28}$$

10.3.2 Full equation in the linearized regime

We use Itô calculus to compute the time evolution of $\mathscr{C}$ [Eq. (10.27)].

$$\begin{aligned}&\mathscr{C}(\mathbf{r}_1,\mathbf{r}_2,\theta_1,\theta_2,t+\delta t) - \mathscr{C}(\mathbf{r}_1,\mathbf{r}_2,\theta_1,\theta_2,t) = \\ &\quad\langle \phi(\mathbf{r}_1,\theta_1,t)\delta\phi(\mathbf{r}_2,\theta_2,t)\rangle + \langle \delta\phi(\mathbf{r}_1,\theta_1,t)\phi(\mathbf{r}_2,\theta_2,t)\rangle + \langle \delta\phi(\mathbf{r}_1,\theta_1,t)\delta\phi(\mathbf{r}_2,\theta_2,t)\rangle,\end{aligned} \tag{10.29}$$

where $\delta\phi(\mathbf{r},\theta,t)$ is the variation of the field during δt. It is given by the linearized Dean equation (10.20). Computing the different terms from the linearized Dean equation (10.20), one shows that

$$\begin{aligned}\partial_t \mathscr{C}(\mathbf{r}_1,\mathbf{r}_2,\theta_1,\theta_2) = &\left[D_0(\nabla_1^2+\nabla_2^2) + D_r(\partial_{\theta_1}+\partial_{\theta_2}) - U(\hat{\mathbf{e}}_{\theta_1}\cdot\nabla_1 + \hat{\mathbf{e}}_{\theta_2}\cdot\nabla_2)\right]\mathscr{C}(\mathbf{r}_1,\mathbf{r}_2,\theta_1,\theta_2) \\ &+ \frac{1}{2\pi}\int_0^{2\pi} d\theta'\left[\nabla_1^2 v * \mathscr{C}(\mathbf{r}_1,\mathbf{r}_2,\theta',\theta_2) + \nabla_2^2 v * \mathscr{C}(\mathbf{r}_1,\mathbf{r}_2,\theta_1,\theta')\right] \\ &+ \left[2D_0\nabla_1\nabla_2 + 2D_r\partial_{\theta_1}\partial_{\theta_2}\right]\delta(\mathbf{r}_1-\mathbf{r}_2)\delta(\theta_1-\theta_2).\end{aligned} \tag{10.30}$$

We immediately use the invariance of the system by translation and write the equation in terms of $C(\mathbf{r},\theta,\theta')$ [Eq. (10.28)],

$$\partial_t C(\mathbf{r},\theta,\theta') = \left[2D_0\nabla^2 + D_r(\partial_\theta + \partial_{\theta'}) + U(\hat{\mathbf{e}}_\theta - \hat{\mathbf{e}}_{\theta'})\cdot\nabla\right]C(\mathbf{r},\theta,\theta') + 2\nabla^2 V(\mathbf{r}) + \frac{\bar{\rho}}{2\pi}\int_0^{2\pi} d\theta''\nabla^2 v * \left[C(\mathbf{r},\theta,\theta'') + C(\mathbf{r},\theta'',\theta')\right]. \quad (10.31)$$

In the following, we are only interested in the stationary correlations. They satisfy the following linear partial differential equation.

$$\left[2D_0\nabla^2 + D_r(\partial_\theta + \partial_{\theta'}) + U(\hat{\mathbf{e}}_\theta - \hat{\mathbf{e}}_{\theta'})\cdot\nabla\right]C^{\mathrm{stat}}(\mathbf{r},\theta,\theta') + \frac{\bar{\rho}}{2\pi}\int_0^{2\pi} d\theta''\nabla^2 v * \left[C^{\mathrm{stat}}(\mathbf{r},\theta,\theta'') + C^{\mathrm{stat}}(\mathbf{r},\theta'',\theta')\right] = -2\nabla^2 V(\mathbf{r}). \quad (10.32)$$

Note that due to the term $\hat{\mathbf{e}}_\theta\cdot\nabla$, it is not possible to write a closed equation for $B(\mathbf{r})$.

10.3.3 Equation for the direct correlation functions

At low enough density, the three-body effects encoded in the term involving a convolution with the potential can be neglected. We consider the *direct correlation functions* $C_d(\mathbf{x},\theta,\theta',t)$ that describe only the two-body effects. They are solution of the time-dependent equation

$$\partial_t C_d(\mathbf{x},\theta,\theta') = \left[2D_0\nabla^2 + D_r(\partial_\theta + \partial_{\theta'}) + U(\hat{\mathbf{e}}_\theta - \hat{\mathbf{e}}_{\theta'})\cdot\nabla\right]C_d(\mathbf{x},\theta,\theta') + 2\nabla^2 V(\mathbf{x}). \quad (10.33)$$

Their stationary value satisfies

$$\left[2D_0\nabla^2 + D_r(\partial_\theta + \partial_{\theta'}) + U(\hat{\mathbf{e}}_\theta - \hat{\mathbf{e}}_{\theta'})\cdot\nabla\right]C_d^{\mathrm{stat}}(\mathbf{r},\theta,\theta') = -2\nabla^2 V(\mathbf{r}), \quad (10.34)$$

and their integral over θ' is called $B_d(\mathbf{r})$,

$$B_d(\mathbf{r}) = \frac{1}{2\pi}\int_0^{2\pi} C_d(\mathbf{r},0,\theta')d\theta'. \quad (10.35)$$

Note that Eqs. (10.33) and (10.34), which are the analogs of Eqs. (10.31) and (10.32), are our definitions of the direct correlation functions.

We shall now explain our choice of words "direct correlation functions". Let us consider the passive case $U = 0$ in which $C^{\mathrm{stat}}(\mathbf{r},\theta,\theta') = B^{\mathrm{stat}}(\mathbf{r})/(2\pi)$. Eq. (10.34) enables us to write the potential v in terms of B^{stat}. Performing the substitution into Eq (10.32) one obtains

$$B^{\mathrm{stat}}(\mathbf{r}) = B_d^{\mathrm{stat}}(\mathbf{r}) + (B_d^{\mathrm{stat}} * B^{\mathrm{stat}})(\mathbf{r}). \quad (10.36)$$

This is the well-known Ornstein-Zernike equation [1] that relates the correlations B to the direct correlations B_d. Moreover, for a passive system, the stationary solution is

$$B_d^{\mathrm{passive}}(\mathbf{x}) = -\frac{\bar{\rho}V(\mathbf{x})}{D_0}. \quad (10.37)$$

This is the usual random phase approximation for the direct correlation functions [1]. Our definition of B_d in the active case is consistent with the usual one for liquids. We also claim that it has the same intuitive meaning: removing the term $\nabla^2 V * C$ amounts to neglecting the part of the correlations between two particles that is mediated by a third one: hence we consider only the correlations that involve interactions directly between two particles. Three-body effects are neglected.

10.3.4 Change of variables and numerical integration

We consider the time-dependent equation (10.33) for the direct correlations C_d,

$$\partial_t C_d(\mathbf{r},\theta,\theta') = \left[2D_0\nabla^2 + D_r(\partial_\theta + \partial_{\theta'}) + U(\hat{\mathbf{e}}_\theta - \hat{\mathbf{e}}_{\theta'})\cdot\nabla\right] C_d(\mathbf{r},\theta,\theta') + 2\nabla^2 V(\mathbf{r}). \tag{10.38}$$

In polar coordinates, we write $\mathbf{r} = r\mathbf{e}_\phi$. The latter equation depends on four coordinates (plus time): (r,ϕ,θ,θ'). By performing a rotation of angle θ, the symmetries enable one to reduce the problem to three parameters (r,α,β),

$$\alpha = \phi - \theta, \qquad \beta = \theta' - \theta. \tag{10.39}$$

We write $\mathbf{x} = r\mathbf{e}_\alpha = (x,y)$, C_d is then a function only of $\mathbf{x}$ and β. Its time evolution is given by

$$\partial_t C_d(\mathbf{x},\beta) = \left[2D_0\nabla^2 + D_r\mathscr{L}_{\text{angles}} + U\left((1-\cos\beta)\frac{\partial}{\partial x} - \sin\beta\frac{\partial}{\partial y}\right)\right] C_d(\mathbf{x},\beta) + 2\nabla^2 V(\mathbf{x}), \tag{10.40}$$

$$\nabla^2 = \frac{\partial^2}{\partial x^2} + \frac{\partial^2}{\partial y^2}, \tag{10.41}$$

$$\mathscr{L}_{\text{angles}} = \left(y^2\frac{\partial^2}{\partial x^2} + x^2\frac{\partial^2}{\partial y^2} - 2xy\frac{\partial^2}{\partial x\partial y} - x\frac{\partial}{\partial x} - y\frac{\partial}{\partial y}\right) + 2\left(-y\frac{\partial}{\partial x} + x\frac{\partial}{\partial y}\right)\frac{\partial}{\partial\beta} + 2\frac{\partial^2}{\partial\beta^2}. \tag{10.42}$$

It is important to note that B_d [Eq. (10.35)] is given by the integration over β,

$$B_d(\mathbf{x}) = \frac{1}{2\pi}\int_0^{2\pi} d\beta\, C_d(\mathbf{x},\beta). \tag{10.43}$$

Starting from $C_d(\mathbf{x},\beta,t=0) = 0$, one can numerically integrate Eq. (10.40) using carefully chosen steps Δt, Δx and $\Delta\beta$ for the time, position and angle. At large time, we reach the stationary solution. In Fig. 10.2, we are able to compare this numerical result for $B_d(\mathbf{r})$ to the correlations obtained in numerical simulations of the coupled Langevin equations at low density $\rho = 0.05$. The very good agreement comforts us in the theoretical study in Eq. (10.34) for the direct correlations functions.

We now study the direct correlation function in the three regimes $U \to 0$, $D_r \to 0$ and $D_0 \to 0$ in which the equation is tractable. This will lead us to a complete phase diagram (Fig. 10.6) for the structure of the correlations.

10.4 Low activity

We now consider the case of weak activity: $U \ll \sqrt{D_0 D_r}$. This is the only case in which we are able to solve for the correlations [Eq. (10.32)] and not only for the direct correlations [Eq. (10.34)].

We attempt to solve Eq. (10.32) perturbatively in the activity U. In Fourier space it reads,

$$\left[-2D_0k^2 + D_r(\partial_\theta + \partial_{\theta'})\right]\tilde{C}(\mathbf{k},\theta,\theta') - \frac{k^2\bar{\rho}\tilde{V}}{2\pi}\int_0^{2\pi} d\theta''\left[\tilde{C}(\mathbf{k},\theta,\theta'') + \tilde{C}(\mathbf{k},\theta'',\theta')\right] = 2k^2\tilde{V} - iU\mathbf{k}\cdot(\hat{\mathbf{e}}_\theta - \hat{\mathbf{e}}_{\theta'})\tilde{C}(\mathbf{k},\theta,\theta'), \tag{10.44}$$

with C that is expanded in powers of U as

$$C(\mathbf{x},\theta,\theta') = C^{(0)}(\mathbf{r}) + UC^{(1)}(\mathbf{r},\theta,\theta') + U^2C^{(2)}(\mathbf{r},\theta,\theta') + \dots \tag{10.45}$$

We now solve order by order.

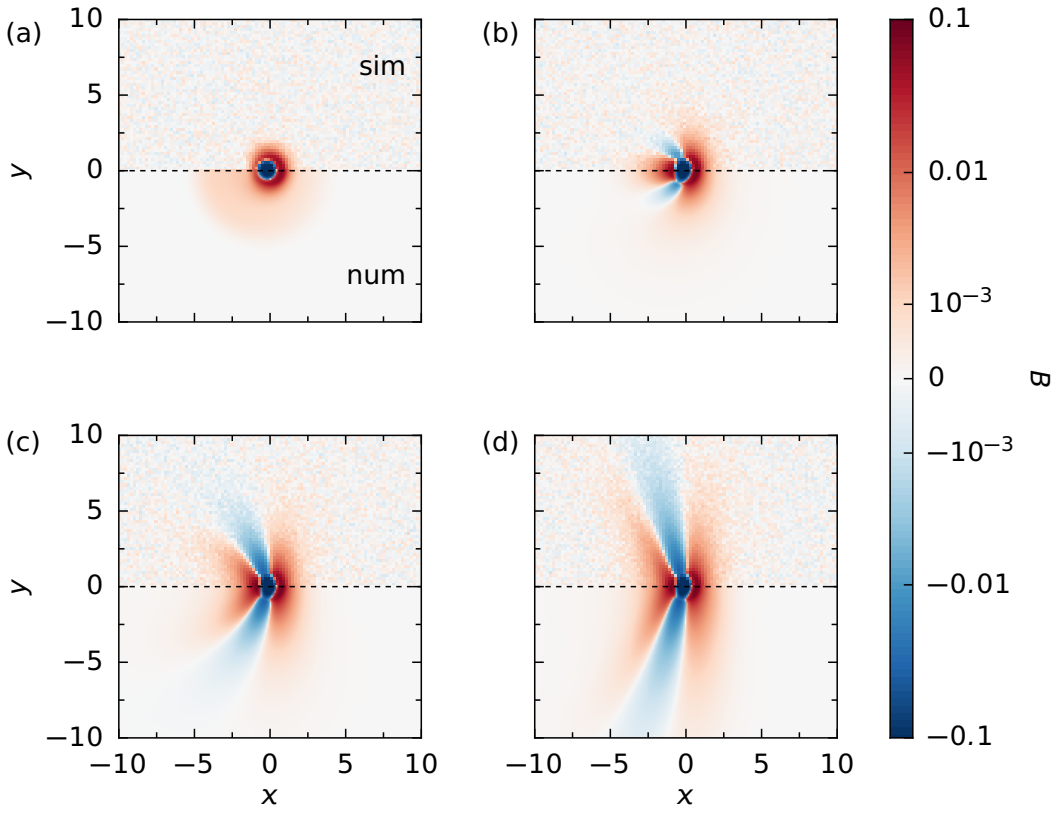

Figure 10.2: Comparison between numerical simulations of $B(\mathbf{r})$ (top) and numerical integration of Eq. (10.40) for the direct correlations $B_d(\mathbf{r})$ (bottom). Throughout this chapter we consider the soft-sphere potential $V(r) = \epsilon(1-r)^2/2$ if $r < 1$, with $\epsilon = 1$. The parameters are $\bar{\rho} = 0.05$, $D_0 = 0.1$, $U = 10$ and from (a) to (d), $D_r = 10, 1, 0.1, 0.01$. When D_r becomes smaller, wings appear. Our theoretical description will account for these wings.

10.4.1 Perturbative expansion

Order 0. The passive correlation ($U = 0$) does not depend on the angles, we immediately obtain

$$\tilde{C}^{(0)}(\mathbf{k}) = \frac{-\tilde{V}(\mathbf{k})}{D_0 + \bar{\rho}\tilde{V}(\mathbf{k})}. \tag{10.46}$$

This is the usual RPA solution that we studied in the previous chapters [Eq. (8.42)].

Order 1. Now, we write Eq. (10.44) at order one,

$$\left[-2D_0k^2 + D_r(\partial_\theta + \partial_{\theta'})\right]\tilde{C}^{(1)}(\mathbf{k},\theta,\theta') - \frac{k^2\tilde{v}}{2\pi}\int_0^{2\pi} d\theta''\left[\tilde{C}^{(1)}(\mathbf{k},\theta,\theta'') + \tilde{C}^{(1)}(\mathbf{k},\theta'',\theta')\right] = -i\mathbf{k}\cdot(\hat{\mathbf{e}}_\theta - \hat{\mathbf{e}}_{\theta'})\tilde{C}^{(0)}(\mathbf{k}), \tag{10.47}$$

with $\tilde{v} = \bar{\rho}\tilde{V}$. We plug in the following Ansatz

$$\tilde{C}^{(1)}(\mathbf{k},\theta,\theta') = i\mathbf{k}\cdot(\hat{\mathbf{e}}_\theta - \hat{\mathbf{e}}_{\theta'})\tilde{D}^{(1)}(\mathbf{k}), \tag{10.48}$$

and quickly obtain

$$\tilde{D}^{(1)}(\mathbf{k}) = \frac{\tilde{C}^{(0)}(\mathbf{k})}{(2D_0 + \tilde{v}(\mathbf{k}))k^2 + D_r}. \tag{10.49}$$

Note that the underlying structure in real space is

$$C^{(1)}(\mathbf{r}, \theta, \theta') = (\mathbf{e}_\theta - \mathbf{e}'_\theta) \cdot \nabla D^{(1)}(\mathbf{r}). \tag{10.50}$$

Order 2. The order 2 of Eq. (10.44) leads to

$$\left[-2D_0k^2 + D_r(\partial_\theta + \partial_{\theta'})\right]\tilde{C}^{(2)}(\mathbf{k}, \theta, \theta') - \frac{k^2\tilde{v}}{2\pi}\int_0^{2\pi} d\theta'' \left[\tilde{C}^{(2)}(\mathbf{k}, \theta, \theta'') + \tilde{C}^{(2)}(\mathbf{k}, \theta'', \theta')\right] = 2k^2[1 - \hat{\mathbf{e}}_\theta \cdot \hat{\mathbf{e}}_{\theta'}]\tilde{D}^{(1)}(\mathbf{k}). \tag{10.51}$$

As we are in dimension 2, $\hat{\mathbf{e}}_\theta \cdot \hat{\mathbf{e}}_{\theta'} = \cos(\theta - \theta')$. We use the following Ansatz,

$$\tilde{C}^{(2)}(\mathbf{k}, \theta, \theta') = \tilde{D}_a^{(2)}(\mathbf{k}) + \tilde{D}_b^{(2)}(\mathbf{k})\ \hat{\mathbf{e}}_\theta \cdot \hat{\mathbf{e}}_{\theta'}. \tag{10.52}$$

After injecting it into the equation, $D_a^{(2)}$ and $D_b^{(2)}$ can be expressed in terms of $D^{(1)}$ as

$$D_a^{(2)}(\mathbf{k}) = \frac{-\tilde{D}^{(1)}(\mathbf{k})}{D_0 + \tilde{v}(\mathbf{k})}, \qquad D_b^{(2)}(\mathbf{k}) = \frac{k^2\tilde{D}^{(1)}(\mathbf{k})}{D_0k^2 + D_r}. \tag{10.53}$$

Higher orders. The development can be pushed to higher orders. The complexity increases fastly with the apparition of harmonics $[\hat{\mathbf{e}}_\theta \cdot \hat{\mathbf{e}}_{\theta'}]^n = \cos^n(\theta - \theta')$. This is not very insightful and we will not detail it here. The complexity of the results that we will find at high activity will convince the reader that no simple development exists at an arbitrary order.

Result up to order 2. To summarize, the structure up to order 2, in Fourier space and in real space, is

$$\tilde{C}(\mathbf{k}, \theta, \theta') = \left[\tilde{C}^{(0)}(\mathbf{k}) + U^2\tilde{D}_a^{(2)}(\mathbf{k})\right] + iU\mathbf{k} \cdot (\hat{\mathbf{e}}_\theta - \hat{\mathbf{e}}_{\theta'})\tilde{D}^{(1)}(\mathbf{k}) + U^2\,(\hat{\mathbf{e}}_\theta \cdot \hat{\mathbf{e}}_{\theta'})\,\tilde{D}_b^{(2)}(\mathbf{k}), \tag{10.54}$$

$$C(\mathbf{r}, \theta, \theta') = \left[C^{(0)}(\mathbf{r}) + U^2D_a^{(2)}(\mathbf{r})\right] + U(\hat{\mathbf{e}}_\theta - \hat{\mathbf{e}}_{\theta'}) \cdot \nabla D^{(1)}(\mathbf{r}) + U^2\,(\hat{\mathbf{e}}_\theta \cdot \hat{\mathbf{e}}_{\theta'})\,D_b^{(2)}(\mathbf{r}), \tag{10.55}$$

$$B(\mathbf{r} = (x, y)) = \left[C^{(0)}(\mathbf{r}) + U^2D_a^{(2)}(\mathbf{r})\right] + \frac{U}{2\pi}\frac{\partial}{\partial x}D^{(1)}(\mathbf{r}) \tag{10.56}$$

with

$$\tilde{C}^{(0)}(\mathbf{k}) = \frac{-\tilde{V}(\mathbf{k})}{D_0 + \bar{\rho}\tilde{V}(\mathbf{k})}, \tag{10.57}$$

$$\tilde{D}^{(1)}(\mathbf{k}) = \frac{-\tilde{V}(\mathbf{k})}{[D_0 + \bar{\rho}\tilde{V}(\mathbf{k})][(2D_0 + \bar{\rho}\tilde{V}(\mathbf{k}))k^2 + D_r]}, \tag{10.58}$$

$$D_a^{(2)}(\mathbf{k}) = \frac{\tilde{V}(\mathbf{k})}{[D_0 + \bar{\rho}\tilde{V}(\mathbf{k})]^2[(2D_0 + \bar{\rho}\tilde{V}(\mathbf{k}))k^2 + D_r]}, \tag{10.59}$$

$$D_b^{(2)}(\mathbf{k}) = \frac{-k^2\tilde{V}(\mathbf{k})}{[D_0k^2 + D_r][D_0 + \bar{\rho}\tilde{V}(\mathbf{k})][(2D_0 + \bar{\rho}\tilde{V}(\mathbf{k}))k^2 + D_r]}. \tag{10.60}$$

Similarly for the direct correlations,

$$C_d(\mathbf{r},\theta,\theta') = \left[C_d^{(0)}(\mathbf{r}) + U^2 D_{d,a}^{(2)}(\mathbf{r})\right] + U(\hat{\mathbf{e}}_\theta - \hat{\mathbf{e}}_{\theta'})\cdot\nabla D_d^{(1)}(\mathbf{r}) + U^2(\hat{\mathbf{e}}_\theta\cdot\hat{\mathbf{e}}_{\theta'})D_{d,b}^{(2)}(\mathbf{r}), \quad (10.61)$$

$$B_d(\mathbf{r}=(x,y)) = 2\pi\left[C_d^{(0)}(\mathbf{r}) + U^2 D_{d,a}^{(2)}(\mathbf{r})\right] + 2\pi U\frac{\partial}{\partial x}D_d^{(1)}(\mathbf{r}) \quad (10.62)$$

with

$$\tilde{C}_d^{(0)}(\mathbf{k}) = \frac{-\tilde{V}(\mathbf{k})}{D_0} \qquad \tilde{D}_d^{(1)}(\mathbf{k}) = \frac{-\tilde{V}(\mathbf{k})}{D_0(2D_0k^2+D_r)} \quad (10.63)$$

$$D_{d,a}^{(2)}(\mathbf{k}) = \frac{\tilde{V}(\mathbf{k})}{D_0^2(2D_0k^2+D_r)}, \qquad D_{d,b}^{(2)}(\mathbf{k}) = \frac{-k^2\tilde{V}(\mathbf{k})}{D_0(2D_0k^2+D_r)(D_0k^2+D_r)}. \quad (10.64)$$

We remark that the modification of the polar part of the correlations occurs at the first order in the velocity $\left(U\partial_x D_d^{(1)}(\mathbf{r})\right)$ while by symmetry $U \leftrightarrow -U$, the isotropic part $h(r)$ is modified only at the second order in the velocity $\left(U^2 D_{d,a}^{(2)}(\mathbf{r})\right)$. Furthermore, the correction to this isotropic part is found to be positive. This is consistent with the effective attractive interactions between particles that have been found by other approaches [96].

10.4.2 Large distance behavior

The large distance limit corresponds to the limit $\mathbf{k}\to\mathbf{0}$. The Fourier transform of the potential is approximated by its value at 0. We make the substitution $\tilde{V}(k)\mapsto\tilde{V}(0)$. This leads us to

$$\tilde{D}^{(1)}(\mathbf{k}) \approx \frac{-\tilde{V}(0)}{D_0+\bar{\rho}\tilde{V}(0)}\frac{1}{(2D_0+\bar{\rho}\tilde{V}(0))k^2+D_r} \quad (10.65)$$

and similar expressions for the other quantities. We recall the following Fourier transform, in dimension 2,

$$\tilde{G}(\mathbf{k}) = \frac{1}{\mathbf{k}^2+\lambda^{-2}} \qquad \Leftrightarrow \qquad G(\mathbf{r}) = \frac{1}{2\pi}K_0\left(\frac{\|\mathbf{r}\|}{\lambda}\right) \quad (10.66)$$

where K_0 is a modified Bessel function of the second kind. This gives

$$D^{(1)}(\mathbf{r}) \underset{r\to\infty}{\sim} \frac{1}{2\pi}\frac{-\tilde{V}(0)}{(D_0+\bar{\rho}\tilde{V}(0))(2D_0+\bar{\rho}\tilde{V}(0))}K_0\left(\frac{\|\mathbf{r}\|}{\sqrt{2}\ell'_U}\right) \quad (10.67)$$

with the typical length

$$\ell'_U = \sqrt{\frac{D_0+\bar{\rho}\tilde{V}(0)/2}{D_r}}. \quad (10.68)$$

Finally, the large distance behavior of the correlations can be written as

$$B(r,\alpha) - B_{\text{passive}}(r,\alpha) = B_0(r) + B_1(r)\cos\alpha, \quad (10.69)$$

$$B_0(r) \underset{r\to\infty}{\sim} U^2\frac{1}{2\pi}\frac{\tilde{V}(0)}{(D_0+\bar{\rho}\tilde{V}(0))^2(2D_0+\bar{\rho}\tilde{V}(0))}K_0\left(\frac{r}{\sqrt{2}\ell'_U}\right), \quad (10.70)$$

$$B_1(r) \underset{r\to\infty}{\sim} U\sqrt{D_r}\frac{1}{2\pi}\frac{\tilde{V}(0)}{(D_0+\bar{\rho}\tilde{V}(0))(2D_0+\bar{\rho}\tilde{V}(0))^{3/2}}K_1\left(\frac{r}{\sqrt{2}\ell'_U}\right). \quad (10.71)$$

Similarly, the large distance behavior of the direct correlations is

$$B_d(r,\alpha) - B_{\text{passive}}(r,\alpha) = B_{d,0}(r) + B_{d,1}(r)\cos\alpha, \tag{10.72}$$

$$B_{d,0}(r) \underset{r\to\infty}{\sim} U^2 \frac{\tilde{V}(0)}{4\pi D_0^3} K_0\left(\frac{r}{\sqrt{2}\ell_U}\right), \tag{10.73}$$

$$B_{d,1}(r) \underset{r\to\infty}{\sim} U\sqrt{D_r}\frac{\tilde{V}(0)}{2\pi\sqrt{2}D_0^{3/2}} K_1\left(\frac{r}{\sqrt{2}\ell_U}\right), \tag{10.74}$$

with $\ell_U = \sqrt{D_0/D_r}$. We perform simulations at low density $\rho = 0.05$ and intermediate density $\rho = 0.5$. The results are shown on Fig. 10.3. At low density, the correlations and direct correlations are identical and our prediction agrees well with the data from simulations. At intermediate density, only the prediction for the correlations matches the simulations. This is the expected behavior: the direct correlations give a good prediction at low density.

We now study two cases which correspond to a high activity: vanishing rotational diffusion and vanishing translational diffusion.

10.5 Vanishing rotational diffusion

10.5.1 Expression of the direct correlations

After having studied the case of small activity, we now turn to another special case, namely the case of vanishing rotation diffusion: $D_r = 0$. Even with this simplification, Eq. (10.32) for the correlations is not tractable. Instead we study Eq. (10.34) for the direct correlations which is valid at low density. This equation is very easy to solve in Fourier space in the case $D_r = 0$. We obtain

$$\left[2D_0\nabla^2 + U(\hat{\mathbf{e}}_\theta - \hat{\mathbf{e}}_{\theta'})\cdot\nabla\right] C_d(\mathbf{r},\theta,\theta') = -2\nabla^2 V(\mathbf{r}), \tag{10.75}$$

$$\tilde{C}_d(\mathbf{k},\theta,\theta') = \frac{-2k^2\tilde{V}(\mathbf{k})}{2D_0k^2 - iU\mathbf{k}\cdot(\mathbf{e}_\theta - \mathbf{e}_{\theta'})}. \tag{10.76}$$

This result is reminiscent of the case of the binary mixture studied in the previous chapter. One should in particular remember the result for a small fraction of driven particles [Eq. (9.30)]. Here we find a "difference of forces"

$$\Delta\mathbf{F}(\theta,\theta') = U(\mathbf{e}_\theta - \mathbf{e}_{\theta'}). \tag{10.77}$$

This interpretation is reasonable because when $D_r = 0$, the orientation of the particles never changes. We can pretend handwavingly that we have an infinity of species corresponding to all orientations. Then the correlation $C_d(\theta,\theta')$ between two species in the dilute limit may be the same as the one of a binary mixture with forces $\mathbf{F}_1 = U\mathbf{e}_\theta$ and $\mathbf{F}_2 = U\mathbf{e}'_\theta$.

10.5.2 Result for the integrated direct correlations

We now want to consider the integration of Eq. (10.76) over the orientation θ' of the second particle. We introduce the relevant length scale

$$\ell_r = \frac{D_0}{U}. \tag{10.78}$$

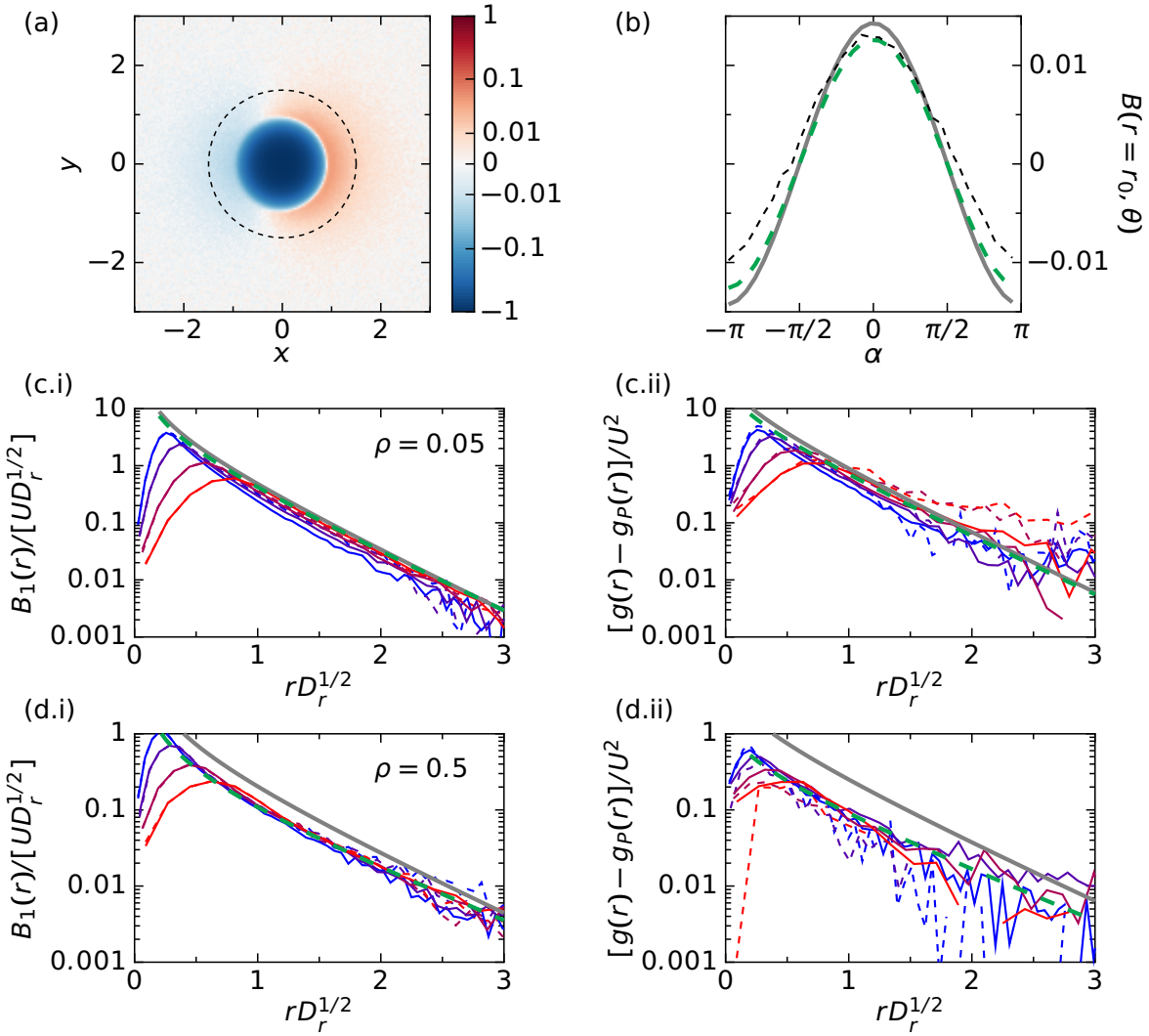

Figure 10.3: Pair correlation functions at small activity. The dashed green lines correspond to predictions for the correlation function [Eqs. (10.69)-(10.71)] while the solid gray line are predictions for the direct correlation functions [Eqs. (10.72)-(10.74)]. (a) Simulation result for the correlations $B(\mathbf{r})$ with parameters $D_0 = 0.1, D_r = 0.5, U = 0.05$. (b) Black line: cut of the correlations at $r = r_0 = 1.5$. Comparison with the predictions of cosine functions. (c.i) Rescaled first Fourier component $B_1(r)$ of $B(\mathbf{r})$. $\rho = 0.05, D_0 = 0.1$; dashed lines $U = 0.05$, solid lines $U = 0.1$; from blue to red $D_r = 0.1, 0.2, 0.5, 1$. (c.ii) Rescaled excess isotropic part of $B(\mathbf{r})$ for the same parameters. (d.i) and (d.ii) are the same as (c.i) and (c.ii) with $\rho = 0.5$ and $D_0 = 0.2$. We note that at low density (case c), both predictions match well the simulation data while at higher density (case d) the discrepancy between the correlation and direct correlation matters and only the first one matches the simulations.

Performing the integration, we obtain

$$\tilde{B}_d(\mathbf{k}) \equiv \frac{1}{2\pi}\int_0^{2\pi} d\theta \tilde{C}_d(\mathbf{k},0,\theta') = -\frac{k^2\tilde{V}(\mathbf{k})}{\pi D_0}\int_0^{2\pi}\frac{d\gamma}{2k^2 - i\ell_r^{-1}k_x + i\ell_r^{-1}k\cos\gamma} \tag{10.79}$$

$$= \frac{-2k^2\tilde{V}(\mathbf{k})}{D_0\sqrt{(2k^2 - i\ell_r^{-1}k_x)^2 + \ell_r^{-2}k^2}} = \frac{-2k^2\tilde{V}(\mathbf{k})}{D_0\sqrt{4k^4 - 4i\ell_r^{-1}k^2k_x + \ell_r^{-2}k_y^2}}. \tag{10.80}$$

As we are interested only in the large distance scaling, we consider the limit $\mathbf{k}\to\mathbf{0}$. As usual, the potential $\tilde{V}(\mathbf{k})$ is replaced by its value at $\mathbf{k}=\mathbf{0}$. We look closely at the relative scalings of k_x and k_y in Eq. (10.80) and find that $k^2k_x \sim k_y^2$. This means that k_y decays faster than k_x. Thus $k^2 \sim k_x^2$, and finally $k_x^3 \sim k_y^2$. Our expression simplifies into

$$\tilde{B}_d(\mathbf{k}) \underset{\mathbf{k}\to\mathbf{0}}{\sim} \frac{-2\tilde{V}(0)k_x^2}{D_0\sqrt{\ell_r^{-2}k_y^2 - 4i\ell_r^{-1}k_x^3}}. \tag{10.81}$$

This expression will soon give us a scaling form in real space, with relative scalings $x^3 \sim y^2$. The first step is to Fourier invert it with respect to k_y,

$$B_d(k_x,y) = \frac{-2\tilde{V}(0)\ell_r}{\pi D_0}k_x^2 K_0\left(|y|\sqrt{-4i\ell_r k_x^3}\right) \tag{10.82}$$

with K_0 the modified Bessel function of order 2 and index 0[1]. We can now compute the inverse Fourier transform with respect to k_x, $B_d(x,y) = (2\pi)^{-1}\int dk_x e^{ik_x x}B_d(k_x,y)$. We perform the following changes of variables: $q = -(\ell_r y^2)^{1/3}k_x$ and $w = x(\ell_r y^2)^{-1/3}$. At the end of the day, we obtain the scaling form,

$$B_d(x,y) \sim -\frac{\tilde{V}(0)}{D_0}\frac{1}{y^2}F\left(\frac{x}{\ell_r^{1/3}|y|^{2/3}}\right) \tag{10.83}$$

$$F(w) = -\frac{1}{\pi^2}\int_{-\infty}^{\infty} e^{-iqw}q^2K_0(2\sqrt{iq^3})dq. \tag{10.84}$$

The relative scalings of x and y are $x \sim |y|^{2/3}$. In Fig. 10.4, we compare this scaling form to numerical simulations at a density $\bar{\rho}=0.05$. We find a very good agreement both in the collapse of the cuts, and of the scaling function F that is plotted without adjusting any parameter.

10.5.3 Remark on the behavior below the characteristic length

We now make a short remark on the correlations below the length ℓ_r. We consider Eq. (10.76) and expand it in the regime $k \gg \ell_r^{-1}$ (that is to say $r \ll \ell_r^{-1}$). We obtain

$$\tilde{C}_d(\mathbf{k}) = -\frac{k^2\tilde{V}(\mathbf{k})}{D_0}\frac{1}{1-\frac{i\mathbf{k}\cdot(\mathbf{e}_\theta-\mathbf{e}_{\theta'})}{2\ell_r k^2}} \approx -\frac{k^2\tilde{V}(\mathbf{k})}{D_0}\left(1+\frac{i\mathbf{k}\cdot(\mathbf{e}_\theta-\mathbf{e}_{\theta'})}{2\ell_r k^2}+\dots\right). \tag{10.85}$$

This can be rewritten as

$$C_d(\mathbf{r},\theta,\theta') \approx C_d^{(0)}(\mathbf{r}) + U(\hat{\mathbf{e}}_\theta - \hat{\mathbf{e}}_{\theta'})\cdot\nabla D_d^{(1)}(\mathbf{r}) \tag{10.86}$$

[1] One notes that $\sqrt{ik^3} = |k|^{3/2}(1\pm i)/2$ for $\operatorname{sign} k = \pm 1$. The Bessel function K_0 is analytical on $\mathbb{C}\setminus(-\infty,0]$ so the expression is well defined (except in $k_x=0$).

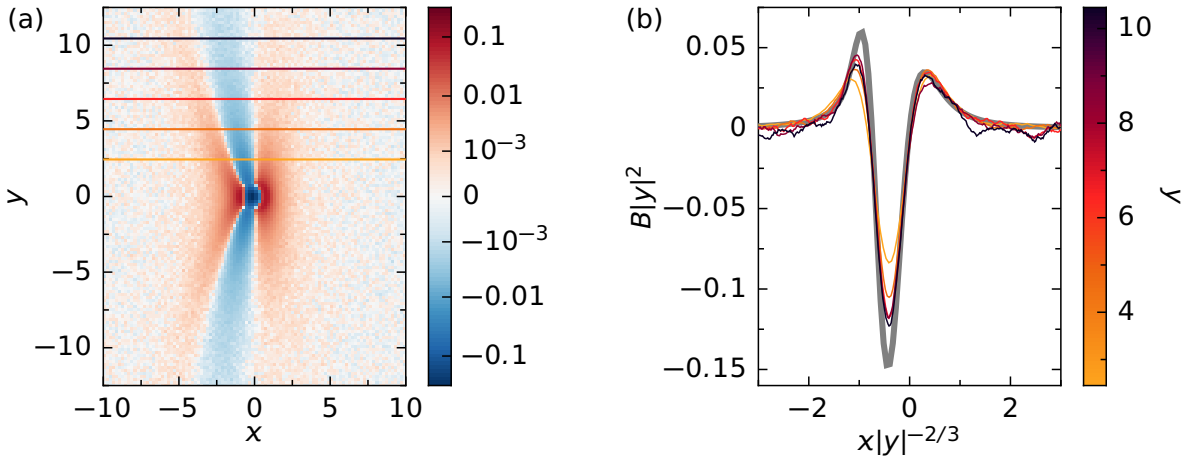

Figure 10.4: (a) Pair correlation function $B(\mathbf{r})$ at $D_r = 0$ and small density $\rho = 0.05$. The other parameters are $D_0 = 0.1$ and $U = 10$. We observe two negative wings along the vertical axis (for $x < 0$). (b) Rescaled horizontal cuts for y from 2.5 to 10.5. The gray line is the prediction from Eq. (10.84) without any adjustment.

with

$$\tilde{C}_d^{(0)}(\mathbf{k}) = \frac{-\tilde{V}(\mathbf{k})}{D_0}, \qquad \tilde{D}_d^{(1)}(\mathbf{k}) = \frac{-\tilde{V}(\mathbf{k})}{2D_0^2 k^2}. \tag{10.87}$$

The reader checks that this corresponds (up to order U) to the result in the low activity limit [Eq. (10.61)] for distances much below $\ell_U = \sqrt{D_0/D_r}$, i.e. $\ell_U^{-1} k \gg 1$. In other words, the regime $U \to 0$ and the regime $D_r = 0$ share the same dipolar correlation when one looks below the typical lengths that are respectively ℓ_U and ℓ_r. This fact will be useful to establish a phase diagram in section 10.7.

10.6 Vanishing translational diffusion

The last limiting case that we study is when the translational diffusion vanishes: $D = 0$. As in the previous section ($D_r = 0$), we focus on the direct correlations C_d which satisfy Eq. (10.34),

$$\left[(\partial_\theta^2 + \partial_{\theta'}^2) + \ell_p(\hat{\mathbf{e}}_\theta - \hat{\mathbf{e}}_{\theta'}) \cdot \nabla\right] C_d(\mathbf{r}, \theta, \theta') = -\frac{2}{D_r} \nabla^2 V(\mathbf{r}). \tag{10.88}$$

$\ell_p = U/D_r$ is the usual persistence length of active Brownian particles.

As usual, we focus on large distances compared to the potential range, and replace the Fourier transform of the potential $\tilde{V}(k)$ by $\tilde{V}(0)$. We obtain the following equation,

$$\left[(\partial_\theta^2 + \partial_{\theta'}^2) + i\ell_p \mathbf{k} \cdot (\hat{\mathbf{e}}_\theta - \hat{\mathbf{e}}_{\theta'})\right] \tilde{C}_d(\mathbf{k}, \theta, \theta') = \frac{2k^2 \tilde{V}(0)}{D_r}. \tag{10.89}$$

In the following, we study its behavior for distances above the persistence length ($\ell_p k \ll 1$) and below the persistence length ($\ell_p k \gg 1$).

10.6.1 Above the persistence length

The solution of Equation (10.89) can be expanded in powers of $\ell_p k$. One checks that the following expression satisfies Eq. (10.89) up to the second order in k (which is the order of the right-hand side),

$$\tilde{C}_d(\mathbf{k},\theta,\theta') = \frac{-\tilde{V}(0)}{D_r}\left\{1 + i\ell_p \mathbf{k}\cdot(\hat{\mathbf{e}}_\theta - \hat{\mathbf{e}}_{\theta'}) + \ell_p^2 k^2 \hat{\mathbf{e}}_\theta \cdot \hat{\mathbf{e}}_{\theta'} + \mathscr{O}\left((\ell_p k)^3\right)\right\}. \tag{10.90}$$

In real space, this corresponds to a Dirac function and derivatives of a Dirac function. One should prove that the expansion in Fourier space converges, and that the function $\tilde{C}_d(\mathbf{k},\theta,\theta')$ is thus analytical. This would imply that the derivatives $\nabla_{\mathbf{k}}^{2n}\tilde{C}_d(\mathbf{k},\theta,\theta')$ are well defined for all integers n. Then, their inverse Fourier transforms $\mathbf{r}^{2n}C_d(\mathbf{r},\theta,\theta')$ decays at infinity,

$$\lim_{\mathbf{r}\to\infty}\left|\mathbf{r}^{2n}C_d(\mathbf{r},\theta,\theta')\right| = 0, \forall n \in \mathbb{N}. \tag{10.91}$$

In other words, one would prove that $C_d(\mathbf{r},\theta,\theta')$ is a fastly decaying function. The same holds for $B_d(\mathbf{r})$.

Aside from the mathematical details, the reader should focus on the physical conclusion: the correlation decays fastly (most likely exponentially) on a length scale given by the persistence length ℓ_p, which is the only length scale of the problem. Indeed, for displacements much larger than the persistence length, active Brownian particles behave as standard random walkers: the memory due to the activity is lost.

We shall now see that a very interesting behavior occurs for distances below the persistence length.

10.6.2 Below the persistence length

We consider distances below ℓ_p but still large compared to a particle diameter (so that the potential $\tilde{v}(k)$ is approximated by v_0). For the moment, we fix the vector $\mathbf{k}$ and focus on the angles. We define the angles γ and γ' in the referential frame of $\mathbf{k}$, $\mathbf{k}\cdot\hat{\mathbf{e}}_\theta = k\cos\gamma$ and $\mathbf{k}\cdot\hat{\mathbf{e}}_{\theta'} = k\cos\gamma'$, where k is the norm of $\mathbf{k}$. Eq. (10.89) reads

$$\left[(\partial_\gamma^2 + \partial_{\gamma'}^2) + i\ell_p k(\cos\gamma - \cos\gamma')\right]\tilde{C}_d(k,\gamma,\gamma') = \frac{2k^2\tilde{V}(0)}{D_r}, \tag{10.92}$$

and we study it in the regime $\ell_p k \gg 1$. A numerical resolution at constant k shows that $\tilde{C}_d(k,\gamma,\gamma')$ concentrates around the two points $(\gamma,\gamma') = (0,0)$ and (π,π). We focus on $(0,0)$ around which the equation reads

$$\left[(\partial_\gamma^2 + \partial_{\gamma'}^2) - \frac{i}{2}\ell_p k(\gamma^2 - \gamma'^2)\right]\tilde{C}_d(k,\gamma,\gamma') = \frac{2\tilde{V}(0)}{D_r}k^2. \tag{10.93}$$

We realize that we can inject the following scalings

$$\tilde{C}_d(k,\gamma,\gamma') \underset{\ell_p k\gg 1}{\sim} \frac{2\tilde{V}(0)}{D_r}(\ell_p k)^{3/2}\tilde{H}\left(\gamma(\ell_p k)^{1/4}, \gamma'(\ell_p k)^{1/4}\right). \tag{10.94}$$

From Eq. (10.92), the function $\tilde{H}(u,v)$, for u and v unbounded, is independent of k and is the solution of the linear partial differential equation

$$\left[\partial_u^2 + \partial_v^2 - \frac{i}{2}\left(u^2 - v^2\right)\right]\tilde{H}(u,v) = 1. \tag{10.95}$$

The scaling for $\tilde{B}_d$ is

$$\tilde{B}_d(k,\gamma) = \frac{1}{2\pi}\int_0^{2\pi} d\gamma' \tilde{C}_d(k,\gamma,\gamma') \underset{\ell_p k \gg 1}{\sim} \frac{\tilde{V}(0)}{\pi D_r}(\ell_p k)^{5/4}\tilde{H}_B\left(\gamma(\ell_p k)^{1/4}\right), \tag{10.96}$$

$$H_B(u) = \int_{-\infty}^{\infty} dv\, H(u,v). \tag{10.97}$$

Using the same reasoning around $\gamma = \pi$, one checks that

$$\tilde{B}_d(k,\pi-\gamma) \underset{\ell_p k \gg 1}{\sim} \frac{\tilde{V}(0)}{\pi D_r}(\ell_p k)^{5/4}\tilde{H}_B^*\left((\pi-\gamma)(\ell_p k)^{1/4}\right), \tag{10.98}$$

with H_B^* the complex conjugate of H_B. We now switch from polar coordinates (k,γ) to cartesian coordinates (k_x,k_y).

$$k_x = k\cos\gamma \simeq \begin{cases} +k & \text{if } \gamma \simeq 0 \\ -k & \text{if } \gamma \simeq \pi \end{cases} \qquad k_y = k\sin\gamma \simeq \begin{cases} k\gamma & \text{if } \gamma \simeq 0 \\ k(\pi-\gamma) & \text{if } \gamma \simeq \pi \end{cases} \tag{10.99}$$

The case $\gamma \simeq 0$ corresponds to $k_x > 0$, and $\gamma \simeq \pi$ to $k_x < 0$. Using the two expressions Eqs (10.96) and (10.98), we obtain a scaling form for the Fourier transform $\tilde{B}_d$,

$$\tilde{B}_d\left(k_x \gtrless 0, k_y\right) = \frac{\tilde{V}(0)}{\pi D_r}(\ell_p|k_x|)^{5/4}\tilde{H}_B^{\pm}\left(\frac{k_y}{\ell_p^{1/4}|k_x|^{3/4}}\right) \tag{10.100}$$

with $H_B^+ = H_B$ used when $k_x > 0$ and $H_B^- = H_B^*$ used when $k_x < 0$. Finally, we perform the Fourier inversion

$$B_d(x,y) = \frac{1}{2\pi}\int dk_x e^{ik_x x}\frac{1}{2\pi}\int dk_y e^{ik_y y}\tilde{B}_d\left(k_x,k_y\right). \tag{10.101}$$

Performing first the integral over k_y, then the one over k_x and using the appropriate changes of variables, we obtain a scaling form for $B_d(x,y)$,

$$B_d(x,y) = \frac{\tilde{V}(0)}{\pi D_r}\frac{\ell_p^4}{y^4}G\left(\frac{\ell_p^{1/3}x}{|y|^{4/3}}\right), \tag{10.102}$$

$$G(w) = \frac{1}{2\pi}\int_0^{\infty} dz e^{iwz}z^2 H_B^+(z^{3/4}) + \frac{1}{2\pi}\int_{-\infty}^{0} dz e^{iwz}z^2 H_B^-(|z|^{3/4}) \tag{10.103}$$

$$= 2\,\mathrm{Re}\left[\int_0^{\infty} dz e^{iwz}z^2 H\left(z^{3/4},0\right)\right] \tag{10.104}$$

where Re denotes the real part. $H_B^{\pm}$ is the inverse Fourier transform of $\tilde{H}_B^{\pm}$, one checks that $H_B^-(a) = (H_B^+)^*(-a) = (H_B^+)^*(a)$ (by parity of H_B). $H(a,b)$ is the inverse Fourier transform of $\tilde{H}(u,v)$, which is the solution of Eq. (10.95),

$$H(a,b) = \frac{1}{(2\pi)^2}\int du dv e^{i(au+bv)}\tilde{H}(u,v). \tag{10.105}$$

Interestingly, $H(a,b)$ satisfies a Green's function problem,

$$\frac{i}{2}\left(\partial_a^2 - \partial_b^2\right)H(a,b) - (a^2+b^2)H(a,b) = \delta(a)\delta(b). \tag{10.106}$$

The main result of this section on vanishing translational diffusion is the scaling form given by Eqs. (10.102) and (10.103). This scaling form is valid for distances smaller than the persistence length $\ell_p = U/D_r$. We are able to observe it in our simulations as shown on Fig. 10.5.

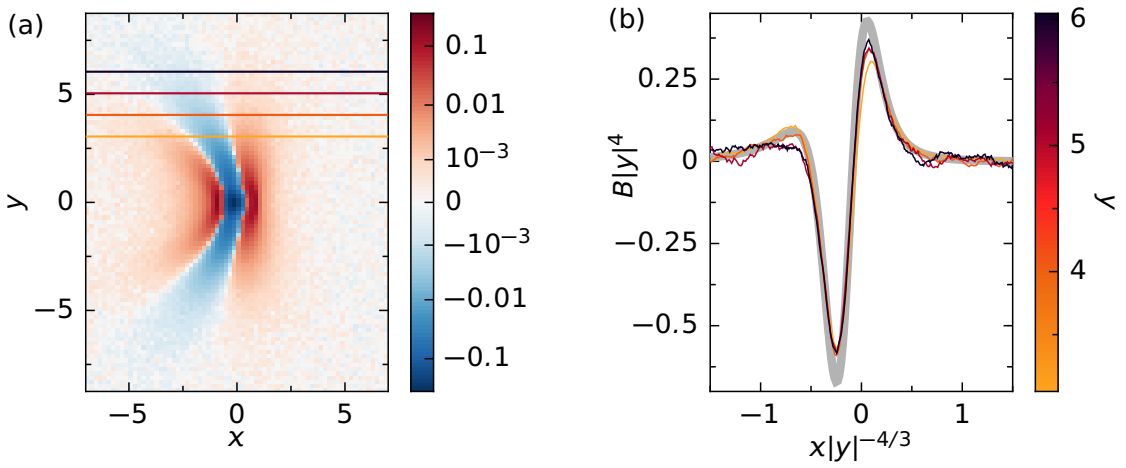

Figure 10.5: (a) Pair correlation function $B(\mathbf{r})$ at $D_0 = 0$ and small density $\rho = 0.05$. The other parameters are $D_r = 0.1$ and $U = 10$. The persistence length $\ell_p = 100$ is much larger than our observation range. We see two negative wings for $x < 0$. (b) Rescaled horizontal cuts for y from 3 to 6. The gray line is the asymptotic behavior of the numerical integration of Eq. (10.40).

10.7 Phase diagram

Let us summarize the last three sections. Correlations of active Brownian particles, at a large distance compared to the particles' radius, are governed by three parameters: the activity U, the rotational diffusion D_r and the translational diffusion D_0. These parameters can be combined into three length scales,

$$\ell_U = \sqrt{\frac{D_0}{D_r}}, \qquad \ell_r = \frac{D_0}{U}, \qquad \ell_p = \frac{U}{D_r}, \tag{10.107}$$

and one dimensionless number that we call the Péclet number

$$\mathrm{Pe} \equiv \frac{U}{\sqrt{D_0 D_r}} = \frac{\ell_p}{\ell_U} = \frac{\ell_U}{\ell_r} = \sqrt{\frac{\ell_p}{\ell_r}}. \tag{10.108}$$

When $\mathrm{Pe} < 1$, the order of the length scales is $\ell_p < \ell_U < \ell_r$, while when $\mathrm{Pe} > 1$ the order is $\ell_r < \ell_U < \ell_p$. This allows us to plot a phase diagram on Fig. 10.6. We plot a rescaled distance r/ℓ_U versus the Péclet number. The lines separating the domains are $r = \ell_r$, $r = \ell_U$ and $r = \ell_p$. We note that for spherical particles undergoing thermal noise, one expects the rotational diffusion coefficient and the translational diffusion coefficient to be linked by a simple constant, $D_0 \sim a^2 D_r$ (with a the diameter of a particle, $a = 1$ in this chapter). This leads to $\ell_U \sim 1$ and means that only the upper half of the phase diagram is observable for such particles.

We studied previously the three limit cases, $U \to 0$, $D_r \to 0$ and $D_0 \to 0$, in which only one of the length scales matters. We recall our results below and show that each case corresponds to a domain of our phase diagram.

- The case $U \to 0$ is the limit $\mathrm{Pe} \to 0$ in the phase diagram of Fig. 10.6. The relevant length scale is ℓ_U. We showed in Eqs. (10.72)-(10.74) that the direct correlations B_d have a dipolar contribution and a positive isotropic contribution. Both decay exponentially over the length

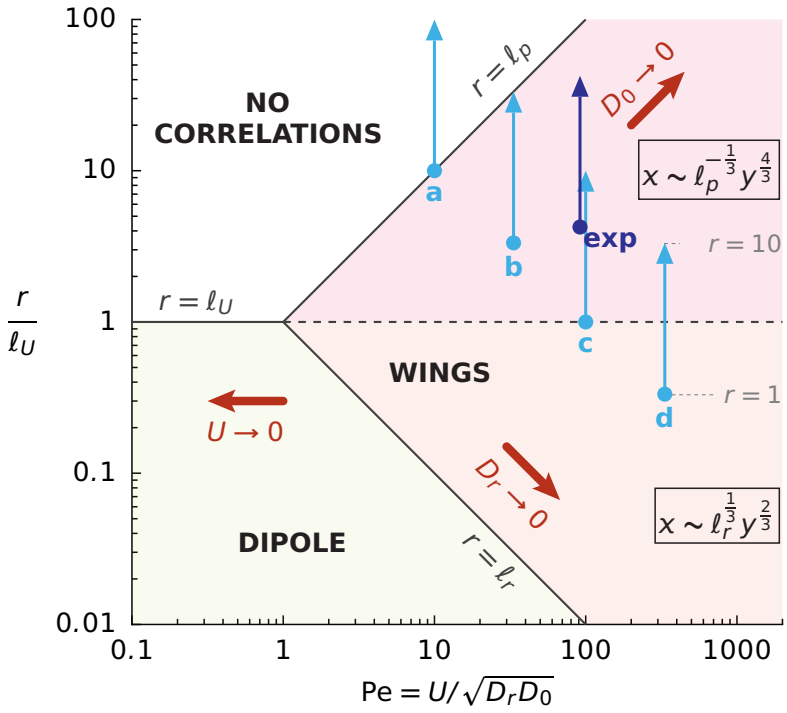

Figure 10.6: Phase diagram of the direct correlations of ABPs. Horizontal axis: Péclet number, vertical axis: rescaled distance. The limiting lines are $r = \ell_r$, $r = \ell_U$ and $r = \ell_p$; they correspond to the crossovers between the regimes. The limit behaviors $D_r, U, D_0 \to 0$ discussed in the text correspond to directions along these lines. Two scaling forms are found at high Péclet number, the limit between the two is at $r = \ell_U$. The light blue arrows correspond to the parameters of Fig. 10.2a-d at distance $r = 1$ to 10 (in units of particle diameter). The dark blue arrow corresponds to the experiments of Chap. 11.

scale ℓ_U. Note that the same holds for the full correlations B [Eqs. (10.69)-(10.71)] with a modified length scale $\ell'_U = \sqrt{(D_0 + \bar{\rho}\tilde{V}(0)/2)/D_r}$ in which the potential plays a role.

- The case $D_r = 0$ corresponds to the limit $\mathrm{Pe} \to \infty$ at constant $\ell_r = D/U$. The direct correlations B_d exhibit wings characterized by Eqs (10.83)-(10.84). The scaling is $x \sim \ell_r^{1/3}|y|^{2/3}$, it corresponds to wings elongated in the vertical direction. The wings decay algebraically at large distance, as $|y|^{-2}$ (note that $\ell_U = +\infty$ when $D_r = 0$). Below ℓ_r, a dipole identical to the domain $U \to 0$ is found. The "dipole" domain on Fig. 10.6 can be extended to $\mathrm{Pe} > 1$ with $r < \ell_r$.

- The case $D_0 = 0$ corresponds to the limit $\mathrm{Pe} \to \infty$ at constant persistence length $\ell_p = U/D_r$. We note that $\ell_U = 0$. Below the persistence length, we found wings with the scaling $x \sim \ell_p^{-1/3}|y|^{4/3}$ [Eqs. (10.102)-(10.103)]. These wings are found for distances smaller than the persistence length ℓ_p. We argued previously that the correlation decays fastly to 0 when the distance is larger than the persistence length.

An interesting remark is that the interface between the $D_r \to 0$ and the $D_0 \to 0$ regime happens when $x \sim \ell_r^{1/3}|y|^{2/3} \sim \ell_p^{-1/3}|y|^{4/3}$, that is to say at $|y| \sim \ell_U$. The line $r = \ell_U$ thus corresponds to the boundary between the two domains in Fig. 10.6.

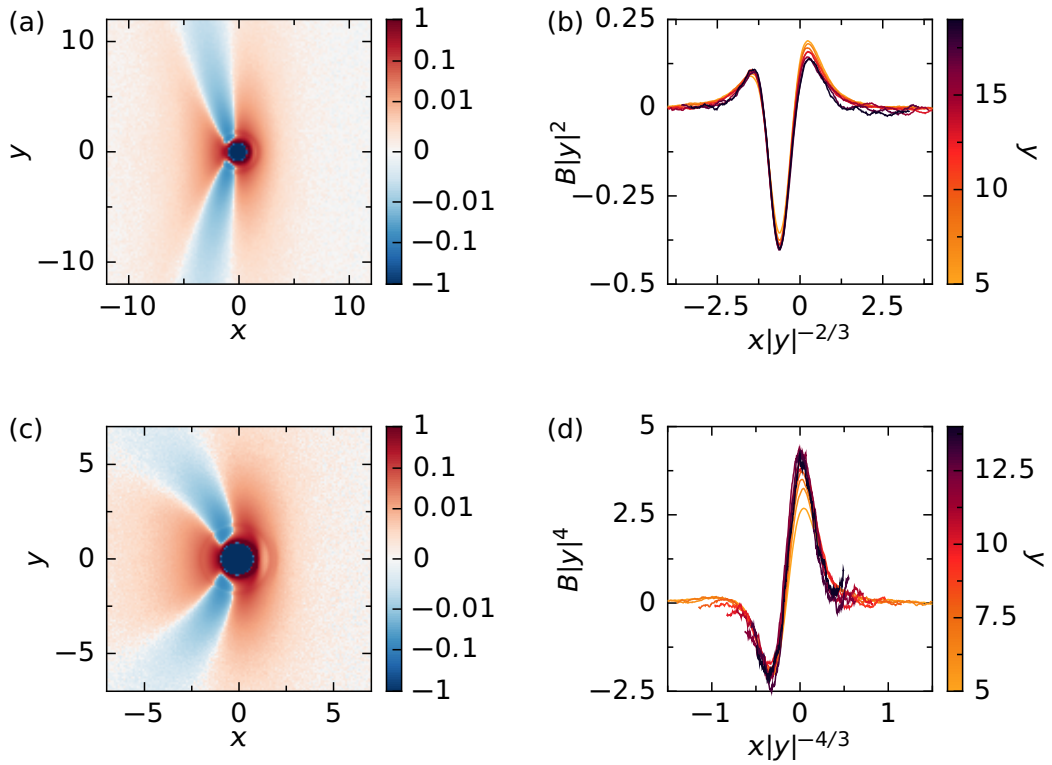

Figure 10.7: Dilute hard particles in the limit cases $D_r = 0$ and $D_0 = 0$. The pair potential is $V(r) = \epsilon(1-r)^2/2$ for $r < 1$, with $\epsilon = 50$ instead of 1 in the previous figures. (a) No rotational diffusion ($D_r = 0$). Correlations $B(\mathbf{r})$ at density $\rho = 0.05$ with $D_0 = 0.1$ and $U = 10$ (similar to Fig. 10.4). (b) Rescaled horizontal cuts of the previous correlations with the exponents predicted by Eq. (10.83). (c) No translational diffusion ($D_0 = 0$). Correlation $B(\mathbf{r})$ at density $\rho = 0.02$ with $D_r = 0.1$ and $U = 10$ (similar to Fig. 10.5). (d) Rescaled horizontal cuts of the previous correlations with the exponents predicted by Eq. (10.102). We note that (a) and (c) exhibit a non-trivial structure at short range due to the hard interactions.

At the end of the day, the study of the three limiting cases ($U, D_r, D_0 \to 0$) enables us to characterize the direct correlations of active Brownian particles, at larger distances than the potential range. Three lengths scales come into play and their relative values delimit domains corresponding to different behaviors. Our most striking results are the two scaling forms found at high Péclet number. Overall, our results are summarized in the phase diagram of Fig. 10.6.

10.8 Hard interactions

The framework used in this part is based on a linearization of the Dean equation. This approach is valid for weak interactions. Consequently in Figs. 10.2, 10.4 and 10.5 we used sets of parameters for which the particles are able to interpenetrate: velocity $U = 10$ with strength of the potential $\epsilon = 1$. We were able to test our predictions quantitatively.

Now, one should remember that in the previous chapter on driven binary mixtures, we realized that our scaling form also holds for hard particles, outside of the validity regime of our approximation (Fig. 9.5). Presently, we perform numerical simulations of dilute and hard active

Brownian particles (potential strength $\epsilon = 50$) in the limit cases $D_r = 0$ and $D_0 = 0$ (Fig. 10.7) and attempt to recover the predictions of Eqs. (10.83) and (10.102). We indeed find a good collapse of the correlations with the predicted exponents and this leads us to state that these exponents are robust.

However, the limit curves are different from our predictions in the weak interaction regime. And while our approach gave us the good short-range structure of the correlations of weakly interacting particles (Fig. 10.2), we notice that we cannot grasp the short-range structure for strong interactions with our linear equations. A last remark is that in Fig. 10.7c-d, we needed to consider a density $\rho = 0.02$ to obtain a good collapse. The reason for that is that at $\rho = 0.05$ three-body effects were most likely present, leading to a deviation of our scaling form. Hence, the regime of "low density" depends on the interactions considered.

10.9 Effective velocity

An isolated active Brownian particle moves at a constant velocity U. However, in the presence of other particles, one expects a slow-down of the particles due to the interactions. This is similar to what has been argued in the case of the binary mixture where the motion of a species is hindered by the other species. Here, we expect each particle to move at an effective velocity $U_{\text{eff}} < U$ along its orientation. This effective velocity has been found to be crucial to compute the pressure in a system of interacting active Brownian particles [95]. We first show that the effective velocity is closely linked to the correlations and explain what kind of insight we can expect from our approach.

We consider the system of N interacting ABPs defined in subsection 10.2.1 and define the effective velocity as the average of the components of the velocities of the particles along their orientation,

$$U_{\text{eff}} = \frac{1}{N}\sum_{i=1}^{N}\left\langle \frac{d\mathbf{X}_i}{dt}\cdot\hat{\mathbf{e}}_{\Theta_i}\right\rangle. \tag{10.109}$$

We use the Langevin equation (10.1) and remember the definitions of the density field f [Eq. (10.5)] and of the correlations C [Eq. (10.24)] and B [Eq. (10.24)]. The potential V is isotropic (∇V is an even function of $\mathbf{r}$), and our two-dimension space can be considered in polar coordinates (r,ϕ). The computation leads us to

$$\begin{aligned}
U_{\text{eff}} &= U - \frac{1}{N}\sum_{i,j}\left\langle \hat{\mathbf{e}}_{\Theta_i}\cdot\nabla_i V(\mathbf{X}_i-\mathbf{X}_j)\right\rangle && (10.110)\\
&= U - \frac{1}{N}\int d\mathbf{r}d\mathbf{r}'\int_0^{2\pi} d\theta d\theta' \left[\hat{\mathbf{e}}_\theta\cdot\nabla_{\mathbf{r}} V(\mathbf{r}-\mathbf{r}')\right]\left\langle f(\mathbf{r},\theta)f(\mathbf{r}',\theta')\right\rangle && (10.111)\\
&= U + \frac{1}{\bar\rho}\int d\mathbf{r}'\int_0^{2\pi} d\theta d\theta' \left[\hat{\mathbf{e}}_\theta\cdot\nabla_{\mathbf{r}'} V(\mathbf{r}')\right]\left(\frac{\bar\rho}{2\pi}\right)^2 C(\mathbf{r}',\theta,\theta') && (10.112)\\
&= U + \frac{\bar\rho}{2\pi}\int_0^\infty r\,dr\int_0^{2\pi} d\phi\int_0^{2\pi} d\theta\cos(\phi-\theta)V'(r)B(r,\phi-\theta). && (10.113)
\end{aligned}$$

At the end of the day, we obtain an expression of the effective velocity in terms of the potential and the correlations,

$$U_{\text{eff}} = U + \bar\rho\int_0^\infty dr\, rV'(r)B_1(r), \tag{10.114}$$

with B_1 the first coefficient of the Fourier component of $B(r,\alpha)$ (polar coordinates),

$$B_1(r) = \frac{1}{2\pi}\int_0^{2\pi} d\alpha\, B(r,\alpha)\cos\alpha. \tag{10.115}$$

Eq. (10.114) is yet another example of relations such as the compressibility equation (8.50), the pressure equation (8.51) and the effective mobility relation (9.66). For a repulsive potential, we have $V'(r) < 0$ and $B_1(r) > 0$ so that $U_{\rm eff} < U$.

Note that Eq. (10.114) requires the quantitative knowledge of B_1 for distance at which the potential does not vanish. For instance, if we consider the soft-sphere potential used in simulations, $V_{\rm SS}(r) = (1-r)^2/2$ for $r \leq 1$, the effective velocity reads

$$U_{\rm eff}^{\rm SS} = U - \bar\rho \int_0^1 dr\, r^2 B_1(r), \tag{10.116}$$

so that we need to know precisely B_1 for $r < 1$. Our approach gives quantitative scaling forms at large distance but should give precise results at short distance for very soft particles only. We can nevertheless write the result of B_1 at low density and low activity from Eq. (10.62),

$$B_1(r) \underset{\substack{\bar\rho\to 0\\ U\to 0}}{\sim} \frac{U\sqrt{D_r}}{2\pi\sqrt{2}D_0^{3/2}} \int d\mathbf{r}'\, K_1\left(\mathbf{r}'\sqrt{\frac{D_r}{2D_0}}\right) V(r\hat{\mathbf{e}}_0 - \mathbf{r}'). \tag{10.117}$$

In these limits, we obtain a very simple dependence of the effective velocity in the velocity and density, $U_{\rm eff} = U(1-\alpha\bar\rho)$. This linear scaling with the density has been postulated more generally in Ref. [52, 95]. Note however that at higher density, we expect density-dependent terms such as $D_0 + \bar\rho\tilde V(\mathbf{k})$, so the picture remains unclear.

Even if our approach may not be precise enough at short distance to obtain quantitatively the effective velocity, we wanted to emphasize that this quantity can be directly computed from the knowledge of the correlations.

10.10 Conclusion and possible extensions

The approach that we developed in the previous chapter for passive liquids and driven binary mixtures has been extended to a paradigmatic model of active matter: active Brownian particles. The linearized Dean equation gives a limit of small interactions. In addition to that, we simplify the problem by looking at low density systems for which we can focus on two-body effects and compute the direct correlation functions. We show that they satisfy a linear equation [Eq. (10.34)] that can be numerically integrated. Its solution is in good agreement with numerical simulations (Fig. 10.2). Furthermore, we investigate the three limit regimes of vanishing activity, rotational diffusion and translational diffusion. In the low activity limit, we find that the correlation is dipolar ($\cos\theta$ dependence on the angle) and decays exponentially at large distance with a typical length that we characterize. In the regime of low rotational diffusion, we uncover a first scaling form for the correlation $B(\mathbf{r})$. It shows negative wings behind a particle and is associated with a power-law decay at large distance. Finally, the regime of low translational diffusion gives another scaling form that holds below the persistence length (the correlations decay exponentially above it). Our results are summarized by the phase diagram of Fig. 10.6 in which the distance r is compared to the three typical length scales of the problem. This phase diagram enables us to predict the structure of the correlations for a given set of parameters.

Active Brownian particles are a minimal model of active matter. Indeed, the particles interact only by spatial interactions. The orientation of a particle evolves completely independently of the other particles. More realistic descriptions involve alignment interactions, or velocity-orientation couplings. It would be interesting to see up to which point our approach and our results can be generalized. At the level of the results, we found one scaling form in the correlations of binary mixtures (previous chapter); and two distinct scalings for correlations of active Brownian particles. Moreover, Ref. [76] uncovers the scalings associated with binary mixtures for a model of active particles. We suspect that the existence of scaling functions in correlations of active matter may be quite generic and we believe that this needs further investigation. At the level of the method, the description of a model in terms of coupled Langevin equations is quite standard. And it is likely that in a variety of cases, one can write a Dean-like stochastic equation for the density field. Then, our linearization approximation enables us to get an insight into the pair correlations. We would be interested in adding, for instance, velocity-orientation couplings and see what can be said on pair-correlation functions within our framework.

In the next chapter, we study an experimental system that can be modeled as an assembly of active Brownian particles: electrophoretic Janus particles. We measure the experimental correlations and compare them to the theory we developed in the present chapter.

Chapter 11

Experimental study of Janus particles

Contents

11.1 Introduction

Janus particles refer to artificial micrometric spherical particles having two hemispheres made of different materials (Fig. 11.1a). When energy is brought into the system, this asymmetry induces a self-propulsion of the particles. As the energy is injected at the local scale, such systems are central instances of artificial active matter setups. One should distinguish between different types of Janus particles. A popular type are catalytic Janus particles [81–83] in which the propulsion is enabled by the dismutation of hydrogen peroxyde which is catalyzed by only one of the two hemispheres. They have been used, among other things, to check theoretical results for independent active Brownian particles, such as the intermediate scattering function [83] or the sedimentation behavior close to a wall [81, 82].

Here we focus on electrophoretic Janus particles, also called "Janus particles fueled by an AC electric field" [77–80]. These particles are made of two hemispheres with different polarizabilities. When an external electric field is applied, the particles move *perpendicularly* to the electric field with a velocity that scales as the square of the amplitude of the field. The propulsion mechanism, called induced-charge electrophoresis, is detailed in Appendix D. We emphasize that it is *not* usual electrophoresis in which particles move along the field with a velocity proportional

to its amplitude. Such motion was first observed for an electric field parallel to the sedimentation plane [77] (only two directions of motion are allowed) but was then studied mostly for a vertical electric field [79, 80] giving an isotropic bidimensional system. At low frequency, electrophoretic Janus particles exhibit no attractive interactions [79] and we will describe them as active Brownian particles. Note however that at high frequencies, strong collective effects such as self-assembly [78] and chain formation [80] are reported.

In this chapter, we present experiments performed in Takeuchi lab, the University of Tokyo in October and November 2019 in collaboration with Daiki Nishiguchi and with the help of Junichiro Iwasawa. The setup was originally developed in Sano laboratory [79, 80]. We first detail the experimental system before modeling it as an assembly of interacting active Brownian particles. Finally, the experimental correlations are measured and are shown to be consistent with the results of Chap 10: the depletion wings are indeed observed.

The results of this chapter have been published in [P5].

11.2 Experimental setup

The experimental setup is very close to the one presented in Ref. [80]. Electrophoretic Janus particles are prepared starting from spherical silica beads of diameter $a = 3.17 \pm 0.32$ µm. One hemisphere is coated by depositing a layer of titanium (thickness 35 nm) using an evaporator with an electron beam. It has been observed that the experiments are more robust if both hemispheres have the same surface properties. For this reason we additionally evaporate a thin layer (thickness 15 nm) of silica on top of titanium using thermal evaporation. See Fig. 11.1a for a sketch of a Janus particle.

The Janus particles are put in a sodium chloride solution of concentration 10^{-4} mol L^{-1}. The velocity of the Janus particles has been shown to be strongly dependent on the ion concentration [77, 80]. Using a fixed concentration enables us to obtain reproducible results and to minimize the temporal variation of the system. The solution is sandwiched between two horizontal ITO electrodes separated by a 50 µm spacer. Indium tin oxide (ITO) electrodes are transparent conductive layers deposited on glass plates so that one can observe the system through the electrodes. Janus particles sediment on the bottom electrode: the system is effectively bi-dimensional. A vertical electric field is applied to the sample. We tried several frequencies and amplitudes. In this chapter, we focus on a representative set of parameters: the frequency is $f = 5$ kHz and the amplitude of the field is $2 \cdot 10^6$ V_{pp} m^{-1} (voltage applied between the electrodes: 10 V_{pp}[1]). At this frequency, the particles exhibit a motion in the direction of the uncoated hemisphere due to a mechanism called induced-charge electrophoresis (see details in Appendix D).

We captured videos of the system with an inverted microscope equipped with a grayscale CMOS camera. To increase the contrast between the two hemispheres of the particles, we used a green filter. The resolution of the images is 3000×2400 pixels and the framerate is 10 fps. The system was monitored for 14 minutes (8400 frames).

Let us now say a few words about the image processing. The particles are detected as circles with the Hough Circle Transform algorithm implemented in the OpenCV library [98]. The centers of the circles give the positions of the particles. Then, we compute the center of mass of the pixels within each circle, with the weights being the values of the pixels. We define the orientation of a given particle as the direction of the vector between the center of mass and the center of the circle. We will see later that this procedure gives an angular precision of about 13°. A view of the

[1] V_{pp}: Volt peak-to-peak.

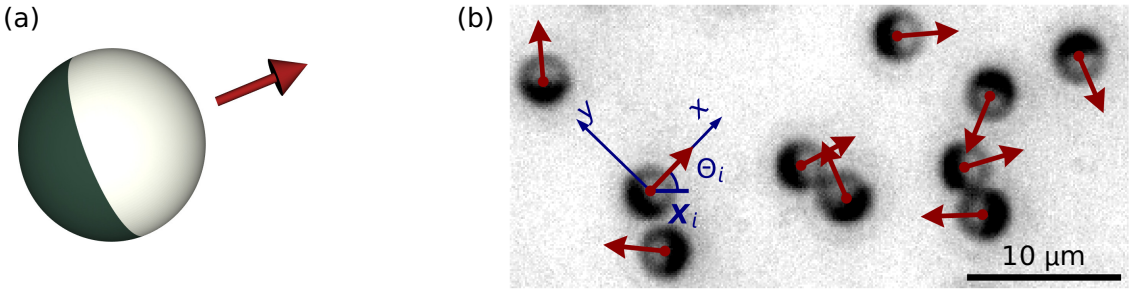

Figure 11.1: (a) Schematic picture of a Janus particle. The light side is uncoated (silica only) while the dark side is coated first with titanium, then with silica. The arrow denotes the direction of motion. (b) Image of the experimental system. The red dots are the detected positions $\mathbf{X}_i$ of the particles and the red arrows the detected orientations Θ_i of the particles. The blue axes are the reference frame in which we compute the correlations.

system, with the positions and orientations that we obtain, is shown in Fig. 11.1b.

11.3 Description as active Brownian particles

The experimental system that we consider does not exhibit polar alignment between particles [79] and we neglect the hydrodynamic interactions between the particles. We thus assume that our system can be described by the model of active Brownian particles studied in Chap 10, that is to say by the Langevin equations (10.1) and (10.2),

$$\frac{d\mathbf{X}_i}{dt} = U\hat{\mathbf{e}}_{\Theta_i(t)} - \sum_{j\neq i}\nabla_i V(\mathbf{X}_i(t)-\mathbf{X}_j(t)) + \boldsymbol{\eta}_i(t), \qquad \frac{d\Theta_i}{dt} = \nu_i, \tag{11.1}$$

where $\mathbf{X}_i(t)$ are the positions of the particles and $\Theta_i(t)$ their orientations (Fig. 11.1b). The Gaussian white noises have variances $\langle \eta_i^\alpha(t)\eta_j^\beta(t')\rangle = 2D_0\delta_{i,j}\delta^{\alpha,\beta}\delta(t-t')$ and $\langle \nu_i(t)\nu_j(t')\rangle = 2D_r\delta_{i,j}\delta(t-t')$. Our goal is to measure the parameters of the model in the experiments.

Note that we are not concerned about the exact potential V as long as it can be assumed to be pairwise, isotropic and short-ranged with a characteristic distance a which is the particle diameter. We observe that the potential consists mainly of hard-core exclusion for $r < a$ but we do not exclude more complicated effects when particles are close from one another.

11.3.1 Estimate of the parameters

Let us investigate the parameters in the experiments, focusing on a single sample (field frequency 5 kHz, field amplitude $2\cdot 10^6$ V_{pp} m^{-1}).

Particle diameter and density. The resolution of the images was measured to be 0.12 µm px^{-1}. The diameter of a particle $a = 3.17 \pm 0.32$ µm appears on the images as $a \simeq 26$ px. Moreover, we count on average 487 particles in a 3000×2400 image. The average density ρa^2 is thus given by $\rho a^2 \simeq 487 \frac{26}{3000}\frac{26}{2400} \simeq 0.05$. At this point, we can assume that we are in a low density regime.

Velocity. We use the Python package Trackpy [99] to obtain the trajectories of the particles. The average velocity can be estimated by two methods. The first one relies on obtaining the instantaneous velocities from a Savitzky–Golay filter [100] applied on the trajectories. This gives an average velocity $U = 56 \pm 7$ px s^{-1}, the standard deviation being given for different particles (Fig. 11.2a). The velocity in the ABP model is thus taken to be $U \simeq 6.7$ µm s^{-1}, about two particle diameters per second. The second method involves the computation of the mean square displacement $\langle \Delta X^2 \rangle$ as a function of time (Fig. 11.2b). We expect $\langle \Delta X^2 \rangle = U^2 (\Delta t)^2$. A least-square fit of a quadratic function [100], taking into account the error bars on different particles, gives $U = 56 \pm 2$ px s^{-1}. This is consistent with the previous result. Considering the most precise of the two measurements, we will use a velocity $U = 6.7 \pm 0.3$ µm s^{-1}. We can compute a typical time associated with the collision between two particles $[U^2 \rho]^{-1/2} \simeq 2$ s. Below this time scale, we assume that the interactions play no role.

Rotational diffusion. The simplest way of measuring the rotational diffusion D_r is to look at the mean square angle as a function of time. One expects

$$\langle \Delta\theta^2 \rangle = \theta_{\text{err}}^2 + 2 D_r \Delta t \tag{11.2}$$

at short time (before collisions). This method has also the advantage of giving us the typical error θ_{err} made on the detection of the orientations. From Fig. 11.2d, we obtain $D_r \simeq 0.12$ s^{-1} and $\theta_{\text{err}} \simeq 0.22$ rad that is to say that we make a detection error of about 13°. Another method is to compute the velocity autocorrelation. For an isolated ABP ($V = 0$ in Eq. (11.1)), one easily shows that the correlation of the velocity $\dot{\mathbf{X}}$ between times t and $t + \Delta t$ decays exponentially with Δt,

$$\langle \dot{\mathbf{X}}(t) \cdot \dot{\mathbf{X}}(t + \Delta t) \rangle = U^2 e^{-D_r \Delta t}. \tag{11.3}$$

We plot the velocity autocorrelation in Fig. 11.2c and focus on the short time regime ($t < 2$ s, before interactions come into play). We find $D_r \simeq 0.11$ s^{-1}, consistently with the previous result.

Translational diffusion. The translational diffusion is small compared to the other effects[2] (velocity and rotational diffusion). It is hard to evaluate experimentally. We use a theoretical estimate based on the Stokes-Einstein relation,

$$D_0 = \frac{k_B T}{6\pi\eta(a/2)\beta}. \tag{11.4}$$

$\eta = 1.0 \cdot 10^{-3}$ Pa s^{-1} is the viscosity of water, $T \simeq 300$ K is the temperature, and β is a correction factor due to the proximity of the bottom electrode. Assuming that Faxen's law [101] is approximately valid for a distance to the wall of the order of a, and that the diffusion in the vertical direction is negligible, we obtain $\beta \simeq 3$. The computation leads to

$$D_0 \simeq 0.05 \text{ µm}^2 \text{ s}^{-1} \simeq (0.07a)^2/\text{s}. \tag{11.5}$$

D_0/a^2 is indeed small compared to U/a and D_r. The fact that the thermal diffusion is negligible compared to the rotational diffusion is closely linked to our choice of diameter $a \simeq 3$ µm: indeed for much smaller diameters the thermal diffusion would be important and particles would swim upwards, something that we want to avoid.

[2] At the length scale a of a particle, we compare the inverse times D_0/a^2, U/a and D_r. By small translational diffusion we mean $D_0/a^2 \ll D_r$ and $D_0/a^2 \ll U/a$.

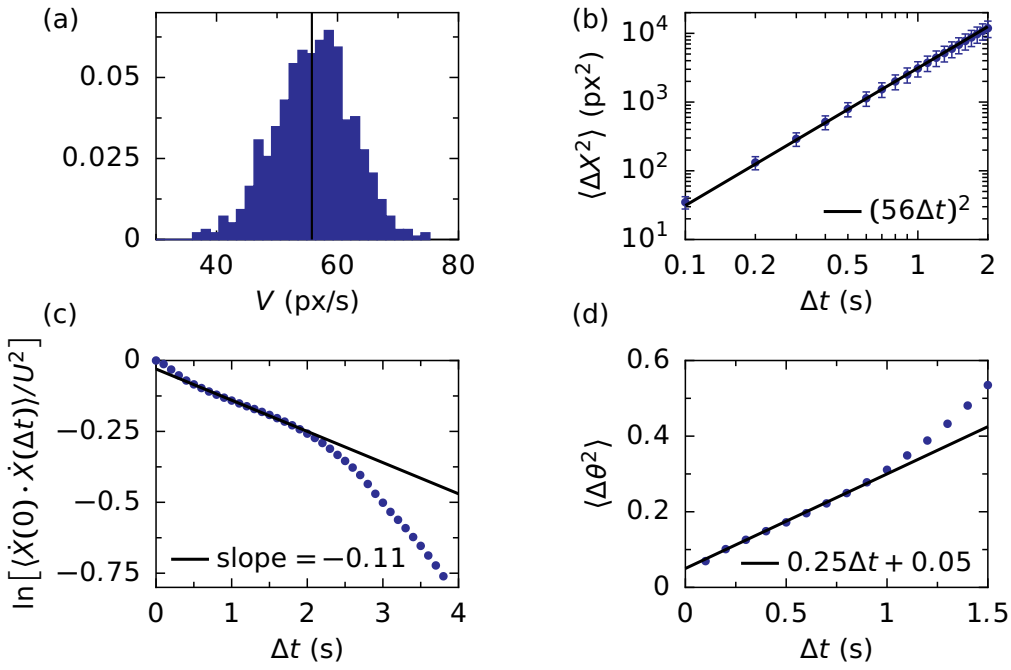

Figure 11.2: Determination of the experimental parameters. 670 particles are tracked for 35 frames on average. (a) Histogram of the average velocities of the particles, the vertical black line is the mean. (b) Mean square displacement. Error bars show the distribution over different particles. (c) Velocity autocorrelation. (d) Mean square angle. (No error bars are given for the last two observables since we consider all available data points for detected trajectories of heterogeneous lengths.)

11.3.2 Péclet number and characteristic lengths

In Chap 10, we saw that the strength of the activity can be quantified by the Péclet number [Eq. (10.108)]. We can compute it in the experiments,

$$\mathrm{Pe} \equiv \frac{U}{\sqrt{D_0 D_r}} \simeq 87. \tag{11.6}$$

This means that the experiments are performed in a high activity regime (right end of the phase diagram of Fig. 10.6).

Furthermore, we can obtain the values of the characteristic length scales defined in Eq. (10.107). The length ℓ_r that corresponds to the theoretical correlations turning from dipole to wings (Fig. 10.6) is

$$\ell_r \equiv \frac{D_0}{U} \simeq 7 \text{ nm} \simeq 0.002a. \tag{11.7}$$

This implies that wings should be observed in the experimental correlations. Then, the length ℓ_U that delimits the two theoretical wing regimes (Fig. 10.6) is

$$\ell_U \equiv \sqrt{\frac{D_0}{D_r}} \simeq 0.7 \text{ µm} \simeq 0.2a. \tag{11.8}$$

$U \simeq 6.7\ \mu\text{m}\,\text{s}^{-1}$	$D_r \simeq 0.12\ \text{s}^{-1}$	$D_0 \simeq 0.05\ \mu\text{m}^2\,\text{s}^{-1}$
$a = 3.17\ \mu\text{m}$	$\rho a^2 \simeq 0.05$	$\text{Pe} \simeq 9 \cdot 10^1$
$\frac{\ell_r}{a} \simeq 0.002$	$\frac{\ell_U}{a} \simeq 0.2$	$\frac{\ell_p}{a} \simeq 2 \cdot 10^1$

Figure 11.3: Table of experimental parameters corresponding to a model of active Brownian particles. The velocity U and the rotational diffusion coefficient D_r are both computed by two different methods. The translational diffusion coefficient is estimated theoretically. As the accuracy of this estimate is hard to assess, and as we are interested only in orders of magnitude, we chose to give a single significant digit for the estimates of the Péclet number Pe and the three characteristic length ℓ_r, ℓ_U and ℓ_p.

This means that the wings in the correlations should be curved. Finally, the persistence length, which is a key parameter of active Brownian particles and encodes the spatial memory of the particles is

$$\ell_p \equiv \frac{U}{D_r} \simeq 56\ \mu\text{m} \simeq 18a. \tag{11.9}$$

This means that the particles keep a memory of their orientations for distances roughly equal to 20 times the particle diameter. Below this distance, the winged shape of the correlations should be observable (Fig. 10.6). A summary of all experimental parameters and characteristic lengths is given in Fig. 11.3. The point corresponding to these parameters is shown in the phase diagram of Fig. 10.6. It lies in the upper-right corner, the one that corresponds to low translational diffusion.

11.4 Results for the correlations

We now turn to the main results of this chapter: the experimental correlations. Their definition is given by Eq. (10.25),

$$B(\mathbf{r}) = \frac{1}{2\pi}\int_0^{2\pi} C(\mathbf{r},0,\theta')d\theta', \quad C(\mathbf{r},\theta,\theta') \equiv \frac{\left\langle f(\mathbf{0},\theta)f(\mathbf{r},\theta')\right\rangle}{[\bar{\rho}/(2\pi)]^2} - \frac{\delta(\mathbf{r})\delta(\theta-\theta')}{\bar{\rho}/(2\pi)} - 1, \tag{11.10}$$

where the density field $f(\mathbf{r},\theta)$ is the probability that there is a particle at position $\mathbf{r}$ with orientation θ. We assume that our experimental system is translationally invariant over the field of view of the camera.

11.4.1 Computation

We first detect the positions[3] and orientations of all particles on every frame as explained in section 11.2. For each particle far enough from the edges of the image (that is to say at a distance larger than the range of observation for the correlations), we consider every other particle and compute its position in the reference frame of the first one. We put the results in bins of size

[3]Unfortunately the detected positions are discrete (indexed by the pixels). This induces an artefact in the correlations. To avoid this, we add a Gaussian noise of standard deviation one pixel to the position of each particle. This noise is smaller than the precision of the detection and regularizes the correlations.

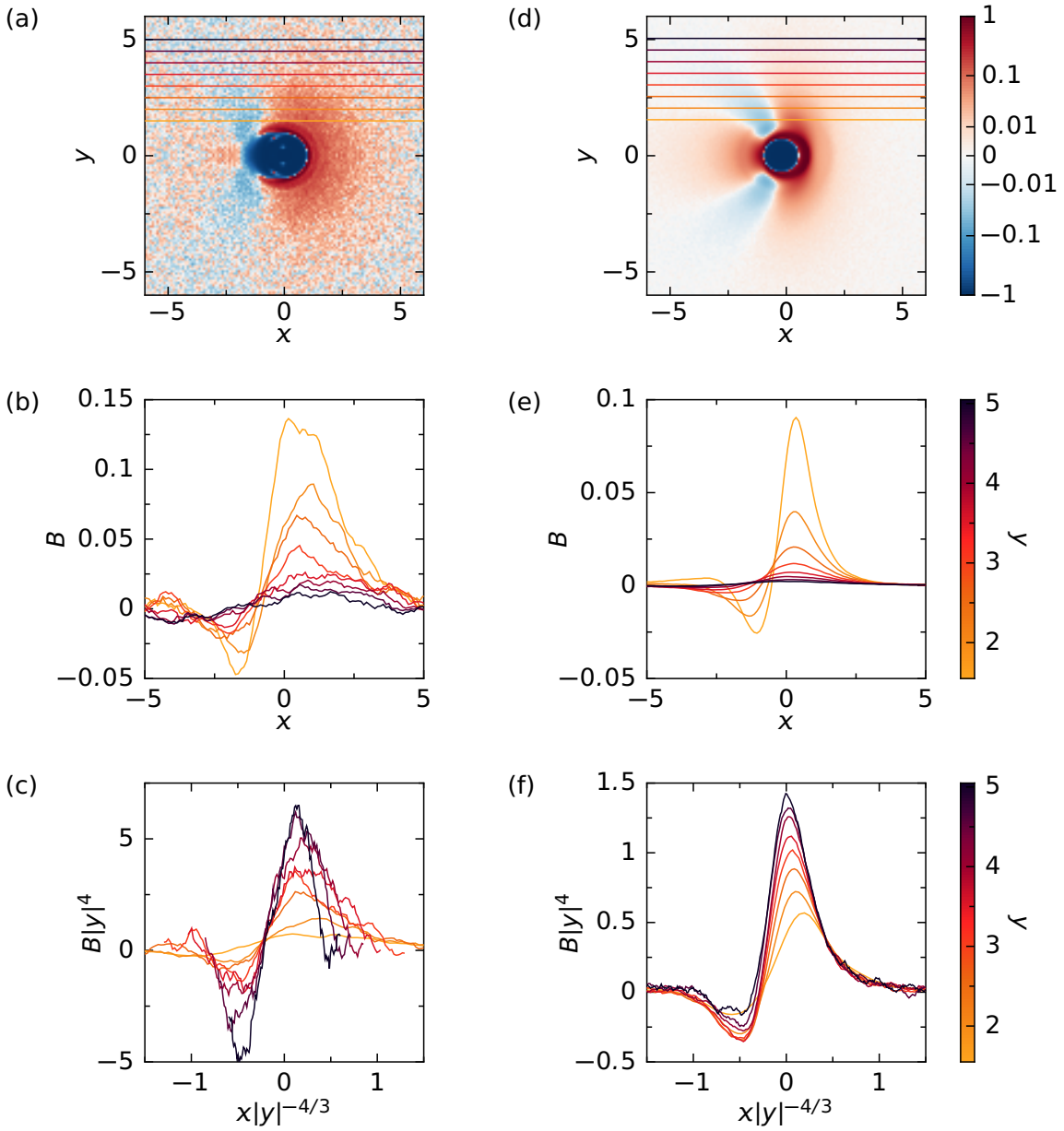

Figure 11.4: Experimental correlations [(a), (b), (c)] compared to numerical simulations with parameters $\rho = 0.05$ and $\epsilon : D : D_r : U = 50 : 0.05 : 1 : 20$ [(d), (e), (f)]. (a) Experimental correlation $B(\mathbf{r})$. The axes are given in units of particle diameter. The horizontal colored lines show the cuts. (b) Horizontal cuts of the correlation function. (c) Horizontal cuts of the correlation function with exponents corresponding to the scaling form of the $D_0 = 0$ regime. (d), (e) and (f) are the equivalent of (a), (b) and (c) for numerical simulations.

$\Delta x = \Delta y = 0.1a$. We process all the frames and normalize the bins. The result is shown in Fig. 11.4a and we now comment it.

11.4.2 Comments

The most important comment is that we experimentally observe two depletion wings in the correlations behind the particle, as expected from the phase diagram (Fig. 10.6) at high Péclet number. Our observation zone is $a \leq r \leq 6a$. Looking at the parameters (Fig. 11.2), this corresponds to the upper right corner of the phase diagram. The depletion wings are seen clearly by taking horizontal cuts of the correlation function (Fig. 11.4b-c).

We perform numerical simulations of harmonic spheres with parameters close to the experimental ones (shown on Fig. 11.4d-f), in particular the potential strength ($\epsilon = 50$) is high enough so that the particles barely overlap. The numerical and experimental correlations are very similar both visually and in the shape of the cuts. The main discrepancy is the sign of the correlation at $(x, y) \simeq (-a, 0)$ (negative in the experiments, positive in the simulations); we may attribute it to non-trivial interactions between Janus particles when they touch each other. Overall, the experiments are still well described by the numerics.

We already noted that the thermal diffusion is weak compared to the other effects. According to the phase diagram (Fig. 10.6), we are in the zone where the correlations may follow a scaling law

$$B(x, y) \sim \frac{1}{y^4} G_{\text{exp}}\left(\frac{x}{y^{4/3}}\right). \tag{11.11}$$

It is thus reasonable to rescale the cuts with these exponents as done in Fig. 11.4c and f. The experimental statistics are insufficient to conclude on the existence or not of a scaling form. We also remark that the collapse does not hold for the numerical simulations. This is most likely due to three-body effects that occur for hard particles if the density is insufficiently low (see discussion of section 10.8). Overall, we are very satisfied to find the non-trivial shape with negative wings in the experiments and to have a qualitative agreement with numerical simulations.

11.5 Conclusion

In this chapter, we presented experiments of electrophoretic Janus particles performed in Takeuchi laboratory. These asymmetrically-coated particles are placed in a vertical electric field and exhibit a motion *perpendicular* to the electric field. That is to say that their direction of motion is isotropic on top of the glass plate on which they sediment. Janus particles are well described by the model of active Brownian particles. We were able to measure the parameters and showed that the experiments correspond to a regime of high activity. The computation of the correlations shows the characteristic negative wings behind a particle that were obtained for ABPs at high activity (see for instance Fig. 10.2c-d). Moreover, the structure of the correlations is in qualitative agreement with numerical simulations performed with the experimental set of parameters.

This chapter, and the previous chapter, highlight the importance of looking at the pair correlations of active matter systems, both in theoretical models and in experiments. We believe that it would be important to measure the experimental correlations in other experimental systems that may be described by active Brownian particles as well as in experimental systems that exhibit alignment interactions or velocity-orientation couplings.

Chapter 12

Conclusion

In this thesis, we investigated the correlations of interacting systems, mostly out of equilibrium. We used various frameworks: exactly solvable one-dimensional models, hydrodynamic equations valid at large distance and large time, and linearized Dean equations. The thesis was divided into two parts in which we investigated two different types of systems. The first one focused on single-file systems and in particular N-point observables with or without biases. The second part concentrated on driven and active bidimensional systems with an emphasis on the behavior of the correlation functions at large distance.

Single-file systems (Chap. 2) are defined by the fact that particles in a channel cannot pass each other. This induces a subdiffusive behavior of a given particle, and a sub-ballistic motion for a driven intruder. The paradigmatic model that we studied is the symmetric exclusion process (SEP) in which particles on a discrete line jump to neighboring sites with hard-core exclusions. We focused first on the dense limit, which can be solved exactly by studying the motion of the vacancies. We first recovered known results for the cumulant-generating function of a driven tagged particle (TP) in the dense SEP at large time, and extended the formula to arbitrary time, and to quenched initial conditions (Chap. 3). We then focused on N unbiased TPs in the SEP to probe collective effects (Chap. 4). At large time, the N TPs behave as a single one, in the sense that the N-tag cumulants are equal to the one-tag cumulants. At high density, we uncover a universal scaling form at intermediate time shared by the N-tag cumulants, independently of the number of particles, the order of the cumulants and the initial configuration. The analysis is then extended to several biased TPs at high density (Chap. 5) and we observe strong collective effects. First, all the TPs behave as a single effective TP at large time, in particular they all move together independently of their biases. For two TPs, this breaks down to several situations that we characterize analytically: (i) if only one TP is biased the other one is entrained, (ii) if the two TPs are biased in the same direction they cooperate and move faster than if they were alone, and (iii) if the two TPs are biased in opposite directions they compete and the direction of motion at large time is given by the most biased one. A natural question is what happens to this binding between TPs at arbitrary density. We answer this question using a hydrodynamic approach for the density profile of the SEP (Chap. 6) and uncover an unbinding transition. At small forces (small biases), two TPs remain bound together as in the high density case. But at high forces, they separate and move away from one another with a time dependence $t^{1/2}$. The critical case, which for antisymmetric forces happens at the equilibrium pressure of the system, is characterized by a motion as $t^{1/4}$. Our approach, first written for the SEP, extends to arbitrary single-file systems

and the unbinding transition should be observable in experimental systems. Finally, we tried to extend the hydrodynamic approach to generalized profiles, that is to say correlations between the density field and the displacement of a TP (Chap. 7). These generalized profiles are directly linked to the cumulant-generating function of the displacement of the TP: obtaining them gives the full probability law of this displacement. While in the general case, the hydrodynamic equations are not closed, we exhibit several cases in which they are: in particular the high and low density limits of the SEP. We believe that this framework that we introduced is powerful and will be the subject of future works. Overall, we have characterized the anomalous behavior of single-file systems, and in particular of the SEP. Our key results were about N-tag observables and we uncovered binding and unbinding effects between TPs. We also obtained explicit expressions for the strong spatial correlations responsible for the anomalous behaviors.

In the second part of this thesis, correlations were discussed for bidimensional interacting systems. The goal was no longer to probe any anomalous behavior, but to exhibit the spatial structure of the pair-correlations which gives a key insight into out-of-equilibrium systems. After stating some results for a passive liquid (Chap. 8), we considered two out-of-equilibrium systems: a driven binary mixture (Chap. 9) and an assembly of active Brownian particles (Chap. 10). In each case, we started from the microscopic Langevin equations and derived the Dean equation for the fluctuating density field of the system. The Dean equation is exact but it is non-linear with multiplicative noise, which makes it hard to handle. We thus linearize it around an homogeneous density profile. This corresponds to a limit of weak interactions. The equation becomes linear and the density field becomes Gaussian. The correlations can then be obtained either explicitly or as the solution of a linear equation involving the pair potential. For the passive liquid, this approach returns the result of the random phase approximation, a mean-field closure relation used in liquid theory. The correlations of the driven binary mixture are defined between particles of the same species and between particles of different species. They are strongly anisotropic with a power-law decay in the longitudinal direction (exponent $-(d+1)/2$ in dimension d) and an exponential decay in the transverse direction. We uncover a diffusive scaling form associated with these decays, and this form is shown to also hold for hard particles (which is outside the validity regime of our theory). Qualitatively, the correlation along the longitudinal axis is positive for particles of the same species and negative for particles of different species. This shows a tendency of particles to align with same-species particles. In the case of active Brownian particles, our approach gives us a linear equation for the correlations in the reference frame of a given particle. This equation can be solved numerically and the limit regimes can be solved analytically. At low velocity, the correlation function has a dipolar shape associated with an exponential decay. At low rotational diffusion, we uncover a scaling form for the correlations ($x \sim y^{2/3}$). And at low translational diffusion, another scaling form ($x \sim y^{4/3}$) is found for distances under the persistence length. Both scaling forms have a characteristic structure with two negative wings behind the particle. All these results are summarized in a phase diagram enabling one to determine the structure of the correlations from the parameters. Finally, we compare the latest results to experiments of Janus particles. We show that the experiments can be described by active Brownian particles in the high activity regime. The experimental correlations exhibit the characteristic winged shape and are in agreement with numerical simulations performed with the experimental set of parameters. Overall, we stressed the importance of the spatial structure of the correlations in out-of-equilibrium systems of interacting particles. We believe that the scaling forms may be a generic feature of the correlations of these systems and suggest that it would be interesting to look for it both in theoretical models, numerical simulations and experiments of systems exhibiting various features (e.g. alignment interactions or velocity-orientation couplings).

The work of this thesis leaves space for further studies. We now list a few directions that could be investigated. The characterization of the dense SEP is almost complete, but a key point is missing: correlations at different times. One should investigate whether the vacancy-based approach can give N-point and M-time observables. This would mean no less than having a full characterization of the stochastic process and would be a major result. Second, we believe that a lot of insight can be gained from hydrodynamic equations for the generalized profiles. A few questions are: Is there a closure relation at arbitrary density that enables to recover the results of Ref. [28]? Can one build a framework for the generalized profiles of arbitrary single-file systems at any order? Can one extend the framework to obtain two-point (and N-point) observables? As for bidimensional interacting systems, we already stressed the possible extensions. Our framework starts from the microscopic Langevin equations and is quite generic. We believe that it can be applied to systems with more complexity such as those with alignment interactions or velocity-orientation couplings. Furthermore, we stressed that it would be interesting to probe experimentally or numerically the spatial structure of the correlations in these systems.

Chapter 13

Publications

[P1] A. PONCET, O. BÉNICHOU, V. DÉMERY & G. OSHANIN; "Universal Long Ranged Correlations in Driven Binary Mixtures"; Phys. Rev. Lett. **118**, p. 118 002 (2017). See Chap. 9.

[P2] O. BÉNICHOU, V. DÉMERY & A. PONCET; "Unbinding Transition of Probes in Single-File Systems"; Phys. Rev. Lett. **120**, p. 070 601 (2018). See Chap. 6.

[P3] A. PONCET, O. BÉNICHOU, V. DÉMERY & G. OSHANIN; "N-tag probability law of the symmetric exclusion process"; Phys. Rev. E **97**, p. 062 119 (2018). See Chap. 4.

[P4] A. PONCET, O. BÉNICHOU, V. DÉMERY & G. OSHANIN; "Bath-mediated interactions between driven tracers in dense single files"; Phys. Rev. Research **1**, p. 033 089 (2019). See Chap. 5.

[P5] A. PONCET, O. BÉNICHOU, V. DÉMERY & D. NISHIGUCHI; "Algebraic winged pair correlations of dilute active Brownian particles"; arXiv:2006.08202 [cond-mat.stat-mech] (2020). See Chaps. 10 and 11.

Appendix A

Full single-tag probability law of the SEP

We devote the appendix to the solution of the full probability law of a tagged particle (TP) in the symmetric exclusion process (SEP) found by Imamura, Sasamoto and Mallick. The large-time results were first published in Ref. [28]. Latter, the method and the arbitrary time results were detailed in Ref. [29]. The system considered is the usual SEP, with exponential rate 1 for *each jump* (not each particle, this induces a difference of time by a factor 2 compared to our results). A TP is initially placed at the origin, the goal is to compute the full probability law of its displacement $X(t)$, in particular the cumulative distribution $\mathbb{P}[X(t) \leq x]$. See Fig. A.1 for details.

We briefly expose the method, without details on the computation. Then we state the results. And finally, we show that we recover known results in both the high density and low density limits.

A.1 Method

A.1.1 Mapping to an interface problem

The first step of the computation is to offer a mapping of the SEP onto an interface problem. We define the occupation of site i at time t as $\eta_i(t) = 1$ if the site is occupied, 0 if the site is empty. And we denote $Q(0,t)$ the "current" at the origin, that is to say the number of particles that have jumped from site 0 to site 1 before time t minus the number of particles that have jumped from

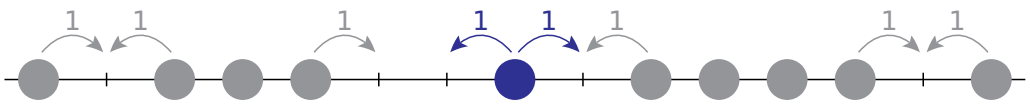

Figure A.1: One TP in the SEP. The density (fraction of occupied sites) is ρ. The TP is initially at site 0. The occupation of site i at time t is $\eta_i(t) = 1$ if the site is occupied, $\eta_i(t) = 0$ otherwise. Note that the convention of Imamura *et al.* is an exponential rate equal to 1 for each jump.

1 to 0. We define an interface $N(x,t)$ as

$$N(x,t) = Q(0,t) + \begin{cases} \sum_{i=1}^{x} \eta_i(t) & \text{if } x > 0 \\ 0 & \text{if } x = 0 \\ \sum_{i=x+1}^{0} \eta_i(t) & \text{if } x < 0 \end{cases}. \tag{A.1}$$

The reader checks that, roughly speaking, the displacement $X(t)$ of the TP is the value of x for which $N(x,t)$ increases from 0 to 1. More precisely, one shows that the cumulative distribution function of $X(t)$ satisfies

$$\mathbb{P}[X(t) \leq x] = \mathbb{P}[N(x,t) > 0]. \tag{A.2}$$

Knowing the probability law of $N(x,t)$ is enough to determine the one of $X(t)$.

A.1.2 Tau-moments of the ASEP

Imamura *et al.* consider an auxiliary problem: the asymmetric simple exclusion process (ASEP), in which all particles on the line are biased. When their exponential clocks tick they move to the right with probability p and to the left with probability q. Like in the SEP, exclusions are enforced. For the ASEP, one can define an interface $N_{\text{ASEP}}(x,t)$ like in Eq. (A.1).

One defines $\tau = p/q$. The τ-moment of order n of the ASEP is $\langle \tau^{n N_{\text{ASEP}}(x,t)} \rangle$ where the average is taken both on the initial conditions and on the evolution of the system. Note that the τ-moments give no information for the SEP ($\tau = 1$). Recent techniques based on the Bethe Ansatz allow one to obtain a expression for the τ-moments of the ASEP. The reader should look at the original article [29] for the method and computation.

The striking feature is that the limit $\tau \to 1$ enables us to compute the moments of $N(x,t)$ of the SEP. More precisely, if one sets $\tau = 1 - \epsilon$, the n-th moment of $N(x,t)$ is shown to be given by

$$\langle N(x,t)^n \rangle = \lim_{\epsilon \to 0} \frac{\left\langle \left[1 - \tau^{N_{\text{ASEP}}(x,t)}\right]^n \right\rangle}{\epsilon^n}. \tag{A.3}$$

One can finally use Eq. (A.2) to obtain all the desired information about the probability law of $X(t)$.

A.1.3 Large deviation functions at large time

One can show that the position $X(t)$ of the TP, $N(x,t)$ and their characteristic functions follow large deviation principles at large time ($t \to \infty$). One writes

$$\mathbb{P}\left[\frac{X_t}{\sqrt{4t}} = -\zeta\right] \asymp e^{-\sqrt{t}\phi(\zeta)} \qquad \langle e^{sX_t} \rangle \asymp e^{-\sqrt{t}C(s)} \tag{A.4}$$

$$\mathbb{P}\left[\frac{N(x,t)}{\sqrt{t}} = q\right] \asymp e^{-\sqrt{t}\Phi(\xi,q)} \qquad \langle e^{\lambda N(x,t)} \rangle \asymp e^{-\sqrt{t}\mu(\xi,\lambda)} \tag{A.5}$$

with the scaling variable $\xi = x/\sqrt{4t}$. $C(s)$ is the rescaled cumulant-generating function of the position of the TP. The following Legendre transforms hold:

$$C(s) = \min_{\zeta} (2s\zeta + \phi(\zeta)), \qquad \Phi(\xi,q) = \max_{\lambda} (\mu(\xi,\lambda) + \lambda q). \tag{A.6}$$

From Eq. (A.2), one shows that the link between $N(x,t)$ and $X(t)$ boils down to

$$\phi(\xi) = \Phi(\xi, q = 0). \tag{A.7}$$

At the end of the day, the rescaled cumulant-generating function $C(s)$ is expressed in terms of the large deviation function $\mu(\xi,\lambda)$ as

$$C(s) = \min_{\xi} \max_{\lambda} [2s\xi + \mu(\xi,\lambda)]. \tag{A.8}$$

A.2 Results

A.2.1 Arbitrary time

The main result of Imamura *et al.* is the expression of the characteristic function of $N(x,t)$. For $\mathrm{sign}(x) = \pm 1$, they obtain

$$\log\langle e^{\lambda N(x,t)}\rangle = \sum_{n=1}^{\infty} \frac{(-1)^{n-1}\omega^n}{n} \mathfrak{I}_n(x,t) \pm x \log[1+\rho_{\pm}(e^{\pm\lambda}-1)] \tag{A.9}$$

$$\omega = \rho_+(e^{\lambda}-1) + \rho_-(e^{-\lambda}-1) + 2\rho_+\rho_-(e^{\lambda}-1)(e^{-\lambda}-1) \tag{A.10}$$

$$\mathfrak{I}_n(x,t) = \mathrm{Tr}\left[(K_{x,t})^n\right] = \oint_{C_0} \dots \oint_{C_0} \left(\prod_{i=1}^{n} \frac{d\xi_i}{2\pi i}\right) K_{x,t}(\xi_1,\xi_2)\dots K_{x,t}(\xi_n,\xi_1) \tag{A.11}$$

$$K_{x,t}(\xi_1,\xi_2) = \frac{\xi_1^{|x|} e^{t(\xi_1+1/\xi_1-2)}}{\xi_1\xi_2 + 1 - 2\xi_2} \tag{A.12}$$

with C_0 a contour in the complex plane around zero small enough as to include no other pole. At the mathematical level, the structure of $\langle e^{\lambda N(x,t)}\rangle$ is a Fredholm determinant.

One can in principle obtain information on the law of $X(t)$ using Eq. (A.2).

A.2.2 Large time

The previous result at arbitrary time is hard to tackle. It takes a simpler form at large time ($t \to \infty$ with $x/\sqrt{t} = \text{const}$). One first shows that

$$\mathfrak{I}_n(\xi\sqrt{4t},t) \underset{t\to\infty}{\sim} \sqrt{\frac{t}{n}}\Xi(-\xi\sqrt{n}), \qquad \Xi(\xi) = \int_{\xi}^{\infty} du\ \mathrm{erfc}\, u. \tag{A.13}$$

Then Eq. (A.9) leads to (for $x > 0$)

$$\mu(\xi,\lambda) \equiv \lim_{t\to\infty} \frac{\log\langle e^{\lambda N(x,t)}\rangle}{-\sqrt{t}} = \sum_{n=1}^{\infty} \frac{(-1)^{n-1}}{n} \omega^n \frac{1}{\sqrt{n}} \Xi(-\sqrt{n}\xi) + 2\xi \log[1+\rho_+(e^{\lambda}-1)]. \tag{A.14}$$

The final result (for $\xi \gtrless 0$) is

$$\mu(\xi,\lambda) = \sum_{n=1}^{\infty} \frac{(-1)^{n-1}}{n^{3/2}} \omega^n A(\sqrt{n}\xi) + \xi \log \frac{1+\rho_+(e^{\lambda}-1)}{1+\rho_-(e^{-\lambda}-1)} \tag{A.15}$$

$$A(\xi) = \xi + \Xi(\xi) = \frac{e^{-\xi^2}}{\sqrt{\pi}} + \xi(1-\mathrm{erfc}\,\xi). \tag{A.16}$$

The large time limit of the cumulants of $X(t)$ is deduced from Eq. (A.8). The first two non-zero cumulants read

$$\frac{\langle X(t)^2\rangle_c}{\sqrt{4t}} \underset{t\to\infty}{\sim} \frac{1-\rho}{\rho\sqrt{\pi}}, \tag{A.17}$$

$$\frac{\langle X(t)^4\rangle_c}{\sqrt{4t}} \underset{t\to\infty}{\sim} \frac{1-\rho}{\rho^3\sqrt{\pi}}\left[1-\left(4-(8-3\sqrt{2})\rho\right)(1-\rho)\frac{12}{\pi}(1-\rho)^2\right]. \tag{A.18}$$

Please note that the convention here is rate 1 for jumps both to the left and to the right instead of jumping with rate 1 and then choosing the direction. One should divide the time by 2 to find results consistent with ours.

A.3 High density limit

In this section we study the high density limit: $\rho_+ = \rho_- = 1-\rho_0$ with $\rho_0 \to 0$. We simplify the expression (A.15) when $\rho_0 \to 0$, noting that ξ (rescaled displacement) should scale as $\xi = \rho_0\tilde{\xi}$.

$$\lim_{\rho_0\to 0}\frac{\mu(\lambda,\rho_0\tilde{\xi})}{\rho_0} = -\frac{1}{\sqrt{\pi}}(\cosh\lambda - 1) + 2\lambda\tilde{\xi} \tag{A.19}$$

We solve for the extremum (A.8):

$$\left.\frac{\partial\mu}{\partial\xi}\right|_{\lambda^*,\xi^*} = -2s \qquad \left.\frac{\partial\mu}{\partial\lambda}\right|_{\lambda^*,\xi^*} = 0, \tag{A.20}$$

$$\lambda^* = -s, \qquad \tilde{\xi}^* = \frac{\sinh\lambda^*}{\sqrt{\pi}} = -\frac{\sinh s}{\sqrt{\pi}}. \tag{A.21}$$

From Eq. (A.8), we finally obtain

$$\lim_{\rho_0\to 0}\frac{C(s)}{\rho_0} = -\frac{1}{\sqrt{\pi}}(\cosh s - 1). \tag{A.22}$$

With a change of notation, this is what we find with our vacancy-based method [Eq. (3.34)].

A.4 Low density limit

We simplify the expression (A.9) when $\rho \to 0$,

$$\mu(\lambda,\xi) = -2\rho\,(\cosh\lambda - 1)A(\xi) + \rho\,\xi\left(e^{\lambda} - e^{-\lambda}\right) \tag{A.23}$$

$$\mu(\lambda,\xi) = -\rho\left[(e^{\lambda}-1)h(\xi) + (e^{-\lambda}-1)h(-\xi)\right]. \tag{A.24}$$

We introduced $h(\xi) = \int_\xi^\infty du\ \mathrm{erfc}\,u = A(\xi) - \xi$ and $h(-\xi) = A(\xi) + \xi$. Our goal is to solve both extrema in Eq. (A.8). We first write $\frac{\partial\mu}{\partial\lambda} = 0$ and obtain

$$e^{\lambda^*} = \sqrt{\frac{h(-\xi)}{h(\xi)}}. \tag{A.25}$$

One checks that this implies

$$\mu(\lambda^*,\xi) = \rho\left[\sqrt{h(\xi)} - \sqrt{h(-\xi)}\right]^2. \tag{A.26}$$

We then solve for the extremum over ξ, $\frac{\partial \mu}{\partial \xi} = -2s$, this gives us

$$-2s = \rho\left[(e^{\lambda^*}-1)\operatorname{erfc}(\xi^*) - (e^{-\lambda^*}-1)\operatorname{erfc}(-\xi^*)\right] \tag{A.27}$$

$$-2s = \rho\left(\sqrt{h(-\xi^*)} - \sqrt{h(\xi^*)}\right)\left[\operatorname{erfc}(\xi^*)\sqrt{\frac{1}{h(\xi^*)}} + \operatorname{erfc}(-\xi^*)\sqrt{\frac{1}{h(-\xi^*)}}\right]. \tag{A.28}$$

Noting that $\xi = \frac{1}{2}[h(-\xi) - h(\xi)] = \frac{1}{2}[\sqrt{h(-\xi)} - \sqrt{h(\xi)}][\sqrt{h(-\xi)} + \sqrt{h(\xi)}]$, we obtain

$$-2s\xi^* = \frac{\rho}{2}\left[\sqrt{h(\xi^*)} - \sqrt{h(-\xi^*)}\right]^2\left[\operatorname{erfc}(\xi^*)\sqrt{\frac{h(-\xi^*)}{h(\xi^*)}} + \operatorname{erfc}(-\xi^*)\sqrt{\frac{h(\xi^*)}{h(-\xi^*)}} + 2\right] \tag{A.29}$$

(We used $\operatorname{erfc}\xi + \operatorname{erfc}(\xi) = 2$.)

At the end of the day, $C(s) = 2s\xi^* + \mu(\lambda^*, \xi^*)$. Our final expression is

$$C(s) = -\frac{\rho}{2}\left[\sqrt{h(\xi^*)} - \sqrt{h(-\xi^*)}\right]^2\left[\operatorname{erfc}(\xi^*)\sqrt{\frac{h(-\xi^*)}{h(\xi^*)}} + \operatorname{erfc}(-\xi^*)\sqrt{\frac{h(\xi^*)}{h(-\xi^*)}}\right], \tag{A.30}$$

with ξ^* the solution of Eq. (A.28)

Equations (A.28) and (A.30) are the ones found by Sadhu and Derrida for interacting Brownian particles on a line (Eq. (42a) and (42b) of Ref. [41]). Interacting Brownian particles on a line are equivalent to the limit $\rho \to 0$ of the SEP. This solution is also equivalent to the results found by other methods in Refs. [44, 45].

Appendix B

Edwards-Wilkinson equation and symmetric exclusion process

The Edwards-Wilkinson (EW) equation [102] for a function $h(z,t)$ is the stochastic equation

$$\frac{\partial h}{\partial t}(z,t) = D\frac{\partial^2 h}{\partial z^2}(z,t) + \eta(z,t) \tag{B.1}$$

with a Gaussian noise $\eta(z,t)$ satisfying

$$\langle \eta(z,t)\rangle = 0, \tag{B.2}$$

$$\langle \eta(z,t)\eta(z',t')\rangle = 2\Gamma\delta(z-z')\delta(t-t'). \tag{B.3}$$

It is usually interpreted as a model of interface growth: h is the height of the interface at point z, D accounts for some elasticity. Here we choose to define the EW equation in dimension 1+1 but the physical space can be of any dimension (see Ref. [102] for results in 2 and 3 dimensions).

The EW equation is a simplified version of the Kardar-Parisi-Zhang (KPZ) equation [102] in which one adds a non-linearity $(\partial_z h)^2$. Note that it has been argued that the KPZ equation is a mapping for the asymmetric exclusion process [103].

A crucial remark about the EW equation is that, as it is linear with a Gaussian noise, the field $h(z,t)$ is Gaussian. It is enough to compute the average $\langle h(z,t)\rangle$ and the two-point correlation $\langle h(z,t)h(z',t')\rangle$ to know the full process. In particular, if a model is mapped to the EW equation, one should not expect to gain information beyond these two quantities.

We shall now look at the link between the symmetric exclusion process (SEP) and the EW equation and explain what kind of insight we gain by studying the EW equation.

B.1 Link with the symmetric exclusion process

In this section we introduce a mapping used for instance in Refs. [30, 103]. Let us consider the symmetric exclusion process (SEP) (see Chapter 2). We label the particles: $z = 0$ is the closest particle to the origin, $z = 1$ the particle to its right, and so on (with negative indices for particles on the left). The displacement of particle z at time t is denoted $X_z(t)$. Alternatively, we define a displacement field

$$h(z,t) \equiv X_z(t), \tag{B.4}$$

the variable z in $h(z,t)$ can now be continuous.

It is standard to assume (see Ref. [103] and Appendix B) that the displacement field $h(z,t)$ is diffusive and obeys the Edwards-Wilkinson equation (B.1), with the same diffusion coefficient as the one of the density of the SEP,

$$D = \frac{1}{2}. \tag{B.5}$$

The only thing that remains to be set is the amplitude of the noise. It is adjusted [103] by matching the variance $\left\langle [h(0,t)-h(0,0)]^2 \right\rangle$ with its known expression [27],

$$\left\langle [h(0,t)-h(0,0)]^2 \right\rangle \equiv \langle [X_0(t)-X_0(0)]^2 \rangle = \frac{1-\rho}{\rho}\sqrt{\frac{2t}{\pi}}. \tag{B.6}$$

Anticipating on our computation [Eq. (B.23)], we set

$$\Gamma = \frac{1}{4}\frac{1-\rho}{\rho} \tag{B.7}$$

where ρ is the average density of the SEP. We shall see that these simple assumptions allow us to derive results for the SEP that should hold in the Gaussian limit.

One should remain careful about the fact that z is not a coordinate in physical space, but a continuous analog of the indices of the particles. However, in the high density limit ($\rho \to 1$), z should be rather close to the spatial coordinate.

B.2 Quenched correlations

We start from the EW equation (B.1) and assume that at time 0, the interface is flat: $h(z, t=0) = 0$. This immediately implies $\langle h(z,t)\rangle = 0$ at all positive times. From the point of view of the set, we took "quenched" (i.e. frozen) initial conditions.

The general solution of the EW equation is the convolution of the noise with the Green function of the diffusion equation.

$$h(z,t) = \int_0^t dt_1 \int_{-\infty}^{\infty} dz_1 \frac{\eta(z_1,t_1)}{\sqrt{2\pi D(t-t_1)}} e^{-\frac{(z-z_1)^2}{4D(t-t_1)}}. \tag{B.8}$$

We define the two-point correlation function (from a flat initial state)

$$c_0(z,t,\tau) \equiv \langle h(0,t)h(z,t+\tau)\rangle. \tag{B.9}$$

It can be computed from Eqs (B.3) and (B.8),

$$c_0(z,t,\tau) = \frac{\Gamma}{\pi D}\int_0^t dt_1 \int_{-\infty}^{\infty} dz_1 \frac{e^{\frac{-(z-z_1)^2}{4D(t+\tau-t_1)}} e^{\frac{-z_1^2}{4D(t-t_1)}}}{\sqrt{(t+\tau-t_1)(t-t_1)}} \tag{B.10}$$

$$= \Gamma\sqrt{\frac{2}{\pi D}}\int_{\tau/2}^{t+\tau/2} ds \frac{e^{-\frac{z^2}{8Ds}}}{\sqrt{s}} \tag{B.11}$$

$$= \Gamma\sqrt{\frac{8t}{\pi D}}\left\{ g\left(\frac{|z|}{\sqrt{4D(2t+\tau)}}\right) - g\left(\frac{|z|}{\sqrt{4D\tau}}\right)\right\} \tag{B.12}$$

with $g(u) = e^{-u^2} - \sqrt{\pi} u \operatorname{erfc}(u)$.

In particular, the variance and the equal-time correlation read

$$\langle h(0,t)^2 \rangle = \Gamma \sqrt{\frac{8t}{\pi D}}, \qquad \langle h(0,t) h(z,t) \rangle = \Gamma \sqrt{\frac{8t}{\pi D}} g\left(\frac{|z|}{\sqrt{8Dt}} \right). \tag{B.13}$$

In the language of the SEP, we predict

$$\langle X_0^2(t) \rangle_{\text{quenched}} = \frac{1-\rho}{\rho} \sqrt{\frac{t}{\pi}}, \qquad \langle X_0(t) X_n(t) \rangle_{\text{quenched}} = \frac{1-\rho}{\rho} \sqrt{\frac{t}{\pi}} g\left(\frac{|n|}{\sqrt{4t}} \right). \tag{B.14}$$

The two-time correlation at the same point yields

$$\langle h(0,t) h(0,t+\tau) \rangle = \Gamma \sqrt{\frac{2}{\pi D}} \int_{\tau/2}^{t+\tau/2} \frac{ds}{\sqrt{s}} = \frac{2\Gamma}{\sqrt{\pi D}} \left(\sqrt{t+\tau+t} - \sqrt{\tau} \right), \tag{B.15}$$

which means for the SEP,

$$\langle X_0(t_1) X_0(t_2) \rangle_{\text{quenched}} = \frac{1-\rho}{\rho} \frac{1}{\sqrt{2\pi}} \left(\sqrt{t_1+t_2} - \sqrt{|t_2-t_1|} \right) \tag{B.16}$$

This time scaling is the one found in Ref. [41] for point-like particles (low density limit of the SEP).

B.3 Annealed correlations

In the last section, we computed the correlations starting from an initially flat profile. We now want to do the same starting from the equilibrium state. For the SEP, this means that we take "annealed" initial conditions.

We consider an initial condition at $t = -T$: $h(z, t = -T) = 0$ and define the correlations of displacements between time 0 and t or $t+\tau$,

$$c_T(z,t,\tau) \equiv \langle [h(z,t+\tau) - h(z,0)] [h(0,t) - h(0,0)] \rangle . \tag{B.17}$$

The limit $T \to \infty$ (initial condition at $t = -\infty$) corresponds to a system that is equilibrated at time 0. Our observable will be $c_\infty(z,t,\tau)$.

We expand the product in c_T and find that, by definition of c_0,

$$c_T(z,t,\tau) = c_0(z, T+t, \tau) - c_0(z, T, t+\tau) - c_0(z, T, t) + c_0(z, T, 0) \tag{B.18}$$

$$= \Gamma \sqrt{\frac{2}{\pi D}} \left\{ \int_{\tau/2}^{T+t+\tau/2} - \int_{t/2+\tau/2}^{T+t/2+\tau/2} - \int_{t/2}^{T+t/2} + \int_0^T \right\} \frac{e^{-\frac{z^2}{8Ds}}}{\sqrt{s}} ds \tag{B.19}$$

$$= \Gamma \sqrt{\frac{2}{\pi D}} \left\{ \int_{\tau/2}^{t/2+\tau/2} + \int_{T+t/2+\tau/2}^{T+t+\tau/2} + \int_0^{t/2} - \int_T^{T+t/2} \right\} \frac{e^{-\frac{z^2}{8Ds}}}{\sqrt{s}} ds. \tag{B.20}$$

The integrals involving T in both bounds vanish when $T \to \infty$ and we obtain

$$c_\infty(z,t,\tau) = \Gamma \sqrt{\frac{2}{\pi D}} \left\{ \int_{\tau/2}^{t/2+\tau/2} \frac{e^{-\frac{z^2}{8Ds}}}{\sqrt{s}} ds + \int_0^{t/2} \frac{e^{-\frac{z^2}{8Ds}}}{\sqrt{s}} ds \right\} \tag{B.21}$$

$$= 2\Gamma \sqrt{\frac{t}{\pi D}} \left\{ g\left(\frac{|z|}{\sqrt{4D(t+\tau)}} \right) + g\left(\frac{|z|}{\sqrt{4Dt}} \right) - g\left(\frac{|z|}{\sqrt{4D\tau}} \right) \right\}. \tag{B.22}$$

In particular, the variance and the pair correlations at equal time are

$$\left\langle [h(0,t)-h(0,0)]^2 \right\rangle = 4\Gamma\sqrt{\frac{t}{\pi D}}, \tag{B.23}$$

$$\langle [h(z,t)-h(z,0)][h(0,t)-h(0,0)]\rangle = 4\Gamma\sqrt{\frac{t}{\pi D}}\, g\left(\frac{|z|}{\sqrt{4Dt}}\right), \tag{B.24}$$

In the language of the SEP, we predict

$$\langle X_0^2(t)\rangle_{\text{annealed}} = \frac{1-\rho}{\rho}\sqrt{\frac{2t}{\pi}}, \qquad \langle X_0(t)X_n(t)\rangle_{\text{annealed}} = \frac{1-\rho}{\rho}\sqrt{\frac{2t}{\pi}}\, g\left(\frac{|n|}{\sqrt{2t}}\right). \tag{B.25}$$

The variance is the well-known result [27]: this justifies our expression of Γ [Eq. (B.7)]. Furthermore, at high density, n is approximately the initial distance between two particles: the expression of the two-point correlation matches our computation at high density.

One notices a $\sqrt{2}$ difference between quenched and annealed initial conditions. This factor shows that the system has infinite memory [35, 41].

The two-time correlation at the same point is

$$\langle [h(0,t)-h(0,0)][h(0,t+\tau)-h(0,0)]\rangle = \Gamma\sqrt{\frac{2}{\pi D}}\left\{\int_{\tau/2}^{t/2+\tau/2}\frac{ds}{\sqrt{s}} + \int_0^{t/2}\frac{ds}{\sqrt{s}}\right\} \tag{B.26}$$

$$= \frac{2\Gamma}{\sqrt{\pi D}}\left\{\sqrt{t+\tau}+\sqrt{t}-\sqrt{\tau}\right\} \tag{B.27}$$

which means for the SEP,

$$\langle X_0(t_1)X_0(t_2)\rangle_{\text{annealed}} = \frac{1-\rho}{\rho}\frac{1}{\sqrt{2\pi}}\left(\sqrt{t_1}+\sqrt{t_2}-\sqrt{|t_2-t_1|}\right). \tag{B.28}$$

This time scaling is again the one found in Ref. [41] for point-like particles. It corresponds to a fractional Brownian motion.

B.4 Localized force

We now add a forcing f on the interface at point 0. The EW equation with forcing is

$$\frac{\partial h}{\partial t}(z,t) = D\frac{\partial^2 h}{\partial z^2}(z,t) + \mu f\,\delta(z) + \eta(z,t), \tag{B.29}$$

with μ the mobility, δ the Dirac delta function, and η is the Gaussian noise given by Eq. (B.3).

The average of h does not depend on the noise, and thus is independent of the initial conditions. We use the Fourier transform $\tilde{h}(k,t) = \int dz e^{-ikz} h(z,t)$ and obtain the following equation

$$\frac{\partial\langle\tilde{h}(k,t)\rangle}{\partial t} = -Dk^2\langle\tilde{h}(k,t)\rangle + \mu f. \tag{B.30}$$

Setting the initial condition $h(z,t=0)=0$, the solution is

$$\langle\tilde{h}(k,t)\rangle = \frac{\mu f}{Dk^2}\left(1-e^{-Dk^2 t}\right). \tag{B.31}$$

Back to real space,

$$\langle h(z,t)\rangle_f = \mu f \sqrt{\frac{t}{\pi D}} g\left(\frac{|z|}{\sqrt{4Dt}}\right). \tag{B.32}$$

(the indice f denotes the forcing). This is the results we found at high density for the entrainment at small force.

This result is very similar to the pair correlations starting from equilibrium initial conditions [Eq. (B.24)]. Indeed we find the following fluctuation-dissipation result linking the pair correlations at equilibrium to the response at a given point to a force applied at another point.

$$c_\infty(z,t,0) = 4\Gamma \frac{\langle h(z,t)\rangle_f}{\mu f}. \tag{B.33}$$

One may now introduce two forces, one at position 0 and the other at position L. The equation is

$$\frac{\partial h}{\partial t}(z,t) = D\frac{\partial^2 h}{\partial z^2}(z,t) + \mu f_1 \delta(z) + \mu f_2 \delta(z-L) + \eta(z,t), \tag{B.34}$$

and its average solution is

$$\langle h(z,t)\rangle = \mu\sqrt{\frac{t}{\pi D}}\left\{f_1 g\left(\frac{|z|}{\sqrt{4Dt}}\right) + f_2 g\left(\frac{|z-L|}{\sqrt{4Dt}}\right)\right\}. \tag{B.35}$$

This is similar to the result we found for the SEP at high density, but here we only have the linear behavior in the forces f_1 and f_2 (small forces) and not the full structure.

Appendix C

Random phase approximation in liquid theory

In this appendix, we focus on standard liquid theory as detailed in the book of Hansen and McDonald [1]. Our goal is not to give detailed proofs of the results but rather to highlight the main steps leading to the Random Phase Approximation results.

C.1 Thermodynamic potentials

We consider a liquid composed of N particles of mass m, having impulsions $\{\mathbf{p}_i\}$ and positions $\{\mathbf{r}_i\}$. Particles i and j interact via a pair potential $V(\mathbf{r}_i,\mathbf{r}_j)$, and we consider an external potential $\varphi(\mathbf{r})$. The energy of the system reads

$$\mathscr{H}(\{\mathbf{p}_i,\mathbf{r}_i\}) = \sum_{i=1}^{N}\frac{\mathbf{p}_i^2}{2m} + \sum_{i\neq j} V(\mathbf{r}_i,\mathbf{r}_j) + \sum_{i=1}^{N}\varphi(\mathbf{r}_i). \tag{C.1}$$

We use the grand canonical ensemble, $\beta = 1/(k_B T)$ is the inverse temperature (with T the temperature and k_B the Boltzmann constant) and μ is the chemical potential. Standard computations give the following results for the grand potential Ω and the grand partition function Ξ.

$$\Xi = \sum_{N=0}^{\infty}\frac{1}{N!}\frac{1}{\Lambda^{3N}}\int d\mathbf{r}_1\ldots d\mathbf{r}_N\left[\prod_{i=1}^{N} e^{\beta[\mu-\varphi(\mathbf{r}_i)]}\right] e^{-\beta\sum_{i\neq j}V(\mathbf{r}_i,\mathbf{r}_j)}, \tag{C.2}$$

$$\Omega = -\frac{1}{\beta}\ln\Xi, \tag{C.3}$$

with the de Broglie thermal wavelength $\Lambda = \sqrt{(\beta h^2)/(2\pi m)}$ (h is the Plank constant). We see that the quantity $\psi(\mathbf{r}) = \mu - \varphi(\mathbf{r})$ naturally appears, we call it the intrinsic chemical potential.

One may ask what is the conjugated quantity associated with $\psi(\mathbf{r})$. To answer this question, we define the fluctuating local density $\rho(\mathbf{r})$ and the average local density $\rho^{(1)}(\mathbf{r})$ by

$$\rho(\mathbf{r}) \equiv \sum_{i=1}^{N}\delta(\mathbf{r}-\mathbf{r}_i), \tag{C.4}$$

$$\rho^{(1)}(\mathbf{r}) \equiv \langle\rho(\mathbf{r})\rangle. \tag{C.5}$$

The average potential energy due to the external field is then given by $\int \rho^{(1)}(\mathbf{r})\phi(\mathbf{r})d\mathbf{r}$. Thus, infinitesimal changes of entropy (δS), number of particles (δN) and external potential ($\delta\varphi(\mathbf{r})$) induce a change of internal energy

$$\delta U = T\delta S + \int \rho^{(1)}(\mathbf{r})\delta\phi(\mathbf{r})d\mathbf{r} + \mu\delta N. \tag{C.6}$$

(We include the confinement in the external potential so as not to consider the volume.) Using the well know relation $\Omega = U - TS - \mu N$, we obtain

$$\delta\Omega = -S\delta T + \int \rho^{(1)}(\mathbf{r})\delta\phi(\mathbf{r})d\mathbf{r} - N\delta\mu = -S\delta T - \int \rho^{(1)}(\mathbf{r})\delta\psi(\mathbf{r})d\mathbf{r}. \tag{C.7}$$

At the end of the day, Ω is a functional of the intrinsic chemical potential $\psi(\mathbf{r})$ and the conjugated quantity associated with $\psi(\mathbf{r})$ is $\rho^{(1)}(\mathbf{r})$.

We now define the intrinsic free energy $\mathscr{F}$ by the Legendre transform

$$\mathscr{F}[T,\rho^{(1)}] \equiv \Omega[T,\psi] + \int d\mathbf{r}\,\rho^{(1)}(\mathbf{r})\psi(\mathbf{r}). \tag{C.8}$$

(The reader should think of this relation as the analog of $F = \Omega + N\mu$.) $\mathscr{F}$ is a functional of $\rho^{(1)}$. For an ideal gas, the intrinsic free energy is

$$\mathscr{F}^{\mathrm{id}}[T,\rho^{(1)}] = k_B T \int \rho^{(1)}(\mathbf{r})\left(\ln\left[\Lambda^3\rho^{(1)}(\mathbf{r})\right] - 1\right)d\mathbf{r}, \tag{C.9}$$

and we define the excess intrinsic free energy as

$$\mathscr{F}^{\mathrm{ex}}[T,\rho^{(1)}] \equiv \mathscr{F}[T,\rho^{(1)}] - \mathscr{F}^{\mathrm{id}}[T,\rho^{(1)}]. \tag{C.10}$$

C.2 Correlation functions and Ornstein-Zernike equation

We first define correlations of the fluctuations of the density field

$$H^{(n)}(\mathbf{r}_1,\ldots,\mathbf{r}_n) \equiv \left\langle \prod_{i=1}^{n}\left[\rho(\mathbf{r}_i) - \rho^{(1)}(\mathbf{r}_i)\right]\right\rangle. \tag{C.11}$$

In particular, $H^{(2)}$ is related to the usual pair correlation function $h^{(2)}$ by

$$H^{(2)}(\mathbf{r},\mathbf{r}') = \rho^{(1)}(\mathbf{r})\rho^{(1)}(\mathbf{r}')h^{(2)}(\mathbf{r},\mathbf{r}') + \rho^{(1)}(\mathbf{r})\delta(\mathbf{r}-\mathbf{r}'). \tag{C.12}$$

A very interesting result [1] is that the correlation functions $H^{(n)}$ can be expressed as functional derivatives of the grand potential Ω with respect to the intrinsic chemical potential $\psi(\mathbf{r})$.

$$H^{(n)}(\mathbf{r}_1,\ldots,\mathbf{r}_n) = -\beta\frac{\delta^n\Omega}{\delta(\beta\psi(\mathbf{r}_1))\ldots\delta(\beta\psi(\mathbf{r}_n))} \tag{C.13}$$

Similarly, Hansen and McDonald define the so-called direct correlation functions as functional derivatives of the excess intrinsic free energy $\mathscr{F}^{\mathrm{ex}}$ with respect to the density profile $\rho^{(1)}(\mathbf{r})$.

$$c^{(n)}(\mathbf{r}_1,\ldots,\mathbf{r}_n) \equiv -\beta\frac{\delta^n\mathscr{F}^{\mathrm{ex}}}{\delta\rho^{(1)}(\mathbf{r}_1)\ldots\delta\rho^{(1)}(\mathbf{r}_n)} \tag{C.14}$$

Having all these definitions, one manages [1] to link the correlations of order 2 to the direct correlations of order 2. This is the Ornstein-Zernike equation:

$$h^{(2)}(\mathbf{r},\mathbf{r}') = c^{(2)}(\mathbf{r},\mathbf{r}') + \int c^{(2)}(\mathbf{r},\mathbf{r}'')\rho^{(1)}(\mathbf{r}'')h^{(2)}(\mathbf{r}'',\mathbf{r}')d\mathbf{r}'' \tag{C.15}$$

The standard view on this equation is to say that the total correlation between two particles $h^{(2)}(\mathbf{r},\mathbf{r}')$ is the sum of a direct contribution $c^{(2)}(\mathbf{r},\mathbf{r}')$ and a contribution mediated by a third particle (at position $\mathbf{r}''$). Hence, the name "direct correlation" for $c^{(2)}(\mathbf{r},\mathbf{r}')$.

In the case of an homogeneous and isotropic fluid, $\rho^{(1)}(\mathbf{r}) = \bar{\rho}$, $h^{(2)}(\mathbf{r},\mathbf{r}') = h(\mathbf{r}-\mathbf{r}') = h(\|\mathbf{r}-\mathbf{r}'\|)$ and $c^{(2)}(\mathbf{r},\mathbf{r}') = c(\mathbf{r}-\mathbf{r}') = c(\|\mathbf{r}-\mathbf{r}'\|)$. The Ornstein-Zernike equation becomes

$$h(\mathbf{r}) = c(\mathbf{r}) + \bar{\rho}\int c(\mathbf{r}-\mathbf{r}')h(\mathbf{r}')d\mathbf{r}', \tag{C.16}$$

$$\tilde{h}(\mathbf{k}) = \frac{\tilde{c}(\mathbf{k})}{1-\rho\tilde{c}(\mathbf{k})}, \tag{C.17}$$

using the Fourier transform $\tilde{h}(\mathbf{k}) = \int d\mathbf{r}e^{-i\mathbf{k}\cdot\mathbf{r}}h(\mathbf{r})$. If one has an expression for the direct correlations functions (or at least a closure relation), one readily obtains the pair correlation function.

The next subsection is dedicated to perturbative theory and in particular to the random phase approximation.

C.3 Random phase approximation

Starting from the expression of the grand potential (C.2), one shows that its functional derivative with respect to the interaction potential V (keeping T and ψ constant) leads to the two-point correlation $\rho^{(2)}(\mathbf{r},\mathbf{r}') \equiv \langle\rho(\mathbf{r})\rho(\mathbf{r}')\rangle$,

$$\rho^{(2)}(\mathbf{r},\mathbf{r}') = 2\frac{\delta\Omega}{\delta V(\mathbf{r},\mathbf{r}')}. \tag{C.18}$$

Using Eq. (C.8), this translates into

$$\rho^{(2)}(\mathbf{r},\mathbf{r}') = 2\frac{\delta\mathscr{F}}{\delta V(\mathbf{r},\mathbf{r}')} = 2\frac{\delta\mathscr{F}^{\text{ex}}}{\delta V(\mathbf{r},\mathbf{r}')}. \tag{C.19}$$

Starting from the ideal gas[1] ($V = 0$, $\mathscr{F}^{\text{ex}} = 0$), we gradually turn on the potential: we apply $\lambda V(\mathbf{r},\mathbf{r}')$ for $0 \leq \lambda \leq 1$. The integration of Eq. (C.19) leads to the following expression for the excess intrinsic free energy,

$$\mathscr{F}^{\text{ex}}[\rho^{(1)}] = \frac{1}{2}\int_0^1 d\lambda \iint d\mathbf{r}d\mathbf{r}'\rho^{(2)}(\mathbf{r},\mathbf{r}';\lambda)V(\mathbf{r},\mathbf{r}'), \tag{C.20}$$

with $\rho^{(2)}(\mathbf{r},\mathbf{r}';\lambda)$ the two-point correlation corresponding to a potential λV. Note that this equation is exact.

At this level, the so-called *random phase approximation* (RPA) is a mean-field (or decoupling) approximation. We write

$$\rho^{(2)}(\mathbf{r},\mathbf{r}';\lambda) \equiv \langle\rho(\mathbf{r})\rho(\mathbf{r}')\rangle(\lambda) \approx \langle\rho(\mathbf{r})\rangle\langle\rho(\mathbf{r}')\rangle \equiv \rho^{(1)}(\mathbf{r})\rho^{(1)}(\mathbf{r}'), \tag{C.21}$$

[1] More generally, one may do perturbations around any reference potential. See Ref. [1].

which leads us to

$$\mathscr{F}^{\mathrm{ex}}[\rho^{(1)}] \approx \frac{1}{2}\int d\mathbf{r}d\mathbf{r}' V(\mathbf{r},\mathbf{r}')\rho^{(1)}(\mathbf{r})\rho^{(1)}(\mathbf{r}'). \tag{C.22}$$

A crucial point is that the density profile $\rho^{(1)}$ does not depend on the interaction potential.

It is now easy to compute the two-point direction correlation function defined in Eq. (C.14).

$$c^{(2)}(\mathbf{r},\mathbf{r}') \equiv -\beta \frac{\delta^2 \mathscr{F}^{\mathrm{ex}}}{\delta\rho^{(1)}(\mathbf{r})\delta\rho^{(1)}(\mathbf{r}')} \approx -\beta V(\mathbf{r},\mathbf{r}'). \tag{C.23}$$

Within the RPA, the direct correlation function is simply given by the interaction potential.

At the end of the day, for an homogeneous isotropic fluid, we can use the Ornstein-Zernike relation (C.17) to obtain the correlations in Fourier space within the RPA.

$$\tilde{c}(k) = -\beta\tilde{V}(k), \tag{C.24}$$

$$\tilde{h}(k) \approx \frac{-\tilde{V}(k)}{k_B T + \rho\tilde{V}(k)}. \tag{C.25}$$

This last result is identical to the result from the linearized Dean equation [Eq. (8.42)]. (As the mobility was set to one, the diffusion coefficient is $D_0 = k_B T$.)

It is remarkable that in the simple case of a passive fluid, we could link our approximation of linearization of the Dean equation to a well-known approximation of liquid theory: the random phase approximation.

Appendix D

Theory of electrophoretic Janus particles

In this appendix, we present the basics of the theory explaining the motion of the Janus particles studied in Chap 11. We first review some electrokinetic phenomena before investigating the one involved in the motion of electrophoretic Janus particles: induced-charge electrophoresis (ICEP). We finally present the dependence of the velocity of the particles on the frequency of the electric field. At high frequency, a mechanism different from ICEP leads to a velocity reversal. Note that the theoretical motivation often comes from experimental setups [77–80].

D.1 Electrokinetic phenomena

Before explaining the motion of Janus particles, we recall some basics about electrokinetic phenomena (Ref. [104], chap. 14.23). Then, we turn to induced-charge electrokinetic phenomena [105, 106] which provide the framework to understand the motion of Janus particles.

In all the phenomena described below, the system will consist of an electrolytic solution (typically salted water) submitted to an electic field (typically a difference of potential applied between two electrodes). When an intruder is introduced, it is typically of nanometric to micrometric dimensions. Before going into the details of the phenomena, we recall that in an electrolytic solution close to a charged surface, oppositely charged ions accumulate close to the surface [104]. This accumulation, known as the electric double layer (EDL), has a thickness given by the Debye length,

$$\lambda_D = \left(\sum_j \frac{q_j^2 n_j^0}{\epsilon k_B T} \right)^{-1/2} \tag{D.1}$$

where the sum j is on the species of ions. q_j and n_j^0 are respectively the charge and the concentration of species j, and ϵ is the dielectric constant of the fluid. For a monovalent salt at concentration C (in $\mathrm{mol\,L^{-1}}$) in water, $\lambda_D = 0.304/\sqrt{C}$ nm.

Electrophoresis[1]**.** (See Fig. D.1b.) The simplest situation is a charged intruder in the solution (for instance a charged colloid). In this case, the intruder moves towards the oppositely charged

[1] The suffix -phoresis denotes the motion of particles due to a force. The word osmosis denotes the motion of a fluid. Both have etymologies from ancient Greek.

electrode. It is slowed down by a friction force due to the ions of the fluid. This phenomenon is known as electrophoresis and is the basis of some microfluidic separation techniques.

Electro-osmosis. (See Fig. D.1a.) Suppose now that the walls of the system (perpendicular to the electrodes) are charged (in practice they are made of a material that has surface charges). An electric double layer (EDL) appears close to the surface. This EDL is dragged by the electric field perpendicular to the surface. This creates a motion not only of the ions but also of the fluid around them. This flow is known as electro-osmosis. For a charged intruder in a tiny channel with charged walls, the interplay between electrophoretic and electro-osmotic effects is non-trivial.

Induced-charge electro-osmosis (ICEO). (See Fig. D.1c.) More recently, the focus has been put on electrokinetic phenomena with dielectric intruders [105, 106]. Let us consider a dielectric intruder fixed in an electrolytic solution, with an external electric field pointing upwards. The intruder becomes polarized: positive charges accumulate on its top, and negative charges on its bottom. The EDL is thus made of negative ions on top, and positive ions below the intruder. Finally, this EDL is dragged by the electric field: negative ions want to move downwards and positive ions want to move upwards. This creates a quadrupolar flow around the intruder.

Induced-charge electrophoresis (ICEP). (See Fig. D.1d.) We can finally explain the main mechanism for the propulsion of Janus particles. We consider the previous situation with two major differences: (i) the intruder is allowed to move, and (ii) the intruder is composed of two hemispheres, with the frontier aligned with the electric field. One hemisphere (the left one) is insulating and cannot be polarized, the other (the right one) is metallic and can be polarized. The discussion of ICEO flow holds only for the metallic hemisphere. The EDL around it is dragged by the electric field and creates an ICEO flow directed towards the right. This symmetry breaking thus pushes the particle to the left. This motion is called induced-charge electrophoresis (ICEP). ICEP is the main propulsion mecanism of the Janus particles that we studied in Chapter 11.

D.2 Induced-charge electrophoresis

Let us now detail a bit the theory of induced-charge electrophoresis, relying mainly on the computation of Squires and Bazant [105]. We focus only on the main features obtained from dimensional analysis arguments. In usual electro-osmosis, ions close to a charged wall move due to a parallel electric field of strength E (Fig. D.1a). This induces a flow of the fluid whose typical velocity $\mathbf{u}_s$ is given by the balance between the drag due to the electric field and the viscous force. This is the Smoluchowski slip velocity

$$\mathbf{u}_s = -\frac{\epsilon\zeta}{\eta}\mathbf{E}, \tag{D.2}$$

where η is the viscosity of the fluid, ϵ its dielectric constant and ζ is the voltage difference across the EDL. ζ is known as the zeta potential, it is proportional to the surface charge of the wall and depends on the concentration of ions in the solution.

We now look at induced electrophoretic effects. In this case, the intruder of size a is polarized by the electric field E. The zeta potential is no longer independent of the electric field. By dimensional analysis, one finds that $\zeta \sim Ea$. This means that the typical velocity of ICEP (or ICEO) is

$$U_0 = \frac{\epsilon a E^2}{\eta}. \tag{D.3}$$

In particular, it depends quadratically on the applied electric field. This square dependence is indeed observed in the experiments [77]. The exact prefactors for the motion of a half-coated

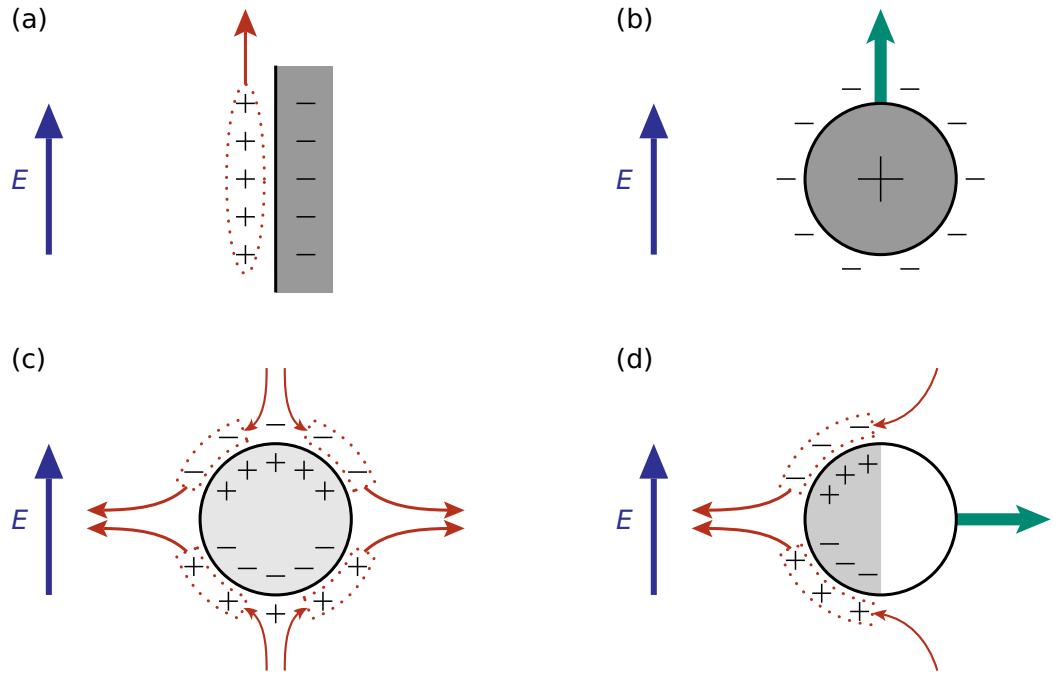

Figure D.1: (a) Electro-osmosis. A negatively charged wall induces a layer of positive ions that are driven by the external electric field. This creates a flow. (b) Electrophoresis. A positively charged particle is driven by the external electric field. Note that the negative EDL is driven and creates an electro-osmotic flow in the opposite direction. This hinders the motion of the particle. (c) ICEO. A fixed dielectric particle is polarized by the external field. The EDLs on both sides of the particles are driven towards the opposite sides. This creates a dipolar flow of the fluid. (d) ICEP. A dielectric particle can be polarized only on one side. This creates an asymmetric flow that induces a motion in the direction of its unpolarized side. This is of course a limit case, it is enough for the two sides to have different polarizabilities to induce a motion of the particle. In our experiments, the most polarizable side is the one coated with titanium.

cylinder (i.e. $U = 2U_0/(3\pi)$) and a half-coated sphere (i.e. $U = 9U_0/64$) can be obtained by computing the steady state of the EDL and the zeta potential in both geometries [105]. In terms of directions, a particle with one coated and one uncoated hemisphere will move towards the uncoated hemisphere (Fig. D.1d).

One may wonder why we considered only particles in the "left-right" configuration in which the boundary between the two hemispheres is aligned with the electric field (and thus the motion is perpendicular to the electric field). The reason is that this is the stable configuration. Indeed, if the boundary between the hemispheres makes an angle γ with the electric field, the particle will have an angular velocity $\dot{\gamma}$ [105] given by

$$\dot{\gamma} \propto -\frac{U_0}{a}\sin(2\gamma). \tag{D.4}$$

Hence the "left-right" configurations ($\gamma = 0$ or π) are stable and the "fore-aft" configurations ($\gamma = \pm\pi/2$) are unstable.

D.3 Frequency dependence

The discussion above was made assuming that the electric field was constant in time (DC). However, experimentally such a field would heat up the sample and make the experiment fail. Experiments are performed using an alternative (AC) field of frequency f. The discussion above remains valid as long as the EDL is able to charge faster than the electric field. Indeed since the effect is induced, the EDL needs to change sign when the field changes sign. The typical time scale for the charge of the EDL is given by [105, 107]

$$\tau_c = \frac{\lambda_D a}{D_s} \tag{D.5}$$

where λ_D is the Debye length, a is the particle diameter and D_s the diffusivity of the ions. Taking a salt concentration 10^{-4} mol L^{-1} leading to $\lambda_D \simeq 0.3/\sqrt{10^{-4}} \approx 30$ nm, a diameter $a = 3$ µm, and a diffusivity[2] $D_s \simeq 10^{-9}$ m^2 s^{-1}, the typical time is $\tau_c \simeq 10^{-4}$ s.

It has been shown [107] that (under some assumptions) the ICEP velocity decays with the frequency as

$$U_{\text{ICEP}}(f) \propto \frac{K}{K^2 + (A\tau_c f)^2} \tag{D.6}$$

with $K \propto a/\lambda_D$ and A a constant.

For frequencies much larger than τ_c^{-1}, one could expect the Janus particles to exhibit no motion. However, it has been observed experimentally [78, 80] that the particles still move but in the opposite direction, that is to say in the direction of their metallic hemisphere (instead of the direction of the glass hemisphere). This velocity reversal has been explained by a mechanism called self-dielectrophoresis [107]. Usual dielectrophoresis (DEP) is the fact that a dielectric particle in a non-uniform electric field gets polarized and exhibits a motion towards the region of high electric field. In the case of Janus particles, numerical simulations show that gradients of electric field are created at the level of the particle at high frequency. These local gradients can induce a velocity scaling with the frequency as

$$U_{\text{DEP}}(f) \propto -\frac{(\tau_c f)^2}{K^2 + (A\tau_c f)^2} \tag{D.7}$$

where the minus sign denotes a direction opposite to the ICEP motion. Balancing the two velocity expressions, one finds a velocity reversal at $f_{\text{cr}} \propto D_s/\sqrt{a\lambda_D^3}$ consistently with the experiments.

In our experiments $f < \tau_c^{-1}$, the particles move in the direction of the glass hemisphere and we expect their motion to be mostly due to ICEP.

[2] Tabulated in standard handbooks

Bibliography

[1] J.-P. Hansen & I. R. McDonald; *Theory of simple liquids: with applications to soft matter*; Academic Press (2013). Cited on pages 1, 10, 12, 13, 15, 19, 111, 112, 114, 117, 119, 121, 147, 191, 192 and 193.

[2] V. Démery & D. S. Dean; "The conductivity of strong electrolytes from stochastic density functional theory"; Journal of Statistical Mechanics: Theory and Experiment **2016**, p. 023 106 (2016). Cited on pages 1, 2, 12, 19, 20, 123, 130 and 136.

[3] S. Cambré, B. Schoeters, S. Luyckx, E. Goovaerts & W. Wenseleers; "Experimental Observation of Single-File Water Filling of Thin Single-Wall Carbon Nanotubes Down to Chiral Index (5,3)"; Phys. Rev. Lett. **104**, p. 207 401 (2010). Cited on pages 1, 2, 19 and 26.

[4] R. H. Tunuguntla, R. Y. Henley, Y.-C. Yao, T. A. Pham, M. Wanunu & A. Noy; "Enhanced water permeability and tunable ion selectivity in subnanometer carbon nanotube porins"; Science **357**, pp. 792–796 (2017). Cited on pages 1, 2, 19 and 26.

[5] V. Gupta, S. S. Nivarthi, A. V. McCormick & H. Ted Davis; "Evidence for single file diffusion of ethane in the molecular sieve AlPO4-5"; Chemical Physics Letters **247**, pp. 596–600 (1995). Cited on pages 1, 2, 19 and 26.

[6] K. Hahn, J. Kärger & V. Kukla; "Single-File Diffusion Observation"; Phys. Rev. Lett. **76**, pp. 2762–2765 (1996). Cited on pages 1, 2, 19 and 26.

[7] V. Kukla, J. Kornatowski, D. Demuth, I. Girnus, H. Pfeifer, L. V. C. Rees, S. Schunk, K. K. Unger & J. Kärger; "NMR Studies of Single-File Diffusion in Unidimensional Channel Zeolites"; Science **272**, pp. 702–704 (1996). Cited on pages 1, 2, 19 and 26.

[8] C. Lutz, M. Kollmann & C. Bechinger; "Single-File Diffusion of Colloids in One-Dimensional Channels"; Phys. Rev. Lett. **93**, p. 026 001 (2004). Cited on pages 1, 2, 19 and 26.

[9] B. Lin, M. Meron, B. Cui, S. A. Rice & H. Diamant; "From Random Walk to Single-File Diffusion"; Phys. Rev. Lett. **94**, p. 216 001 (2005). Cited on pages 1, 2, 8, 19, 26, 27, 74, 85 and 86.

[10] Q.-H. Wei, C. Bechinger & P. Leiderer; "Single-File Diffusion of Colloids in One-Dimensional Channels"; Science **287**, pp. 625–627 (2000). Cited on pages 1, 2, 8, 19, 26, 27, 74 and 85.

[11] H. P. ZHANG, A. BE'ER, E. L. FLORIN & H. L. SWINNEY; "Collective motion and density fluctuations in bacterial colonies"; Proceedings of the National Academy of Sciences **107**, pp. 13 626–13 630 (2010). Cited on pages 1, 19 and 142.

[12] D. NISHIGUCHI, K. H. NAGAI, H. CHATÉ & M. SANO; "Long-range nematic order and anomalous fluctuations in suspensions of swimming filamentous bacteria"; Phys. Rev. E **95**, p. 020 601 (2017). Cited on pages 1, 19 and 142.

[13] H. LI, X. SHI, M. HUANG, X. CHEN, M. XIAO, C. LIU, H. CHATÉ & H. P. ZHANG; "Data-driven quantitative modeling of bacterial active nematics"; Proceedings of the National Academy of Sciences **116**, pp. 777–785 (2019). Cited on pages 1, 19 and 142.

[14] Y. SUMINO, K. H. NAGAI, Y. SHITAKA, D. TANAKA, K. YOSHIKAWA, H. CHATÉ & K. OIWA; "Large-scale vortex lattice emerging from collectively moving microtubules"; Nature **483**, pp. 448–452 (2012). Cited on pages 1, 19 and 142.

[15] A. SCHADSCHNEIDER, W. KLINGSCH, H. KLUEPFEL, T. KRETZ, C. ROGSCH & A. SEYFRIED; "Evacuation Dynamics: Empirical Results, Modeling and Applications"; in "Encyclopedia of Complexity and System Science", Springer (2008); https://arxiv.org/abs/0802.1620. Cited on pages 1, 19 and 124.

[16] M. MOUSSAÏD, E. G. GUILLOT, M. MOREAU, J. FEHRENBACH, O. CHABIRON, S. LEMERCIER, J. PETTRÉ, C. APPERT-ROLLAND, P. DEGOND & G. THERAULAZ; "Traffic Instabilities in Self-Organized Pedestrian Crowds"; PLoS Comput Biol **8**, pp. 1–10 (2012). Cited on pages 1, 19 and 124.

[17] N. BAIN & D. BARTOLO; "Dynamic response and hydrodynamics of polarized crowds"; Science **363**, pp. 46–49 (2019). Cited on pages 1, 19 and 142.

[18] A. CAVAGNA, A. CIMARELLI, I. GIARDINA, G. PARISI, R. SANTAGATI, F. STEFANINI & M. VIALE; "Scale-free correlations in starling flocks"; Proceedings of the National Academy of Sciences **107**, pp. 11 865–11 870 (2010). Cited on pages 1, 19 and 142.

[19] F. GINELLI, F. PERUANI, M.-H. PILLOT, H. CHATE, G. THERAULAZ & R. BON; "Intermittent collective dynamics emerge from conflicting imperatives in sheep herds"; Proceedings of the National Academy of Sciences **112**, pp. 12 729–12 734 (2015). Cited on pages 1, 19 and 142.

[20] L. PELITI; *Statistical mechanics in a nutshell*; Princeton University Press (2011). Cited on pages 1, 15, 19, 20, 85, 111, 113, 114, 117 and 121.

[21] B. DIU, B. ROULET, C. GUTHMANN & D. LEDERER; *Eléments de physique statistique*; Hermann (1989). Cited on pages 1, 19 and 113.

[22] R. BALIAN; *From microphysics to macrophysics: methods and applications of statistical physics*; Springer Science & Business Media (2007). Cited on pages 1, 19, 20 and 113.

[23] M. KARDAR; *Statistical physics of particles*; Cambridge University Press (2007). Cited on pages 1, 19, 20, 113 and 114.

[24] V. DÉMERY, O. BÉNICHOU & H. JACQUIN; "Generalized Langevin equations for a driven tracer in dense soft colloids: construction and applications"; New Journal of Physics **16**, p. 053 032 (2014). Cited on pages 2, 12, 20, 123, 129 and 132.

[25] D. S. DEAN, B.-S. LU, A. C. MAGGS & R. PODGORNIK; "Nonequilibrium Tuning of the Thermal Casimir Effect"; Phys. Rev. Lett. **116**, p. 240 602 (2016). Cited on pages 2, 12 and 123.

[26] S. ALEXANDER & P. PINCUS; "Diffusion of labeled particles on one-dimensional chains"; Phys. Rev. B **18**, pp. 2011–2012 (1978). Cited on pages 2 and 27.

[27] R. ARRATIA; "The Motion of a Tagged Particle in the Simple Symmetric Exclusion System on Z"; The Annals of Probability **11**, pp. 362–373 (1983). Cited on pages 2, 10, 27, 29, 36, 43, 99, 186 and 188.

[28] T. IMAMURA, K. MALLICK & T. SASAMOTO; "Large Deviations of a Tracer in the Symmetric Exclusion Process"; Phys. Rev. Lett. **118**, p. 160 601 (2017). Cited on pages 2, 20, 27, 30, 36, 47, 48, 90, 97, 98, 105, 107, 175 and 179.

[29] T. IMAMURA, K. MALLICK & T. SASAMOTO; "Distribution of a tagged particle position in the one-dimensional symmetric simple exclusion process with two-sided Bernoulli initial condition"; arXiv:1810.06131 [math-ph] (2018). Cited on pages 2, 20, 27, 30, 90, 97, 107, 179 and 180.

[30] S. MAJUMDAR & M. BARMA; "Two-tag correlation functions in one-dimensional lattice gases"; Physica A: Statistical Mechanics and its Applications **177**, pp. 366–372 (1991). Cited on pages 2, 5, 44, 54 and 185.

[31] S. SABHAPANDIT & A. DHAR; "Exact probability distribution for the two-tag displacement in single-file motion"; Journal of Statistical Mechanics: Theory and Experiment **2015**, p. 07 024 (2015). Cited on pages 2, 27 and 43.

[32] R. RAJESH & S. N. MAJUMDAR; "Exact tagged particle correlations in the random average process"; Phys. Rev. E **64**, p. 036 103 (2001). Cited on pages 2, 27, 44 and 66.

[33] J. CIVIDINI, A. KUNDU, S. N. MAJUMDAR & D. MUKAMEL; "Correlation and fluctuation in a random average process on an infinite line with a driven tracer"; Journal of Statistical Mechanics: Theory and Experiment **2016**, p. 053 212 (2016). Cited on pages 2, 5, 27, 44, 54, 59 and 66.

[34] A. KUNDU & J. CIVIDINI; "Exact correlations in a single-file system with a driven tracer"; EPL (Europhysics Letters) **115**, p. 54 003 (2016). Cited on pages 2, 27, 44 and 59.

[35] T. OOSHIDA & M. OTSUKI; "Two-tag correlations and nonequilibrium fluctuation–response relation in ageing single-file diffusion"; Journal of Physics: Condensed Matter **30**, p. 374 001 (2018). Cited on pages 2, 4, 6, 40, 59, 66 and 188.

[36] M. J. A. M. BRUMMELHUIS & H. J. HILHORST; "Tracer particle motion in a two-dimensional lattice gas with low vacancy density"; Physica A: Statistical Mechanics and its Applications **156**, pp. 575–598 (1989). Cited on pages 3, 28 and 30.

[37] P. ILLIEN; *Fluctuations and correlations of a biased tracer in a hardcore lattice gas*, Ph.D. thesis; Université Pierre et Marie Curie (2015). Cited on pages 3, 27, 28, 30, 90 and 91.

[38] P. ILLIEN, O. BÉNICHOU, C. MEJÍA-MONASTERIO, G. OSHANIN & R. VOITURIEZ; "Active Transport in Dense Diffusive Single-File Systems"; Phys. Rev. Lett. **111**, p. 038 102 (2013). Cited on pages 3, 4, 20, 27, 28, 29, 30, 36, 41, 59 and 78.

[39] P. ILLIEN, O. BÉNICHOU, G. OSHANIN & R. VOITURIEZ; "Velocity Anomaly of a Driven Tracer in a Confined Crowded Environment"; Phys. Rev. Lett. **113**, p. 030 603 (2014). Cited on pages 3 and 30.

[40] T. E. HARRIS; "Diffusion with "Collisions" between Particles"; Journal of Applied Probability **2**, pp. 323–338 (1965). Cited on pages 3, 26 and 30.

[41] T. SADHU & B. DERRIDA; "Large deviation function of a tracer position in single file diffusion"; Journal of Statistical Mechanics: Theory and Experiment **2015**, p. 09 008 (2015). Cited on pages 4, 10, 20, 27, 29, 40, 104, 183, 187 and 188.

[42] S. F. BURLATSKY, G. OSHANIN, M. MOREAU & W. P. REINHARDT; "Motion of a driven tracer particle in a one-dimensional symmetric lattice gas"; Phys. Rev. E **54**, pp. 3165–3172 (1996). Cited on pages 7, 27, 30, 43, 59, 74, 76, 77 and 97.

[43] C. LANDIM, S. OLLA & S. B. VOLCHAN; "Driven Tracer Particle in One Dimensional Symmetric Simple Exclusion"; Communications in Mathematical Physics **192**, pp. 287–307 (1998). Cited on pages 7, 27, 30, 43, 59, 74, 76, 77, 97 and 98.

[44] C. HEGDE, S. SABHAPANDIT & A. DHAR; "Universal Large Deviations for the Tagged Particle in Single-File Motion"; Phys. Rev. Lett. **113**, p. 120 601 (2014). Cited on pages 10, 20, 27, 29, 104 and 183.

[45] P. L. KRAPIVSKY, K. MALLICK & T. SADHU; "Large Deviations in Single-File Diffusion"; Phys. Rev. Lett. **113**, p. 078 101 (2014). Cited on pages 10, 20, 27, 29, 90, 104, 106, 107 and 183.

[46] H. SPOHN; "Long range correlations for stochastic lattice gases in a non-equilibrium steady state"; Journal of Physics A: Mathematical and General **16**, pp. 4275–4291 (1983). Cited on pages 10, 20, 90, 91 and 106.

[47] P. L. KRAPIVSKY, K. MALLICK & T. SADHU; "Dynamical properties of single-file diffusion"; Journal of Statistical Mechanics: Theory and Experiment **2015**, p. 09 007 (2015). Cited on pages 10, 27, 40, 90, 106 and 107.

[48] T. VISSERS, A. WYSOCKI, M. REX, H. LÖWEN, C. P. ROYALL, A. IMHOF & A. VAN BLAADEREN; "Lane formation in driven mixtures of oppositely charged colloids"; Soft Matter **7**, pp. 2352–2356 (2011). Cited on pages 10 and 124.

[49] K. R. SÜTTERLIN, A. WYSOCKI, A. V. IVLEV, C. RÄTH, H. M. THOMAS, M. RUBIN-ZUZIC, W. J. GOEDHEER, V. E. FORTOV, A. M. LIPAEV, V. I. MOLOTKOV, O. F. PETROV, G. E. MORFILL & H. LÖWEN; "Dynamics of Lane Formation in Driven Binary Complex Plasmas"; Phys. Rev. Lett. **102**, p. 085 003 (2009). Cited on pages 10 and 124.

[50] J. DZUBIELLA, G. P. HOFFMANN & H. LÖWEN; "Lane formation in colloidal mixtures driven by an external field"; Phys. Rev. E **65**, p. 021 402 (2002). Cited on pages 10 and 124.

[51] T. GLANZ & H. LÖWEN; "The nature of the laning transition in two dimensions"; Journal of Physics: Condensed Matter **24**, p. 464 114 (2012). Cited on pages 10, 124 and 139.

[52] M. E. CATES & J. TAILLEUR; "Motility-Induced Phase Separation"; Annual Review of Condensed Matter Physics **6**, pp. 219–244 (2015). Cited on pages 10, 142 and 162.

[53] P. DIGREGORIO, D. LEVIS, A. SUMA, L. F. CUGLIANDOLO, G. GONNELLA & I. PAGONABARRAGA; "Full Phase Diagram of Active Brownian Disks: From Melting to Motility-Induced Phase Separation"; Phys. Rev. Lett. **121**, p. 098 003 (2018). Cited on pages 10, 20 and 142.

[54] U. M. B. MARCONI & C. MAGGI; "Towards a statistical mechanical theory of active fluids"; Soft Matter **11**, pp. 8768–8781 (2015). Cited on pages 10 and 142.

[55] T. F. F. FARAGE, P. KRINNINGER & J. M. BRADER; "Effective interactions in active Brownian suspensions"; Phys. Rev. E **91**, p. 042 310 (2015). Cited on pages 10 and 142.

[56] J. BIALKÉ, H. LÖWEN & T. SPECK; "Microscopic theory for the phase separation of self-propelled repulsive disks"; EPL (Europhysics Letters) **103**, p. 30 008 (2013). Cited on pages 10, 20 and 143.

[57] A. HÄRTEL, D. RICHARD & T. SPECK; "Three-body correlations and conditional forces in suspensions of active hard disks"; Phys. Rev. E **97**, p. 012 606 (2018). Cited on pages 10 and 143.

[58] D. S. DEAN; "Langevin equation for the density of a system of interacting Langevin processes"; Journal of Physics A: Mathematical and General **29**, pp. L613–L617 (1996). Cited on pages 12, 20, 21, 111, 112, 114, 117 and 145.

[59] H. TOUCHETTE; "The large deviation approach to statistical mechanics"; Physics Reports **478**, pp. 1–69 (2009). Cited on pages 19, 36, 46 and 55.

[60] M. KOHL, A. V. IVLEV, P. BRANDT, G. E. MORFILL & H. LÖWEN; "Microscopic theory for anisotropic pair correlations in driven binary mixtures"; Journal of Physics: Condensed Matter **24**, p. 464 115 (2012). Cited on pages 20, 124 and 139.

[61] J. TONER & Y. TU; "Long-Range Order in a Two-Dimensional Dynamical XY Model: How Birds Fly Together"; Phys. Rev. Lett. **75**, pp. 4326–4329 (1995). Cited on pages 20 and 142.

[62] J. TONER; "Reanalysis of the hydrodynamic theory of fluid, polar-ordered flocks"; Phys. Rev. E **86**, p. 031 918 (2012). Cited on pages 20 and 142.

[63] A. TALONI, O. FLOMENBOM, R. CASTAÑEDA-PRIEGO & F. MARCHESONI; "Single file dynamics in soft materials"; Soft Matter **13**, pp. 1096–1106 (2017). Cited on pages 25 and 26.

[64] C. RÖDENBECK, J. KÄRGER & K. HAHN; "Calculating exact propagators in single-file systems via the reflection principle"; Phys. Rev. E **57**, pp. 4382–4397 (1998). Cited on page 27.

[65] P. L. KRAPIVSKY, K. MALLICK & T. SADHU; "Tagged Particle in Single-File Diffusion"; Journal of Statistical Physics **160**, pp. 885–925 (2015). Cited on page 27.

[66] L. TONKS; "The Complete Equation of State of One, Two and Three-Dimensional Gases of Hard Elastic Spheres"; Phys. Rev. **50**, pp. 955–963 (1936). Cited on pages 27 and 85.

[67] B. DERRIDA & A. GERSCHENFELD; "Current fluctuations of the one dimensional symmetric simple exclusion process with step initial condition"; Journal of Statistical Physics **136**, pp. 1–15 (2009). Cited on page 27.

[68] O. BÉNICHOU, P. ILLIEN, G. OSHANIN, A. SARRACINO & R. VOITURIEZ; "Diffusion and Subdiffusion of Interacting Particles on Comblike Structures"; Phys. Rev. Lett. **115**, p. 220 601 (2015). Cited on page 30.

[69] B. D. HUGHES; *Random walks and random environments*; volume 1; Oxford University Press (1995). Cited on pages 34 and 51.

[70] N. LEIBOVICH & E. BARKAI; "Everlasting effect of initial conditions on single-file diffusion"; Phys. Rev. E **88**, p. 032 107 (2013). Cited on page 40.

[71] C. MEJÍA-MONASTERIO & G. OSHANIN; "Bias- and bath-mediated pairing of particles driven through a quiescent medium"; Soft Matter **7**, pp. 993–1000 (2011). Cited on page 68.

[72] F. SPITZER; "Recurrent random walk of an infinite particle system"; Transactions of the American Mathematical Society **198**, pp. 191–199 (1974). Cited on pages 94 and 98.

[73] B. OKSENDAL; *Stochastic differential equations: an introduction with applications*; Springer Science & Business Media (2013). Cited on pages 115, 116 and 144.

[74] E. M. FOULAADVAND & B. AGHAEE; "Driven binary colloidal mixture in a 2D narrow channel with hard walls"; The European Physical Journal E **39**, pp. 1–7 (2016). Cited on page 124.

[75] J. CIVIDINI, C. APPERT-ROLLAND & H.-J. HILHORST; "Diagonal patterns and chevron effect in intersecting traffic flows"; EPL (Europhysics Letters) **102**, p. 20 002 (2013). Cited on page 125.

[76] N. BAIN & D. BARTOLO; "Critical mingling and universal correlations in model binary active liquids"; Nature Communications **8**, p. 15 969 (2017). Cited on pages 135 and 163.

[77] S. GANGWAL, O. J. CAYRE, M. Z. BAZANT & O. D. VELEV; "Induced-Charge Electrophoresis of Metallodielectric Particles"; Phys. Rev. Lett. **100**, p. 058 302 (2008). Cited on pages 142, 165, 166, 195 and 196.

[78] S. GANGWAL, O. J. CAYRE & O. D. VELEV; "Dielectrophoretic Assembly of Metallodielectric Janus Particles in AC Electric Fields"; Langmuir **24**, pp. 13 312–13 320 (2008). Cited on pages 142, 165, 166, 195 and 198.

[79] D. NISHIGUCHI & M. SANO; "Mesoscopic turbulence and local order in Janus particles self-propelling under an ac electric field"; Phys. Rev. E **92**, p. 052 309 (2015). Cited on pages 142, 165, 166, 167 and 195.

[80] D. NISHIGUCHI, J. IWASAWA, H.-R. JIANG & M. SANO; "Flagellar dynamics of chains of active Janus particles fueled by an AC electric field"; New Journal of Physics **20**, p. 015 002 (2018). Cited on pages 142, 165, 166, 195 and 198.

[81] J. PALACCI, C. COTTIN-BIZONNE, C. YBERT & L. BOCQUET; "Sedimentation and Effective Temperature of Active Colloidal Suspensions"; Phys. Rev. Lett. **105**, p. 088 304 (2010). Cited on pages 142 and 165.

[82] F. GINOT, A. SOLON, Y. KAFRI, C. YBERT, J. TAILLEUR & C. COTTIN-BIZONNE; "Sedimentation of self-propelled Janus colloids: polarization and pressure"; New Journal of Physics **20**, p. 115 001 (2018). Cited on pages 142 and 165.

[83] C. KURZTHALER, C. DEVAILLY, J. ARLT, T. FRANOSCH, W. C. K. POON, V. A. MARTINEZ & A. T. BROWN; "Probing the Spatiotemporal Dynamics of Catalytic Janus Particles with Single-Particle Tracking and Differential Dynamic Microscopy"; Phys. Rev. Lett. **121**, p. 078 001 (2018). Cited on pages 142 and 165.

[84] A. BRICARD, J.-B. CAUSSIN, N. DESREUMAUX, O. DAUCHOT & D. BARTOLO; "Emergence of macroscopic directed motion in populations of motile colloids"; Nature **503**, pp. 95–98 (2013). Cited on page 142.

[85] D. GEYER, D. MARTIN, J. TAILLEUR & D. BARTOLO; "Freezing a Flock: Motility-Induced Phase Separation in Polar Active Liquids"; Phys. Rev. X **9**, p. 031 043 (2019). Cited on page 142.

[86] J. DESEIGNE, O. DAUCHOT & H. CHATÉ; "Collective Motion of Vibrated Polar Disks"; Phys. Rev. Lett. **105**, p. 098 001 (2010). Cited on page 142.

[87] O. DAUCHOT & V. DÉMERY; "Dynamics of a Self-Propelled Particle in a Harmonic Trap"; Phys. Rev. Lett. **122**, p. 068 002 (2019). Cited on page 142.

[88] T. VICSEK, A. CZIRÓK, E. BEN-JACOB, I. COHEN & O. SHOCHET; "Novel Type of Phase Transition in a System of Self-Driven Particles"; Phys. Rev. Lett. **75**, pp. 1226–1229 (1995). Cited on page 142.

[89] F. GINELLI; "The Physics of the Vicsek model"; The European Physical Journal Special Topics **225**, pp. 2099–2117 (2016). Cited on page 142.

[90] C. A. WEBER, T. HANKE, J. DESEIGNE, S. LÉONARD, O. DAUCHOT, E. FREY & H. CHATÉ; "Long-Range Ordering of Vibrated Polar Disks"; Phys. Rev. Lett. **110**, p. 208 001 (2013). Cited on page 142.

[91] M. E. CATES & J. TAILLEUR; "When are active Brownian particles and run-and-tumble particles equivalent? Consequences for motility-induced phase separation"; EPL (Europhysics Letters) **101**, p. 20 010 (2013). Cited on page 142.

[92] A. P. SOLON, M. E. CATES & J. TAILLEUR; "Active brownian particles and run-and-tumble particles: A comparative study"; The European Physical Journal Special Topics **224**, pp. 1231–1262 (2015). Cited on page 142.

[93] C. KURZTHALER, S. LEITMANN & T. FRANOSCH; "Intermediate scattering function of an anisotropic active Brownian particle"; Scientific reports **6**, p. 36 702 (2016). Cited on page 142.

[94] U. BASU, S. N. MAJUMDAR, A. ROSSO & G. SCHEHR; "Active Brownian motion in two dimensions"; Phys. Rev. E **98**, p. 062 121 (2018). Cited on page 142.

[95] A. P. SOLON, J. STENHAMMAR, R. WITTKOWSKI, M. KARDAR, Y. KAFRI, M. E. CATES & J. TAILLEUR; "Pressure and Phase Equilibria in Interacting Active Brownian Spheres"; Phys. Rev. Lett. **114**, p. 198 301 (2015). Cited on pages 142, 161 and 162.

[96] É. FODOR, C. NARDINI, M. E. CATES, J. TAILLEUR, P. VISCO & F. VAN WIJLAND; "How Far from Equilibrium Is Active Matter?" Phys. Rev. Lett. **117**, p. 038 103 (2016). Cited on pages 142 and 151.

[97] J. BICKMANN & R. WITTKOWSKI; "Predictive local field theory for interacting active Brownian spheres in two spatial dimensions"; Journal of Physics: Condensed Matter **32**, p. 214 001 (2020). Cited on page 143.

[98] OpenCV; *The OpenCV Reference Manual*; 2nd edition (2019); http://docs.opencv.org. Cited on page 166.

[99] D. ALLAN, C. VAN DER WEL, N. KEIM, T. A. CASWELL, D. WIEKER, R. VERWEIJ, C. REID, THIERRY, L. GRUETER, K. RAMOS, APISZCZ, ZOEITH, R. W. PERRY, F. BOULOGNE, P. SINHA, PFIGLIOZZI, N. BRUOT, L. UIEDA, J. KATINS, H. MARY & A. AHMADIA; "soft-matter/trackpy: Trackpy v0.4.2"; Zenodo (2019); http://dx.doi.org/10.5281/zenodo.3492186. Cited on page 168.

[100] P. VIRTANEN, R. GOMMERS, T. E. OLIPHANT, M. HABERLAND, T. REDDY, D. COURNAPEAU, E. BUROVSKI, P. PETERSON, W. WECKESSER, J. BRIGHT, S. J. VAN DER WALT, M. BRETT, J. WILSON, K. JARROD MILLMAN, N. MAYOROV, A. R. J. NELSON, E. JONES, R. KERN, E. LARSON, C. CAREY, İ. POLAT, Y. FENG, E. W. MOORE, J. VANDERPLAS, D. LAXALDE, J. PERKTOLD, R. CIMRMAN, I. HENRIKSEN, E. A. QUINTERO, C. R. HARRIS, A. M. ARCHIBALD, A. H. RIBEIRO, F. PEDREGOSA, P. VAN MULBREGT & CONTRIBUTORS; "SciPy 1.0: Fundamental Algorithms for Scientific Computing in Python"; Nature Methods **17**, pp. 261–272 (2020). Cited on page 168.

[101] J. HAPPEL & H. BRENNER; *Wall Effects on the Motion of a Single Particle*; Springer Netherlands, Dordrecht (1983). Cited on page 168.

[102] P. L. KRAPIVSKY, S. REDNER & E. BEN-NAIM; *A Kinetic View of Statistical Physics*; Cambridge University Press (2009). Cited on page 185.

[103] S. GUPTA, S. N. MAJUMDAR, C. GODRÈCHE & M. BARMA; "Tagged particle correlations in the asymmetric simple exclusion process: Finite-size effects"; Phys. Rev. E **76**, p. 021 112 (2007). Cited on pages 185 and 186.

[104] J. N. ISRAELACHVILI; *Intermolecular and surface forces*; Academic press (2015). Cited on page 195.

[105] T. M. SQUIRES & M. Z. BAZANT; "Breaking symmetries in induced-charge electro-osmosis and electrophoresis"; Journal of Fluid Mechanics **560**, pp. 65—101 (2006). Cited on pages 195, 196, 197 and 198.

[106] M. Z. BAZANT & T. M. SQUIRES; "Induced-charge electrokinetic phenomena"; Current Opinion in Colloid & Interface Science **15**, pp. 203–213 (2010). Cited on pages 195 and 196.

[107] A. BOYMELGREEN, G. YOSSIFON & T. MILOH; "Propulsion of Active Colloids by Self-Induced Field Gradients"; Langmuir **32**, pp. 9540–9547 (2016). Cited on page 198.

Remerciements

Mes remerciements vont tout d'abord aux deux rapporteurs, Éric Bertin et Andrea Parmeggiani, pour le temps qu'ils ont bien voulu consacrer à la lecture et à l'évaluation du présent manuscrit. Je remercie également Jean-François Joanny (qui a endossé le rôle de président du jury), Cécile Appert-Rolland et Thomas Guérin d'avoir accepté d'évaluer mes travaux de thèse et de participer à la soutenance.

Un grand merci à Olivier Bénichou et Vincent Démery pour m'avoir fait confiance et m'avoir encadré pendant ces trois années. J'ai beaucoup appris à leurs côtés, aussi bien scientifiquement qu'humainement. Merci à Olivier pour les longues heures consacrées à l'avancement du projet, pour ses conseils avisés notamment en matière d'écriture et de présentation orale scientifiques, et pour son optimisme quotidien. Merci à Vincent pour les discussions scientifiques très régulières, autour d'un tableau ou par visioconférence, qui ont permis à mon travail d'avancer ; mais aussi pour les discussions extra-scientifiques, autour d'un repas ou d'une bière.

Je tiens à exprimer ma gratitude envers Kazumasa Takeuchi qui a accepté de m'accueillir deux mois dans son laboratoire à l'université de Tokyo, ce fut une expérience formidable. Merci à Daiki Nishiguchi de m'avoir initié aux arcanes de la matière active expérimentale à cette occasion ; j'espère que nous aurons l'occasion de travailler ensemble de nouveau.

Ma thèse m'a également amené à collaborer avec Gleb Oshanin et Pierre Illien : qu'ils soient ici remerciés pour les discussions fructueuses que nous avons eues ensemble et pour les réflexions pertinentes qu'ils ont formulées.

Le LPTMC m'a procuré un très bon cadre de travail pendant ces trois ans. Je remercie Bertrand Delamotte, le directeur actuel, pour son soutien administratif, ses conseils avisés ainsi que pour les discussions informelles que nous avons eues sur les arts martiaux japonais. Merci également à Pascal Viot, officiellement mon tuteur scientifique, d'une grande aide en ce qui concerne les simulations numériques et l'information sur les perspectives extra-académiques. Plus généralement, merci à tous ceux avec qui j'ai eu l'occasion de manger à la cantine (que je ne peux pas tous citer ici) et avec qui j'ai eu des discussions animées. Merci enfin à l'équipe administrative et technique du LPTMC (Diane Domand, Liliane Cruzel, Patricia Antunes, Michel Quaggetto) pour leur travail de fond qui permet au laboratoire de fonctionner.

Je tiens aussi à remercier le laboratoire Gulliver (ESPCI) dans son ensemble, aussi bien pour les discussions que j'ai eues avec certains de ses membres que pour les deux formidables opportunités scientifiques qu'ont été le « voyage de Gulliver » à l'ENS Lyon et l'école d'hiver sur la matière active à l'université de Tel Aviv.

Pendant ma thèse, j'ai eu la chance d'enseigner dans le cycle CPES de l'université PSL. Je remercie la direction des études pour la confiance accordée, François-Xavier Coudert pour les échanges autour de l'enseignement de la physique statistique, ainsi que les élèves des trois pro-

motions successives auprès desquels j'ai pris beaucoup de plaisir.

Un grand merci à tous les doctorants et post-doctorants avec lesquels j'ai partagé ces trois ans au LPTMC. Mention spéciale pour Alex Barbier–Chebbah qui a animé le bureau 519 en y apportant sa bonne humeur et son dynamisme. Ce fut également un plaisir de croiser le chemin de Maxim Dolgushev, d'abord post-doctorant dans l'équipe et maintenant maître de conférences au laboratoire (félicitations !). Plus généralement, merci à tous ceux avec qui j'ai partagé des séminaires doctorants, des repas ou des sorties au bar : Antony, Claude, Étienne, Gregory, Hugo, Lætitia, Léopold, Marc, Matthias, Mélody, Olivier, Romain, et j'en oublie très certainement.

Je tiens également à mentionner mes amis doctorants physiciens (ou presque) hors LPTMC avec qui j'ai partagé cette expérience déroutante qu'est le doctorat, et qui mériteraient d'être remerciés séparément pour des raisons variées : Alia, Annette, Antoine, David, Louise, Mendes, Nicolas, Paul, Sébastien. Bon courage à ceux qui n'ont pas encore terminé ! Au-delà d'eux, mes amis m'ont soutenu et encouragé pendant ma thèse. Je remercie tout particulièrement le groupe qui se reconnaîtra sous le nom de « B6 » et dont il serait trop long de citer tous les membres. Depuis six ans, j'ai le plaisir de partager avec eux des vacances en hiver et en été ainsi que de nombreuses soirées durant l'année. Ils font profondément partie de mon univers. Merci en particulier à Marion pour les longues discussions que nous avons eues et pour son soutien constant.

Pendant ces trois ans, j'ai suivi (avec assiduité j'espère) les séances du club d'aïkido « La fleur et le sabre » basé à l'ENS. Je tiens à remercier très chaleureusement les deux professeurs, Yolaine Cellier et Pierre-Franck Ehster, pour leur enseignement (dont on osera dire qu'il s'étend au delà des tatamis) et leur gentillesse renouvelée de semaine en semaine. Merci également aux membres du bureau qui font vivre le club, à tous les pratiquants avec qui j'ai partagé de très bons moments, ainsi qu'aux professeurs invités qui ont accepté de nous rendre visite.

Je glisse ici quelques mots discrets à l'intention de Maëliss qui m'a apporté son soutien au quotidien et a aimablement accepté de relire en détail le présent manuscrit.

Pour finir, je remercie du fond du cœur mes parents et ma sœur Lise qui m'ont toujours encouragé dans mon parcours, m'ont soutenu tout au long de ma thèse, et à qui je dois énormément.

Alexis PONCET **15 septembre 2020**

Dynamique et corrélations de systèmes diffusifs forcés

Résumé : Nous examinons les effets collectifs et les corrélations dans les systèmes en file, puis dans des systèmes bidimensionnels hors d'équilibre. Les systèmes en file sont quasi-unidimensionnels et présentent une diffusion anormale liée à de fortes corrélations spatiales que nous caractérisons dans un modèle sur réseau. Nous utilisons d'abord une approche exacte à haute densité qui nous permet d'obtenir la loi de probabilité à N points, puis de mettre en évidence des effets surprenants de coopérativité et compétition entre des intrus biaisés. Nous établissons ensuite des équations hydrodynamiques pour le champ de densité à grande échelle et découvrons une transition de déliaison entre deux intrus entraînés dans des directions opposées. Une extension de cette méthode nous donne la loi de probabilité complète à un point dans certaines limites. Nous examinons aussi les corrélations de paire dans deux systèmes bidimensionnels hors d'équilibre : le mélange binaire forcé composé de deux espèces entraînées dans des directions opposées, et un système de particules browniennes actives qui s'auto-propulsent avec un bruit angulaire. Notre approche repose sur la linéarisation d'une équation exacte pour le champ de densité et est valide à interaction faible. Notre résultat principal est la caractérisation de la structure spatiale des corrélations qui, pour les deux systèmes, montre des formes d'échelle associées à une décroissance algébrique des corrélations.

Mots-clés : processus stochastiques, systèmes en file, matière active, marches aléatoires, théorie des champs

Dynamics and correlations of driven diffusive systems

Abstract: We investigate the collective effects and the correlations in both single-file systems and out-of-equilibrium bidimensional systems. Single-file systems are quasi-one-dimensional and display anomalous subdiffusion due to strong spatial correlations that we characterize in a lattice model. We first use a vacancy-based approach exact at high density that enables us to derive the N-tag probability law, and to uncover remarkable cooperativity and competition effects between biased intruders. We then derive hydrodynamic equations for the large-scale density field and unveil an unbinding transition for two intruders driven in opposite directions. An extension of this method gives us the full one-tag probability law in various limits. We also investigate the pair correlations in two out-of-equilibrium bidimensional systems: a driven binary mixture composed of two species forced towards opposite directions, and an assembly of active Brownian particles which self-propel with angular noise. Our framework builds upon the linearization of an exact stochastic equation for the density field and is valid for weak interactions. Our main result is the characterization of the spatial structure of the correlations. For both systems it shows intriguing scaling forms associated with a power-law decay of the correlations.

Keywords: stochastic processes, single-file systems, active matter, random walks, field theory